

Concrete filled steel pipe piles to concrete cap connection

T.T.J. van der Star

Master of Science Thesis

Concrete filled steel pipe piles to concrete cap connection

by

T.T.J. (Tim) van der Star

to obtain the degree of Master of Science

at the Delft University of Technology,

to be defended publicly on Friday October 10, 2025 at 09:00 AM.

Student number:	5424011	
Project duration:	August 23, 2024 – August 25, 2025	
Thesis committee:	Prof. dr. ir. M. A. N. Hendriks,	TU Delft, chairman
	Dr. F. Kavoura,	TU Delft, supervisor
	Dr. ir. P. A. Korswagen,	TU Delft, supervisor
	Ing. A. S. Rodenhuis,	Dura Vermeer, external supervisor
	Ir. N. Koeman,	Dura Vermeer, external supervisor

An electronic version of this thesis is available at <http://repository.tudelft.nl/>.

Preface

This thesis marks the completion of my Master of Science in Structural Engineering - Concrete Structures at Delft University of Technology. The research originated from a practical design challenge at Dura Vermeer concerning local stress exceedances in concrete caps at the tip of the steel casing of Concrete-Filled Steel Pipe (CFSP) piles, for which Eurocode standards offer no explicit guidance. I was able to undertake this work thanks to an internship opportunity at Dura Vermeer, made possible through contacts from a previous placement.

I am grateful to have contributed to a detail that is both important and widely applied across civil engineering practice, and to have done so within a company with a warm, family-like culture. I extend my sincere thanks to Albert Rodenhuis and Nico Koeman for initiating the thesis topic and for their expertise throughout. I also thank my other colleagues at Dura Vermeer whose insights and support aided the progress of this work.

I am indebted to my graduation committee for their time, feedback, and guidance. In particular, I thank Prof. Max Hendriks for his clear direction during progress meetings and for his emphasis on methodological rigour and validation; Paul Korswagen for his thoughtful ideas on DIANA Finite Element Analysis modelling and his comments on the draft report; and Dr. Florentia Kavoura for her help in determining cross-sectional stress distributions at critical moments and for keeping an overview of the thesis as a whole.

My appreciation also goes to my fellow student, Glenn Mulder, with whom I spent much of my time during the Master's programme. Your company, motivation, and humour made this journey far more enjoyable.

Finally, this achievement would not have been possible without the unwavering support of my family and friends. Thank you for your patience, encouragement, and positivity throughout this process. I hope that the findings of this thesis will assist future design challenges involving CFSP-pile to concrete cap connections.

Tim van der Star
Delft, September 2025

Summary

This thesis investigates the role of confinement on the structural performance of Concrete-Filled Steel Pipe (CFSP) pile to concrete cap connections in the absence of dedicated force transfer provisions such as dowels or shear rings. In current practice, Eurocode 2 provides no explicit guidance on confinement in partially loaded areas, leading to uncertainties in the design of these widely used connections. The central research question was: *“What is the impact of confinement on the structural performance of CFSP-pile to concrete element connections in the absence of force transfer provisions, such as dowels or rings?”*

Methods

A literature review identified two key theoretical frameworks: Mander’s model for confined concrete and Markić’s Dual-Wedge Stress Field (DWSF) approach. Mander’s model describes the passive lateral confining stress generated by reinforcement activated through lateral deformation, while the DWSF model provides a method to capture geometric confinement and improved stress distribution through discretised stress fields. Both models have been verified by extensive experimental research, the results of which were used in this thesis to support the verification of the outcomes. The insights of these models formed the basis for the analytical schematisation, in which both were combined and slightly adjusted to make them applicable to the case study.

A numerical approach was then applied to the case study. After deriving the most comprehensive modelling approach by imitating experimental campaigns and progressively modifying the input until results aligned, it was found that a fully non-linear Finite Element Analysis (FEA) was unfeasible because of stress singularities. A quasi-non-linear FEA model was therefore developed to simulate the pile–cap interface. In this approach, concrete stiffness was manually reduced in high-stress regions according to the stress–strain relationship, which enabled the model to capture the ascending branch of Mander’s confined concrete stress–strain curve and thus investigate confinement effects up to peak stress. The confinement effect was artificially applied by decreasing concrete stiffness in accordance with the confined concrete stress–strain behaviour. This meant that the FEA assumed the confining reinforcement to be fully activated by the lateral deformation of the concrete caused by the pile reaction force. Verification of this assumption would require either a fully non-linear FEA or a physical experiment, both of which fall beyond the scope of this research. For further analysis, it was therefore assumed that the confining reinforcement was fully activated. Analytical calculations, numerical simulations, and comparisons with existing experimental data and Eurocode 2 guidelines were combined to provide a comprehensive assessment of the formation of the DWSF and the corresponding bearing strength.

Results

The study found that confinement increases the bearing capacity of the pile–cap interface to 4.97 times the uniaxial concrete compressive stress, compared to a maximum value of 1.73 according to Eurocode 2. An improved stress distribution was also observed, with a width of 60.8 mm instead of the maximum of 30 mm proposed by Eurocode 2. In addition, the compressive stress in the strut and the inclination of the strut within the DWSF, as obtained by both the analytical and FEA approaches, corresponded closely with the experimental results of Markić et al., while being far more favourable than Eurocode 2 predictions. At the same time, the distributed compressive stress at the end of the stress field remained of almost identical magnitude to the Eurocode values, suggesting a similar stress distribution into unconfined concrete. Passive confinement was assumed to be mobilised by the reinforcement net in the cap, while geometric confinement was provided by the formation of the DWSF and the decomposition of stress tensors along its discontinuity lines, as shown by the results. The analytical models and FEA outcomes were consistent with the upper range of experimental findings reported in the literature by Markić et al. to verify the DWSF model. By contrast, Eurocode 2 systematically underestimated bearing capacity because it does not explicitly include confinement in partially loaded areas. Although the FEA approach could not reproduce post-peak ductility behaviour, it confirmed that confinement delayed crushing and enhanced load transfer with a peak compressive stress of 149.05 MPa at a corresponding

strain of 0.0075.

Discussion

The proposed confinement model is practical and broadly applicable because it relies on simple geometric and material inputs, but its accuracy is limited by several assumptions. Key uncertainties include the idealised rectangular confinement zone, omission of lateral stresses from the pile core reaction, and the degree to which reinforcement located away from the primary load-spread is activated. Moreover, the analytical and numerical models assume homogeneous concrete, whereas heterogeneity in mix and aggregate size can influence behaviour in localised failure zones, creating discrepancies between predicted and actual performance. Overall, the model offers a useful and conservative framework for CFSP-pile to cap connections, yet targeted experiments are required to validate assumptions, refine confinement geometry, and incorporate pile-core effects, thereby improving confidence in its reliability and extending applicability.

Conclusion

This thesis concludes that, provided the confining reinforcement is fully activated, confinement plays a decisive and beneficial role in CFSP-to-cap connections without additional force transfer measures. Through the combined action of passive and geometric confinement, both strength and ductility are enhanced, leading to safer and more efficient structural performance. In practice, this suggests that carefully detailed confinement may reduce the need for costly supplementary transfer provisions, provided that confinement effects are reliably considered in design.

Contents

Preface	i
Summary	ii
1 Introduction	1
1.1 Research content	1
1.2 Research problem	2
1.3 Research objectives	3
1.4 Research scope	3
1.5 Research questions	4
2 Background	6
2.1 Case study	6
2.1.1 Current situation	7
2.1.2 New situation	7
2.2 Problem statement	9
2.2.1 Eurocode 2 - article 6.7	11
2.2.2 Application of EC2 - Article 6.7 to case study	12
2.2.3 Eurocode 2 - article 7.2.1.5	14
2.3 Concrete confinement	15
2.3.1 Eurocode 2 - article 3.1.9	16
3 Literature review	19
3.1 Overview of confinement in structural elements	19
3.1.1 Effects of Confinement on Structural Performance	19
3.1.2 Common Confinement Models	20
3.1.3 Applications of Confinement in Structural Design	20
3.2 Mechanisms of confinement	21
3.2.1 Passive confinement by transverse reinforcement	21
3.2.2 Passive confinement by longitudinal reinforcement	22
3.2.3 Passive confinement by unloaded concrete beyond the concentrated load area	22
3.3 Theoretical models of confinement effects	22
3.3.1 Mander's Model for Confined Concrete	22
3.4 Stress distribution in partially loaded areas	27
3.4.1 Strut and tie model	28
3.4.2 Markic Dual-Wedge stress field	28
3.5 Expected influence on CFSP-pile to concrete connections	32
4 Application and modification of the Theoretical Models	33
4.1 Principal of application	33
4.2 Structural load combinations	35
4.3 Stress and strain distribution at the interface between pile and the cap	35
4.4 Application of Mander's model for confined concrete	38
4.5 Application of Markic Dual Wedge stress field	40
5 Finite Element Analysis development and results	41
5.1 FEA Method	41
5.1.1 Axisymmetric modelling	41
5.1.2 Element type	43
5.1.3 Mesh Size	45
5.2 Material Properties	47

5.2.1	Material Model Selection	47
5.2.2	Confined Thorenfeldt Model with Extended Softening Behaviour	48
5.2.3	Material Behaviour Evaluation in FEA	49
5.2.4	Imitate experimental campaign	57
5.2.5	Material properties for modelling confined concrete	67
5.2.6	Confining reinforcement in a quasi-non-linear FEA	68
5.3	FEA of the 'Oostertoegang' case study project	68
5.3.1	Case study FEA geometry	69
5.3.2	Case study FEA boundary and interface conditions	69
5.3.3	Equivalent load	70
5.3.4	Quasi-Non-linear Modelling Approach for the Concrete Cap	73
5.3.5	Mesh Refinement	79
5.3.6	Results and Verification	80
5.3.7	Sensitivity analysis	89
6	Comparative analysis	92
6.1	Comparison criteria	92
6.1.1	Analytical results	92
6.1.2	FEA results	92
6.1.3	Experimental results	93
6.1.4	Eurocode 2 results	94
6.2	Comparison	95
6.3	Implications of the results	97
7	Discussion	98
7.1	Modelling Assumptions and Idealisations	98
7.2	Applicability and Versatility of the Proposed Model	99
7.3	Sources of Uncertainty and Limitations	100
8	Conclusion and Recommendations	102
8.1	Conclusion	102
8.1.1	Answers to the Sub-Research Questions	102
8.1.2	Answer to the Main Research Question	103
8.2	Relevance for the 'Oostertoegang' case study	104
8.3	Recommendations for Further Research	104
	References	106
A	Python Scripts for Analytical Bearing Stress Calculations	108
A.1	Python Script Stress Distribution at Pile to Cap Interface	108
A.2	Python Script Modified Mander's Model for Confined Concrete	114
A.3	Python Script Markic Dual-Wedge Stress Field Model	116
B	Imitation of Markic et al. Experimental Campaign	118
B.1	Experimentally obtained curves	118
B.2	Linear Axisymmetric FEA of Markić et al. specimens	119
B.3	Linear 3D FEA of Markić et al. specimens	124
B.4	Linear 3D FEA of Markić et al. specimens with reduced E	129
B.5	Analytical calculations for verification	134
C	Python Scripts for Quasi-Non-Linear FEA Verification	139
C.1	Python script corresponding load penetration	139
C.2	Python script secant moduli	140
D	Derivation of the Distributed Force Function on the Pile Core	142
E	Secant Modulus according to Mander's Model for Confined Concrete	144
E.1	Secant Modulus according to the First Iteration	145
E.2	Secant modulus according to the final iteration	147
E.3	Iteration history for the Expected Stress–Strain Behaviour	149
E.4	Iteration history for the lower limit Stress–Strain Behaviour	150

E.5 Iteration history for the upper limit Stress–Strain Behaviour	150
---	-----

Introduction

This chapter describes the context of the research and its main objectives. This also includes the research questions that this thesis attempted to answer.

1.1. Research content

The concrete-filled steel tube (CFST) has long been recognized as a highly attractive option for concrete structures. CFSTs have been widely used in various applications including pressurized members, such as high-rise buildings, underground tunnels, large-span bridges, and offshore structures (Wang et al. 2021). These CFSTs are commonly used as foundation piles for such structures then also called CFST-piles. CFST-piles consists of an inner concrete column enclosed by an outer steel tube. The outer steel tube provides external reinforcement and protects the inner concrete column from potential damage. Additionally, it enhances the durability of the pile foundation in harsh conditions, ensuring a longer lifespan. In return, the inner concrete column contributes to local stability and improves the buckling behaviour of the outer steel tube, while also providing compressive strength. The CFST-pile benefits from the mechanical advantages of both materials (Liu et al. 2023). These piles offer numerous material and mechanical benefits, such as enhanced compressive strength, improved seismic resistance, greater ductility, and better energy absorption. The combination of steel tubes and concrete cores mitigates the inherent brittleness of concrete, thereby providing better damping resistance capacity. CFST-piles can be manufactured in a variety of cross-sectional shapes (see Figure 1.1), including circular, square, rectangular, polygonal, and elliptical (Wang et al. 2021).

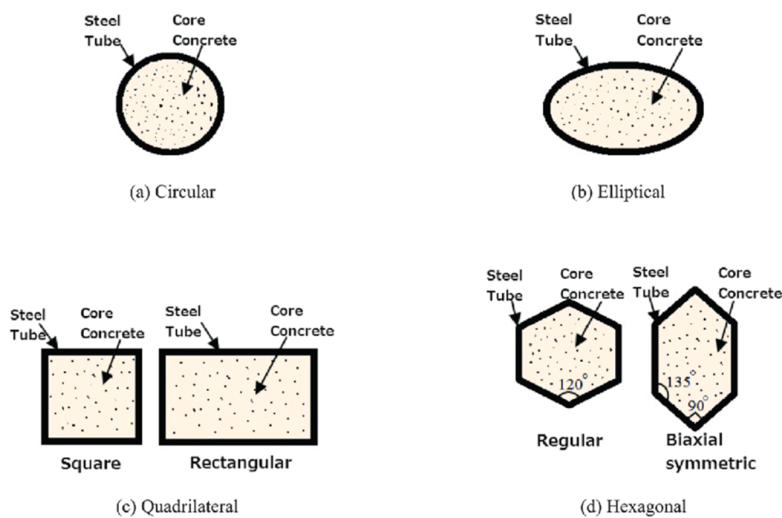


Figure 1.1: CFSTs cross-sectional shapes (Ami et al. 2023)

For foundations it is common to use circular piles filled with concrete. These are named concrete filled steel pipe (CFSP) piles for foundations and are typically installed using either impact driving or drilling methods. The choice of installation method depends primarily on soil conditions and the presence of surrounding structures. Drilled CFSP-piles are particularly effective when a specific penetration depth must be achieved, when the ground contains highly impenetrable layers, when high concentrated loads need to be transferred, and when nearby structures are sensitive to vibrations and ground heave caused by pile driving (Leskela et al. 2005).

CFSP piles are often used in conjunction with concrete caps to form the foundations for bridge pier columns. The concrete cap distributes the forces from the superstructure into the piles. Figure 1.2 shows a schematic representation of how such a substructure is constructed.

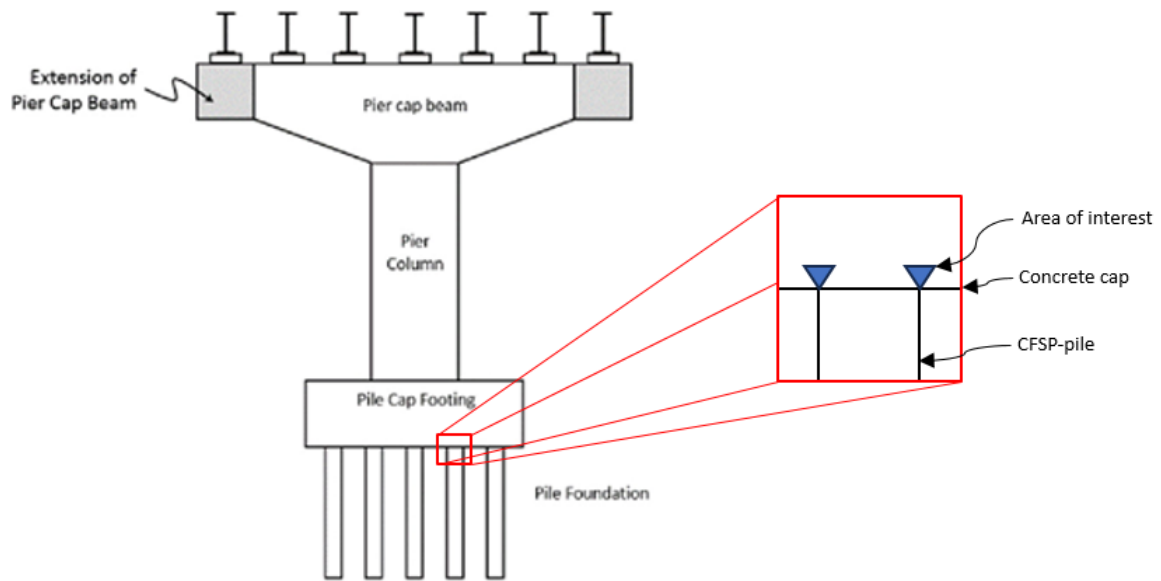


Figure 1.2: Schematisation of a typical bridge substructure (Tan et al. 2019)

This thesis focuses on the connection between the piles and the pile cap, with particular emphasis on the bearing capacity of the concrete directly above the casing of the CFSP-piles.

1.2. Research problem

Although CFSP-piles offer numerous advantages, they also present several challenges when designing structures that utilise them. One frequently debated issue during the design phase is whether the concrete above the steel casing will crush.

This concern arises from the significant differences in stiffness between the various components of CFSP-piles. A CFSP-pile comprises high-stiffness steel elements, such as the pile reinforcement and casing, alongside a relatively low-stiffness concrete core. Figure 1.1 illustrates the cross-section of such a pile. The load is distributed among these components in proportion to their stiffness, meaning that the stiffer elements bear a larger share of the force than the less stiff ones. In scenarios such as the connection between the concrete cap and the CFSP-pile, a substantial amount of force is directly transferred to the steel casing. Given that the area of the steel casing is relatively small, this results in high stresses in that region. Eurocode 2, Article 6.7, is applied to assess the bearing capacity of the concrete in such cases, as it provides an empirical equation for the compressive strength of concrete in partially loaded areas. However, the Eurocode adopts a general approach and does not account for specific factors in this type of connection, such as the high density of reinforcement and the considerable mass of concrete surrounding the loaded area, both of which could enhance the bearing strength by confining the concrete.

In current design approaches, the effect of confinement is not considered; instead, a relatively simple solution is employed to prevent excessive compressive stresses in the concrete above the steel casing. This solution involves welding an annular ring around the top of the steel casing (see Figure 1.4) to increase the surface area over which the force is distributed. While effective, this method is both costly and time-consuming, particularly for piles with large diameters that require heavy rings to be attached using long welds.



Figure 1.3: Cut CFSP-pile

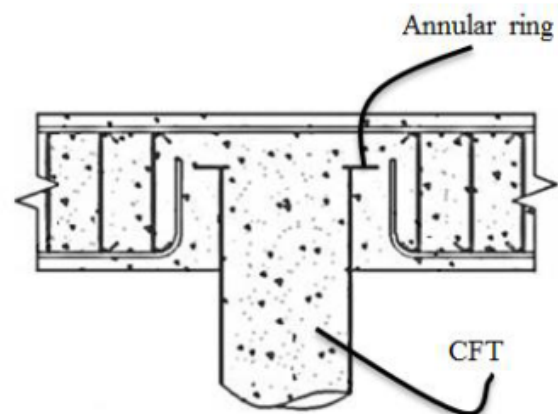


Figure 1.4: Annular ring

1.3. Research objectives

The objective of this study is to deepen the understanding of how confinement affects the structural performance of connections between concrete-filled steel pipe piles (CFSP-piles) and concrete elements. This research aims to explore the underlying mechanisms of confinement, assess its influence in the context of the specific case study, and evaluate the impact of variations in dimensions and material properties. The ultimate goal is to provide a well-founded estimate for the uniaxial compressive strength of concrete, ensuring an even distribution of load over a partially loaded area. Additionally, if it can be demonstrated that no additional provisions are necessary for transferring forces from the concrete to the steel pipe pile, future design discussions could be simplified, and production costs significantly reduced.

1.4. Research scope

This thesis investigates the connection between a concrete-filled steel pipe (CFSP) pile and a reinforced concrete cap, as designed for the foundation of the governing railway bridge in the case-study project; background is provided in chapter 2. This study will focus exclusively on the dimensions, material classes, and loading combinations of bridge four. The scope is limited to this particular case because similar connections are used in various applications, which cannot all be addressed within a single research project with limited time. All calculations and assumptions will adhere to the regulations of Eurocode 2: Design of Concrete Structures, Eurocode 3: Design of Steel Structures, Eurocode 4: Design of composite steel and concrete structures as well as additional principles and preconditions set by ProRail (OVS00030-6 and OVS00030-1).

1.5. Research questions

Based on the problem outlined in 1.2 and the problem analysis, the following research question has been formulated:

What is the impact of confinement on the structural performance of CFSP-pile to concrete element connections in the absence of force transfer provisions, such as dowels or rings?

To find an answer to the main question, this study will employ a structured approach to explore the impact of confinement on the structural performance of CFSP-pile to concrete element connections. The research begins with a comprehensive literature review to establish a theoretical foundation. This is followed by a theoretical analysis to conceptualize the effects of confinement in the context of the case study. Finite Element Analysis (FEA) will be used to model and simulate the structural behaviour under different conditions, with a focus on variations in dimensions and material properties. The accuracy of the FEA models will be assessed through sensitivity analysis, and the results will be compared with existing literature and Eurocode guidelines. The study will conclude with recommendations based on the findings, aiming to optimize design practices and reduce costs.

As a guide to ensure the correct steps are followed and all relevant information is considered when answering the main research question, several sub-questions have been formulated. The tables below presents the sub-questions, specifying the purpose, methodology, tools required, desired outputs and sections of this report where each sub-question is answered.

Sub question 1	What are the underlying mechanisms of confinement in structural elements?
Purpose	Establish a clear theoretical understanding of how confinement works within structural elements, including the physics and mechanics involved.
Methodology	A literature study is conducted to define the conditions under which confinement occurs and how it affects the strength and ductility of concrete.
Products	A schematisation of confinement is provided, along with an explanatory text based on the literature.
Tools	Literature sources, including both internet and books, and LaTeX for documentation.
Section	chapter 3. Literature review chapter 4. Application and modification of the Theoretical Models
Sub question 2	Which structural components contribute to the development of lateral confining stress in CFSP-pile to concrete element connections?
Purpose	Directly link the mechanisms of confinement to the case study, focusing on which elements in the case study situation could possibly contribute to improved concrete strength and ductility.
Methodology	A comparative literature review was conducted to identify structural components that contribute to lateral confinement in concrete. Key mechanisms found in literature were then compared with the configuration of the CFSP-to-concrete cap connection in the case study. This made it possible to determine which confinement mechanisms are likely active in the studied setup.
Products	A schematic description from the case study is provided and the components which could impact the strength and ductility of the connection are defined. Also a python script is written that calculates the lateral confining stress and increased bearing strength of the concrete.
Tools	Literature review, Python for coding and AutoCAD to create drawings.
Section	chapter 4. Application and modification of the Theoretical Models

Sub question 3	What is the most comprehensive approach for modelling confinement in CFSP-pile to concrete connections?
Purpose	Develop a comprehensive modelling strategy to numerically simulate the confinement effect in connections based on the literature.
Methodology	Determine the necessary parameters to accurately simulate how stresses develop based on confinement in FEA models. Recreate FEA models from experimental test setups and refine material parameters until the results align.
Products	A detailed description of the setup for the FEA simulations, including the conditions, parameters, and their justifications.
Tools	Diana FEA software and experimental results from literature review
Section	chapter 5. FEA
Sub question 4	What are the effects of confinement on structural performance according to the finite element results of the test setup?
Purpose	Investigate and quantify the impact of confinement based on the outcomes from the FEA.
Methodology	The results of the FEA simulations are presented and evaluated, emphasizing how confinement affects structural performance, including the reaction forces, ductility, stiffness, and overall behaviour.
Results	Output plots from Diana, showing displacement, normal stress, lateral stress and principal stress to evaluate material behaviour.
Products	A detailed explanation of outcomes including contour plots and curves.
Tools	Diana FEA software, Excel for plotting curves, python for calculations and Latex for documentation.
Section	chapter 5. FEA
Sub question 5	How do the theoretical model and FEA results of the research compare with existing literature and Eurocode guidelines?
Purpose	Indicate how reliable and accurate the results of this master thesis are.
Methodology	Compare the findings with those of literature research and identify any strong overlaps or contradictions. Review the implications of these results for the CFSP to concrete cap connection design field.
Products	Figures and tables illustrating and describing the findings from literature and the results of this thesis, outlining the differences/similarities between the two.
Tools	Literature review, Diana FEA software, Excel for plotting curves and latex for documentation.
Section	chapter 6. Comparative Analysis

2

Background

This chapter provides context for the study by discussing the significance of CFSP-pile to concrete element connections in construction and the role of confinement in enhancing structural performance. It also introduces the case study that serves as a reference for this master thesis, offering a general overview of the project and detailing the design and load combinations related to the connection explored in this thesis. Additionally, it explains how forces are transferred from the superstructure to the substructure, highlighting the problem that this thesis aims to address.

2.1. Case study

This master's thesis was made possible by Dura Vermeer, one of the leading contractors in the Netherlands. Dura Vermeer is active in residential construction, utility construction, infrastructure and technology. Their core activities include designing, developing and realising construction and infrastructure projects, encompassing management and maintenance, renovation and transformation.

Owing to Dura Vermeer's extensive experience, ProRail¹ selected Dura Vermeer as the contractor for the 'Amsterdam Oostertoegang' project. This project involves the replacement of five railway bridges on the east side of Amsterdam Central Station as part of the broader 'Programma Hoogfrequent Spoorvervoer' (PHS) contract, which also includes adjustments to Amsterdam Central Station and the surrounding tracks. These modifications are intended to enhance the capacity, quality and robustness of the rail infrastructure around Amsterdam Central Station in the coming years.



Figure 2.1: Location of the case study project 'Oostertoegang Amsterdam Central Station'

¹Railway manager of the Netherlands.

2.1.1. Current situation

The current train entrance on the east side of Amsterdam Central Station consist of four steel through bridges and one more recently build concrete through bridge. The bridges have reached the end of their lifespan and from the corrosion on the outside it is visible that the bridges need to be replaced.

In the right top corner image of Figure 2.1 each bridge has been assigned a number. The bridge that has assigned number 5 to it is the concrete bridge which was built later than the steel bridges number 1 to 4. All five bridges will be replaced for new static determined steel through bridges.

2.1.2. New situation

In the new configuration, new embankments will be constructed behind the existing embankments of bridges 1 to 4. The embankment for bridge 5 has been deemed sufficiently strong and will be reused. Currently, the middle pillars of the bridges are located on the quay. In the new setup, the middle pillars will be placed next to the quay, inside the waterway. Due to the changes in support locations, the first and third bridge segments will be longer than the middle segment. Figure 2.2 illustrates the new positions of the bridge pillars and embankments, as well as the lengths of the new bridge spans.

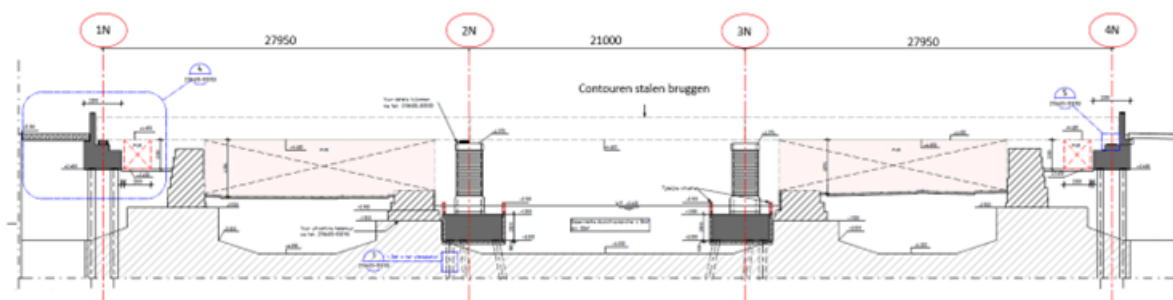


Figure 2.2: Dimensions of the new bridges compared to the old bridges (light grey)

At the locations where the embankments and middle pillars are shifted a new foundation should be built for these supports. The foundation of the bridge embankment and pillars will consist of concrete-filled steel pipe piles with a concrete cap on top, as shown in Figure 2.3. A more detailed image of the connection between the piles and the concrete cap is provided in Figure 3. Both figures depict a portion of the actual design for the 'Oostertoegang' project. In this project, the embankments and pillars are founded on Hekpiles. The Hekpile system consists of a steel casing tube equipped with a detachable screw point. A drilling motor drives this screw point to the desired depth, after which the reinforcement and concrete mix are inserted (Van 't Hek, 2024). Before the piles can be drilled into the subsoil they have to go through a 2 meters thick layer of tamped concrete which is part of the current bridge foundation.

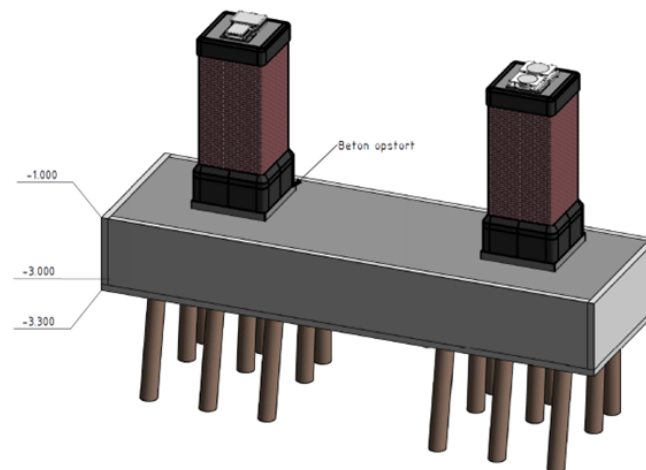


Figure 2.3: Substructure at middle pillar in new situation of the case study project

All the installed piles will have a casing with a diameter of 508mm and a wall thickness of 10mm. The screw point used to drive the piles to -22.00m below N.A.P. will have a diameter of 680mm. Once the piles are in place, the reinforcement will be installed in different segments as shown in Figure 2.4. After the reinforcement is in place the piles will be filled with concrete C30/37.

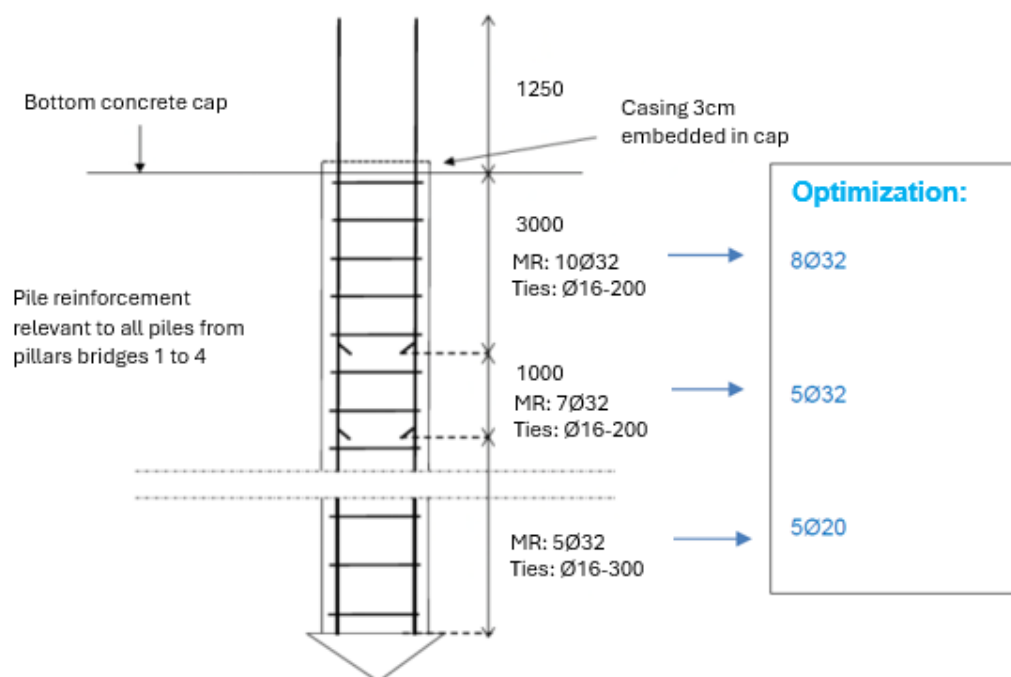


Figure 2.4: Optimization of pile reinforcement for piles at middle pillars in new situation of the case study project

The pile cap that forms the platform for the middle pillars of the bridge and the embankment are placed on top of the piles and consist of reinforced C30/37 concrete. The pile reinforcement will have an anchorage length of 830mm into the concrete elements on top of the piles. The cross section of the concrete element is 4,5m wide and 2,0m high and the element is provided with longitudinal and latitudinal reinforcement. A drawing of the cross section is illustrated in Figure 2.5.

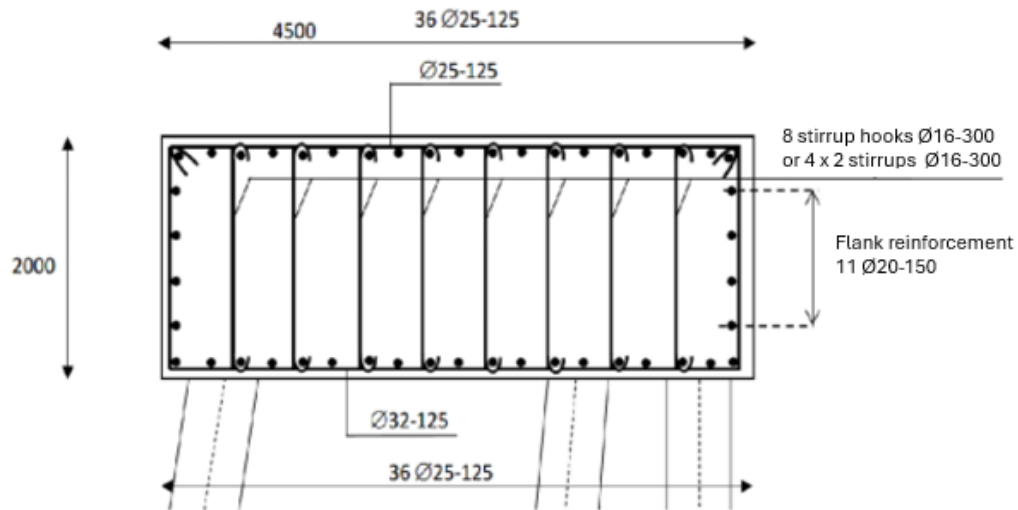


Figure 2.5: Cross section of the concrete pile cap at middle pillars in new situation of the case study project

2.2. Problem statement

During the design stage of the Amsterdam Oostertoegang project it was found that the compressive stress in the concrete cap directly on top of the steel pipe pile casing exceeds the compressive strength of the concrete. According to the calculations in the report 'DO berekeningsrapport onderbouw pijlers brug 1 t/m 4' (Rodenhuis 2023), the governing axial compressive force found in the piles at the middle pillars of the bridges is 2353 kN. The steel casing of the foundation piles ($\text{Ø}508 \times 10 \text{ mm}$) is embedded 30 mm into the concrete. The contact stress between the top of the pipe pile and the concrete (C30/37) is checked based on EC2 – article 6.7 (2). The maximum pile reaction is taken into account, distributed proportionally according to the stiffness over the concrete cross-section and the steel casing. Note that the governing pile head forces do not include a bending moment. Load cases involving bending moments will be considered later in this report.

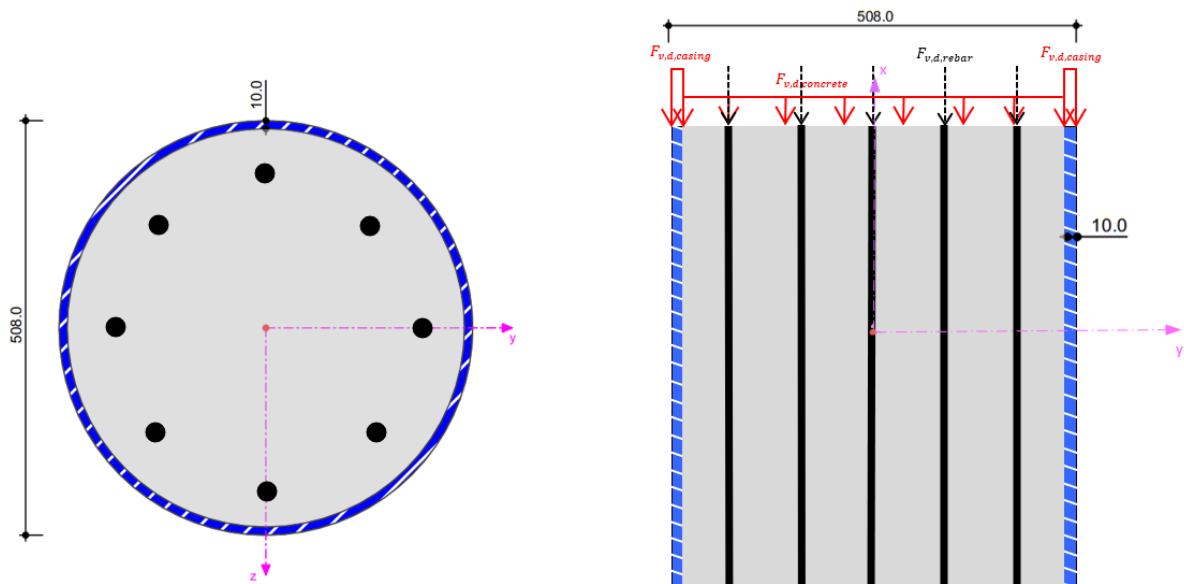


Figure 2.6: Horizontal and vertical cross section of CFSP-pile with load distribution over steel casing and concrete core

To determine the ratio between the load being distributed to the steel casing and the load being distributed to the concrete core, the following calculations were made:

$$\text{ratio}_{\text{casing}} = \frac{EA_{\text{casing}}}{EA_{\text{casing}} + EA_{\text{rebar}} + EA_{\text{concrete}}} = 0.38 \quad \text{Eq. 2.1}$$

$$\text{ratio}_{\text{rebar}} = \frac{EA_{\text{rebar}}}{EA_{\text{casing}} + EA_{\text{rebar}} + EA_{\text{concrete}}} = 0.16 \quad \text{Eq. 2.2}$$

$$\text{ratio}_{\text{concrete}} = \frac{EA_{\text{concrete}}}{EA_{\text{casing}} + EA_{\text{rebar}} + EA_{\text{concrete}}} = 0.46 \quad \text{Eq. 2.3}$$

where:

$$\begin{aligned} EA_{\text{casing}} &= E_{\text{casing}} \times A_{\text{casing}} \\ EA_{\text{rebar}} &= E_{\text{rebar}} \times A_{\text{rebar}} \\ EA_{\text{concrete}} &= E_{\text{concrete}} \times A_{\text{concrete}} \\ A_{\text{casing}} &= \frac{1}{4} \times \pi \times (D_{\text{pile}}^2 - (D_{\text{pile}} - 2 \times t_{\text{pile}})^2) = 15.645 \text{ mm}^2 \\ A_{\text{rebar}} &= n_{\text{bars}} \times 0.25 \times \pi \times D_{\text{bar}}^2 = 6433.98 \text{ mm}^2 \\ A_{\text{concrete}} &= \frac{1}{4} \times \pi \times (D_{\text{pile}} - 2 \times t_{\text{pile}})^2 = 187.037 \text{ mm}^2 \end{aligned}$$

and:

$$\begin{aligned} E_{\text{casing}} &= 200.000 \text{ N/mm}^2 && \text{is the modulus of elasticity of the steel casing} \\ E_{\text{rebar}} &= 210.000 \text{ N/mm}^2 && \text{is the modulus of elasticity of the steel rebar} \\ E_{\text{concrete}} &= 20.000 \text{ N/mm}^2 && \text{is the modulus of elasticity of the concrete core} \\ D_{\text{pile}} &= 508 \text{ mm} && \text{is the outer diameter of the pile} \\ t_{\text{pile}} &= 10 \text{ mm} && \text{is the thickness of the steel casing} \\ n_{\text{bars}} &= 8 && \text{is the number of reinforcement bars} \end{aligned}$$

According to EC2 – article 6.7 (2), the compressive strength of the concrete may be multiplied by a factor of 3 for an even distribution of the load over a partially loaded area. However, EC2-4 – article 7.2.1.5 states that the compressive strength could be multiplied by a factor of 7.5 in the specific case of the pull-out resistance of headed fasteners. It is interesting to note that in comparable cases when looking at partially loaded areas, the compressive strength of the concrete may be increased by a significantly larger factor than that stated in EC2 – article 6.7 (2). Why is there such a difference, and how does this impact the concrete crushing at the top of steel pile casings?

2.2.1. Eurocode 2 - article 6.7

Eurocode 2, Article 6.7, addresses the design considerations for partially loaded areas in reinforced concrete structures. These are regions where the applied load does not act uniformly over the entire area but is concentrated on a portion of it, such as a load applied by a column or a concentrated point load on a slab. The code explains how the load is distributed across the concrete surface. It takes into account the spreading of the load within the concrete, which leads to a stress distribution that is more favourable than the concentrated load itself.

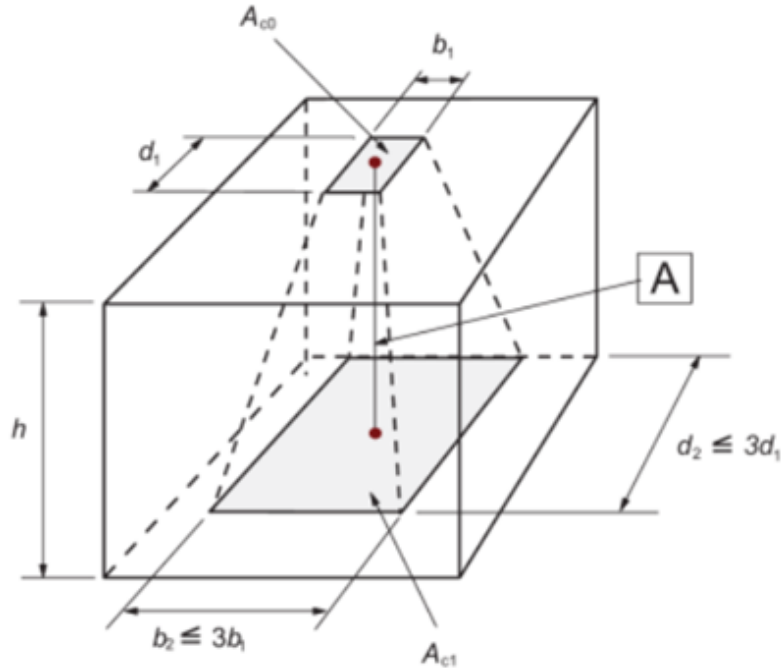


Figure 2.7: Spreading of a concentrate load according to Eurocode 2 - article 6.7 (Standardization (CEN) 2011)

To account for this distribution, the article defines an "effective area" around the loaded region. The effective area is larger than the actual loaded area and depends on the geometry and the load path through the concrete element. The effective area, defined by dimensions b_2 and d_2 , can be up to three times the width and three times the length of the loaded area, which is defined by dimensions b_1 and d_1 . The maximum bearing capacity for partially loaded areas is described in the code as:

$$F_{Rdu} = A_{c0} \times f_{cd} \times \sqrt{\frac{A_{c1}}{A_{c0}}} \leq A_{c0} \times f_{cd} \times 3.0 \quad \text{Eq. 2.4}$$

where:

A_{c0} is the loaded area.

A_{c1} is the maximum area over which the load is spread according to the design and which has an equal shape as that of area A_{c0}

In this equation the factor 3.0 on the right side of the equation is directly related to the limitation of the effective area being 3 times wider and longer than the loaded area. This is validated by a simple calculation where $b_1 = d_1 = 1$ and $b_2 = d_2 = 3$:

$$\sqrt{\frac{3 \times 3}{1 \times 1}} = \sqrt{\frac{9}{1}} = \sqrt{9} = 3.0$$

This shows that only geometrical influences are taken into account for the favourable bearing capacity of the concrete. Besides the maximum size of the effective area (A_{c1}) compared to the loaded area (A_{c0}), the effective area must also meet the following conditions:

1. The height (h) for the distribution of the load in the load direction should correspond to the conditions given in the figure above;
2. The centre of the area A_{c1} of the arithmetic distribution should lie on the line of force through the centre of the loaded area A_{c0} ;
3. If more than one compressive force acts on the concrete cross-section, the areas of the arithmetic distribution should not overlap;
4. To take up any tensile forces in lateral direction due to the uniaxial loading, reinforcement should be placed.

The main objective of Article 6.7 is to ensure that concentrated loads do not lead to excessive local stresses that could cause failure or significant damage to the concrete element.

2.2.2. Application of EC2 - Article 6.7 to case study

When applying Eurocode 2, Article 6.7, to the case study in this thesis, the calculations are divided into two parts, each representing stresses within their respective stress distribution zones. These zones will eventually be combined due to the overlapping stress areas. The first set of calculations describes the stress distribution resulting from the reaction forces of the concrete core in the CFSP piles. The reaction force of the concrete core is equal to 46% of the total pile reaction force, as determined by the stiffness ratio outlined in section 2.2. The compressive stress σ_0 at the level of the loaded area A_0 and σ_1 at the level of the effective area A_1 can be calculated by dividing the compressive load on each area by the respective area.

$$\sigma_{0,core} = \frac{F_{vd,core}}{A_0} = 5.73 \text{ N/mm}^2 \leq 3.0 \times f_{cd} = 3.0 \times \frac{30}{1.5} = 60 \text{ N/mm}^2 \quad \text{Eq. 2.5}$$

$$\sigma_{1,core} = \frac{F_{vd,core}}{A_1} = 0.64 \text{ N/mm}^2 \leq f_{cd} = \frac{30}{1.5} = 20 \text{ N/mm}^2 \quad \text{Eq. 2.6}$$

where:

$\sigma_{0,core}$	is the compressive stress at the loaded area
$\sigma_{1,core}$	is the compressive stress at the effective area
$F_{vd,core} = 0.46 \times F_{vd,pile} = 1071 \text{ kN}$	is the load distributed to the concrete core)
$F_{vd,pile} = 2353 \text{ kN}$	is the total load on the pile
$A_{0,core} = A_{concrete} = 187.037 \text{ mm}^2$	is the loaded area of the concrete core
$A_{1,core} = \frac{1}{4} \times \pi \times D_1^2 = 1.683.341 \text{ mm}^2$	is the effective area of the concrete core

Due to the Poisson's ratio of the concrete, compressive forces within the material also generate tensile stresses in the lateral direction. Assuming the activation of the reinforcement is negligible, the lateral stress is not transferred to the reinforcement according to the common strut and tie model but is instead distributed linearly through the concrete over the height of the stress zone. The lateral stress is defined as the product of the material's compressive strength and its Poisson's ratio.

$$\sigma_{L0,core} = \sigma_{0,core} \times \nu = 1.15 \text{ N/mm}^2 \leq f_{ctd} = 1.35 \text{ N/mm}^2 \quad \text{Eq. 2.7}$$

$$\sigma_{L1,core} = \sigma_{1,core} \times \nu = 0.13 \text{ N/mm}^2 \leq f_{ctd} = 1.35 \text{ N/mm}^2 \quad \text{Eq. 2.8}$$

where:

$\sigma_{L0,core}$	is the lateral tensile stress at the loaded area
$\sigma_{L1,core}$	is the lateral tensile stress at the effective area
$\nu = 0,2$	is the Poisson's ratio of concrete

According to Eq. 2.5, Eq. 2.6, Eq. 2.7 and Eq. 2.8, neither the concrete compressive strength nor the concrete tensile strength is exceeded by the compressive and tensile stresses resulting from the reaction forces from the concrete core of the CFSP piles. The schematisation of the stress distribution which follows from Eurocode 2 – article 6.7 and associated calculations is shown in Figure 2.8.

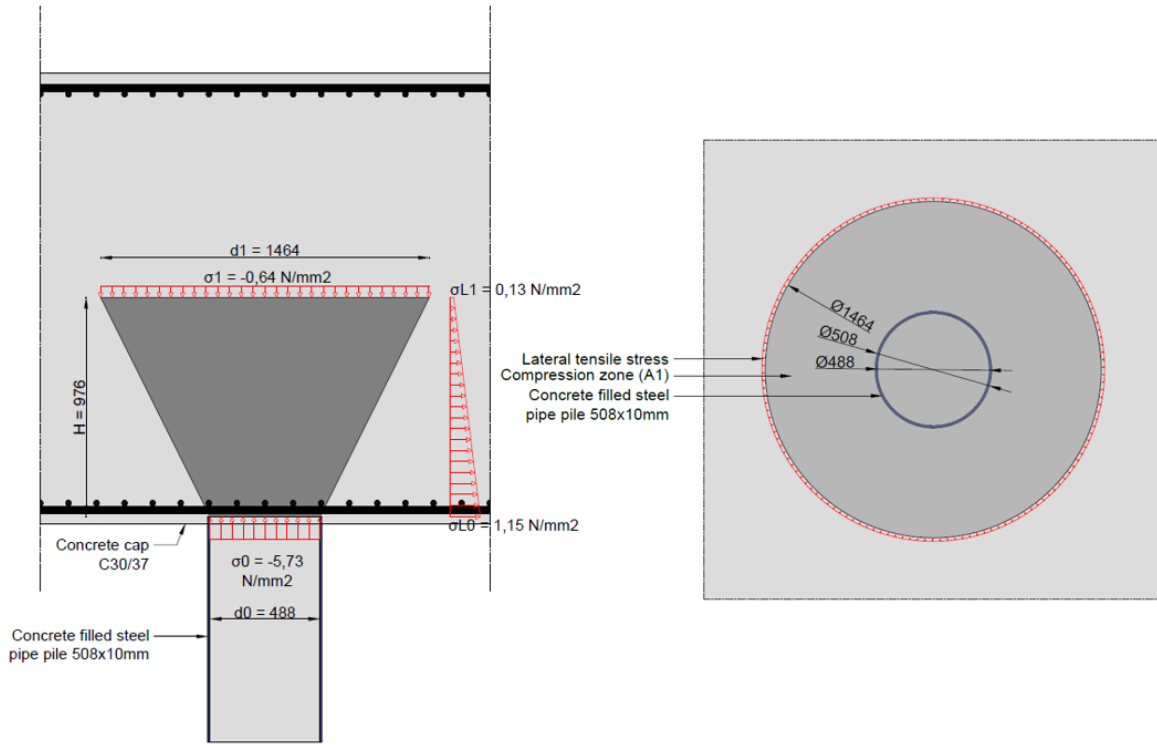


Figure 2.8: Stress distribution reaction forces concrete core CFSP-piles

The second set of calculations describes the stress distribution resulting from the reaction forces of the steel casing of the CFSP piles. The reaction force of the steel casing is equal to 38% of the total pile reaction force, as determined by the stiffness ratio outlined in section 2.2. However, in this case the load can only spread in one radial direction, since the reaction force acts as a closed circular line load rather than over a finite area. Consequently, lateral spreading in the orthogonal direction is precluded (i.e. $d_1 = d_2$) and the bearing stress increases by a factor of $\sqrt{3}$ rather than 3.

$$\sigma_{0,casing} = \frac{F_{vd,casing}}{A_0} = 57.24 \text{ N/mm}^2 > \sqrt{3.0} \times f_{cd} = \sqrt{3.0} \times \frac{30}{1.5} = 34.64 \text{ N/mm}^2 \quad \text{Eq. 2.9}$$

$$\sigma_{1,casing} = \frac{F_{vd,casing}}{A_1} = 19.08 \text{ N/mm}^2 < f_{cd} = \frac{30}{1.5} = 20 \text{ N/mm}^2 \quad \text{Eq. 2.10}$$

where:

$\sigma_{0,casing}$

$\sigma_{1,casing}$

$F_{vd,pile} = 2353 \text{ kN}$

$F_{vd,casing} = 0.38 \times F_{vd,pile} = 895.59 \text{ kN}$

$A_{0,casing} = A_{casing} = 15.645 \text{ mm}^2$

$A_{1,casing} = 3 \times A_{casing} = 46.935 \text{ mm}^2$

is the compressive stress at the loaded area

is the compressive stress at the effective area

is the total load on the pile

is the load distributed to the steel casing

is the loaded area of the steel casing

is the effective area of the steel casing

$$\sigma_{L0,casing} = \sigma_{0,casing} \times \nu = 6.93 \text{ N/mm}^2 > f_{ctd} = 1.35 \text{ N/mm}^2 \quad \text{Eq. 2.11}$$

$$\sigma_{L1,casing} = \sigma_{1,casing} \times \nu = 3.82 \text{ N/mm}^2 > f_{ctd} = 1.35 \text{ N/mm}^2 \quad \text{Eq. 2.12}$$

where:

$\sigma_{L0,casing}$ is the lateral tensile stress at the loaded area

$\sigma_{L1,casing}$ is the lateral tensile stress at the effective area

$\nu = 0,2$ is the Poisson's ratio of concrete

According to Eq. 2.9, Eq. 2.10, Eq. 2.11 and Eq. 2.12, both the concrete compressive strength and the concrete tensile strength is exceeded by the compressive and tensile stresses resulting from the reaction forces from the steel casing of the CFSP piles, even without taking into account the overlap of the stress regions which would even further increase the stress levels in the concrete above the steel casing. The schematisation of the stress distribution which follows from Eurocode 2 – article 6.7 and associated calculations is shown in Figure 2.9.

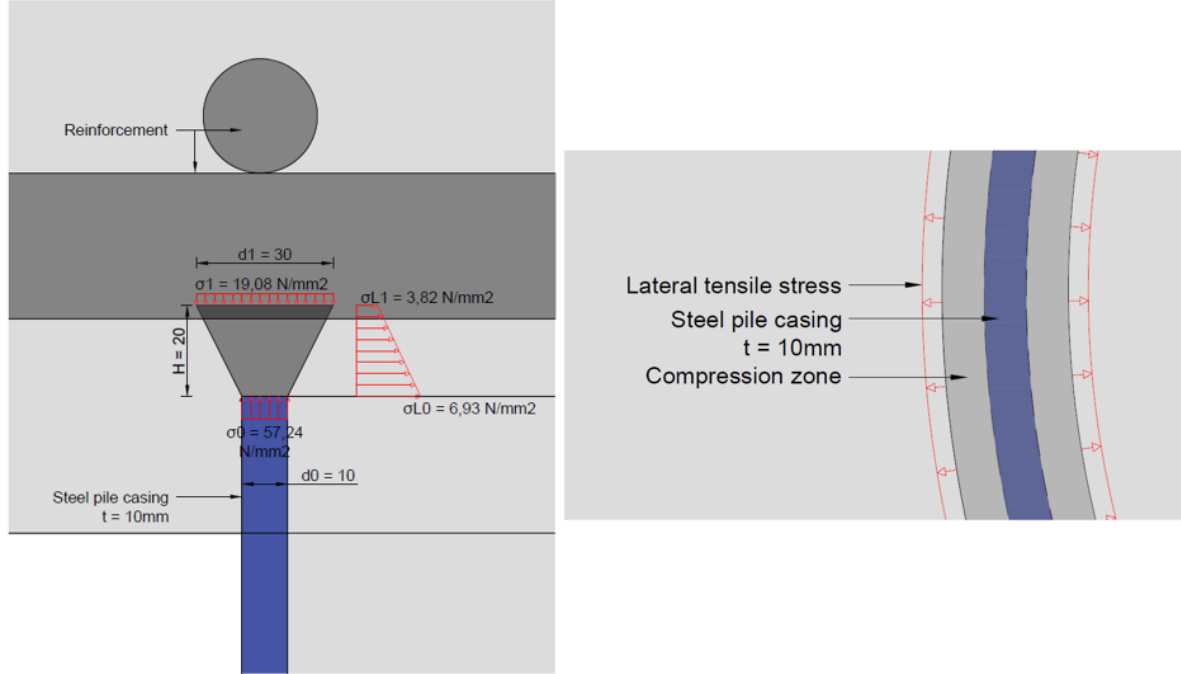


Figure 2.9: Stress distribution reaction forces steel casing CFSP-piles

In conclusion, only in very localised areas on the steel pile casing is the concrete compressive strength exceeded by the axial compression. Due to this axial compression and the Poisson's ratio of the concrete, a lateral tensile stress develops within the concrete. The high compression force also leads to an exceedance of the concrete's tensile strength in the lateral direction. This lateral tensile stress could cause the concrete to crack if there is insufficient reinforcement in the tensile zone to absorb these stresses.

2.2.3. Eurocode 2 - article 7.2.1.5

Eurocode 2-4 – article 7.2.1.5 (Standardization (CEN) 2018) describes the pull-out failure of fasteners. The characteristic resistance $N_{Rk,p}$ of headed fasteners is limited by the concrete pressure under the head of the fastener which is described by the following formula:

$$N_{Rk,p} = k_2 \times A_h \times f_{ck} \quad \text{Eq. 2.13}$$

where:

- A_h is the load bearing area of the head of the fastener;
- $k_2 = 7.5$ for fasteners in cracked concrete;
- $k_2 = 10.5$ for fasteners in uncracked concrete;

The 7.5 and 10.5 factors are empirically determined based on a combination of experimental research, field studies, and statistical analysis. They are included in Eurocode 2-4 to provide a standardized approach to estimating the pull-out resistance of fasteners in both cracked and uncracked concrete, ensuring safety and reliability in design.

Both k_2 factors are greater than the maximum value of 3.0, which is the highest allowable increase in concrete bearing capacity according to EC2, Article 6.7. There is a relatively large difference in magnitude between the two articles, and the methods used to determine the factors also appear to differ. While k_2 is determined empirically, the factor of 3.0 seems to be derived purely through an analytical consideration of the dimensions.

This difference immediately reflects the knowledge gap in the mechanical understanding of high compressive forces on concrete members over limited contact areas that arises in many engineering fields. Previous studies have demonstrated that the maximum average contact pressure achievable across the loaded area, often referred to as bearing capacity or bearing strength, can be several times greater than the uniaxial compressive concrete strength (Markic et al. 2022b). One of the effects that could contribute to this increased compressive strength is the beneficial effect of biaxial confinement just below the loaded area.

2.3. Concrete confinement

Biaxial confinement can be attributed to two main factors: the deviation of compressive stress trajectories and the restriction of lateral expansion by the surrounding, non-loaded parts of the concrete specimen. The first factor, which depends primarily on the geometry and load concentration ratio, functions independently of lateral deformations, akin to the transverse compression applied in triaxial tests (active confinement). The second factor necessitates the transverse expansion of concrete for activation, known as passive confinement. Extensive testing has shown that all forms of confinement enhance the axial compressive strength of concrete by approximately four times the confining stress, along with a significant increase in ductility (see Figure 2.10) ((Markic et al. 2018)).

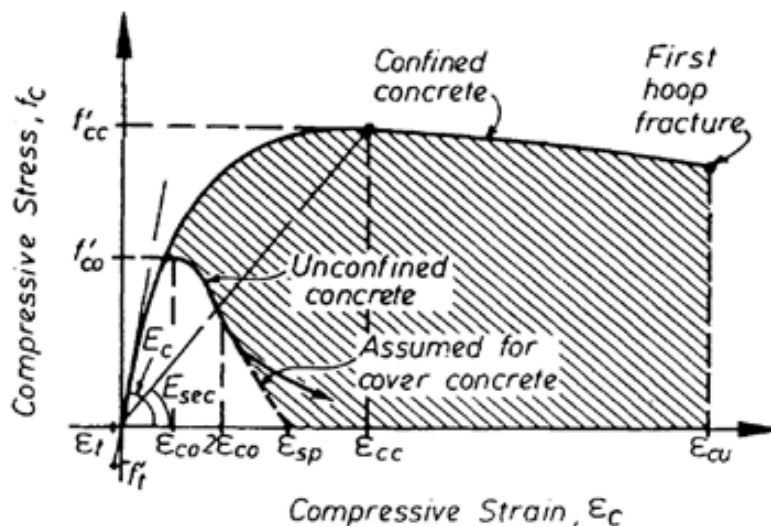


Figure 2.10: Stress-strain relation in confined and unconfined concrete (Mander et al. 1988b)

But to what extent does this affect imply to the situation of the case study? In most studies confinement is found in places where stirrups are applied. However, as shown in Figure 2.11, no stirrups are located at the location of the piles. There is only longitudinal Ø25-125 (purple), transverse Ø32-125 (blue) and pile reinforcement 8-Ø32. Can the longitudinal and transverse reinforcement be considered as forming a stirrup that creates a confined region between them?

2.3.1. Eurocode 2 - article 3.1.9

Eurocode 2 allows for an increase in compressive strength (f_{cd}) as a function of the confining pressure (σ_2) provided by the reinforcement. Volume 2 of the CEB-FIB Model Code 2010 (Structural Concrete (fib) 2012) provides the following equation for calculating the confining pressure exerted by the reinforcement:

$$\sigma_2 = \omega_c f_{cd} \left(1 - \frac{s_c}{a_c}\right) \left(1 - \frac{s_c}{b_c}\right) \left(1 - \frac{\sum b_i^2/6}{a_c b_c}\right) \quad \text{Eq. 2.14}$$

where:

σ_2	Effective confining pressure in lateral direction for rectangular cross sections
f_{cd}	Design compressive strength of concrete
ω_c	Confinement effectiveness factor
s_c	Spacing of the stirrups
a_c, b_c	Dimensions of the concrete section
b_i	Width of confined concrete

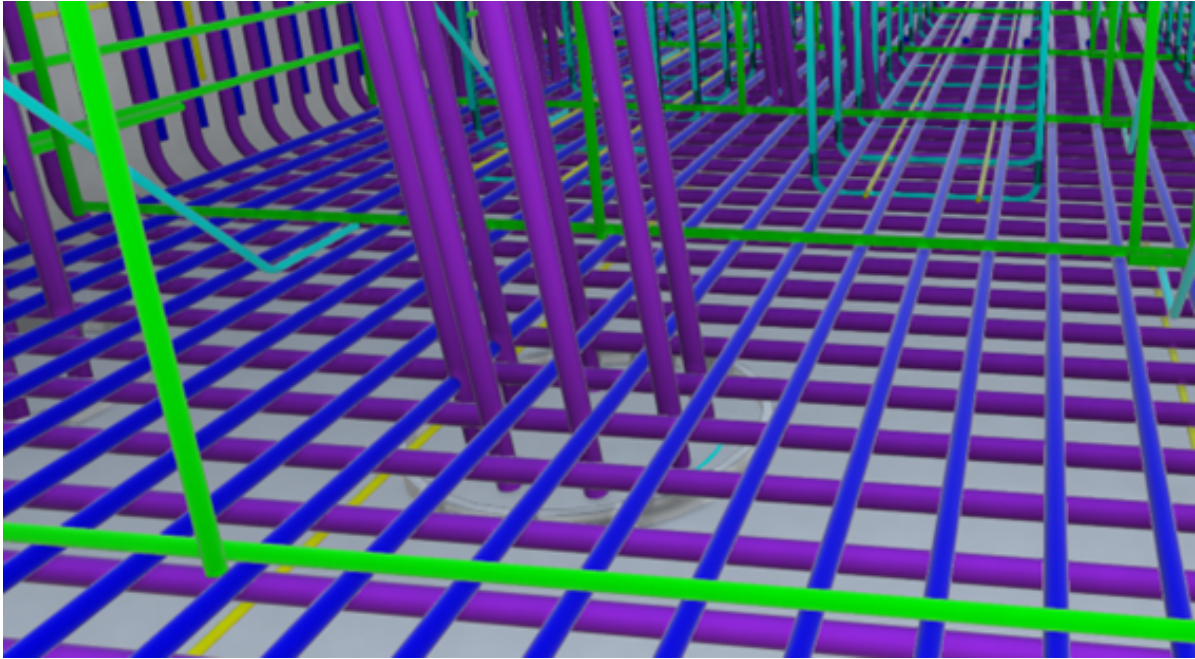
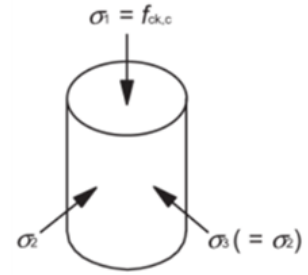


Figure 2.11: Reinforcement in the pile to cap connection in the situation of the case study

For rectangular cross-sections, the confinement effectiveness factor ω_c is calculated as:

$$\omega_c = \min \left(\omega_y = \frac{A_{sy} f_{yd}}{a_c s_c f_{cd}}, \omega_z = \frac{A_{sz} f_{yd}}{b_c s_c f_{cd}} \right) \quad \text{Eq. 2.15}$$

where:

ω_y, ω_z	Confinement effectiveness factors in the y and z directions
A_{sy}, A_{sz}	Area of the steel reinforcement in the y and z directions
f_{yd}	Yield strength of the steel reinforcement

The increase in compressive strength is given by:

$$f_{ck,c} = f_{ck} \left(1.000 + 5.0 \frac{\sigma_2}{f_{ck}} \right) \quad \text{for } \sigma_2 \leq 0.05 f_{ck} \quad \text{Eq. 2.16}$$

$$f_{ck,c} = f_{ck} \left(1.125 + 2.50 \frac{\sigma_2}{f_{ck}} \right) \quad \text{for } \sigma_2 > 0.05 f_{ck} \quad \text{Eq. 2.17}$$

where:

- $f_{ck,c}$ Increased compressive strength
- f_{ck} Characteristic compressive strength of the concrete
- σ_2 Effective confining pressure in lateral direction

The strain values are calculated as follows:

$$\varepsilon_{c2,c} = \varepsilon_{c2} \left(\frac{f_{ck,c}}{f_{ck}} \right) \quad \text{Eq. 2.18}$$

$$\varepsilon_{cu2,c} = \varepsilon_{cu2} + 0.2 \frac{\sigma_2}{f_{ck}} \quad \text{Eq. 2.19}$$

where:

- $\varepsilon_{c2,c}$ Compressive strain at $f_{ck,c}$
- $\varepsilon_{cu2,c}$ Ultimate compressive strain
- ε_{c2} Compressive strain at f_{ck}
- ε_{cu2} Ultimate compressive strain without confinement

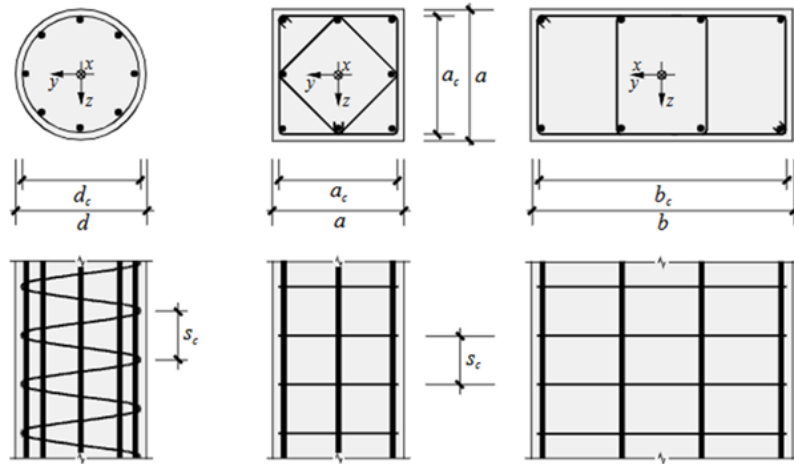


Figure 2.12: Compression members with confining reinforcement according to CEB-FIB Model Code 2010 volume 2 article 7.2.3.1.6 (Structural Concrete (fib) 2012)

In conclusion, Eurocode 2 Article 3.1.9 emphasizes the importance of confinement in concrete to increase its strength and ductility, particularly in structural elements subjected to high compressive forces, making it a vital consideration in structural design.

Unfortunately, it is not possible to apply EC2, Article 3.1.9, to this case study as it only involves a single reinforcement mesh in the compression zone. This leads to $s_c = 0$, which makes the calculation of ω_c infeasible due to division by zero. However, could a single reinforcement mesh directly located within the compression zone still exert a passive confinement effect on the compressed concrete? Moreover, beyond the influence of a single reinforcement mesh on confinement, what effect does a large volume

of surrounding concrete have on the loaded area? Does this increase the uniaxial compressive strength by a factor of up to 3, as described in Eurocode 2, Article 6.7? Or could a combination of both factors lead to an even greater increase in the concrete's compressive strength? To address these questions, the theoretical principles of concrete confinement must first be explored in a literature review.

3

Literature review

This chapter provides an overview of the available research on concrete confinement, with a focus on the effects of reinforcement and the surrounding concrete volume in the loaded area. The objective of this chapter is to gather sufficient data to develop models that yield precise results and can be validated using the information from this literature review.

3.1. Overview of confinement in structural elements

Confinement in reinforced concrete and other structural materials refers to the use of materials or structural designs that restrict the lateral expansion of the core material, thereby enhancing its strength and ductility. In the context of reinforced concrete, confinement is often provided by steel reinforcement or external wraps that prevent the concrete core from expanding outward under compressive loads. The confinement of concrete is particularly important in earthquake-resistant design, where structures are subjected to dynamic loads that require both strength and ductility to prevent catastrophic failure.

The concept of confinement has been widely researched, leading to various models and theories describing its effects on structural performance, especially concerning compressive strength, ductility, and energy absorption. The most notable studies include those by researchers like Mander, Priestley, and Park, who developed widely accepted stress-strain models for confined concrete. These models are now integral to seismic design codes around the world.

3.1.1. Effects of Confinement on Structural Performance

Enhanced Compressive Strength

Confinement increases the compressive strength of concrete beyond its unconfined capacity. When concrete is confined, its lateral expansion is restricted, which results in a triaxial stress state in the concrete. This state enhances the load-bearing capacity of the concrete core, allowing it to resist higher compressive stresses before failure (see figure 2.10). Experimental research, particularly by Mander et al. (Mander et al. 1988a), has demonstrated that confined concrete can achieve compressive strengths significantly higher than unconfined concrete. This increase depends on factors such as the amount, spacing, and configuration of the transverse reinforcement (e.g., spirals or hoops) that provides the confinement.

Improved Ductility

Ductility, defined as the capacity of a material to sustain significant plastic deformation prior to failure, is a critical property in structural elements subject to seismic forces. Confinement enhances the ductility of concrete, enabling it to endure larger strains without undergoing abrupt, brittle failure. As illustrated in Figure 2.10, confined concrete achieves higher strain levels before reaching its ultimate compressive strength ($\epsilon_{cc} > \epsilon_{c0}$). Rather than exhibiting sudden failure, confined concrete demonstrates a gradual reduction in strength following peak stress. This behaviour is essential not only in seismic design (particularly in columns and bridge piers where energy dissipation is crucial) but also in structures exposed to other forms of dynamic loading. In bridge piers subjected to repeated traffic loads, impact

forces, or environmental vibrations, confinement contributes to improved fatigue resistance, enhanced damping capacity, and sustained structural integrity after cracking. Therefore, the increased ductility resulting from confinement enhances the overall resilience of the structure in both seismic and non-seismic dynamic scenarios.

Energy Absorption Capacity

Confinement also enhances the energy absorption capacity of structural elements, a key factor in seismic design. Structures with high energy absorption capacity can absorb and dissipate the energy released during an earthquake, thereby reducing the demand on other structural components. The energy absorption capacity is typically represented by the area beneath the stress–strain curve. Figure 2.10 illustrates that the area beneath the curve for confined concrete is significantly larger than that for unconfined concrete, indicating an increased energy absorption capacity when the concrete is confined. Studies have shown that confined concrete elements can absorb more energy due to their improved strength and ductility, thereby enhancing the overall resilience of the structure under dynamic loading conditions. This capacity to absorb energy is particularly important in plastic hinge zones, where inelastic deformations are expected to concentrate during severe loading events.

3.1.2. Common Confinement Models

Mander's Model for Confined Concrete

One of the most influential models for confined concrete was proposed by Mander, Priestley, and Park in 1988. This model provides a comprehensive stress-strain relationship for confined concrete, accounting for the increased strength and ductility due to confinement. Mander's model is based on the concept that the lateral pressure exerted by transverse reinforcement on concrete delays its failure and allows for greater stress and strain capacities. This model is widely used in the design and analysis of reinforced concrete structures and is incorporated into many design codes.

The Modified Kent-Park Model

The Kent-Park model, later modified by Scott et al. (1982), is another well-known model for confined concrete. This model originally described the stress-strain behavior of unconfined concrete but was adapted to account for confinement effects by modifying the post-peak behavior. The modified model includes a descending branch that reflects the improved ductility due to confinement, allowing for more accurate modeling of concrete behavior in regions subject to high seismic demands.

3.1.3. Applications of Confinement in Structural Design

Confinement is particularly critical in the design of certain structural components where high strength and ductility are necessary to ensure overall structural stability and resilience.

Seismic-Resistant Columns

In earthquake engineering, columns are often confined to improve their load-bearing and ductile capacities. For instance, in high-rise buildings, columns are wrapped with transverse reinforcement (such as steel hoops or spirals) or with external materials like fiber-reinforced polymers (FRP) to ensure that they can withstand lateral seismic forces without brittle failure. The confined columns can undergo large deformations, allowing them to absorb and dissipate seismic energy and preventing collapse.

Bridge Piers

Bridge piers are critical in supporting bridge structures and are subject to both compressive and bending stresses, especially during seismic events. Confinement in bridge piers is typically provided by transverse reinforcement and, in some cases, by using high-strength materials like FRP wraps. This confinement improves the ductility and strength of the piers, enabling them to resist the dynamic forces generated during earthquakes and reducing the likelihood of structural collapse.

Retrofit of Existing Structures

For older structures that were not originally designed to withstand seismic forces, confinement through retrofitting provides an effective means of improving structural performance. Techniques such as jacketing (wrapping columns and beams with additional materials) enhance the strength and ductility of these elements, bringing them up to modern seismic design standards. Common materials used in

retrofitting for confinement include carbon fiber-reinforced polymers (CFRP), glass fiber-reinforced polymers (GFRP), and steel jackets.

3.2. Mechanisms of confinement

This thesis focuses on passive confinement rather than active confinement, as the case study does not involve any lateral pressure from outside the specimen. Passive confinement generally arises from the restriction of lateral expansion in loaded concrete elements by surrounding materials, such as enclosed steel tubes, fibre-reinforced polymer (FRP) wrapping, rigid steel plates for load introduction, unloaded concrete outside the concentrated load area, or transverse reinforcement within the concrete. In this case study, confinement by transverse reinforcement and by unloaded concrete beyond the concentrated load area are relevant.

3.2.1. Passive confinement by transverse reinforcement

Several conditions are necessary for transverse reinforcement to contribute effectively to confinement. First, in all forms of passive confinement, the concrete must undergo lateral deformation due to longitudinal loading. Additionally, the transverse reinforcement must sufficiently restrain this lateral deformation. One type of lateral reinforcement that inherently provides this restraint is stirrups. However, circular stirrups are more effective at confining the concrete within than rectangular stirrups. This difference arises because rectangular stirrups tend to deform towards a circular shape under load, whereas circular stirrups already exhibit their final, stable shape.

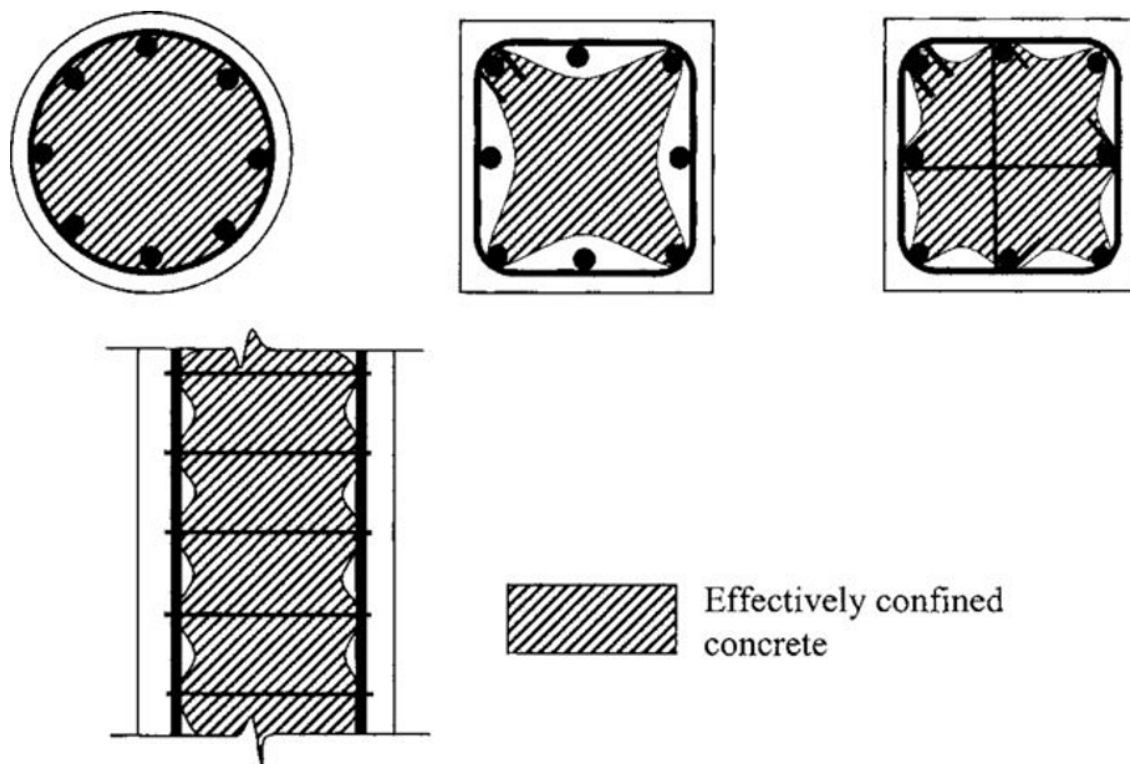


Figure 3.1: Effective confined area in columns with different transverse reinforcement (Tabsh 2007)

Figure 3.1 illustrates the three different types of reinforcement configurations for concrete columns and how they confine the concrete core. The shaded regions in each diagram indicate the "effectively confined concrete" the area where lateral confinement by the stirrups or hoops actively improves the concrete's strength and ductility.

In the circular section, the hoops provide confinement uniformly around the core of the column. The circular stirrups exert even lateral pressure on the concrete, making the entire core area effectively confined. This configuration is efficient in creating a high degree of confinement throughout the cross-

section, which is beneficial for columns that need to resist seismic or other lateral loads. The shaded area shows that almost the entire concrete core is effectively confined, as circular hoops distribute the confinement evenly.

In the square section without cross ties, the confinement is provided by rectangular stirrups around the perimeter. Due to the shape of the stirrups, the concrete in the corners is effectively confined, while the central areas along the sides receive less lateral support and are less confined. The shaded regions are concentrated in the corners, indicating that only these areas receive effective confinement. The concrete along the middle sections of each side of the rectangle lacks sufficient confinement, making it more susceptible to cracking or spalling under high loads.

The last configuration includes rectangular stirrups with additional cross ties that connect the stirrups across the section. The cross ties improve confinement by restraining the concrete not only in the corners but also towards the centre of each side of the section. As a result, a larger portion of the concrete is effectively confined, as indicated by the extended shaded areas, which cover more of the cross-sectional area compared to the rectangular section without cross ties. This design increases the confinement efficiency, making it particularly suitable for structures exposed to high loads or seismic forces, as it prevents buckling of the longitudinal reinforcement and enhances the concrete's load-bearing capacity. (Filaj et al. 2016)

3.2.2. Passive confinement by longitudinal reinforcement

In addition to the impact of transverse reinforcement, in columns, longitudinal reinforcement also contributes to confinement. As the concrete attempts to expand outward under load, the longitudinal bars, tightly held by the transverse reinforcement, also experience compression. This creates a synergistic effect, where the confined concrete core and the reinforcement work together to resist deformations (Filaj et al. 2016). This restraint provided by the longitudinal bars enhances the confinement effect, enabling the concrete to withstand higher stresses before failure. The quantity and distribution of longitudinal reinforcement influence the effectiveness of confinement. When sufficient longitudinal reinforcement is evenly distributed across the section, the concrete core is more uniformly supported by the lateral reinforcement, increasing the confined area and improving the column's overall capacity.

3.2.3. Passive confinement by unloaded concrete beyond the concentrated load area

If the loaded concrete core is surrounded by additional concrete, this surrounding plain concrete resists the lateral deformation, creating a confining pressure. This confining pressure reduces the lateral strain in the core, thereby improving its compressive strength and ductility. According to the previous explained square root equation in section 2.2.1 and experimental results from (Adebar et al. 1993) the confining effect by plain concrete depends on the geometry, thickness, and relative strength of the surrounding concrete.

3.3. Theoretical models of confinement effects

3.3.1. Mander's Model for Confined Concrete

Mander et al. developed a theoretical stress-strain model for concrete confined by transverse reinforcement, such as circular hoops, spirals, or rectangular hoops with or without supplementary cross ties. This model accounts for the influence of confinement on the strength and ductility of concrete under uniaxial compressive loading and is applicable to monotonic, cyclic, and dynamic loading conditions.

Mander et al. performed an experiment to validate Mander's theoretical model by observing the stress-strain behaviour of reinforced concrete columns under axial compressive loading. Thirty-one columns with various cross-sectional shapes (circular, square, and rectangular) were tested under quasi-static and high strain rates to investigate how different reinforcement configurations affect the confined behaviour of concrete.

Theoretical Stress-Strain Relationship

The stress-strain curve for confined concrete (see figure 2.10) is derived from an equation suggested by Popovics (1973) and takes the form:

$$f_c = \frac{f'_{cc} \cdot x \cdot r}{r - 1 + x^r} \quad \text{Eq. 3.1}$$

where:

$x = \varepsilon_c / \varepsilon_{cc}$	Strain ratio [-]
f_c	longitudinal compressive concrete stress [MPa]
f'_{cc}	peak compressive strength of confined concrete [MPa]
ε_c	longitudinal compressive strain in concrete [-]
$\varepsilon_{cc} = \varepsilon_{c0} [1 + 5((f'_{cc}/f'_{c0}) - 1)]$	strain at peak stress f'_{cc} [-]
$\varepsilon = 0,002$	Assumed strain at unconfined concrete peak strength [-]
f'_{c0}	Unconfined concrete strength [MPa]
$r = E_c / (E_c - E_{sec})$	E-modulus ratio [-]
$E_c = 5.000 \sqrt{f'_{c0}}$	initial tangent modulus of elasticity of unconfined concrete [MPa]
$E_{sec} = f'_{cc} / \varepsilon_{cc}$	secant modulus of elasticity at peak stress [MPa]

Confinement Effectiveness

The method for calculating confinement effectiveness according to Mander's theorem differs between circular and rectangular transverse reinforcement. Given that the longitudinal and transverse reinforcement in concrete caps on CFSP piles exclusively form rectangular confining reinforcement, this thesis only considers the confinement effectiveness of rectangular transverse reinforcement. To calculate the effect of transverse reinforcement on the confinement of the concrete, the effective lateral confining stress f'_l is determined:

$$f'_l = f_l \cdot k_e \quad \text{Eq. 3.2}$$

where:

f_l	lateral pressure from the transverse reinforcement, assumed to be uniformly distributed over the surface of the concrete core [MPa]
k_e	confinement effectiveness coefficient [-]

The confinement effectiveness coefficient k_e varies based on the configuration of the transverse reinforcement. For rectangular hoops which are relevant to the case studies application:

$$k_e = \frac{A_e}{A_{cc}} \quad \text{Eq. 3.3}$$

where:

A_e	area of the effectively confined concrete core [mm^2]
$A_{cc} = A_c(1 - \rho_{cc})$	area of core within centrelines of perimeter hoops excluding area of longitudinal steel [mm^2]
A_c	area of the core of the section enclosed by the centrelines of the perimeter hoop [mm^2]
ρ_{cc}	ratio of area of longitudinal reinforcement to area of core of section [-]

In figure 3.2, the arching action is modeled as second-degree parabolas, starting with an initial tangent slope of 45° . This arching occurs vertically between the layers of transverse hoop bars and horizontally between the longitudinal bars. The effectively confined concrete area at the hoop level is determined by subtracting the area of the parabolas containing the ineffectively confined concrete. For a single parabola, the ineffectively confined area is given by $(w_i)^2/6$, where w_i is the i -th clear distance between adjacent longitudinal bars (see figure 3.2). Thus, the total plan area of the ineffectively confined core concrete at the level of the hoops, when there are n longitudinal bars, is:

$$A_i = \sum_{i=1}^n \frac{(w_i')^2}{6} \quad \text{Eq. 3.4}$$

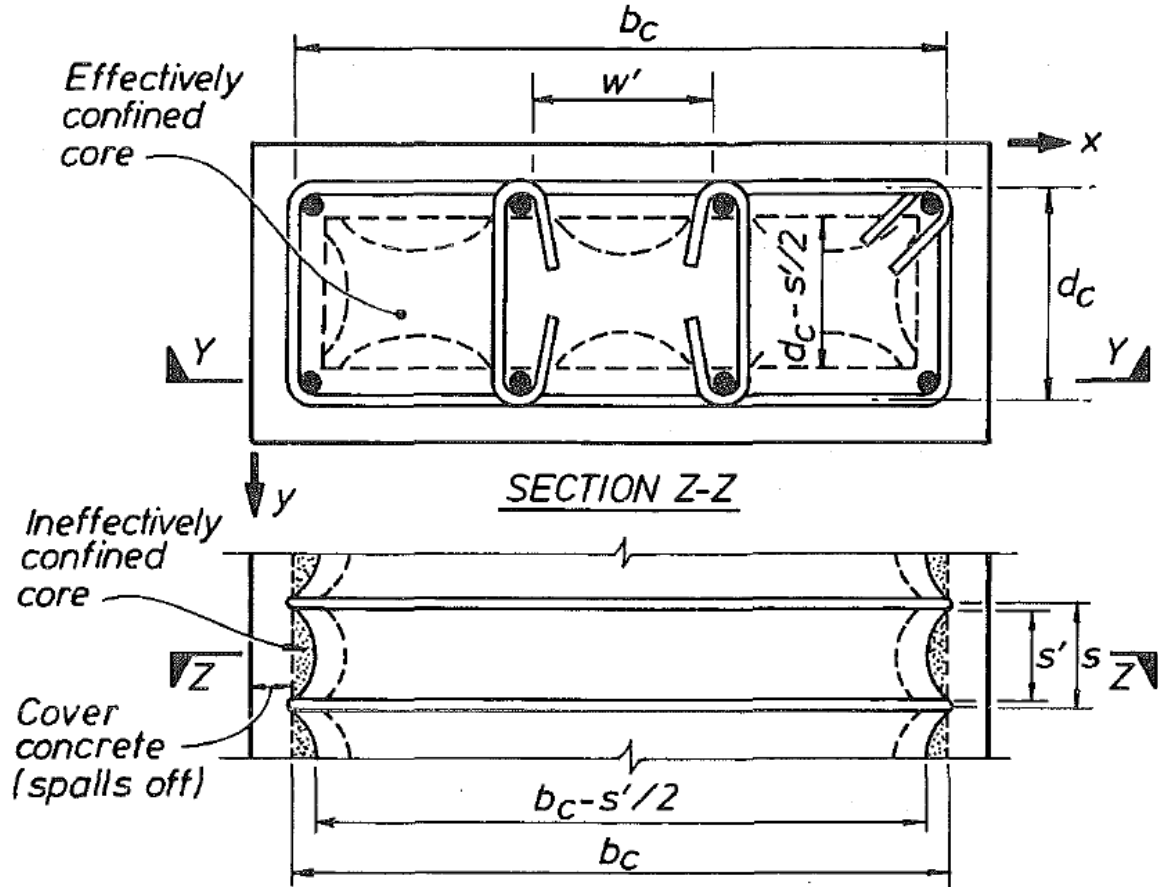


Figure 3.2: Effectively confined core for rectangular hoop reinforcement (Mander et al. 1988b)

Taking into account the impact of the ineffective areas in the elevation (as shown in Fig. 3), the effectively confined concrete core area at the midpoint between the transverse hoop reinforcement levels is:

$$A_e = \left(b_c d_c - \sum_{i=1}^n \frac{(w'_i)^2}{6} \right) \left(1 - \frac{s'}{2b_c} \right) \left(1 - \frac{s'}{2d_c} \right) \quad \text{Eq. 3.5}$$

where:

b_c core width to centrelines of perimeter hoop in x direction [mm]

d_c core width to centrelines of perimeter hoop in y direction [mm]

$b_c \geq d_c$

With now the area of effectively confined concrete A_e and the area of core within centrelines of perimeter hoops A_{cc} expressed, Equation 3.3 can be rewritten which gives:

$$k_e = \frac{\left(1 - \sum_{i=1}^n \frac{(w'_i)^2}{6b_c d_c} \right) \left(1 - \frac{s'}{2b_c} \right) \left(1 - \frac{s'}{2d_c} \right)}{(1 - \rho_{cc})} \quad \text{Eq. 3.6}$$

Rectangular reinforced concrete members may have varying amounts of transverse confining steel in the x and y directions. As a result, the lateral confining stress on the concrete, defined as the total transverse bar force divided by the vertical area of the confined concrete, could differ between the x- and y-directions due to differing transverse reinforcement ratios. This leads to the following expressions for lateral confining stress on the concrete:

- lateral confining stress in x-direction:

$$f_{lx} = \frac{A_{sx}}{sd_c} f_{yh} = \rho_x f_{yh} \quad \text{Eq. 3.7}$$

- lateral confining stress in y-direction:

$$f_{ly} = \frac{A_{sy}}{sb_c} f_{yh} = \rho_y f_{yh} \quad \text{Eq. 3.8}$$

where:

A_{sx} the total area of transverse bars running in x-direction [mm^2]
 A_{sy} the total area of transverse bars running in y-direction [mm^2]
 f_{yh} yield strength of the transverse reinforcement [MPa]

From equation 3.2 the effective lateral confining stresses in x- and y-directions are:

- effective lateral confining stress in x-direction:

$$f'_{lx} = k_e \rho_x f_{yh} \quad \text{Eq. 3.9}$$

- effective lateral confining stress in y-direction:

$$f'_{ly} = k_e \rho_y f_{yh} \quad \text{Eq. 3.10}$$

Where the confinement effectiveness coefficient k_e is defined by Equation 3.6, and the lateral confining stress in the x- and y-directions is given by Equation 3.7 and Equation 3.8, respectively.

Peak Compressive Strength

To determine the compressive strength of confined concrete f'_{cc} , a constitutive model is utilised that specifies an ultimate strength surface for multiaxial compressive stresses. The "five-parameter" failure surface described by William and Warnke (1975) is employed, as it shows excellent agreement with triaxial test results. The ultimate strength surface, calculated from the triaxial tests conducted by Schickert and Winkler (1977), serves as the foundation for this approach, with detailed calculations provided by Elwi and Murray (1979).

The general solution to the multiaxial failure criterion is derived by incorporating the effects of the two lateral confining stresses. This solution is depicted in Fig. 4, illustrating the relationship between the effective lateral stresses and the enhanced compressive strength of the confined concrete.

where f'_{co} is the unconfined compressive strength of concrete.

Ultimate Strain

The ultimate strain ε_{cu} at which the transverse reinforcement fractures is calculated using an energy balance approach:

$$U_{sh} = U_{cc} + U_{sc} - U_{co} \quad \text{Eq. 3.11}$$

where:

U_{sh} strain energy capacity of transverse reinforcement [MJ/m^3]
 U_{cc} strain energy stored by confined concrete [MJ/m^3]
 U_{sc} energy required to maintain yield in longitudinal steel [MJ/m^3]
 U_{co} strain energy of unconfined concrete [MJ/m^3]

The model allows for reliable moment-curvature analysis by quantifying the enhancement in strength and ductility provided by the transverse reinforcement.

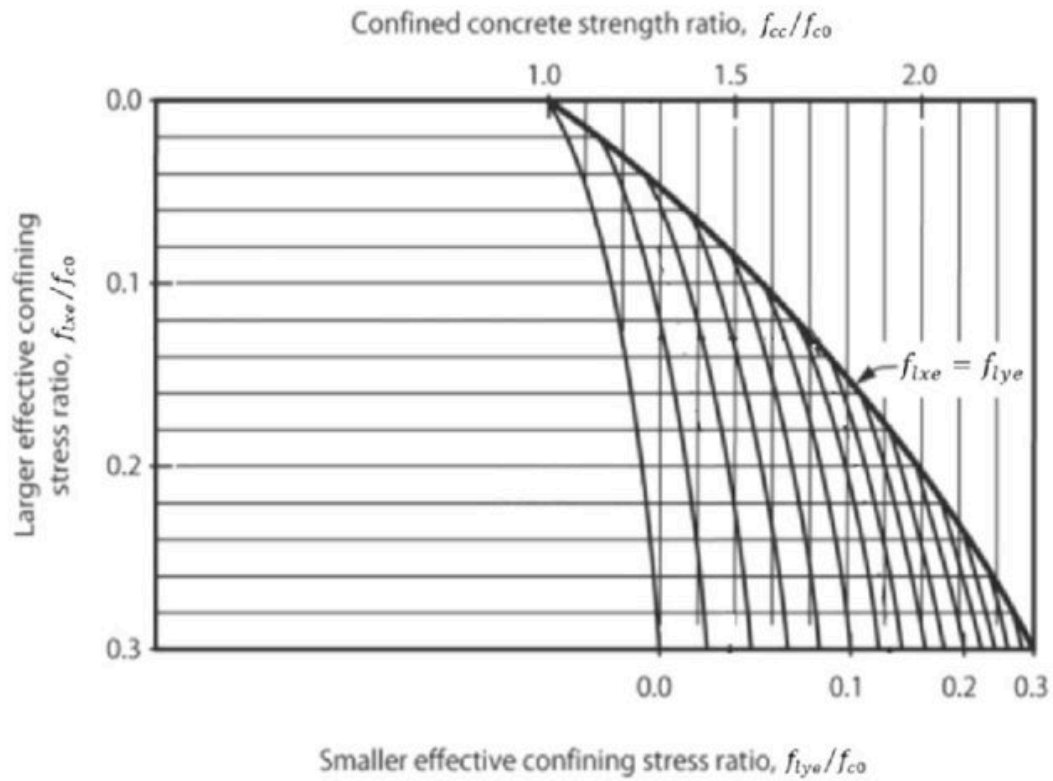


Figure 3.3: Confined Strength Determination from Lateral Confining Stresses for Rectangular Sections (Mander et al. 1988b)

Specimen Details and Reinforcement

The tested columns varied in geometry and reinforcement configuration:

1. **Circular Sections:** Reinforced with longitudinal and spiral reinforcement.
2. **Square Sections:** Reinforced with longitudinal bars and either square or octagonal transverse hoops.
3. **Rectangular Wall Sections:** Reinforced with rectangular hoops, sometimes supplemented with cross-ties.

Testing Setup and Procedure

The tests were conducted using a DARTEC 10 MN servohydraulically controlled testing machine, capable of applying strain rates up to 0.015/s. The specimens were concentrically loaded, and longitudinal and transverse strains were measured using linear potentiometers and electric resistance strain gauges. The instrumentation focused on a central 450 mm gage length to ensure accurate monitoring of failure behaviour.

Experimental Observations and Results

Mander et al. observed distinct failure patterns in circular columns depending on the volumetric ratio of confining reinforcement. Columns with low ratios exhibited diagonal failure planes after peak load, while columns with higher ratios demonstrated enhanced strength and an extended falling branch of the stress-strain curve. Notably, spiral reinforcement fractured sequentially, without unwinding. It was found that the most significant variable in the tests was the volumetric ratio, ρ_s , of spiral reinforcement. An increase in ρ_s raises the peak stress, f'_{cc} , the strain at peak stress, ϵ'_{cc} , and the fracture strain, ϵ_{cu} , while reducing the slope of the descending branch of the stress-strain curve. The pitch of the spiral reinforcement, on the other hand, did not significantly affect the peak stress and strain capacity. Although a smaller pitch resulted in a less steep descending branch, the influence remained minimal.

Observed Stress-Strain Curves

The experimental stress-strain curves revealed significant enhancements in strength and ductility for confined concrete compared to unconfined samples. Increased confinement led to higher peak stress, greater fracture strains, and a gentler slope on the falling branch (see figure 3.4).

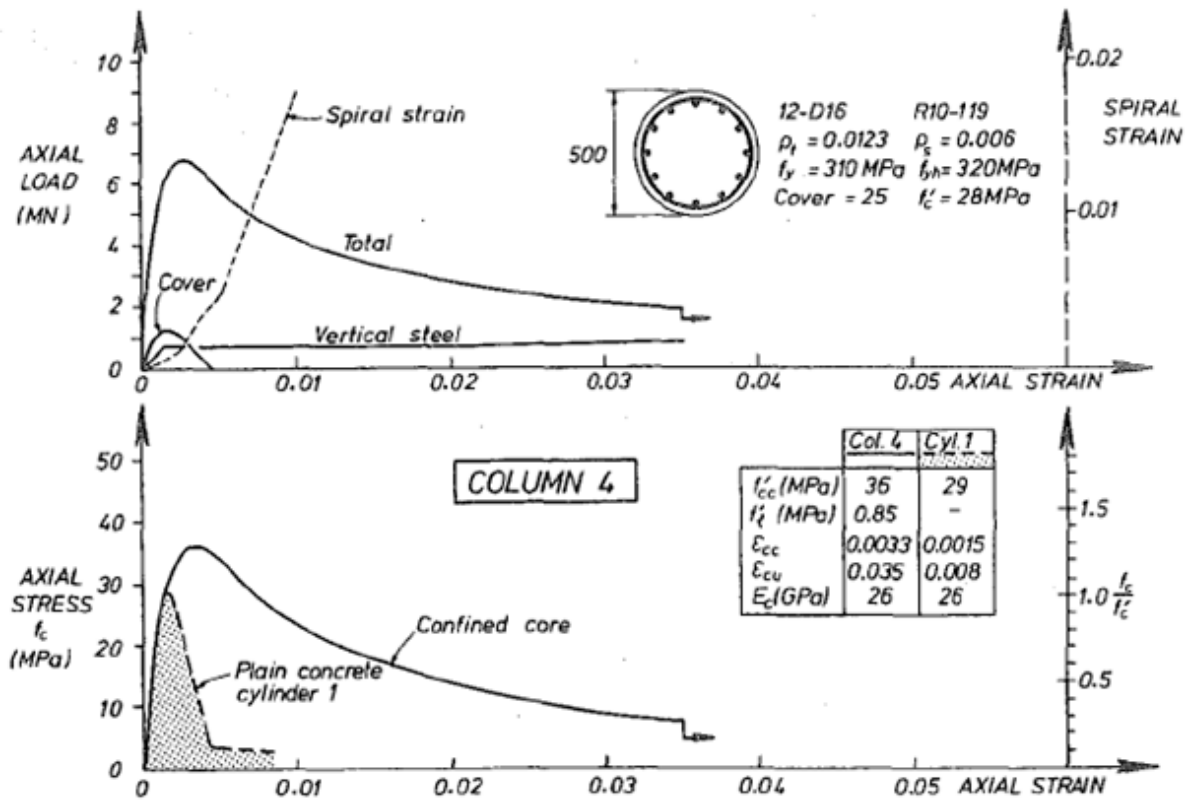


Figure 3.4: Typical Experimental Stress-Strain Curves for Spirally Reinforced Circular Columns by Mander et al. (Mander et al. 1988a)

Theoretical Model Comparison

The experimental results were compared with Mander's theoretical predictions. The confined concrete compressive strength f'_{cc} , strain at peak strength ϵ_{cc} , and ultimate compressive strain ϵ_{cu} were essential control parameters. Effective confining stresses f'_t were calculated using the confinement effectiveness coefficient k_e , accounting for the effectively confined concrete core area. The peak experimental and theoretical confined concrete strengths, f'_{cc} , were listed and compared. In most cases, there is very close agreement, with experimental concrete strengths exceeding the predicted values by an average of 1.7%. On average, the experimental confined strain at peak stress, ϵ_{cc} , is 1.3% lower than the predicted strain. The experimental strain at the point of initial hoop fracture exceeded the predicted strain by an average of 9.5%. These close agreements in average behaviour, combined with the relatively low variation, suggest that Mander's theoretical model provides an excellent prediction of the stress-strain curves for concrete confined by spirals or hoops.

3.4. Stress distribution in partially loaded areas

The mechanical behaviour of partially loaded areas in concrete has been extensively studied over the past century. These areas are subject to high, concentrated compressive forces over limited contact regions, resulting in stress distributions that significantly influence their bearing capacity.

When a concentrated load is applied to a concrete surface over a limited area, the resulting compressive stresses spread and approach a uniform distribution at increasing depths. A distinction can be made between spatial cases as shown in figure 3.5(a) and plane cases of partial loading in figure 3.5(b) and (c).

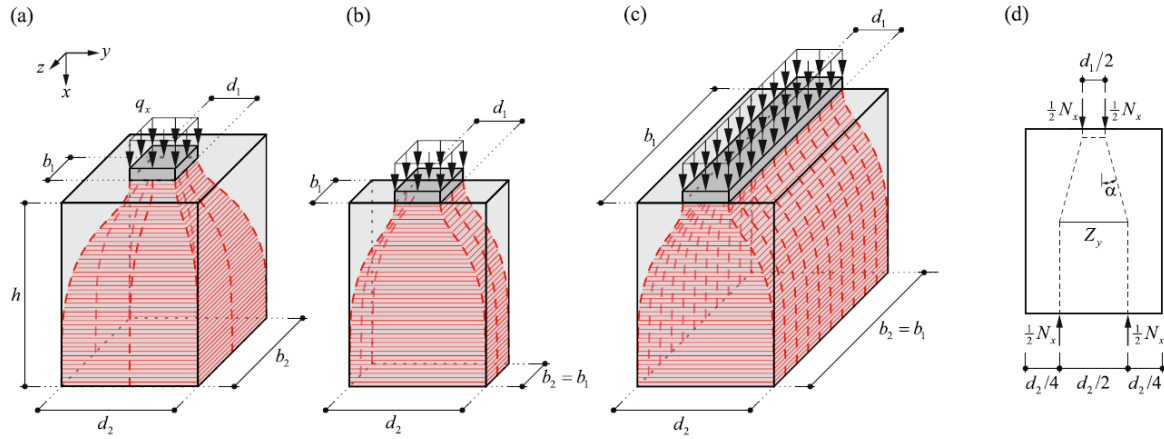


Figure 3.5: Cases of partial area loading: (a) Spatial case; (b) plate, and (c) strip loading; (d) Strut-and-tie model for plane cases (b) and (c). (Markic et al. 2022b)

Current design approaches for partially loaded areas are predominantly empirical, relying on simplified models and assumptions. The commonly used square-root equation (see equation 2.4) relates the average bearing capacity to the uniaxial compressive strength. However, this empirical model often yields conservative estimates, particularly for reinforced blocks, leading to inefficient designs. This motivated researchers to develop approaches based on stress fields.

3.4.1. Strut and tie model

The strut-and-tie model shown in figure 3.5(d) provides a simplified mechanical representation of stress distribution in partially loaded areas of reinforced concrete. This model is used to analyse the transfer of loads from the loaded area to the surrounding structure.

- **Struts:** Represent the compressive stress paths in concrete (dashed lines).
- **Ties:** Represent the tensile forces, typically carried by reinforcement in the bursting region (solid lines).

The model assumes idealized stress trajectories and uniform stress distribution, providing a practical yet conservative basis for designing the reinforcement in the bursting region.

This model forms the foundation for more advanced stress field solutions, such as the Markic Dual-Wedge and Dual-Cone models, which incorporate biaxial stress states and confinement effects for improved accuracy, both published by Markic et al. (Markic et al. 2022b). Markic et al. have built upon the work of Chen et al., refining and simplifying these stress field solutions. Before presenting the models, they summarised the key assumptions and simplifications, which can be found in Section 3 of the report *Partially Loaded Areas in Reinforced Concrete: Mechanical Modelling* (Markic et al. 2022b). The bearing load on the pile casing can be treated as a circular line load on the concrete, making the Dual-Wedge stress field the appropriate model.

3.4.2. Markic Dual-Wedge stress field

The Dual-Wedge (DW) stress field provides a theoretical model for analysing partially loaded areas in reinforced concrete under plane stress conditions. It builds upon the principles of the lower-bound theorem of plasticity and combines the effects of geometric and passive confinement to increase the bearing capacity.

In contrast to simple strut-and-tie models, which feature orthogonal boundaries between nodal zones and struts and require equal compressive stresses in all directions of the (x, y) -plane, $\sigma_1 = \sigma_3$, the Dual-Wedge stress field allows for general biaxial compressive stress states, $\sigma_1 \geq \sigma_3$, within the nodes. This approach facilitates a more efficient utilization of the confined concrete's compressive strength (Markic et al. 2022b).

The Dual-Wedge model divides the loaded area into three parts (see Figure 3.6): the first nodal zone ABK, where the load is applied; the second nodal zone BEF; and the strut BFK. From the nodal zone ABK, the load is transferred to the strut BFK. In the transition from region ABK to BFK, the load inclines by an angle α into a direction parallel to the strut. This results in the strut being subjected to a uniaxial compressive stress σ_α in the (x, y) -plane.

Geometrical confinement

The inclined uniaxial stress in the strut BFK induces a horizontal compressive stress component, $\sigma_3 = \sigma_\alpha \sin^2 \alpha$, which geometrically confines the nodal zone ABK and thereby increases its compressive strength, $\sigma_1 = \sigma_{x0}$. The stress field of the strut BFK also decomposes into horizontal and vertical components at the discontinuity line BF. However, this creates a horizontal bursting stress σ_s .

Bursting stress

In unreinforced concrete, this bursting stress must be carried by the concrete itself, which will likely fail due to cracking. In reinforced concrete, prior to cracking, there will be a homogeneous biaxial tension-compression state in the (x, y) -plane. After cracking, the tensile bursting stress is redistributed into the reinforcement, leaving only uniaxial compression within the concrete. And by vertical equilibrium of the stress field, it is found that $\sigma_{xd} = d_1/d_2 \cdot \sigma_{x0}$.

So far, the region ABK is geometrically confined, and the region FJK remained stress-free. However, if passive confinement by surrounding reinforcement is taken into account, an even larger bearing capacity could be reached. The area influenced by passive confinement by the reinforcement depends on the amount and location of confining reinforcement around the loaded area. The effectiveness of the lateral reinforcement can be determined according to equation 3.2 in section 3.3.1.

Stress Transition at Discontinuity Lines

To better understand the effect of geometrical and passive confinement, a Mohr circle is constructed to illustrate the transformation of the stress state from region BFK to region ABK via the discontinuity lines FK and BK. A similar approach is used to analyse the stress state transition from region BFK to BEF through discontinuity lines FK and BF taking into account the confining effect of bursting reinforcement.

Figure 3.6.b shows the forces influencing the stress state in region ABK and the corresponding Mohr circle. The blue circle represents the stress state in region BFK without confinement. The blue line, inclined by angle α , is parallel to the discontinuity line FK and indicates the direction of the principal compressive stress in region BFK. The intersection of the blue Mohr circle and the blue line is marked with a pole, which represents the combination of normal and shear stress acting along the discontinuity line FK.

The pole is then shifted to the left (indicating increased compression) by a magnitude equal to the confinement stress. Adding confinement stress not only shifts the circle but also reduces its diameter. This is because the confinement alters the internal stress distribution, decreasing the shear stress (τ) required to maintain equilibrium. As a result, the radius of the new Mohr circle becomes smaller since it is directly related to the maximum shear stress τ_{\max} , which is reduced under confinement. The pole on the new Mohr circle still represents the stress state parallel to discontinuity line FK, but now it accounts for the effect of passive confinement.

Following the discontinuity line FK up to point K leads to discontinuity line BK. It is important to note that the same stress state persists along the entire discontinuity line FK. This means that the new pole serves as the reference point for the stress state in the new Mohr circle, and all stresses on planes with varying orientations are derived from this pole. The line parallel to BK, departing at an angle γ , represents the stress state in a plane parallel to BK in the physical space.

By extending the line parallel to discontinuity line BK in the Mohr circle, a new pole is located on the new Mohr circle. Region ABK is subjected to pure compression, denoted as σ_{x0} . To determine the ultimate normal stress capacity of ABK, a line perpendicular to BK is drawn from the pole representing the stress state parallel to BK. The point where this line intersects the σ -axis (where shear stress $\tau = 0$) corresponds to the maximum normal stress σ_{x0} .

This perpendicular line reflects the transition to a plane where the shear stress is fully relieved, leaving only the normal stress component. In the Mohr circle, points along the σ -axis represent pure normal stress states without shear stress. Therefore, the intersection of this perpendicular line with the σ -axis indicates the point of pure compression in ABK, corresponding to the maximum normal stress σ_{x0} the region can withstand.

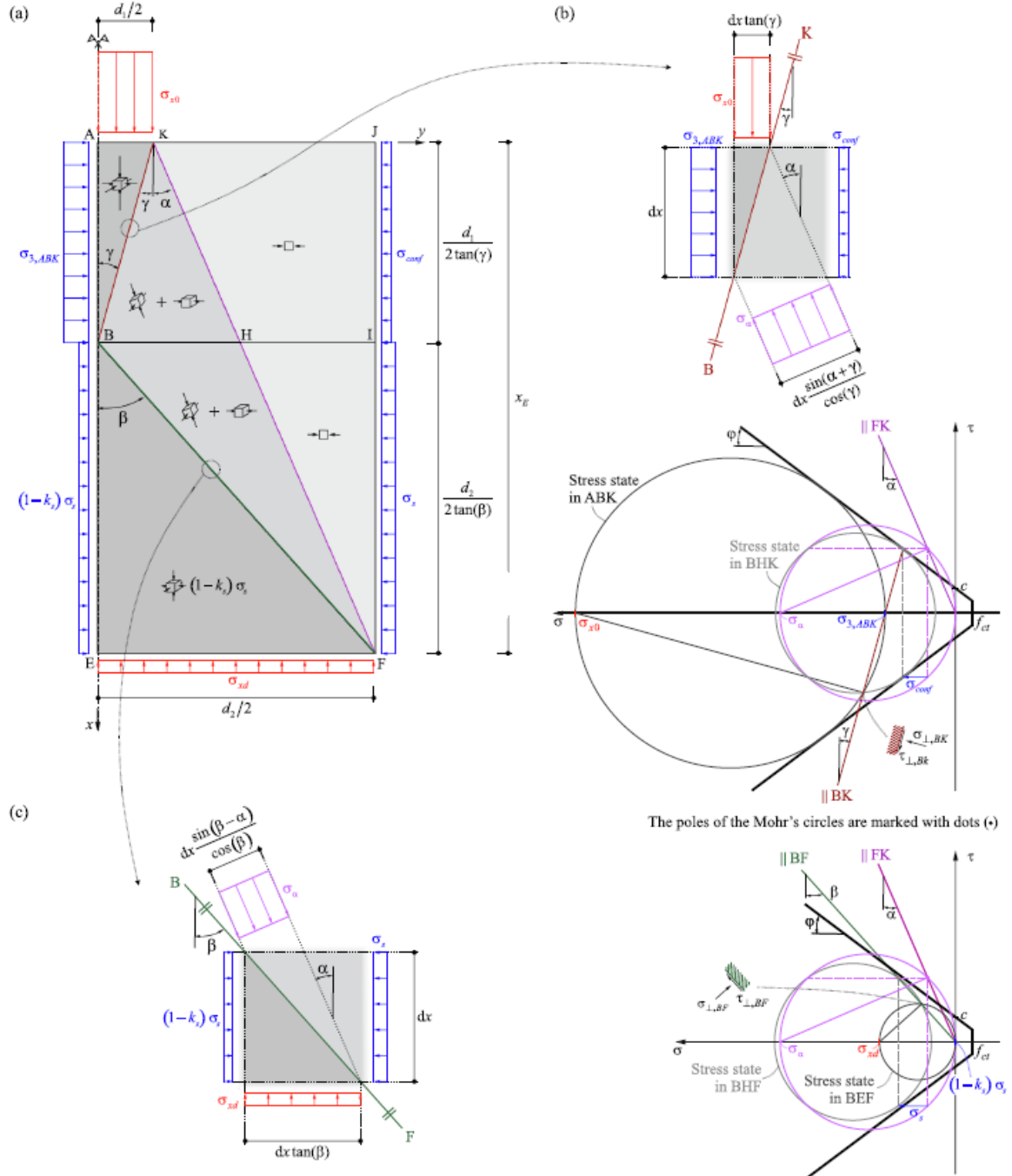


Figure 3.6: Dual-Wedge stress field by Markic (Markic et al. 2022b)

Mathematical formulation of the DW stress field

The stress model maximises confinement effects by superimposing stress fields:

$$\sigma_{x0} = \sigma_{1,ABK} = \frac{d_2}{d_1} \frac{\sigma_\alpha \cos^2 \alpha}{1 + \frac{\sigma_\alpha \sin^2 \alpha}{k_s \sigma_s}} \quad \text{Eq. 3.12}$$

where:

- σ_α : Compressive stress in the diagonal strut.
- α : Inclination angle of the compressive strut.
- k_s : Parameter controlling the distribution of bursting reinforcement stresses.
- σ_s : Stress from bursting reinforcement.
- d_1, d_2 : Widths of the loaded and confinement areas, respectively.

Stress Field Behaviour and Optimization

The stress trajectories are inclined at an angle α to the loading direction, allowing the compressive stresses to be distributed uniformly over the available block width d_2 . The upper wedge (ABK) experiences biaxial compression, with the horizontal stress component $\sigma_3 = \sigma_\alpha \sin^2 \alpha$ confining the node and increasing its compressive strength in the vertical direction.

To maximize bearing capacity, the DW stress field combines reinforcement effects:

- Confinement reinforcement generates horizontal stresses σ_{conf} .
- Bursting reinforcement extends beyond critical zones, adding to the confinement stresses in the triangular stress field (BFH).

The resulting equilibrium conditions include:

$$0 \leq \sigma_{conf} \leq f_{c0} \quad \text{Eq. 3.13}$$

$$0 \leq \sigma_s \leq f_{c0} \quad \text{Eq. 3.14}$$

$$0 \leq k_s \leq \min \left\{ 1 - \frac{\frac{d_1}{d_2} \sigma_x - f_{c0}}{4\sigma_s}, 1 \right\} \quad \text{Eq. 3.15}$$

$$\sin^2(\alpha) = \max \left\{ \frac{k_s \sigma_s \frac{1}{2}(f_{c0} + \sigma_\alpha) - (f_{c0} + 4\sigma_{conf}) \frac{d_1}{d_2} + 2\sigma_{conf} + \sigma_b - \sigma_a}{\sigma_\alpha (f_{c0} + 4\sigma_{conf}) \frac{d_1}{d_2} - 3k_s \sigma_s}, \sin^2(\alpha_{min}) \right\} \quad \text{Eq. 3.16}$$

$$\sigma_a^2 = \frac{1}{4}(f_{c0} - \sigma_\alpha + 4\sigma_{conf})^2 + \sigma_b^2 + \frac{1}{2}k_s \sigma_s \left[(f_{c0} + 4\sigma_{conf}) \left(\frac{d_1}{d_2} - 5 \right) + \sigma_\alpha \left(7 \frac{d_2}{d_1} - 3 \right) \right] \quad \text{Eq. 3.17}$$

$$\sigma_b = \frac{1}{2}k_s \sigma_s \left(\frac{d_2}{d_1} + 3 \right) \quad \text{Eq. 3.18}$$

$$\sin^2(\alpha_{min}) = \frac{(d_2 - d_1)^2}{4x_{E,max}^2 + (d_2 - d_1)^2} \quad \text{Eq. 3.19}$$

$$\sigma_\alpha \leq \min\{\sigma_{\alpha,adm,BHK}, \sigma_{\alpha,adm,BFH}\} \quad \text{Eq. 3.20}$$

$$\sigma_{\alpha,adm}(\sigma_j) = \frac{1}{16}(6f_{c0} + \sigma_j(9 + 25 \cos 2\alpha) + \sqrt{64(f_{c0} - \sigma_j)(f_{c0} + 4\sigma_j) + (6f_{c0} + \sigma_j(9 + 25 \cos 2\alpha))^2}) \quad \text{Eq. 3.21}$$

where:

f_{c0}	Uniaxial compressive concrete strength
$\sigma_j = \sigma_{conf}$	Lateral confining stress in region BHK
$\sigma_j = \sigma_s$	Lateral confining stress in region BFH

Practical Implications

The DW stress field offers several practical advantages:

- It integrates confinement and bursting regions into a single consistent model.
- It predicts higher bearing capacities compared to traditional empirical models.
- It provides detailed guidance on reinforcement placement and detailing for efficient load transfer.

The model's results have been validated against experimental data, demonstrating its reliability and accuracy in predicting bearing capacities and reinforcement requirements.

3.5. Expected influence on CFSP-pile to concrete connections

Although the case study does not incorporate follow-up stirrups or hoops, the reinforcement bars in the lower net continuously encircle the loaded area, thereby replicating the function of hoops with ties. In concrete caps, large-diameter reinforcement is often employed with a relatively small centre-to-centre spacing; consequently, the reinforcement ratio should compensate for the absence of follow-up reinforcement. It is therefore anticipated that results comparable to those observed in the experimental campaign (Markic et al. 2022a) used to validate the Markic Dual-Wedge Stress Field theory could be achieved. Primarily determined by the amount of reinforcement contributing to passive confinement and the accessible height and width of the DW stress field, the resulting bearing capacity is expected to be between 2 and 6,5 times higher than the uniaxial compressive strength of the concrete.

4

Application and modification of the Theoretical Models

This chapter explains how the theoretical models found in the literature study and explained in chapter 3 are applied on the case study, and which modification were required to make the theories applicable to the case study. It explains which assumption were made and why these assumptions are reasonable.

4.1. Principal of application

In section 2.2, it is evident that the primary objective of this thesis is to define the overcapacity of the concrete bearing strength directly above the steel pile casing. An examination of the concrete cap, as shown in Figure 2.11, reveals two potential sources from which this additional capacity can be derived. The first source is the substantial volume of concrete that surrounds the loaded area of the pile, and the second is the relatively high ratio of reinforcement present in the lower net. These components offer opportunities to enhance the bearing strength of the concrete.

Section 2.3 outlines the fundamental principles and various types of concrete confinement, as well as their applications in structural design according to the Eurocode. Furthermore, chapter 3 summarises existing studies on concrete confinement, detailing its influence on different applications. In general, concrete confinement is expected to enhance compressive strength, improve ductility, and increase energy absorption capacity, attributes that are particularly advantageous for a connection characterised by the high stiffness of the steel casing and the relatively lower stiffness of the concrete cap.

The challenge lies in quantifying the influence of confinement on such a connection. Here, Mander's theoretical model is introduced. This model describes how the effective laterally confined area is determined and, based on the amount and location of reinforcement, establishes the magnitude of the lateral confining stress. However, Mander's model is primarily applied to walls, blocks, and other reinforced concrete elements that are fully enclosed by reinforcement. The question is how to adapt this model for a situation where only a lower reinforcement net and some pile reinforcement are present.

Therefore it is postulated that a whole or a part of the pile cross-section at the interface with the concrete cap is in compression, thereby generating a compressive stress field accompanied by lateral tensile stresses. The lower reinforcement net within the concrete cap, comprising both lateral and longitudinal reinforcement bars, traverses this stress field. These bars, which surround the stress field, can be regarded as hoop reinforcement and the bars crossing the stress field, can be regarded as ties, akin to the concept proposed by Mander, to confine the concrete within the hoop (see Figure 4.1). Consequently, they may provide passive lateral confinement to the stress field, resulting in an increased normal stress in that region. This effect applies to the entire portion of the interface between the pile and the concrete cap that is subjected to compression. However, owing to the stiffness disparity between the concrete cap and the pile casing, the enhanced concrete strength is observed only at this interface.

Therefore, the region of interest and hence the application of the Markic DW stress field as explained

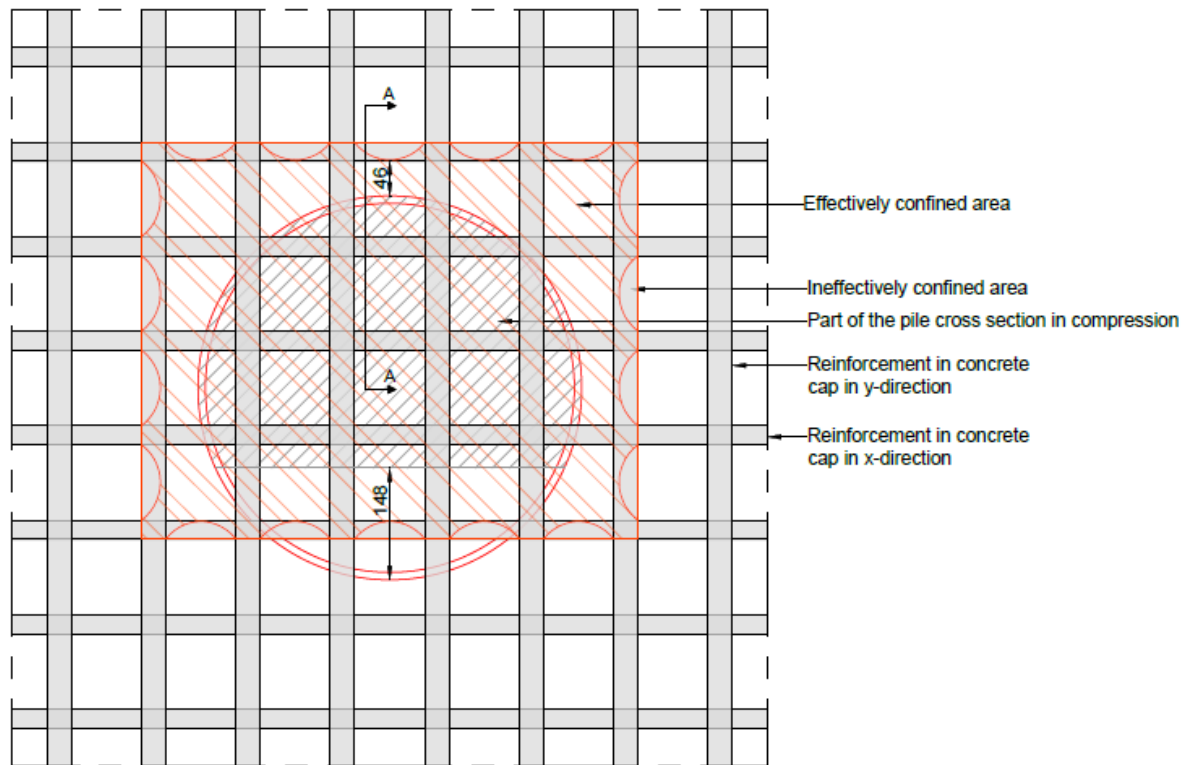


Figure 4.1: Lateral effectively confined area applied to the case study

in section 3.4.2 is concentrated on the interface between the pile casing and the concrete cap at the location where the maximum strain, and thus the maximum compressive stress, occurs. In this way, beyond the effect of passive confinement, the Markic DW stress field is employed on top of the casing to account for the influence of geometric confinement resulting from the stress development via the inclined strut. This principal is shown in figure 4.2.

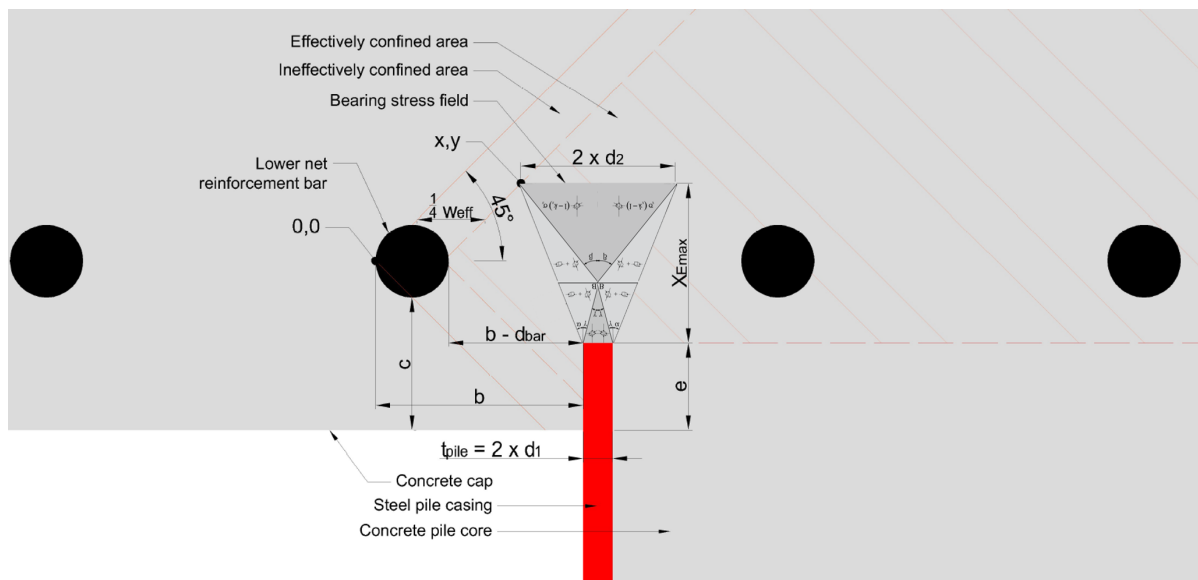


Figure 4.2: Principal of the application of the theory to the case study (cross section A-A in figure 4.1)

4.2. Structural load combinations

In practice, for the application of forces to the head of the pile two specific load combinations are typically considered as governing. In chapter 2, the first combination, where the pile is subjected solely to a normal force, is discussed. The second combination, which frequently occurs, involves the concurrent application of a normal force (whether in tension or compression) and a bending moment. However, since this case study focuses on concrete compressive strength, only a compressive normal force is taken into account. It should be noted that, in this second load combination, the bending moment may act about both the y-axis (M_y) and the x-axis (M_x), depending on the circumstances.

To apply the established theory to the case study, the original three-dimensional problem is reformulated into a two-dimensional analysis. This is achieved by employing the bending moment resultant ($M_{x,y}$) to determine the stress distribution within the contact area between the pile and the concrete cap. The resulting two-dimensional load cases are illustrated in figure 4.3.

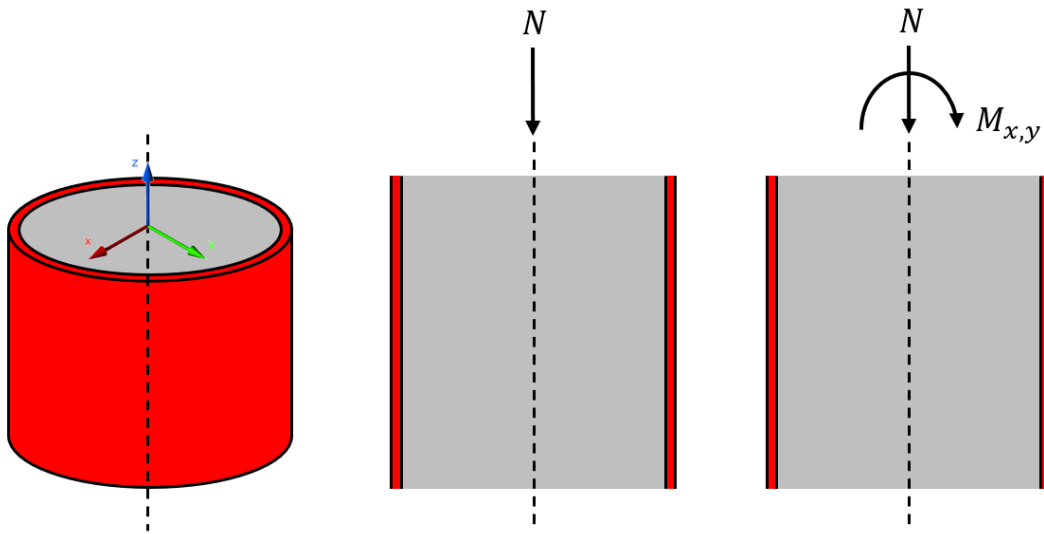


Figure 4.3: Considered structural load combinations

In situations where the pile is exclusively subjected to a normal compressive force, this typically occurs when only permanent loads act on the structure. Permanent loads include the weight of the bridge's superstructure and substructure, as well as any superimposed dead loads, such as rails, barriers, and other permanent fixtures, which generally form the fundamental basis for each load combination used to verify structural stability.

Conversely, the introduction of a bending moment at the pile head is often caused by dynamic or quasi-static loads. In the case study project Amsterdam Oostertoegang, this is typically manifested by factors such as trains traversing the bridge, train braking forces, pedestrian movements on the platforms, and wind loading. While permanent loads provide the primary load combination, the dynamic and quasi-static loads introduce variations that ensure every potential governing load case is duly considered.

According to the governing load combination for the Amsterdam Oostertoegang project, the maximum pile head reaction forces are a compressive normal force of -2061 kN and a resultant bending moment of 258 kNm. The following section explains how these reaction forces are converted into a strain and stress distribution at the interface between the pile and the concrete cap.

4.3. Stress and strain distribution at the interface between pile and the cap

Given the limited duration of this master thesis, it is not feasible to account for the varying bond capacities between the concrete core of the pile and its reinforcement and steel casing. Consequently, a fully bonded condition is assumed to determine the strain distribution across the cross section, resulting in a linear strain distribution.

Considering the combined effects of bending moment and compressive normal force, three distinct strain distribution scenarios may arise. Firstly, if the pile is subjected solely to a normal compressive force, the strain is uniformly negative across the entire cross section. Secondly, if the bending moment is sufficiently large, a neutral axis develops, with the cross section on one side experiencing tensile (positive) strain and on the other side, compressive (negative) strain. Lastly, when the normal force predominates over the bending moment, the entire cross section remains in compression, albeit with a linear distribution that results in one side experiencing greater compression than the other.

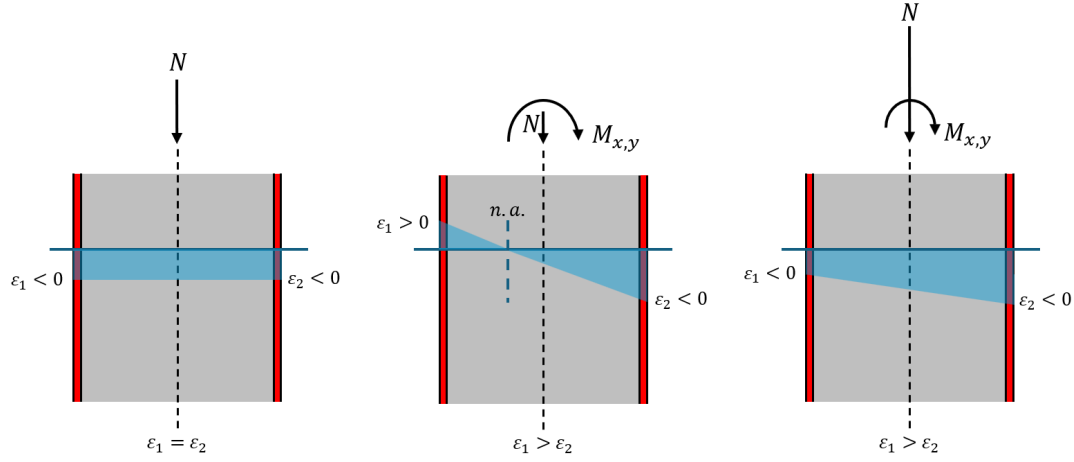


Figure 4.4: strain distribution scenarios

It is important to note that this case study is primarily concerned with the concrete bearing strength at the top of the casing of a concrete-filled steel pipe pile, a focus clearly illustrated by the strain diagrams. In every scenario, the maximum strain is observed at the outer fibre of the steel casing under compression. Given the high stiffness of the steel casing, a substantial contact stress develops at the interface between the steel casing and the concrete cap often creating an overrun of the theoretical concrete compressive strength.

Typically, the connection between the CFSP pile and the concrete cap is achieved using pile reinforcement, which facilitates the transfer of tensile forces and, consequently, bending moments. To determine the stress distribution across the cross-section resulting from the applied external forces, an equilibrium must be established between the internal and external forces. In this analysis, it is crucial to recognise that not all elements of the cross-section contribute in tension; indeed, only the pile reinforcement is capable of resisting tensile forces, as it is anchored within both the concrete and the pile. Expressing these considerations in the equilibrium equations yields the following:

Equilibrium conditions for normal forces:

$$N_{external} = N_{internal} \quad \text{Eq. 4.1}$$

$$N_{internal} = N_{compression} + N_{tension} \quad \text{Eq. 4.2}$$

$$N_{compression} = N_{concrete} + N_{casing} + N_{reinforcement} \quad \text{Eq. 4.3}$$

$$N_{tension} = N_{reinforcement} \quad \text{Eq. 4.4}$$

Equilibrium conditions for bending moments:

$$M_{external} = M_{internal} \quad \text{Eq. 4.5}$$

$$M_{internal} = M_{compression} + M_{tension} \quad \text{Eq. 4.6}$$

$$M_{compression} = M_{concrete} + M_{casing} + M_{reinforcement} \quad \text{Eq. 4.7}$$

$$M_{tension} = M_{reinforcement} \quad \text{Eq. 4.8}$$

Note that compressive normal forces have a negative value and tensile normal forces have a positive value.

To determine the contribution of each element to the internal force, the cross-section is subdivided into segments. The concrete core is partitioned into horizontal rectangular strips, note that this approach introduces a slight deviation, as the sides of these segments are straight, whereas the concrete core is circular. The steel casing is segmented by lines radiating from the centre of the pile at equal angular intervals, ensuring that the entire area of the steel casing is covered without introducing imperfections. Each individual pile reinforcement bar is modelled as a separate segment, with the bar's centre representing its x and y coordinates.

Each segment is characterised by its material properties (including the modulus of elasticity and yield or compressive strength), cross-sectional area, and strain magnitude. The strain is determined by its position along the height of the cross-section, under the assumption of a linear strain distribution. Iterative variable inputs for the strain at the bottom and top of the cross-section are utilised. Consequently, the force and moment contributions of each segment can be calculated by:

$$N_{element} = \sum_{n=i}^{n_{seg}} A_i \times E_i \times \varepsilon_i \quad \text{Eq. 4.9}$$

$$M_{element} = \sum_{n=i}^{n_{seg}} N_{seg} \times y_i \quad \text{Eq. 4.10}$$

Where y_i is the distance from the element centre to the neutral axis.

Using an iterative process that considers the strains at both the bottom and top of the cross-section as variables to achieve force and moment equilibrium, a Python script was developed (see Appendix A.1). This script employs a numerical approach to establish force equilibrium while accounting for the geometrical and material constraints. Given the governing reaction forces at the pile head for this case study, the script produces the following strain and stress distribution diagrams, complete with the neutral axis and rebar indications.

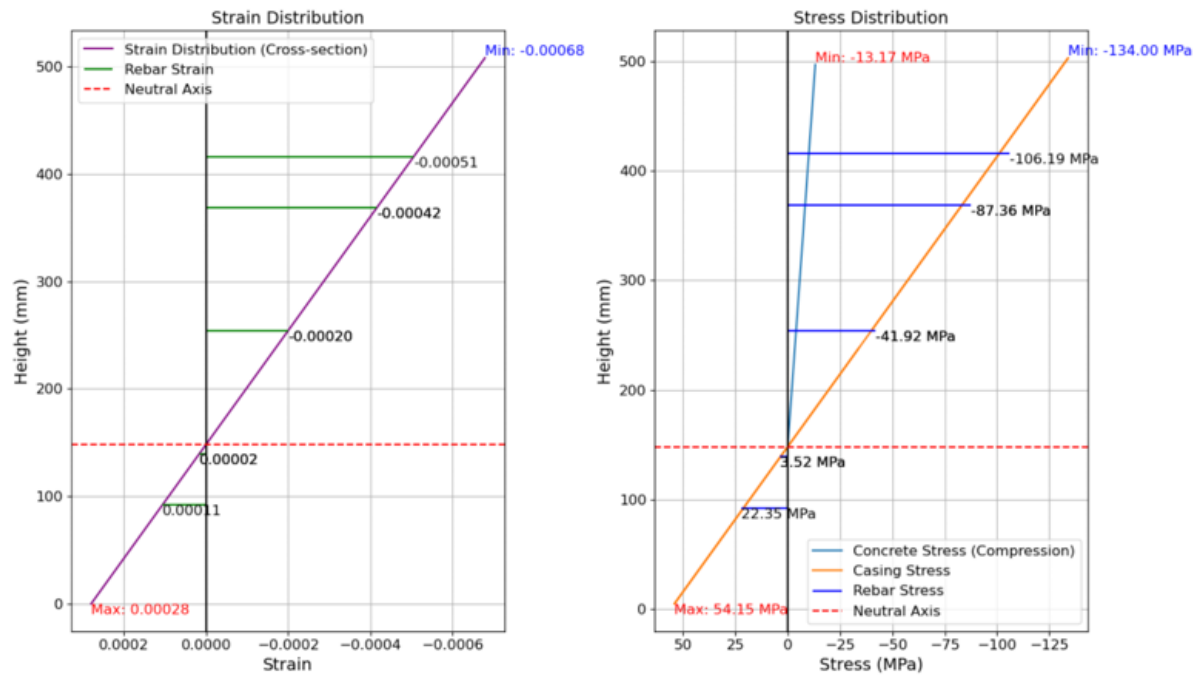


Figure 4.5: Results python script strain- and stress distribution

In this case, the stress distribution shown in figure 4.5 indicates that the maximum compressive stress occurs at the top of the cross-section, with a magnitude of 134 MPa. This value is 4.46 times greater than the characteristic uniaxial compressive strength of concrete C30/37, suggesting that the concrete at the interface is prone to crushing and that local failure is a significant concern. An additional important

output from the Python script is the location of the neutral axis, which is determined to be at a height of 148.33 mm. The strain diagram clearly shows that the area above the neutral axis is in compression, as evidenced by the negative strain values in that region. This finding initiates the second step: the determination of the lateral confining stress from the lower reinforcement net, according to Mander's model for confined concrete as explained in section 3.3.1.

4.4. Application of Mander's model for confined concrete

To assess the impact of passive confinement provided by the lower reinforcement net, Mander's model for confined concrete is employed. However, to apply Mander's model to this case study, certain modifications are required. As outlined in Section 3.3.1, the original theory was developed and validated for concrete blocks and walls reinforced with stirrups, hoops, and ties. An example of such an element is illustrated in Figure 3.2, which differentiates between the effectively confined core and the ineffectively confined core. The extent of effective confinement in the concrete depends on several factors, including the spacing (s) between the hoops or stirrups, the core width in the x-direction (b_c), the core width in the y-direction (d_c), and the spacing (w') between the ties.

The application of Mander's confined concrete model to this case study is based on the premise that the reinforcement bars of the lower net enclosing the perimeter of the compressed zone act as hoops, while all bars from the lower net intersecting the compressed zone function as ties. Under this consideration, the only unknown parameter is the hoop spacing (s), as there is no successive reinforcement net along the height of the concrete cap.

So the parameters defining the effectively confined area in the horizontal plane are:

- b_c is the distance between the centre of the rebars in y-direction directly outside the compression zone;
- d_c is the distance between the centre of the rebars in x-direction directly outside the compression zone;
- w'_x is the effective distance between the rebars in y-direction;
- w'_y is the effective distance between the rebars in x-direction;

To define the effectively confined area in the horizontal plane, an adjustment to the theory is made by making an assumption. The boundaries of the effectively confined region are defined by parabolic curves extending from the outer edge of the first hoop to the outer edge of the hoop above. Notably, these parabolas originate at an angle of 45 degrees from the rear of the hoops.

To define the effectively confined concrete using a single hoop, it is assumed that the boundary follows a 45-degree trajectory until it intersects with the corresponding line originating from the opposite side of the hoop. The vertical distance from the base of the concrete cap to the point of intersection represents the total height of the effectively confined region. This height, denoted as 's' according to Mander, characterises the extent of the region influenced by a single hoop.

At a certain height, the corner of the Markic Dual Wedge (DW) stress field on top of the casing intersects with the boundary line of the effectively confined area (indicated by the point x,y in figure 4.2). At this height, the effectively confined area of interest is identified, as the height and width of the DW stress field are optimised, resulting in the greatest bearing capacity.

If the DW stress field extends beyond the effectively confined area, part of the stress field would remain unconfined, causing the stress in the strut (σ_α) to be limited to the uniaxial compressive strength of the concrete. Therefore, the smallest effective area is determined at the point where the DW stress field intersects with the boundary of the effectively confined region.

Applying the modified Mander's model to the case study requires the following parameters, which correspond to those illustrated in Figure 4.2:

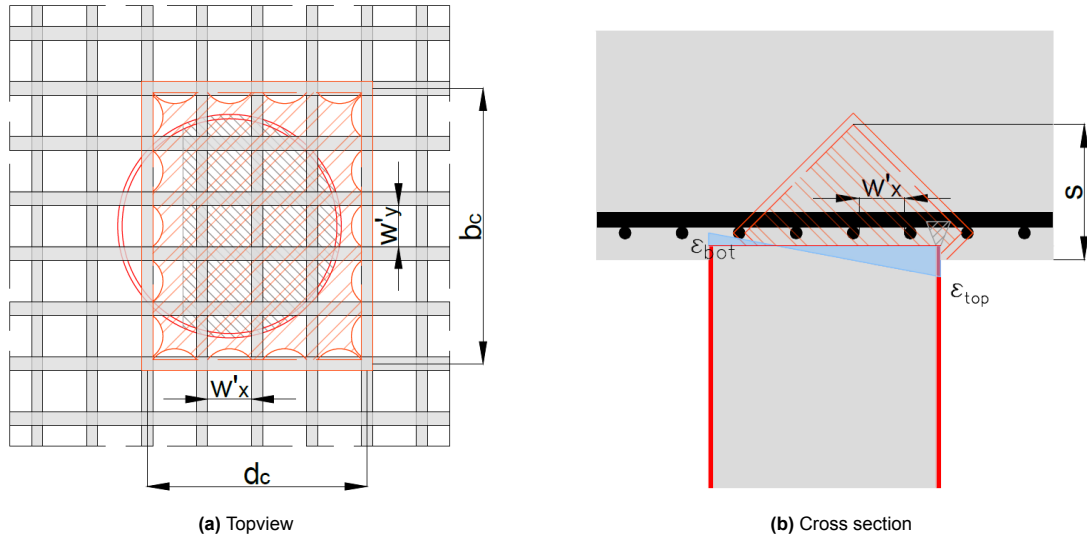


Figure 4.6: Dimension parameters required for Mander's model

$d_{bar,x} = 25 \text{ mm}$	Diameter of the rebars in the x-direction in the lower net;
$d_{bar,y} = 32 \text{ mm}$	Diameter of the rebars in the y-direction in the lower net;
$w_x = 125 \text{ mm}$	Spacing between the rebars in the x-direction;
$w_y = 125 \text{ mm}$	Spacing between the rebars in the y-direction;
$b = 71 \text{ mm}$	Distance between the outer fibre of the nearest rebar and the steel casing;
$c = 50 \text{ mm}$	Concrete cover;
$e = 30 \text{ mm}$	Embedment depth of the pile casing in the concrete cap;
$\alpha = 25.57^\circ$	Inclination of the DW stress field strut, determined iteratively using a Python script for the DW stress field.

Where the inclination of the DW stress field strut (α) is a variable that optimises the interaction between passive confinement effects on the strut within the DW stress field, the available width and height for stress distribution, and the size of the effectively confined area.

By applying the above parameters in the Python script with the modified Mander's model (see Appendix A.2), the following effective lateral confining stresses, as well as the optimal width and height of the DW stress field, are obtained:

$f_{eff,lx} = 6.52 \text{ MPa}$	Effective lateral confining stress in the x-direction;
$f_{eff,ly} = 10.25 \text{ MPa}$	Effective lateral confining stress in the y-direction;
$d_2 = 60.80 \text{ mm}$	Width of the available load distribution area;
$X_{E;max} = 53.10 \text{ mm}$	Available height for the DW stress field.

As described in the results above, a difference exists between the lateral confining stresses in the x- and y-directions. This disparity arises primarily due to the variation in rebar diameters in these directions ($\varnothing 25 \text{ mm}$ and $\varnothing 32 \text{ mm}$, respectively). Additionally, deviations could occur due to differences in centre-to-centre spacing of the rebars in each direction; however, this is not the case for the case study. Note that, in this case, for subsequent calculations, the effective lateral confining stress in the y-direction should be used when determining the bearing strength, as the casing in the critical area is oriented in the x-direction.

4.5. Application of Markic Dual Wedge stress field

The Dual-Wedge (DW) stress field model is directly applicable to the case study without modification, as the width of the loaded area (d_1) is equal to the thickness of the pile casing, and the uniaxial concrete compressive strength is derived from the 28-day compressive strength of the concrete mixture used. The modified Mander's model for confined concrete determines all dimensional input parameters by accounting for the limitations imposed by the boundaries of the effectively confined area. The parameters corresponding to the case study are:

$f_{c0} = 30 \text{ MPa}$	Characteristic uniaxial compressive strength concrete C30/37;
$\sigma_{conf} = \sigma_s = f_{eff,ly} = 10.25 \text{ MPa}$	Effective lateral confining stress;
$d_2 = 30.40 \text{ mm}$	Half the width of the available load distribution area;
$X_{E;max} = 53.10 \text{ mm}$	Available height for the DW stress field;
$d_1 = t_{casing} = 10 \text{ mm}$	Width of the loaded area;
$d_2 = 60.80 \text{ mm}$	Width of the available load distribution area.

Applying the Markic DW stress field theorem to the case study (using the Python script in Appendix A.3) yields a strut inclination angle (α) of 25.57° . This value corresponds to the input for the modified Mander's model, resulting in the aforementioned parameters for the Markic DW stress field model and a maximum bearing capacity of 149.05 MPa.

This result implies that, according to the theorem, the bearing capacity of the concrete directly above the steel pile casing is nearly five times greater than the uniaxial compressive strength of the concrete used (C30/37). The experimental campaign by Markic et al. (Markic et al. 2022a) indicates that, depending on the configuration of the concrete, the loaded area, and the reinforcement, the bearing strength could reach up to 6.44 times the uniaxial compressive strength. Furthermore, Eurocode 2-1 article 6.7 and Eurocode 2-4 article 7.2.1.5, as explained in Sections 2.2.1 and 2.2.3, respectively, suggest that increased compressive strengths range from three to 7.5 times the uniaxial compressive strength. These findings indicate that the factor of five derived from the combined and modified theorem is plausible.

Although the bearing capacity of 149.05 MPa represents a design bearing strength and demonstrates that the concrete would not be crushed by the applied load—since the maximum bearing stress determined in Section 3.4 is 134 MPa, which is lower than 149.05 MPa—for design purposes this is still insufficient. This is because the partial safety factor for concrete (γ_c) is 1.5, resulting in a design bearing capacity of just under 100 MPa, which is inadequate to resist the bearing stress imposed by the governing load combination.

5

Finite Element Analysis development and results

This chapter presents the finite element analysis (FEA) methodology used to assess the effects of confinement on CFSP-pile to concrete element connections in the absence of force transfer provisions such as dowels or shear rings. The chapter first outlines the modelling approach, including the selection of an axisymmetric geometry, the types of elements employed, and mesh refinement considerations. It then explains the material properties used in the simulation, which were selected to replicate experimental conditions found in relevant literature. Finally, the results of a case study are presented and discussed in the context of the research objectives, offering insights into the structural response due to confinement and validating the modelling approach through comparison with theoretical models and design codes.

5.1. FEA Method

Diana FEA software is used to model the connection between the CFSP-pile and concrete cap as designed for the case study project. This section describes the analysis method employed, the element types and mesh discretisation adopted, and the rationale for these choices.

5.1.1. Axisymmetric modelling

To simulate the interaction between the CFSP pile and the surrounding concrete element with computational efficiency and sufficient fidelity, a two-dimensional axisymmetric finite element model was adopted. Axisymmetric modelling is particularly well suited for problems involving rotational symmetry in both geometry and loading. In this approach, a two-dimensional cross-section is defined in the radial-vertical plane (the XY-plane in DIANA), and it is numerically revolved 360 degrees around the Y-axis, which DIANA interprets as the axis of symmetry (see Figure 5.1). Each element in the model thus represents a ring of material, allowing the structural response of the full three-dimensional system to be captured using a 2D representation.

In reality, however, the physical system under investigation consists of a CFSP pile embedded within a continuous, reinforced concrete cap. This type of configuration introduces significant geometric and reinforcement asymmetries that cannot be directly modelled with an axisymmetric formulation. Therefore, certain simplifications were made to enable the use of axisymmetry in the analysis.

Most notably, the continuous concrete cap was idealised as a circular concrete block centred around the CFSP pile. This simplification assumes that the structural response in the region immediately surrounding the pile is governed primarily by local confinement effects, which can be reasonably approximated by a circular domain. As such, the model does not capture global bending or shear behaviour of the larger concrete cap but rather focuses on the local interaction and confinement mechanism that are critical for assessing the pile-to-concrete connection.

Another important simplification concerns the reinforcement detailing. In the real concrete cap, reinforcement is provided in the form of longitudinal bars and stirrups, typically forming an orthogonal grid in the horizontal plane. However, in the axisymmetric model, this configuration cannot be represented directly. To approximate the effect of reinforcement, the lower reinforcement mesh of the concrete cap was translated into a combination of two reinforcement types:

1. Hoop reinforcement in the tangential direction, representing the circumferential action of the transverse bars.
2. Spread radial reinforcement, modelled explicitly in the radial direction to account for reinforcement crossing the pile interface.

In DIANA, the radial reinforcement is modelled as a reinforcement grid (see Figure 5.1), with zero equivalent thickness in the local y-direction and an equivalent thickness of 3.93 mm in the local x-direction (calculated as $0.25 \times \pi \times 25^2 / 125 = 3.93$) to represent 25 mm rebars at 125 mm spacing. The hoop reinforcement is represented by embedded bar elements of 32 mm diameter, arranged at 125 mm centre-to-centre spacing.

While this transformation alters the mechanical idealisation of the reinforcement, it preserves the essential contribution of the steel in resisting radial expansion and distributing confinement-induced stress. This makes it possible to study the effects of confinement under vertical loading while maintaining computational efficiency and model clarity.

The axisymmetric domain consisted of the steel casing of the CFSP pile, the concrete infill, and the idealised surrounding circular concrete region. Boundary conditions were applied to reflect symmetry along the Y-axis and vertical restraint at the base, while allowing free deformation elsewhere. The vertical interface between the CFSP-pile casing and the surrounding concrete was modelled as a contact surface, i.e. fully unbonded, in accordance with Eurocode provisions, which mandate this assumption for all capacity and stiffness calculations. The normal stiffness of the interface elements was set to a high value of 10.000 N/mm^3 to prevent non-physical penetration of one material into the other. Conversely, the shear stiffness modulus was reduced to zero, permitting unrestricted tangential movement between the components and thereby simulating a fully unbonded interface.

To verify that the effect of confinement is accurately captured in the axisymmetric finite element model, the same cube model used for determining appropriate material parameters later in this chapter (see section 5.2), was also employed to compare the stress-strain response across 2D, 3D, and axisymmetric modelling approaches. The resulting stress-strain curves are presented in Figure 5.2. This figure reveals that the confined 3D and axisymmetric models produce identical curves, confirming that the axisymmetric approach effectively captures the effects of passive lateral confinement.

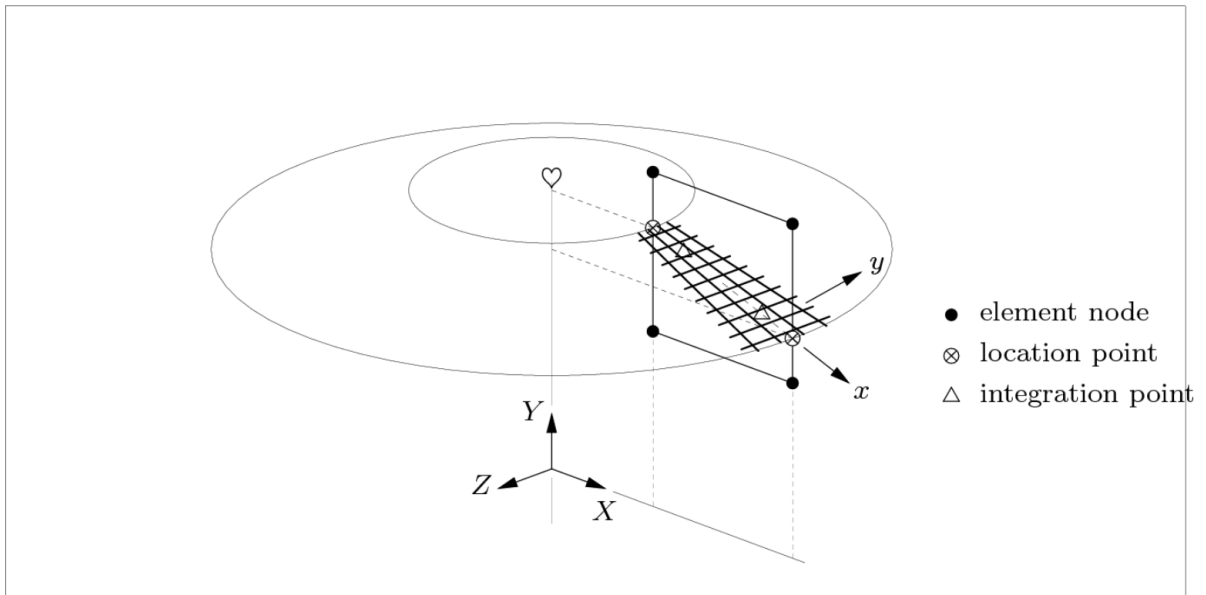


Figure 5.1: Axisymmetry FEA model (DIANA 2017a)

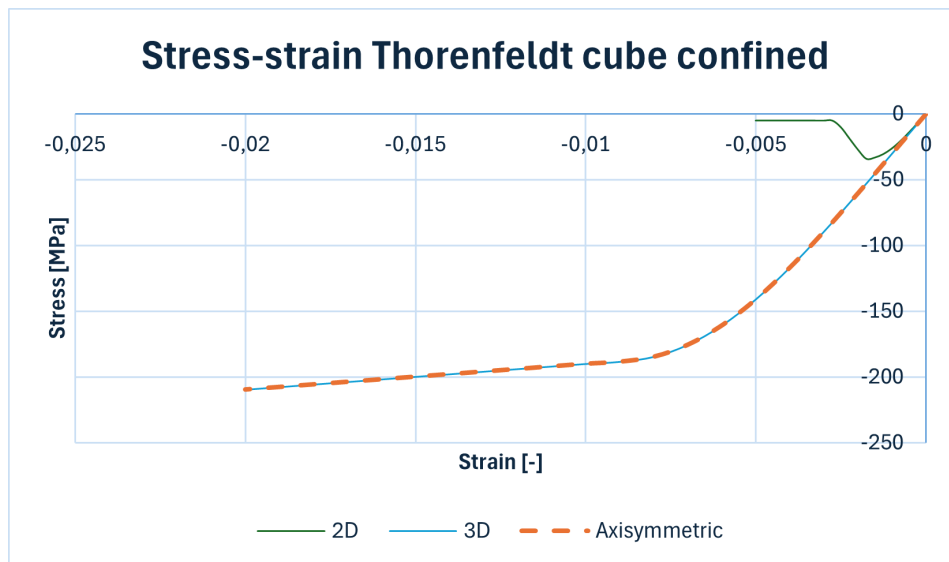


Figure 5.2: Stress-strain curves for different ways of modelling in FEA

5.1.2. Element type

In the finite element analysis of the CFSP-pile to concrete element connections, the choice of element type is critical to ensure an accurate representation of the structural behaviour, particularly in regions where stress concentrations and confinement effects are expected. Given the axisymmetric configuration of the model and the need for high-resolution stress and strain output, the CQ16A element was selected.

The CQ16A is an eight-node isoparametric quadrilateral solid ring element designed specifically for axisymmetric analyses within the DIANA finite element environment. It is based on quadratic interpolation functions (DIANA 2017b), which allow for a more refined representation of displacement fields compared to linear elements. The geometry of this element permits the accurate simulation of complex deformation modes and stress distributions, especially in cases involving curved interfaces or non-linear material responses, such as those present in the steel–concrete interaction zone.

The element uses a 2×2 Gauss integration scheme, which ensures a balanced compromise between computational efficiency and numerical precision (DIANA 2017b). This integration method is sufficient to capture non-linear behaviour without introducing locking effects, which can occur in bending-dominated regions or with poorly shaped elements.

The CQ16A element is particularly well suited for this study for several reasons:

1. Compatibility with axisymmetric modelling: It is formulated specifically for problems with rotational symmetry around the Y-axis in DIANA, ensuring that each element represents a ring of material upon revolution around the axis.
2. High fidelity in stress analysis: The quadratic interpolation functions allow the element to resolve steep stress gradients near the pile–concrete interface, where confinement effects are most pronounced.
3. Robustness in non-linear analysis: Its integration scheme and interpolation order are well adapted for use in geometrically and materially non-linear problems, which are common in simulations involving concrete cracking, steel yielding, and confinement.

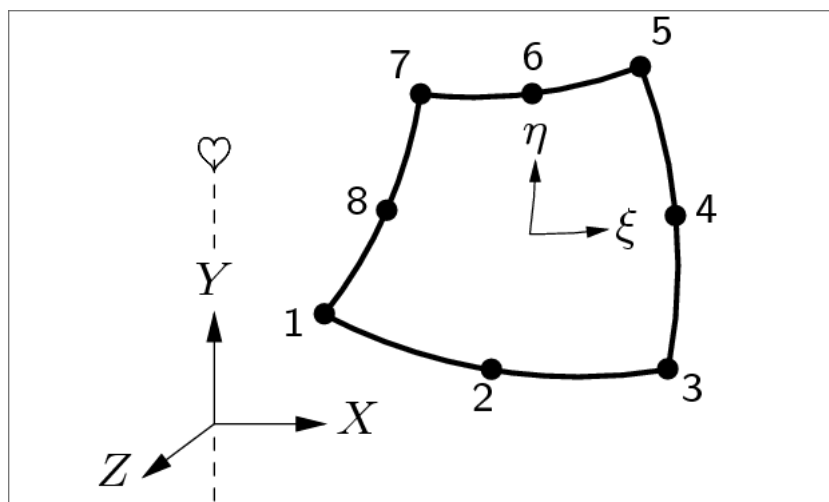


Figure 5.3: CQ16A element (DIANA 2017b)

In line with the simplifications introduced in the axisymmetric model, the continuous concrete cap in the real structure was idealised as a circular concrete region centred around the CFSP pile. This required the reinforcement layout to be translated into a form compatible with axisymmetric modelling. The lower reinforcement mesh of the cap, typically composed of orthogonally placed longitudinal bars and stirrups, was approximated by modelling reinforcement as tangential hoops and radially distributed bars. This allowed the principal confinement contributions of the reinforcement to be preserved within the axisymmetric idealisation.

Both the steel casing of the CFSP pile and the surrounding concrete block were discretised using CQ16A elements. The use of the same element type for both materials ensured numerical consistency and avoided compatibility issues at the material interface. The reinforcement within the concrete infill, where modelled explicitly, was incorporated using embedded reinforcement definitions, allowing the reinforcement bars to share degrees of freedom with the surrounding CQ16A concrete mesh.

The choice of CQ16A elements thus supports the overarching goal of the analysis: to evaluate the confinement effect in CFSP-to-concrete connections with high accuracy, particularly in the absence of dedicated force transfer components such as dowels or shear rings.

5.1.3. Mesh Size

The generation of a high-quality mesh is critical in finite element analysis, especially when modelling the interaction between different materials and capturing non-linear behaviour. In this study, meshing was conducted with particular attention to the pile–concrete interface, where steep stress gradients were expected due to confinement effects and potential relative displacement.

A structured meshing strategy was employed, with an emphasis on maintaining square-shaped, uniformly sized elements wherever possible to optimise numerical stability and reduce distortion-related errors. The mesh was refined over horizontal strips near the critical zone around the tip of the steel casing, ensuring an adequate resolution of the contact stresses and strain localisation effects. In this region, the element size was reduced progressively toward the interface, forming a transition zone that avoids abrupt changes in element density.

In contrast, the mesh in regions further away from the interface (where stress gradients were expected to be lower) was kept coarser to reduce the computational burden without compromising accuracy.

Special care was taken to ensure node alignment across material interfaces, particularly between the steel casing and the concrete, to facilitate effective stress transfer and avoid compatibility issues. The embedded reinforcement bars were positioned within the host concrete mesh such that DIANA's embedded reinforcement functionality could accurately interpolate the surrounding displacement field, allowing the bars to share strain with the concrete through embedded coupling.

Figure 5.4 shows the meshed model, including boundary conditions and domain partitioning. All supports are modelled as roller supports, restraining only translation perpendicular to the boundary plane; in-plane translations and rotations remain free. The supports are idealised as infinitely stiff. All grey domains resemble concrete and the steel is assigned a blue colour. Also important to note is the mesh size of all the domains:

- Out of concrete cap section of the pile core and casing: 10 mm
- In concrete cap section of pile core and casing: 5 mm
- Fine part of the concrete cap: 5 mm
- Mid part of the concrete cap: 10 mm
- Coarse part of the concrete cap: 20 mm

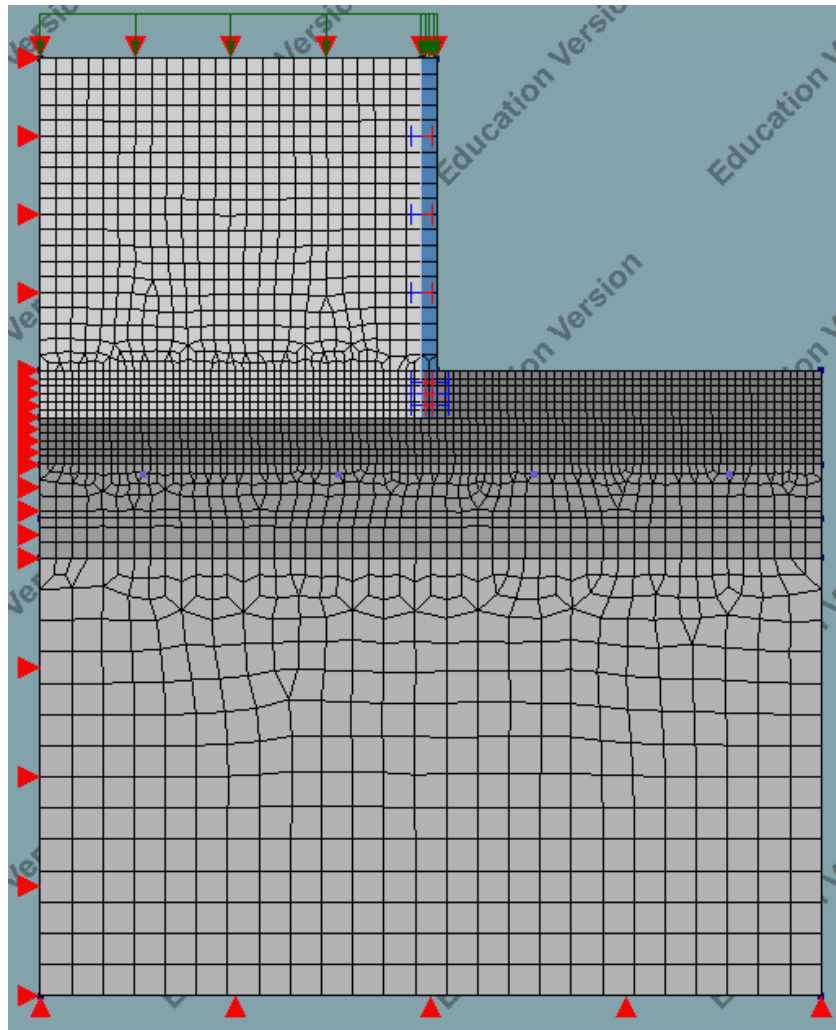


Figure 5.4: Meshed axisymmetric case-study model (inverted orientation; see section 5.3 for explanation)

5.2. Material Properties

To construct a representative finite element model that accurately captures the effects of confinement, it is essential to select an appropriate material behaviour model along with corresponding material parameters. In this study, selected specimens from the experimental campaign by Markic et al. (Markic et al. 2022a) were replicated in an axisymmetric finite element model. The material parameters were calibrated such that the numerical results aligned closely with the experimentally observed behaviour. Prior to this calibration, a suitable constitutive model and its associated input parameters were identified and justified.

5.2.1. Material Model Selection

DIANA requires the user to specify a constitutive model for concrete, offering several predefined material laws. An examination of the stress-strain curve obtained experimentally by Manders et al. (Mander et al. 1988a) reveals a characteristic descending branch post peak stress (see Figure 5.5). This softening behaviour is initially steep and gradually flattens. Comparing this to DIANA's standard material models (see Figure 5.6) shows that the experimental curve most closely resembles the Thorenfeldt model, as well as the CEB-FIP Model Code 1990 and 2010 formulations.

When the CEB-FIP material laws are selected, DIANA automatically assigns all relevant compressive parameters as prescribed by the respective model codes, requiring no additional input. The Thorenfeldt model, in contrast, necessitates manual specification of compression parameters based on its functional formulation. The plain Thorenfeldt curve is described by the following formulation:

$$f = -f_p \frac{\alpha}{\alpha_p} \left(\frac{n}{n - \left(1 - \left(\frac{\alpha}{\alpha_p} \right)^{nk} \right)} \right) \quad \text{Eq. 5.1}$$

where the shape parameters n and k are determined using:

$$n = 0.80 + \frac{f_{cc}}{17} \quad \text{Eq. 5.2}$$

$$k = \begin{cases} 1 & \text{if } \alpha_p < \alpha < 0 \\ 0.67 + \frac{f_{cc}}{62} & \text{if } \alpha \leq \alpha_p \end{cases} \quad \text{Eq. 5.3}$$

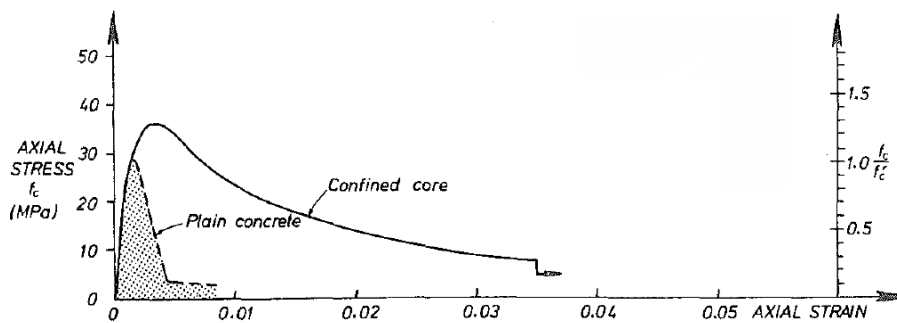


Figure 5.5: Typical confined specimen experimental stress-strain curves (Mander et al. 1988a)

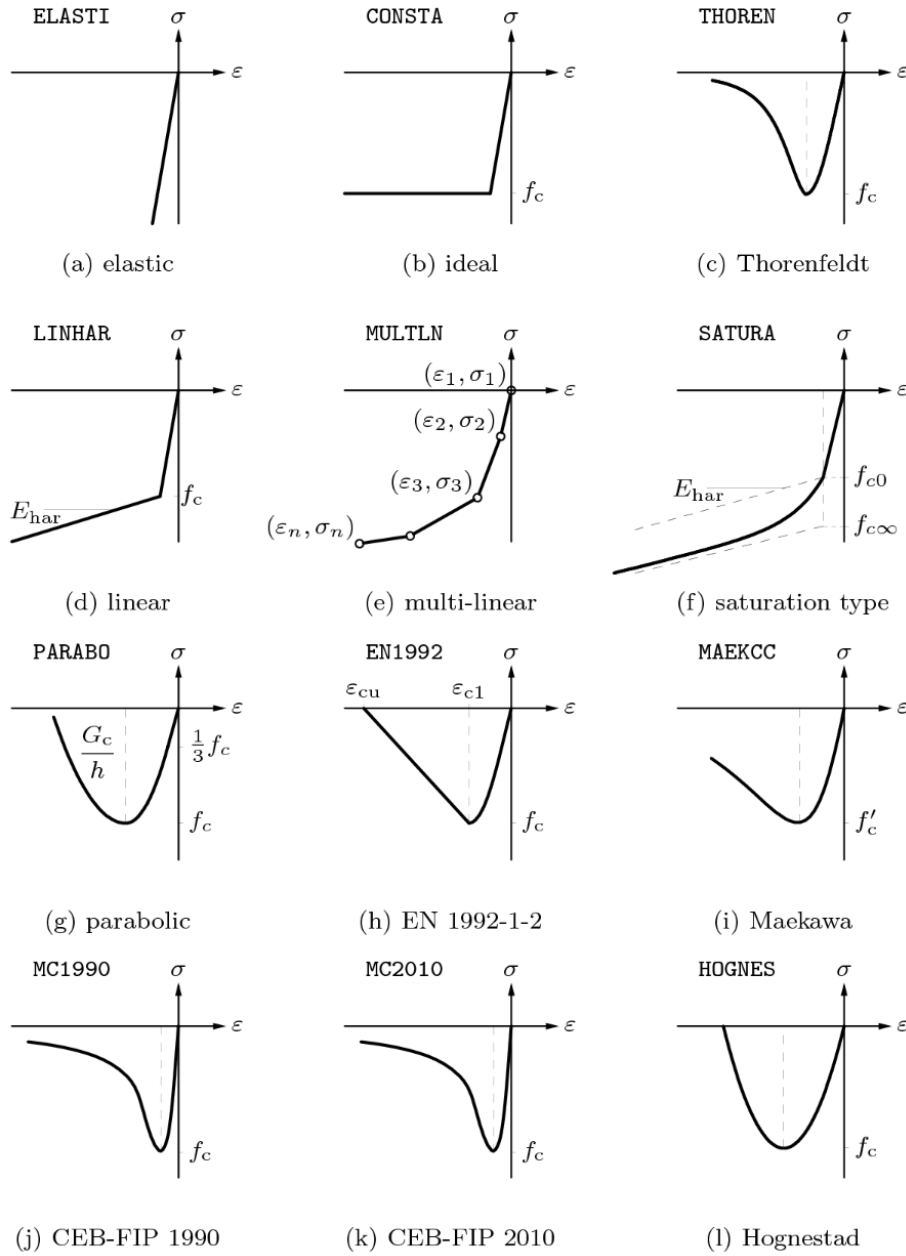


Figure 5.6: Concrete material models in DIANA (DIANA 2015b)

5.2.2. Confined Thorenfeldt Model with Extended Softening Behaviour

In DIANA, the Thorenfeldt compressive stress–strain curve can be extended to incorporate confinement effects using a series of formulations that adjust both the peak and post-peak behaviour (DIANA 2015a). The confined peak strain ε_p is defined as a multiple of the initial strain ε_0 by a confinement-dependent factor K_σ :

$$\varepsilon_p = K_\sigma \varepsilon_0 \quad \text{Eq. 5.4}$$

where the initial strain ε_0 is given by:

$$\varepsilon_0 = -\frac{n}{n-1} \cdot \frac{f_{cc}}{E} \quad \text{Eq. 5.5}$$

with n the Thorenfeldt shape parameter, f_{cc} the confined compressive strength, and E the Young's modulus. These equations yield a gradual increase in strength under confinement, maintaining a linear initial stiffness governed by the modulus of elasticity. In a fully confined triaxial stress state, the failure surface may not be reached, resulting in a fully linear stress–strain response.

To represent the increased ductility of confined concrete, DIANA modifies the descending branch of the Thorenfeldt curve by applying a linear compression-softening law:

$$f_j = -f_p \left[1 - (1 - r) \cdot \frac{\alpha_j - \alpha_p}{\alpha_u - \alpha_p} \right] \leq -r f_p \quad \text{Eq. 5.6}$$

where f_j is the compressive stress at strain α_j , f_p is the peak stress, α_p is the strain at peak, α_u is the ultimate strain, and r is the residual strength factor. The ultimate strain is defined as:

$$\alpha_u = \left(\frac{f_p}{f_{cc}} \right)^\gamma \alpha_p \quad \text{Eq. 5.7}$$

where γ is a scalar exponent typically taken as 3. The residual strength ratio r also depends on the peak-to-compressive strength ratio:

$$r = \left(\frac{f_p}{f_{cc}} \right)^\gamma r_0 \quad \text{Eq. 5.8}$$

with r_0 an initial residual strength factor, commonly taken as 0.1. The use of this linear softening formulation is conditional: it is only activated if the peak strength is significantly higher than the base compressive strength ($f_p/f_{cc} > 1.05$). For smaller ratios, typically associated with lateral cracking or limited confinement, the model does not artificially increase ductility. However, in the case study presented in this thesis, the peak strength f_p is assumed to be significantly higher than the confined compressive strength f_{cc} , satisfying the condition $f_p/f_{cc} > 1.05$. As a result, DIANA applies the linear softening law to increase ductility in the post-peak regime, as defined by the confined Thorenfeldt model.

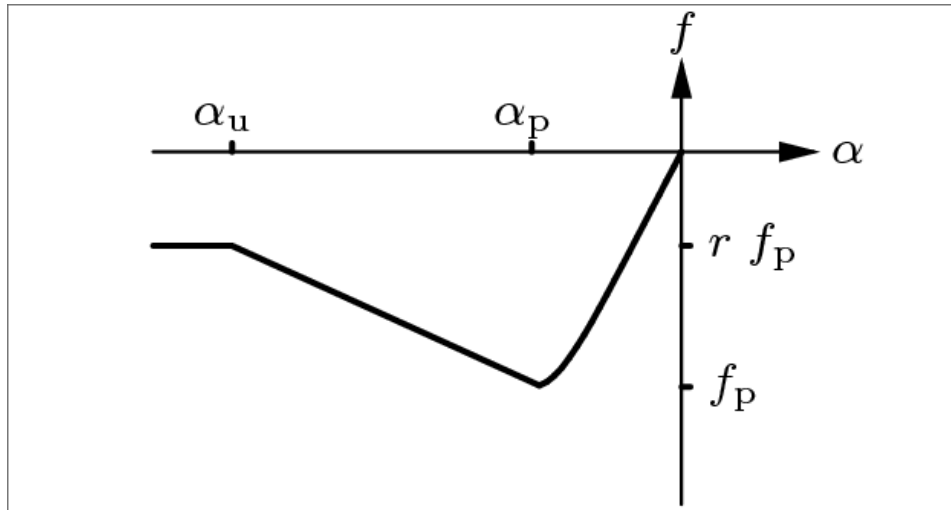


Figure 5.7: Confined Thorenfeldt compressive behaviour curve (DIANA 2015a)

5.2.3. Material Behaviour Evaluation in FEA

To compare the response of the CEB-FIP 1990, CEB-FIP 2010, and Thorenfeldt models under confinement, a simplified square specimen was analysed. A 2D plane stress model measuring 500 mm \times 500 mm was used, with translation support fixed in x- and y-direction at the base and a prescribed vertical displacement of -2.5 mm at the top surface (see Figure 5.8).

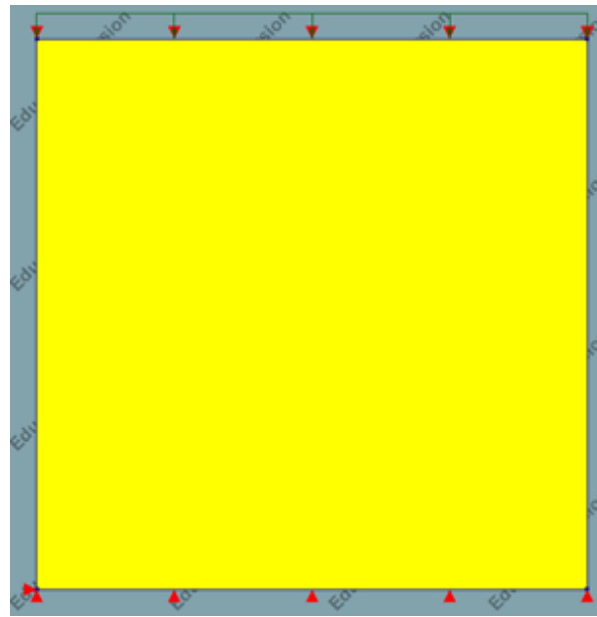


Figure 5.8: Plane stress 2D cube, 500 mm \times 500 mm, unconfined

Identical parameters for elastic modulus, crack orientation and tensile behaviour were assigned to all models (see Figure 5.9). The primary differences lay in the compressive behaviour. To represent the tensile behaviour of concrete a linear-crack energy approach was applied together with a rotating crack orientation. This setup is particularly suitable for simulating confinement effects in reinforced concrete structures.

The tensile strength was set to 3 N/mm², and the Mode-I fracture energy to 100 N/m, which are realistic values for normal-strength concrete (C30/37). These parameters control the initiation and propagation of cracks, which is essential when modelling confinement, as cracking significantly influences the stress redistribution and stiffness degradation around confined regions.

The residual tensile strength is set to zero, meaning although conservative but also realistic no post-peak tensile capacity is assumed. This is appropriate for concrete in tension, as it typically loses its load-carrying capacity once cracked. The crack bandwidth specification is set to “Rots”, which aligns the softening behaviour with the mesh size, ensuring objectivity in energy dissipation regardless of element size which is a key requirement for realistic fracture simulation in finite element models.

The choice of the rotating crack model is particularly relevant for modelling confinement. Unlike fixed crack models, rotating crack models allow the crack orientation to evolve with the principal strain directions during the analysis. This better reflects the actual behaviour of concrete under multiaxial stress states, such as those present in confined zones, where load paths and crack patterns can change significantly during loading. It results in a more stable and physically realistic representation of crack development under complex loading conditions.

(a) Linear material properties

(b) Tensile behaviour

Figure 5.9: Common input parameters for all cube models

To simulate the effect of confinement, the Selby-Vecchio confinement model was applied to each material variant. This model introduces a continuous and physically realistic relationship between lateral restraint and enhanced compressive behaviour, surpassing traditional multi-linear approximations.

For CEB-FIP 1990, only the uniaxial compressive strength was required. The 2010 version additionally needed strain values at peak stress and failure. For the Thorenfeldt model, inputs included the compressive strength, shape parameters n and k , residual strength, and a length scale parameter to regulate post-peak softening (see Figure 5.10).

In constitutive models that incorporate strain-softening behaviour, such as the Thorenfeldt compression model, the inclusion of a length scale parameter is essential to ensure mesh-independent results. After reaching the peak compressive stress, concrete exhibits a progressive loss of strength, which, if not properly regulated, can lead to excessive energy dissipation that is strongly dependent on the finite element size. The length scale parameter addresses this by localising the softening behaviour over a representative distance, typically taken as the characteristic element size in the direction of expected crushing. This ensures that the energy dissipated during post-peak deformation remains physically realistic and consistent across different mesh resolutions. In DIANA, this parameter effectively links the strain-softening response to a fracture energy per unit area, allowing the model to reproduce the correct energy absorption associated with crushing of concrete. This means that when creating a model that consist of different size elements. Also materials with corresponding length scale parameters should be assigned.

This means that when a model consists of elements with varying sizes, it is important to assign material models with corresponding length scale parameters. Doing so ensures that the strain-softening behaviour remains consistent across the mesh and that the energy dissipation associated with material degradation is not influenced by differences in element size.

The damage-based Poisson's ratio reduction model is applied to ensure a realistic representation of concrete's lateral behaviour after cracking. When concrete cracks in tension, it not only loses stiffness in the loading direction but also exhibits reduced lateral deformation. By linking the reduction of Poisson's ratio to the damage variable, the model captures this effect accurately. This is particularly relevant in confinement scenarios, where lateral expansion influences the interaction with surrounding elements. Without this reduction, the model may overestimate confinement effects and produce unrealistic lateral strains.

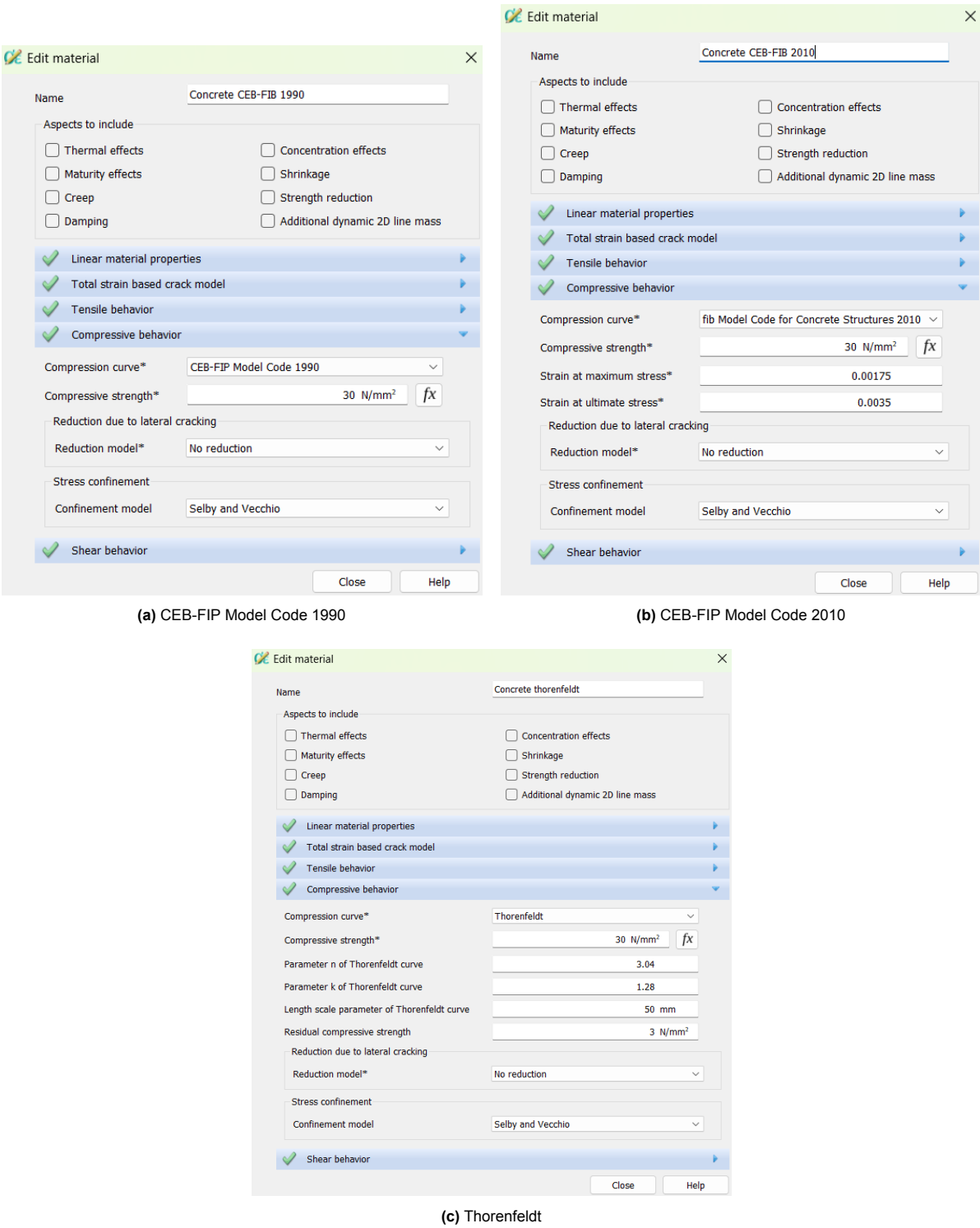


Figure 5.10: Compressive material models used in the cube simulations

Verification of passive confinement response was done by calculating the expected lateral deformation using Poisson's ratio ($\nu = 0.2$). For an axial strain of 0.005, the lateral strain is 0.001, leading to an expected lateral deformation of 0.5 mm across a 500 mm specimen for a 2.5 mm prescribed deformation. All material models produced lateral deformations in agreement with this theoretical value (see Figure 5.11).

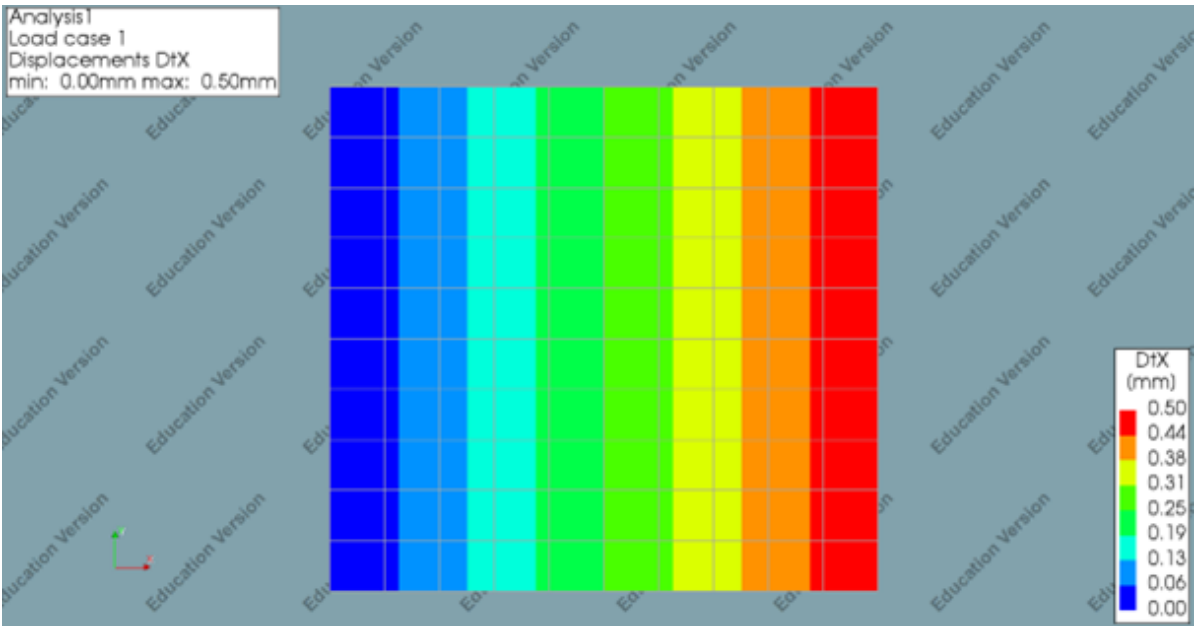


Figure 5.11: Lateral deformation in the 2D cube model

Stress-strain and force-displacement curves for each model are presented in Figure 5.12 and Figure 5.13. The CEB-FIP 2010 model showed unrealistic behaviour, including stress reversal, and was therefore excluded from further consideration. The remaining models differed mainly in ductility and energy absorption, with the CEB-FIP 1990 exhibiting a flatter descending branch and higher strain at peak stress.

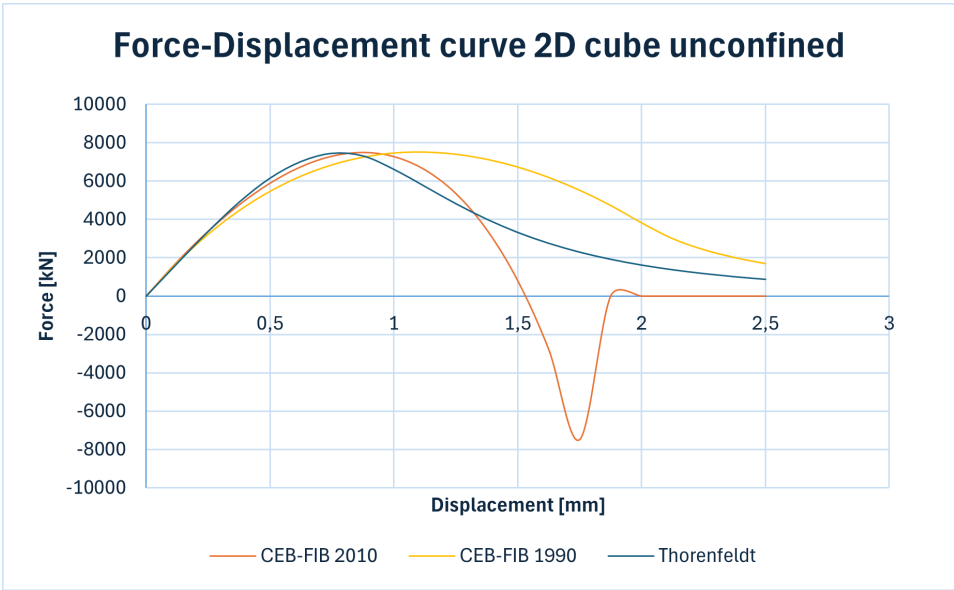


Figure 5.12: Force-displacement curves: unconfined 2D cube

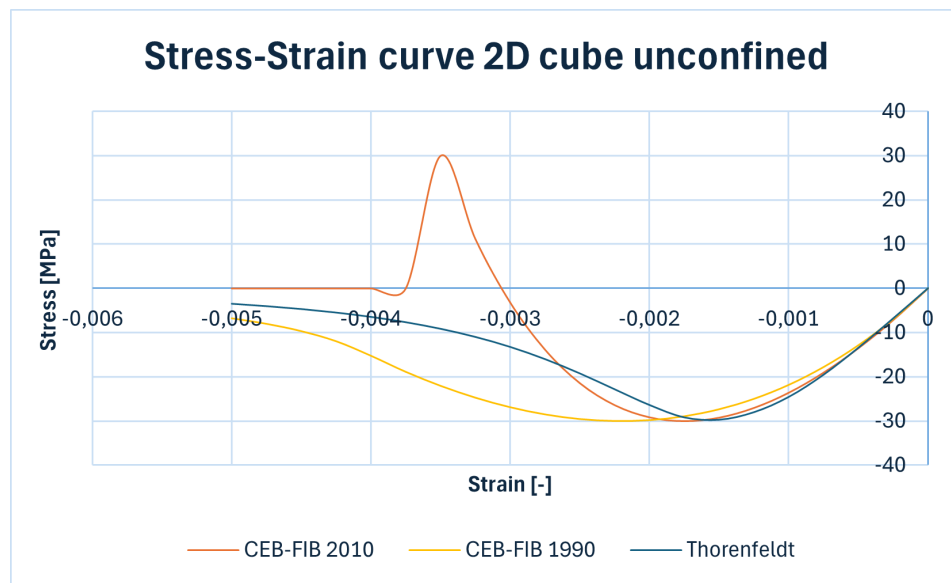


Figure 5.13: Stress-strain curves: unconfined 2D cube

To evaluate confinement sensitivity, a fully confined version of the cube model was created with lateral restraints on all sides (see Figure 5.14). While the level of confinement applied is unrealistic, it serves to highlight the upper bound effect of passive confinement.

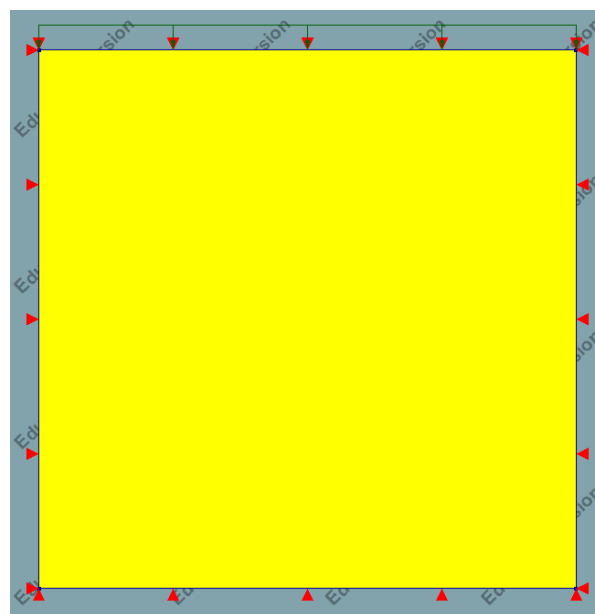


Figure 5.14: Confined 2D cube with full lateral restraints

Results (Figure 5.15) indicate increased peak stress and strain due to confinement, with the relative difference between CEB-FIP 1990 and Thorenfeldt remaining consistent. The magnitude of improvement, however, remains limited. This is attributed to the fundamental limitations of 2D plane stress models, which assume zero out-of-plane stress and therefore cannot develop tangential confinement effects. As such, true confinement mechanisms are not fully represented. In contrast, three-dimensional and axisymmetric models allow for the development of out-of-plane stress components and can therefore capture confinement more accurately.

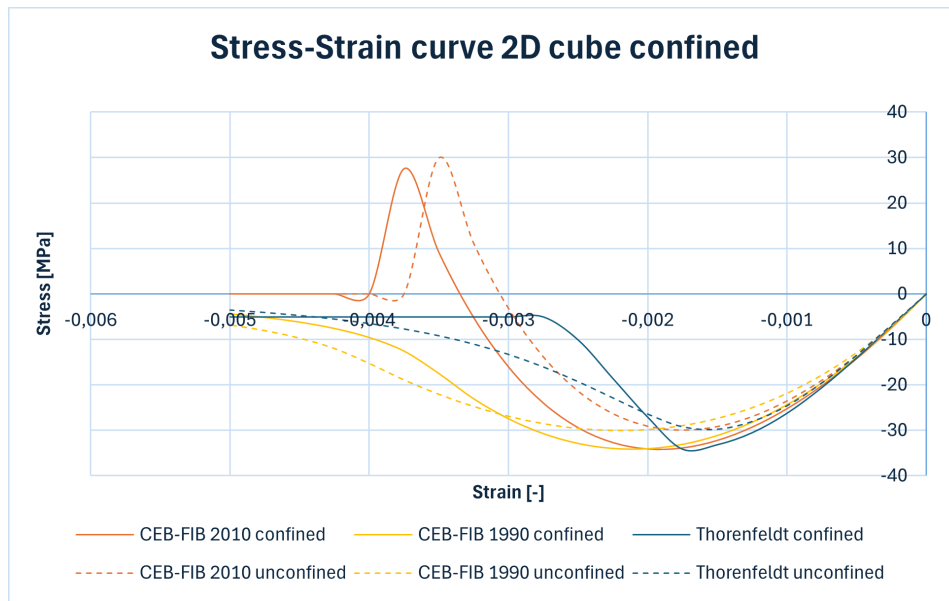
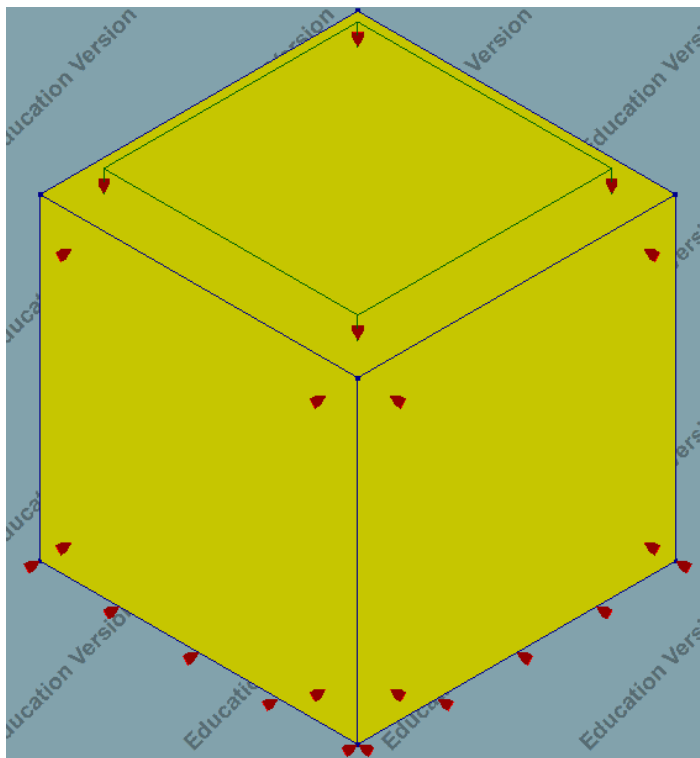
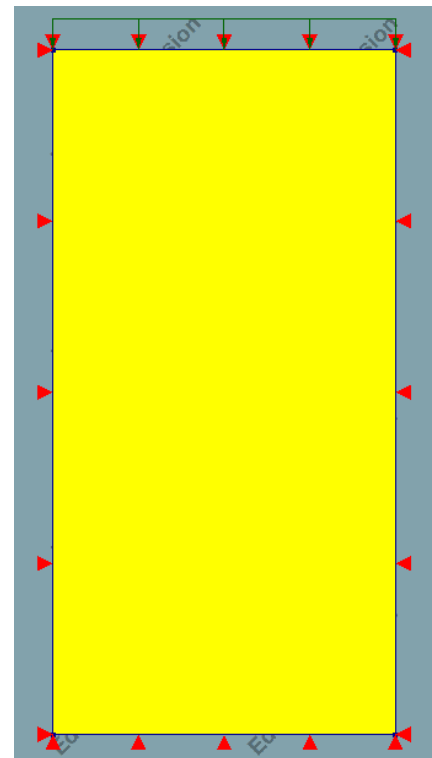


Figure 5.15: Stress-strain curves: confined 2D cube

To further investigate the compressive behaviour of the CEB-FIP 1990 and Thorenfeldt material models under confinement, both a three-dimensional (3D) analysis and an axisymmetric finite element analysis of the 500 mm × 500 mm cube were conducted (see Figure 5.16). The same material properties as previously described were used in both simulations to ensure a consistent comparison. The resulting stress-strain curves for the unconfined and confined conditions in the 3D model are presented in Figure 5.17 and Figure 5.18, respectively.



(a) 3D confined cube model



(b) Axisymmetric confined cube model

Figure 5.16: FEA cube models

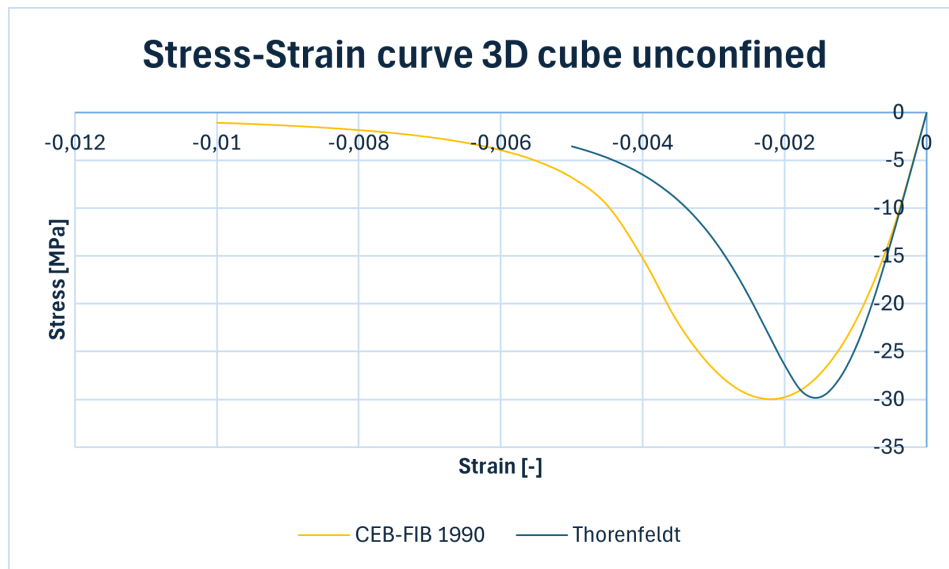


Figure 5.17: Stress-strain curve unconfined 3D cube

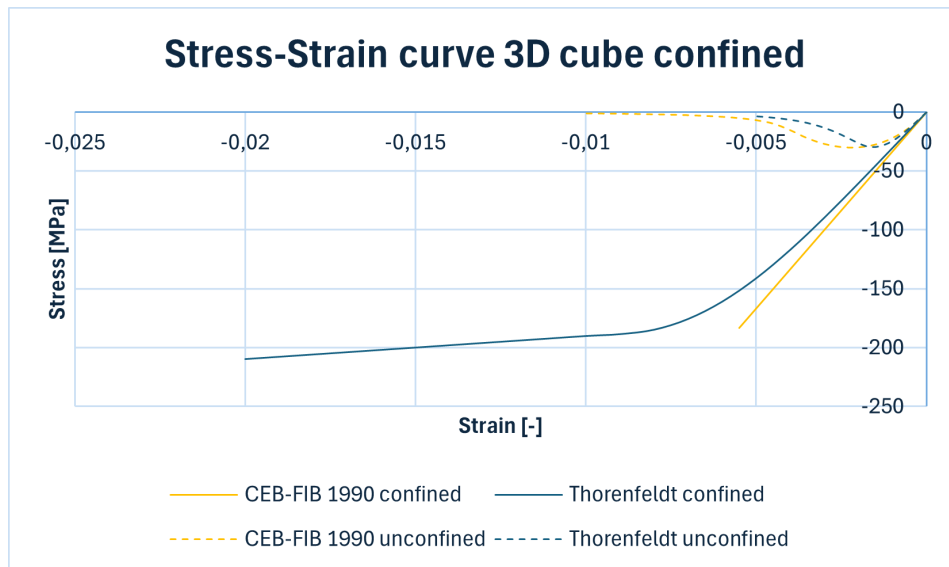


Figure 5.18: Stress-strain curve confined 3D cube

The stress-strain curves obtained from the 3D finite element models demonstrate a similar relationship between the CEB-FIP 1990 and Thorenfeldt material types as was observed in the 2D analyses. However, in contrast to the plane stress models, a significant increase in both the stress and strain capacity is evident. Notably, the stress-strain curve for the confined CEB-FIP 1990 model exhibits a linear trend until an abrupt termination of the analysis. Despite the application of displacement-controlled loading, the simulation failed to reach convergence beyond this point. Such behaviour, characterised by a purely linear response followed by divergence, deviates from the experimentally observed behaviour presented in Figure 3.4, where a more gradual transition is evident.

Although the Thorenfeldt model shows strain hardening beyond the peak stress rather than the strain-softening trend reported in the experimental results the Thorenfeldt model nonetheless appears to offer a more realistic approximation of confined concrete behaviour. This discrepancy between hardening and softening may be attributed to the modelling approach: in the cube models, confinement is introduced through fully restrained lateral boundaries, whereas in the experimental specimens, confinement

was achieved through reinforcement hoops. The difference in confinement mechanism likely influences the post-peak response.

To further explore the influence of confinement stiffness on material response, a preliminary parametric study was conducted using the axisymmetric model. In this study, lateral supports were modelled with varying stiffness levels. Three configurations were considered: a model with infinitely stiff supports (representing the initial axisymmetrical case without springs), a model with a support stiffness of 1000 N/mm^3 distributed along the full height, and a third model with a reduced stiffness of 100 N/mm^3 . The corresponding results are shown in Figure 5.19.

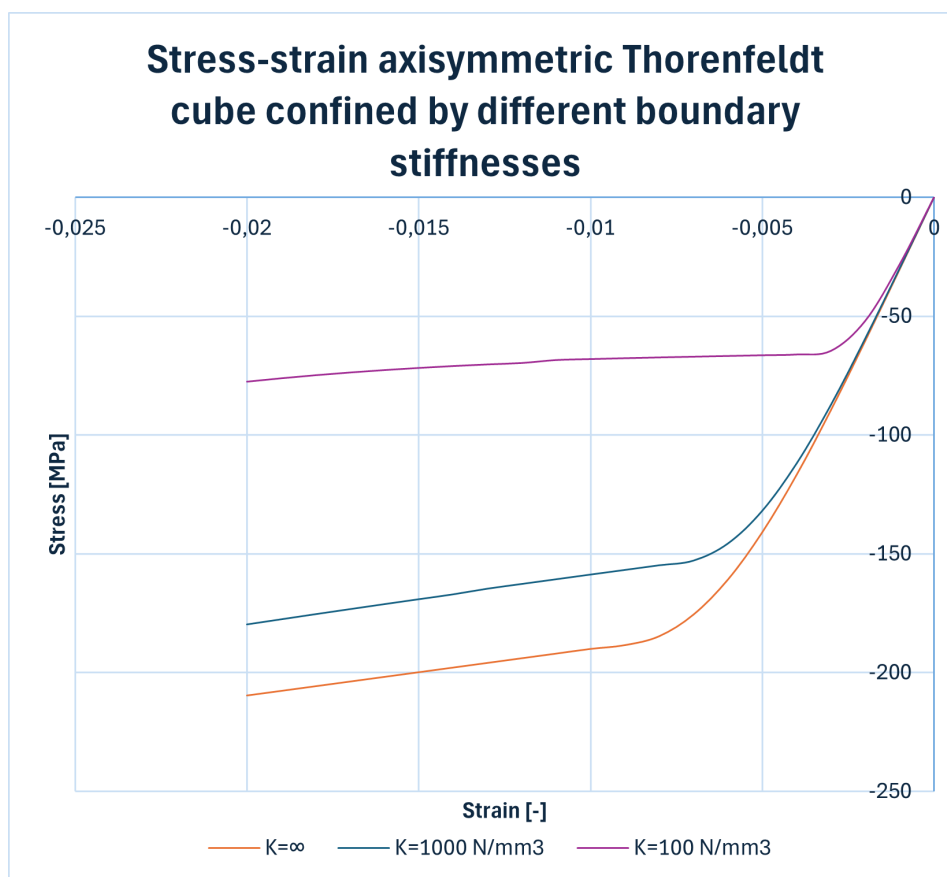


Figure 5.19: Axisymmetric models with varying lateral boundary stiffness

As illustrated in Figure 5.19, the slope of the ascending branch following the initial linear phase decreases with reduced support stiffness. This trend is consistent with theoretical expectations: as lateral deformation is permitted, less passive confinement develops, thereby reducing the effective compressive strength of the concrete.

Based on these observations, it is concluded that the Thorenfeldt model provides the most appropriate representation of confined concrete behaviour among the options evaluated. It not only approximates the expected stress-strain response more accurately, but also enables investigation of the influence of passive confinement through parametric control. In order to finalise the material parameters required for implementation of the Thorenfeldt model in DIANA, a specimen from the experimental campaign by Markic et al. was simulated and calibrated accordingly.

5.2.4. Imitate experimental campaign

The authors of (Markic et al. 2022a) conducted an extensive experimental campaign on partially loaded reinforced concrete blocks, in which a total of 62 specimens were tested to failure. The test matrix included variations in reinforcement detailing, loading type (strip, plate, and spatial), and load distribution

configurations. To validate the selected material properties and assess the applicability of the constitutive models, specimens NC-4.5, NC-18, NC-27 and HC-27 were reproduced in a finite element model.

All specimens consists of a 350 mm × 350 mm reinforced concrete block, confined with $\varnothing 12$ mm steel rectangular stirrups. The concrete cover to the reinforcement is 35 mm. The blocks are subjected to a centrally applied strip load with a width $d_1 = 52.5$ mm and a varying length b_1 . The yield strength of the reinforcing steel is 546 MPa, and the compressive strength of the concrete for all NC specimens is 32.6 MPa and for the HC is 77.4 MPa. A schematic representation of the experimental setup is provided in Figure 5.20.

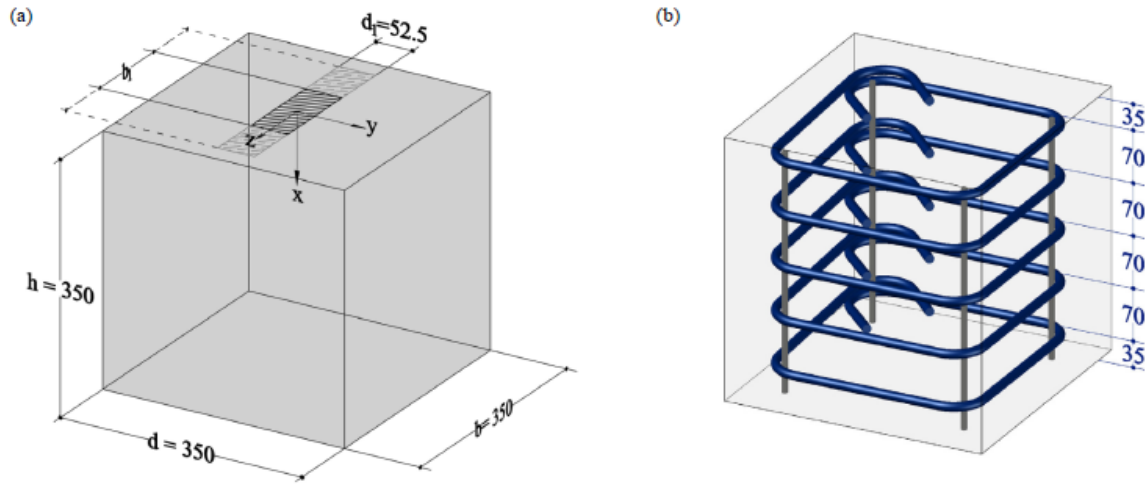


Figure 5.20: Specimen NC-27 from Markic et al. experimental campaign (Markic et al. 2022a)

The experimental results were presented in a graph in which the bearing stress (q_x), normalised by the concrete compressive strength (f_{c0}), is plotted against the penetration depth (δ_x). The resulting curve for all four specimens is shown in Figure 5.21.

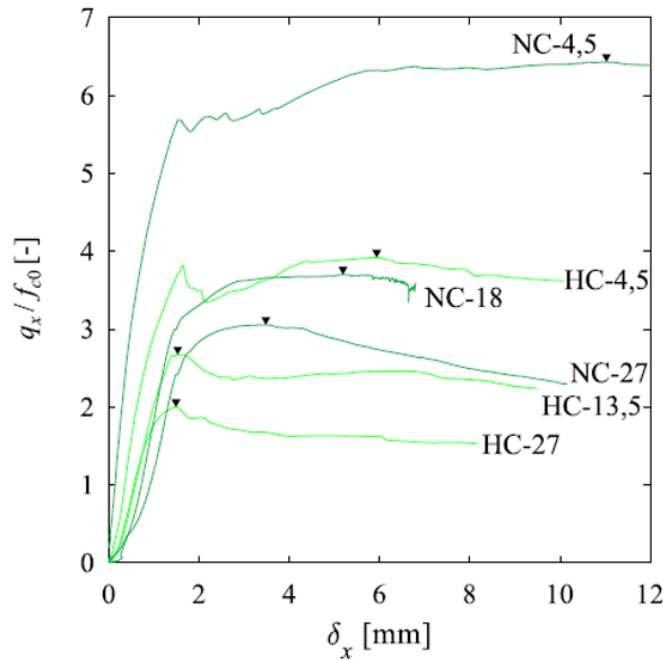


Figure 5.21: Normalized stress-penetration curve Markic et al. experimental campaign (Markic et al. 2022a)

So far, it has been demonstrated that axisymmetric modelling provides accurate results for capturing local material behaviour, such as the stress-strain relationship. For reasons of computational efficiency and modelling simplicity, it was therefore decided to construct axisymmetric models of the experimental specimens. This approach introduces certain idealisations, most notably in the loading configuration: whereas the experiment applies load over a rectangular surface, the axisymmetric model necessarily assumes a circular loaded area. Consequently, the numerical results are not expected to replicate the exact behaviour of the experiment, but they should fall within the range of variation observed across the experimental programme and remain comparable to the results.

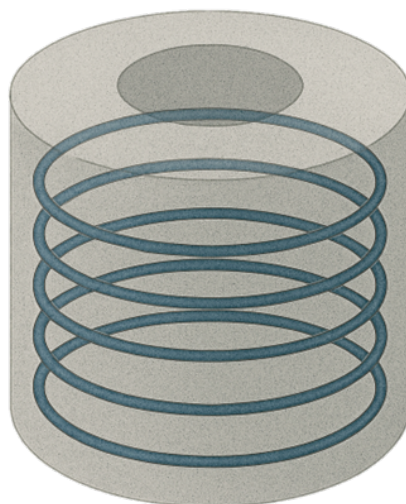


Figure 5.22: Illustration of simplified axisymmetrical model of Markić's experimental campaign cubic specimens

According to the Markić Dual-Wedge stress-field theory, bearing capacity is governed by the available concrete volume through which the load can disperse. As specimens with identical cross-sectional configurations but differing load-strip lengths demonstrated large variations in bearing stress capacity, it was elected to use the boundary distance from the loaded area rather than the area of the loaded surface itself as the key distinguishing parameter in our axisymmetric models. Accordingly, in the numerical simulations the load is represented by a circular contact area whose diameter equals the original strip length, thereby preserving the boundary distance while standardising the load geometry. Due to the axisymmetric formulation, the reinforcement geometry was also adapted, the rectangular stirrups used in the test specimen were modelled as circular hoops. This geometric change is expected to increase the degree of passive confinement, as circular hoops provide more uniform restraint against lateral deformation. The resulting enhancement of confinement is consistent with the mechanism described in subsection 3.2.1.

Initially, the same material properties used in the cube model of subsection 5.2.3 were assigned to the axisymmetric simulation of the experiment specimens. The developed finite element model is shown in Figure 5.23. The axisymmetric replication of the experimental model is depicted in Figure 5.22, and highlights clear deviations from the experimental specimen schematised in Figure 5.20.

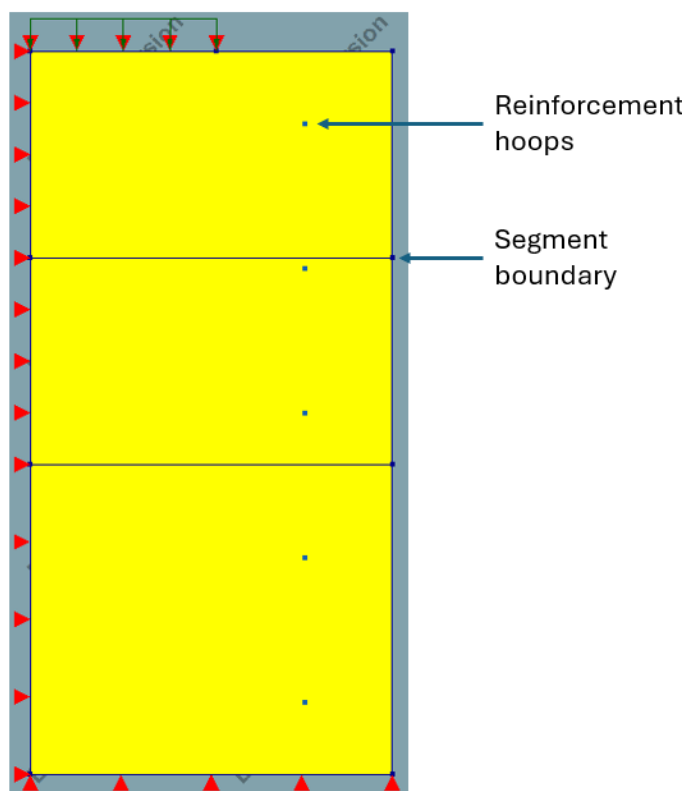


Figure 5.23: Axisymmetric FEA model imitating selected Markic et al. experimental campaign specimens

Non-linear analysis experimental specimen NC-18

First, a non-linear analysis was performed replicating specimen NC-18.

The model is subdivided into three regions, with mesh density progressively refined towards the loaded surface. This meshing strategy permits detailed stress resolution immediately beneath the load while preserving computational efficiency elsewhere.

To enable direct comparison with the experimental results, the vertical penetration of the loading surface is prescribed via controlled vertical displacement in the finite element model. According to the NC-18 curve in Figure 5.21, a vertical translation of approximately 7 mm is required to replicate the full experimental trajectory.

When this displacement was applied using the assigned material parameters, the non-linear analysis failed to converge prematurely (terminating after only the second of 100 incremental steps) likely due to geometric instability, unexpected material behaviour, or a combination of both. To investigate the model's behaviour prior to divergence, the prescribed deformation was reduced to 0.5 mm. Under this adjustment, DIANA successfully completed 24 load steps, corresponding to a total deformation of 0.12 mm. Although this represents only a small fraction of the experimental penetration, it suffices to generate meaningful contour plots and response curves that help localise the source of numerical instability and assess the material performance.

Contour plots of the normal, lateral and shear stresses in Figure 5.24 indicate that stress concentrations occur at the right side of the loaded region. Such concentrations are commonly associated with singularities and are likely responsible for the non-convergence of the non-linear analysis. Indeed, the stress magnitudes in the affected elements exceed the concrete's tensile capacity (3 MPa) and significantly surpass the material's shear strength, causing the solver to terminate. As these concentrations are confined to the right boundary of the load, it can be concluded that a geometric singularity at this location prevents the model from replicating the experimental campaign.

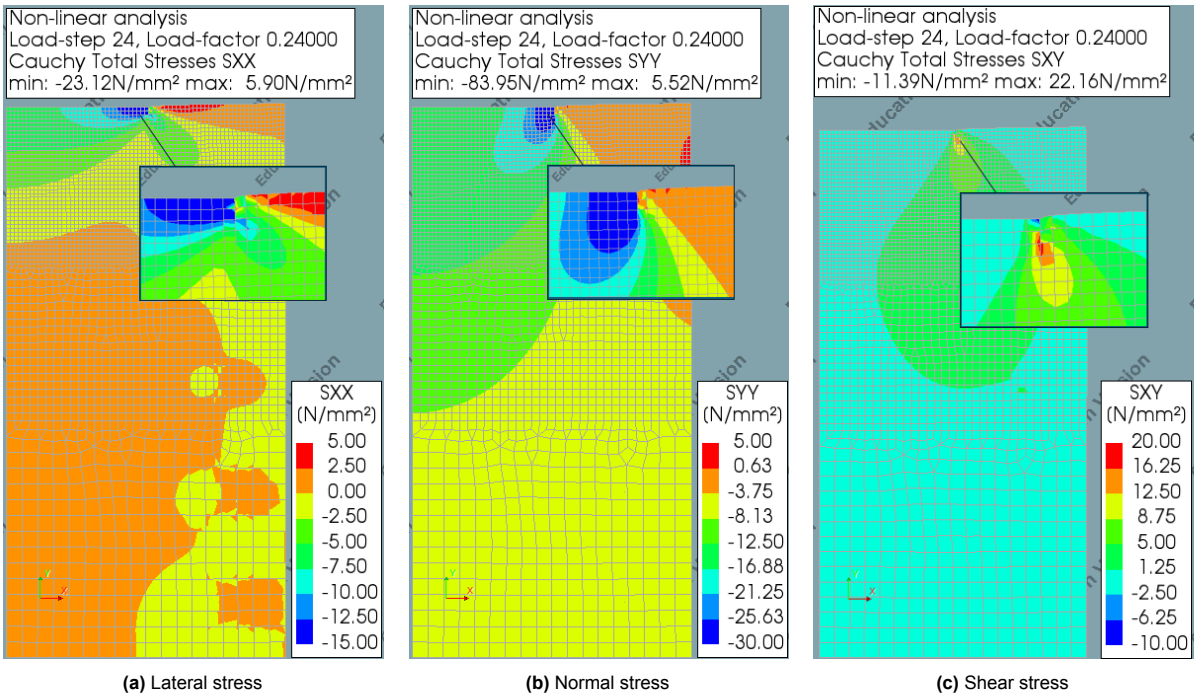


Figure 5.24: Stress in NC-18 FEA model

For direct comparison, Figure 5.21 plots penetration depth against average bearing stress. The penetration depth at each load step is calculated by multiplying the number of completed steps by the total prescribed deformation of 0.5 mm. The average bearing stress is obtained by dividing the sum of the reaction forces by the area of the loaded surface. In addition, the response curve for the governing node is shown to illustrate the local relationship between penetration depth and bearing stress.

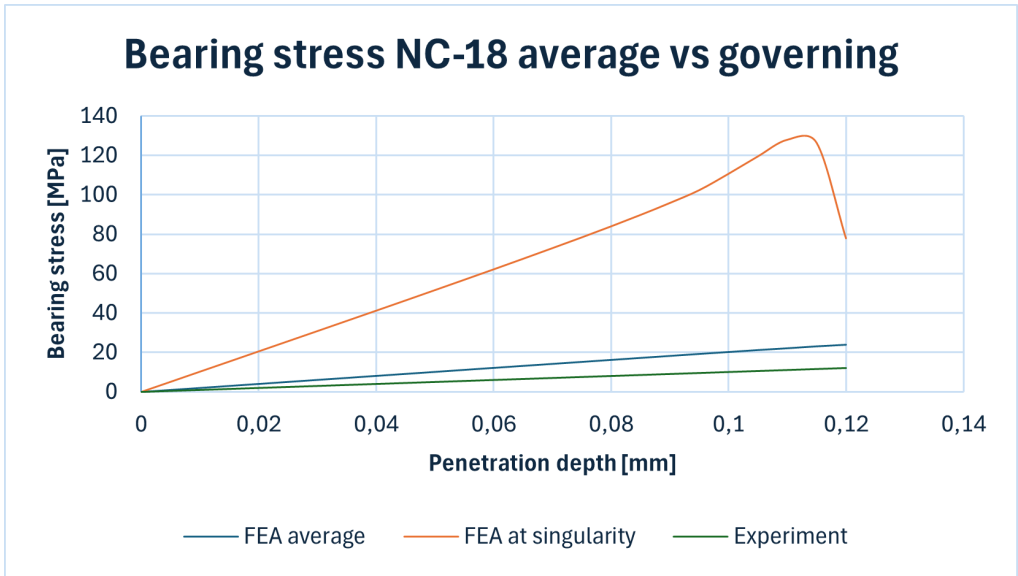


Figure 5.25: Bearing stress to penetration depth NC-18 FEA model

A clear divergence between the two FEA curves is evident. The average bearing stress increases linearly with penetration, whereas the governing node's response increases much faster and becomes non-linear beyond approximately 0.085 mm of penetration, confirming the singularity observed in the contour plots. Notably, the governing node reaches a peak stress of about 128 MPa. This is comparable

to the experimental peak stress for specimen NC-18 (3.70 times the uniaxial compressive strength of 32.6 MPa which is about equal to 120 MPa). Although the governing node attains critical stress levels very rapidly, these findings demonstrate that stress magnitudes similar to those reported by Markic et al. can indeed be reached. The strictly linear trend of the average stress curve also do not deny that, in the absence of singularities, other nodes would follow a more ductile trajectory and achieve comparable peak stresses. Preventing the singularity is therefore crucial to allow the analysis to continue and capture the full stress distribution.

Attempts to Eliminate the Artificial Singularity

Several strategies were implemented in an attempt to eliminate the artificial singularity at the boundary of the loaded area, but none succeeded in restoring full convergence:

1. **Local mesh refinement**

The mesh was further refined around the end of the load, using smaller quadratic elements to capture steep stress gradients. Despite the increased resolution, the singularity persisted, and the non-linear iterations continued to stall.

2. **Selective linear-elastic material assignment**

A purely linear-elastic concrete model was imposed on the elements nearest the end of the loaded area, preventing them from entering the post-peak regime. This “stress-cap” approach stabilised the very first increments but ultimately failed to eliminate the convergence breakdown as deformation increased because the singularity was just shifted to nodes beyond the stress-cap.

3. **Finer load increments**

The total prescribed displacement was applied over a greater number of smaller steps to improve the Newton–Raphson solver’s tracking of stiffness changes. While this allowed a few additional increments, the analysis still terminated prematurely.

4. **Steel load-spreading plate with interface restraint**

A linear-elastic steel plate was introduced at the loading interface to distribute the applied load more uniformly before it reached the concrete. An interface definition was applied between the steel and the concrete to prevent the lateral confining stress imposed by the much stiffer steel on the concrete’s compressive deformation. However, both realistic and unrealistic values for the steel plate stiffness failed to prevent stress concentrations from occurring.

5. **Vertical displacement interface at the load boundary**

A vertical interface condition was applied through the concrete block at the boundary of the loaded region to permit a large differential in vertical displacement between the last loaded element and the first unloaded element. This measure was intended to prevent the development of excessive shear stresses at that interface but also this measurement did only shift the singularity.

6. **Spring boundary interfaces at supports**

Elastic springs were introduced at the support locations to simulate more realistic supports. These spring boundary interfaces aimed to mitigate rigid boundary constraints and allow more realistic stress distribution, but convergence issues persisted.

7. **Distributed force control**

A distributed load was applied across the loading surface instead of a prescribed displacement, both alone and in combination with the previously mentioned measures. This approach sought to replicate the physical loading more accurately, but the singularity remained uneliminated.

8. **Arc-length control**

An arc-length algorithm was employed to follow the equilibrium path beyond limit points. While this non-linear solution method allowed the model to capture snap-back behaviour and small additional increments, it did not overcome the singularity.

Despite these concerted efforts, the artificial singularity persists, rendering a non-linear analysis infeasible. Nevertheless, a linear finite-element analysis remains possible and will enable a limited comparison of the model’s linear response with the experimental data.

Linear FEA presents a simplified approach in which materials are assumed to remain elastic, stress–strain relationships are linear, and deformations are small. While this allows for computational efficiency

and ease of implementation, it imposes several critical limitations when modelling structural behaviour in scenarios where material non-linearities and stress redistributions are significant, such as in the presence of passive confinement.

One of the principal shortcomings of linear FEA is its inability to capture stress redistribution following the onset of material non-linearity. As structural elements begin to crack, yield, or soften, internal forces are redistributed to surrounding regions that retain residual capacity. This redistribution is essential for accurately predicting the structural response under increasing load. The experimental results clearly show this phenomenon in a contour plot of three different specimens at three different stages of loading (see Figure 5.26). A linear analysis, by contrast, assumes constant stiffness and does not accommodate any form of load redistribution, which can result in inaccurate estimations of both strength and deformation capacity.

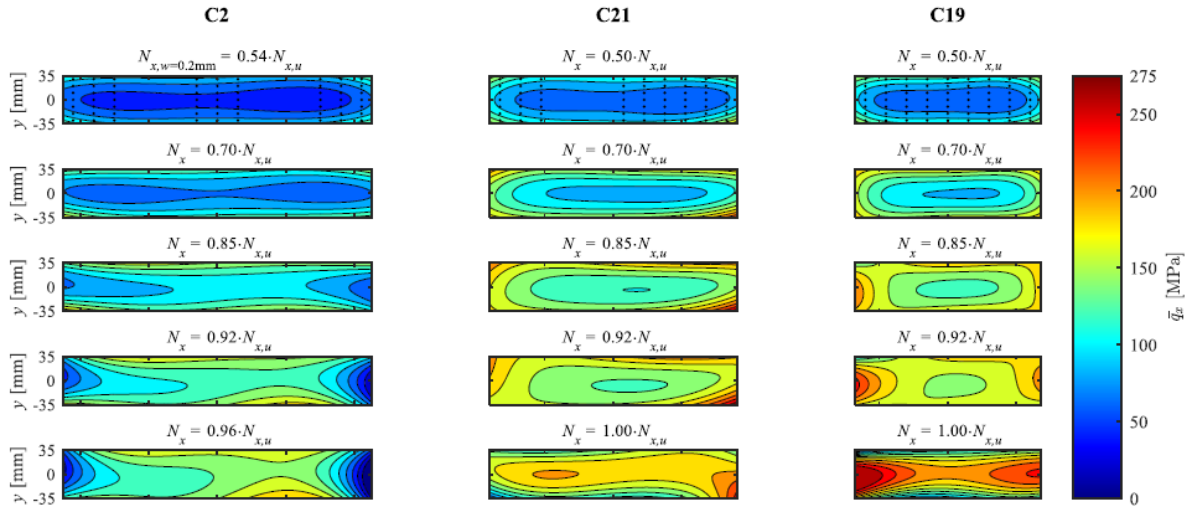


Figure 5.26: Stress redistribution at load interface (Markic et al. 2022a)

In the context of confinement, this becomes particularly problematic. Since the beneficial effects of confinement only emerge as materials enter non-linear ranges of behaviour, a linear FEA fails to represent the corresponding increases in strength and ductility. It treats all materials as if they respond uniformly across all stress levels, thereby neglecting the evolving internal stress states and their interaction with the confining mechanisms. As a result, the structural capacity of confined members is often significantly underestimated in a linear model.

Moreover, linear analysis is inherently unable to simulate post-elastic phenomena such as concrete cracking, reinforcement yielding, or crushing. These behaviours are crucial for capturing the full structural response, especially under ultimate loading conditions. Confinement influences many of these behaviours, particularly in delaying or altering failure modes. Without the ability to model non-linear stress–strain relationships, linear FEA excludes these effects entirely, making it unsuitable for realistic assessment in confinement-sensitive regions.

In addition, linear models cannot accommodate the strain-dependent nature of confinement. Because confinement effects intensify with increasing lateral strain and deformation, their accurate representation requires a modelling approach that accounts for material evolution under load. Linear FEA, which assumes strain-independent material properties, is incapable of doing so.

It is hypothesised that a linear FEA will predict significantly higher bearing stresses at a given level of load penetration compared to a non-linear FEA while showing much smaller lateral confining effects as reinforcement activation, lateral deformation and lateral confining stress. This discrepancy can be attributed to the linear model's assumption of constant material stiffness, which prevents it from accounting for stress redistribution, plastic deformations, and stiffness degradation that naturally occur in confined concrete under increasing load. In contrast, a non-linear analysis allows for the progressive softening and redistribution of stresses away from highly loaded regions, resulting in a more distributed

and realistic stress field. Consequently, for the same level of penetration, the linear model concentrates stresses unrealistically near the contact zone, leading to an overestimation of local bearing stress.

Linear axisymmetrical FEA of the selected experimental specimens

Since linear FEA cannot reproduce the post-elastic response, valid comparison must be restricted to the purely linear elastic portion of the experimental curves. A closer inspection of Figure 5.21 reveals an initial, gradual increase in bearing stress, which Markić et al. attribute to the settlement of the steel brush into the surface irregularities of the concrete (Markić et al. 2022a). Once the brush has seated, the response follows a linear path until the onset of concrete plastic deformation. By drawing a straight “fictive” line from the point of full brush settlement to the start of plasticity, one obtains a reference line for comparison with the FEA results. The initial, non-linear settlement phase is excluded because the FEA model assumes a perfectly smooth contact surface, and thus its linear response begins immediately upon load application.

In appendix B, these fictive lines are plotted and the corresponding stress and penetration values indicated. These are the target outcomes for the FEA, and should validate if the FEA method is appropriate for modelling confinement or adjustments are required. To confirm that an agreement between experimental and FEA results is not coincidental for a single specimen, four specimens were simulated in DIANA and their results compared.

The axisymmetric model employed for the non-linear analysis (Figure 5.23) was reused, with only the width of the loaded area adjusted to match each specimen in appendix B. Some simplifications remain, for instance, each loaded area is modelled as circular, with radius equal to half the length of the longest side of the actual loaded surface. Although this alters the size and form of loaded area, the critical edge distance is preserved, which is known to exert the greatest influence on the results. Additionally, axisymmetric modelling necessitates representing the lateral confining reinforcement as continuous hoops, rather than the rectangular stirrups used in the experimental specimens.

The load was applied using force control to avoid artificial stress concentrations at the edges of the loaded area. Penetration was determined from the resulting vertical (y-direction) displacement. The results are presented in Table 5.1.

Table 5.1: Experimental versus FEA linear results

specimen	E_{assumed} [MPa]	f_{c0} [MPa]	q_x / f_{c0} [-]	q_x [MPa]	$\delta_{x,exp}$ [mm]	$\delta_{x,FEA}$ [mm]	Δ [mm]
NC-4,5	30.000	-32.6	1.89	-61.61	0.25	0.09	0.16
NC-18	30.000	-32.6	2.89	-94.20	0.94	0.55	0.39
NC-27	30.000	-32.6	2.39	-77.91	0.93	0.69	0.24
HC-27	40.000	-77.4	1.41	-109.13	0.52	0.73	0.21

The table reveals a substantial discrepancy between the experimentally obtained and FEA-derived normalised bearing-stress factors. Although it was expected that modelling the lateral reinforcement as continuous hoops (instead of the rectangular stirrups used in the experiments) would elevate the simulated bearing stresses, this alone cannot account for the magnitude of the difference. Likewise, measurement uncertainty in defining the “fictive” linear portions of the experimental stress–penetration curves may introduce error, but is unlikely to explain such large deviations.

Furthermore, the experimental study did not report the Young’s moduli of the concrete specimens. Therefore values of 30 GPa were assumed for the concrete with a compressive strength of 32.6 MPa and 40 GPa for that with 77.4 MPa, estimates drawn from comparable literature specimens and consistent with Eurocode recommendations. Even allowing for reasonable variation in these moduli, the gap between the FEA and experimental normalised factors remains substantial. This suggests that other modelling simplifications such as the axisymmetric representation of the load area or the idealised contact conditions may be influencing the results.

Linear 3D FEA of the selected experimental specimens

Since the discrepancies between the axisymmetric FEA results and the experimental data proved too large, more accurate three-dimensional models were developed. In these 3D analyses, the reinforcement geometry and material properties precisely replicate the experimental specimens, and the loaded area is defined to match the actual test configuration. The load is applied under force control, rather than displacement control, to avoid artificial stress concentrations at the edges of the loaded zone, thereby more faithfully capturing the real stress redistribution in regions of high concentration. The “fictive” linear segments of the normalised bearing stress–penetration curves (see appendix B) yield the normalised bearing stresses at the end of the linear regime. These values were imposed as distributed loads in the numerical replications, with the primary outcome of interest being the penetration depth corresponding to those loads.

Figure 5.27 illustrates the 3D FEA model. Apart from minor simplifications, this finite-element model is identical to Markić et al.’s specimens NC-4.5, NC-18, NC-27 and HC-27 (see Figure 5.20). As such, it provides a robust basis for comparing the FEA predictions with the experimental measurements: a close agreement of the linear-elastic trajectories will confirm the validity of the chosen input parameters.

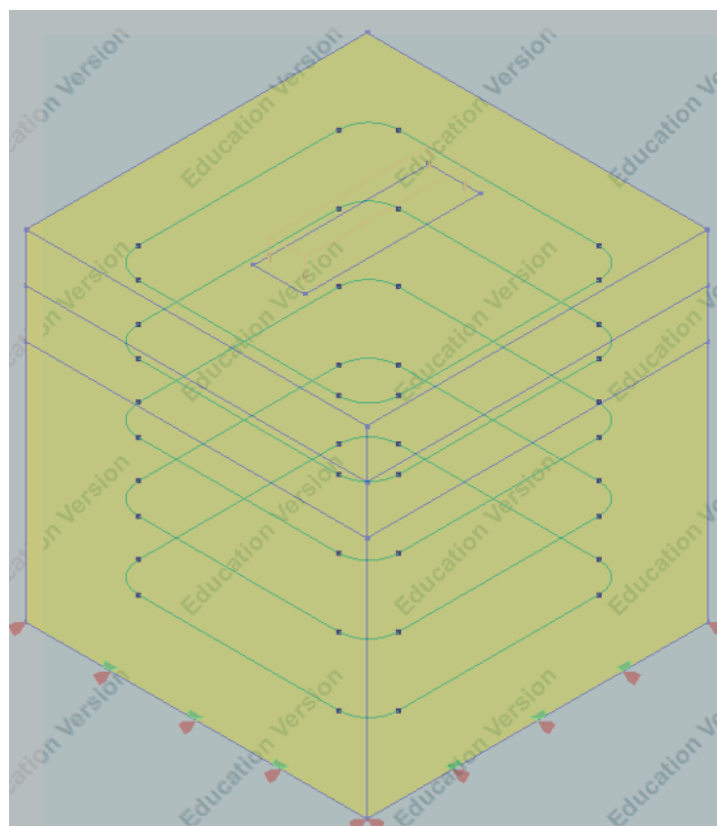


Figure 5.27: 3D FEA Markic et al. experiment replica with reinforcement

The results of the FEA are presented in appendix B.3. For comparison, all results are summarized in the table below (see Table 5.2).

Table 5.2: Experimental versus linear 3D FEA results

specimen	E_{assumed} [MPa]	f_{c0} [MPa]	q_x / f_{c0} [-]	q_x [MPa]	$\delta_{x,exp}$ [mm]	$\delta_{x,FEA}$ [mm]	$\delta_{x,analytical}$ [mm]
NC-4,5	30.000	-32.6	1.89	-61.61	0.25	0.11	0.13
NC-18	30.000	-32.6	2.89	-94.20	0.94	0.29	0.28
NC-27	30.000	-32.6	2.39	-77.91	0.93	0.27	0.27
HC-27	40.000	-77.4	1.41	-109.13	0.52	0.28	0.28

To assess the plausibility of the FEA results, analytical calculations were performed for all four specimens using a simplified three-spring model based on the FEA stress distributions (see appendix B). Each compressed concrete region was idealised as a spring whose stiffness was determined from its cross-sectional area, segment length and the concrete's Young's modulus. By applying the same force as in the linear portion of the experiments, the resulting spring deformations were computed and compared with the penetrations measured experimentally and those predicted by FEA.

The analytically derived deformations correlate closely with the FEA results; however, both remain markedly lower than the experimental values. This discrepancy indicates that the effective stiffness of the concrete in the experiments (i.e. within partially loaded areas) is less than the initial secant modulus of the material. Literature (Betoniek 2024) demonstrates that concrete's Young's modulus decreases once compressive stress exceeds 40 % of its uniaxial strength, yet DIANA's outputs imply a constant modulus of approximately 30 GPa, even under high stresses, thereby producing unrealistically small penetrations.

A second set of hand-calculations employing reduced moduli (typically 20 GPa and, in the region closest to the load, as low as 10 GPa) yields penetration values that align much more closely with the experimental campaign of Markić et al. These findings confirm that incorporating a locally reduced Young's modulus provides a more realistic representation of the bearing response in partially loaded regions.

Table 5.3 compares the experimental load penetrations with those obtained analytically and by FEA when reduced values of Young's modulus are adopted.

Table 5.3: Comparison of experimentally and numerically obtained load penetrations using reduced Young's moduli

Specimen	Reduced E [GPa]			Penetration δ_x [mm]		
	Segment 1	Segment 2	Segment 3	Experiment	FEA	Analytical
NC-4.5	10	15	20	0.25	0.14	0.19
NC-18	10	15	20	0.94	0.66	0.67
NC-27	10	15	20	0.93	0.59	0.55
HC-27	20	25	30	0.52	0.55	0.42

All results, both with and without reduced Young's modulus, are plotted in Figure 5.28. Although the linear-elastic phase is the only regime under consideration, the bar chart clearly indicates a substantial reduction in effective stiffness beneath the loaded area. In particular, for specimen NC-4.5, the small loaded area and comparable bearing stress mean that most stress is confined to the upper 50 mm, where the lowest modulus applies; thus, reducing the modulus in the deeper regions has little effect. Nevertheless, the experimental penetration remains significantly higher than any linear prediction, implying additional local softening directly beneath the load.

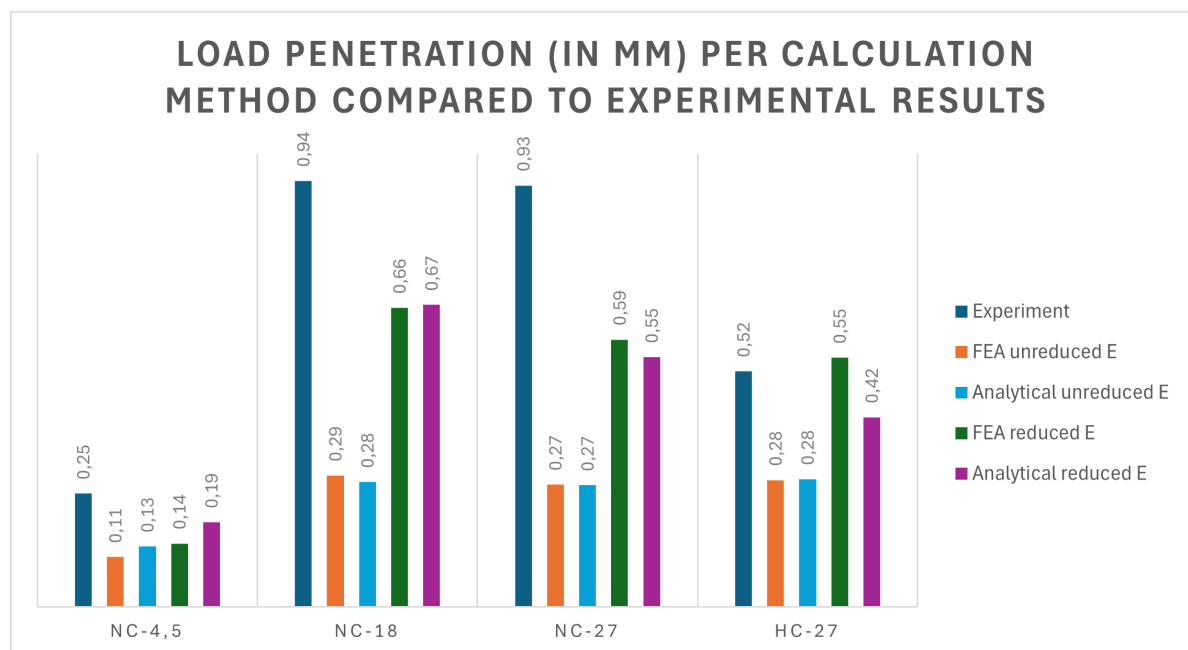


Figure 5.28: Load penetration with and without reduced young's modulus compared to experimental results

In experiments on concrete under concentrated bearing loads, the initial portion of the load–penetration curve often appears linear. However, purely linear FEA or analytical models (both assuming homogeneous, isotropic, perfectly elastic behaviour) systematically underestimate the measured penetrations. This discrepancy arises because, at the local scale beneath the loading plate, stress gradients and Poisson-induced transverse tensile stresses generate early microcracking and inelastic strain, even at global stress levels well below the compressive strength. Such microcracking dissipates energy quantified by the fracture energy (G_f) and reduces local stiffness before any visible damage occurs, violating the assumptions of classical linear elasticity.

To reconcile this within a linear-FEA framework, a compliant “cushion” layer can be introduced beneath the load plate: a thin, linear-elastic material with reduced Young’s modulus that mimics the compliance of the damaged zone. This strategy gives the model quasi-non-linear characteristics, enabling accurate replication of the observed load-penetration behaviour while retaining computational stability and avoiding the convergence challenges of fully non-linear analyses.

These results confirm that, when a fully non-linear analysis is precluded by singularities or severe stress concentrations, a linear finite-element analysis incorporating reduced concrete stiffness in highly stressed regions and a compliant cushion layer to represent micro-crack-induced softening and stress redistribution (i.e. a quasi-non-linear FEA approach) provides the most realistic approximation of the physical behaviour.

5.2.5. Material properties for modelling confined concrete

By employing simplified cube models and replicate selected specimens from Markić et al.’s experimental campaign, it was determined that a total strain based crack model combined with the Thorenfeldt material model, featuring a linear compression-softening post-peak branch, most accurately captures the confinement effect in a non-linear analyses. The Thorenfeldt model permits precise calibration of material behaviour via input parameters for compressive strength, shape parameters n and k , residual strength, and a length-scale parameter to govern post-peak softening. In addition to these compressive parameters, DIANA requires tensile and crack-orientation inputs, the use of linear-crack energy with ‘Rots’ crack-bandwidth specification, together with a rotating crack orientation, produced the most realistic results.

When singularities or stress concentrations precipitate premature non-convergence and make a fully non-linear analysis infeasible, the preferred alternative is a quasi-non-linear analysis. This approach

retains linear-elastic properties as the Young's modulus, Poisson's ratio and density, but introduces a reduction in concrete stiffness within highly stressed regions. Such a technique enables a close representation of the entire ascending branch of the stress–strain curve, rather than terminating at the onset of non-linear behaviour.

While the use of a compliant layer or locally reduced modulus in a linear finite element model offers a practical means of replicating the initial stiffness observed in experiments, this quasi-non-linear approach is based on several assumptions. It presumes that all non-linear effects are localised beneath the load and that the remainder of the concrete behaves as a homogeneous, linear elastic material. The compliant layer itself is a simplified representation of microcracking, stress redistribution, and contact compliance, but does not model damage evolution or fracture mechanics. Furthermore, it assumes constant, isotropic stiffness within the modified zone, and does not account for confinement activation or stiffness degradation with increasing load. As such, while this method allows for improved alignment with experimental stiffness in the pre-damage regime, it is not predictive beyond the initial elastic range and should be interpreted accordingly.

5.2.6. Confining reinforcement in a quasi-non-linear FEA

In the quasi-non-linear finite element model, the confining reinforcement exhibits very low tensile stress, indicating that passive confinement is not effectively activated. This contrasts with the expected behaviour in the experimental specimens, where confinement plays a significant role in enhancing the bearing strength of the concrete core.

The absence of confinement activation in the linear model can be explained by the underlying mechanics of passive confinement. In reality, as the concrete beneath the bearing plate is subjected to high compressive stresses, it tends to expand laterally due to Poisson's effect and inelastic deformation. This lateral expansion is resisted by the surrounding transverse reinforcement, which develops tensile forces and, in doing so, applies passive confinement pressure on the concrete core. This confinement delays the onset of damage and increases the effective bearing capacity.

However, in a linear elastic model, the concrete material is assumed to behave homogeneously and elastically, without any damage, cracking or plastic deformation. As a result, the lateral strains remain very small ($\nu \times D\epsilon_y$) and are insufficient to engage the confining reinforcement. Because no significant transverse dilation occurs, the ties remain essentially unstressed. Consequently, the model fails to replicate the confinement-induced strength enhancement observed in the experimental results.

This limitation is inherent to the linear modelling approach. Without non-linear material behaviour such as dilation, crushing or tensile cracking, the necessary conditions for activating passive confinement are not met. While the reinforcement is present and correctly modelled geometrically, it remains mechanically inactive due to the lack of lateral expansion in the surrounding concrete. As such, the bearing stress predicted by the linear model reflects an unconfined response, even in specimens that are, in practice, confined.

By adjusting the linear material properties, it is possible to approximate the initial bearing stiffness and make a substantiated estimate of the bearing stress corresponding to a given penetration depth. However, capturing the full global response of the specimen, including the activation of passive confinement, remains feasible only through a non-linear analysis incorporating appropriate material models and geometrical representations, as described in subsection 5.2.5.

5.3. FEA of the 'Oostertoegang' case study project

Returning to the case study, which comprises a CFSP-pile-concrete cap connection, our point of interest is the bearing stress in the concrete immediately above the steel casing. Owing to the pronounced stress concentrations that typically develop in this region, conventional theoretical models fail to demonstrate adequate bearing capacity. This chapter assesses whether the modified theoretical model for bearing stress in partially loaded concrete, developed earlier in this thesis (see section 4.4), is applicable to the case study. Based on prior FEA replications of experimental campaigns and comparison of the results, best practices for FEA modelling and expected outcomes have been established.

The first section of this chapter (see section 5.1) outlines the essential modelling considerations, includ-

ing the choice of analysis type, element type and mesh refinement in regions of interest. The second section reviews the selected material models and properties for both linear and non-linear analyses. Due to the geometry of the case study, a singularity is expected at the inner corner between the exterior of the pile casing and the underside of the concrete cap, rendering a fully non-linear finite-element analysis infeasible because of early non-convergence. Consequently, the research indicates that a quasi-non-linear FEA incorporating a locally reduced Young's modulus in highly stressed zones and a compliant cushion layer beneath the load, provides the most realistic representation of the confined concrete when a full non-linear analysis cannot be performed.

5.3.1. Case study FEA geometry

In the Amsterdam Oostertoegang project, the concrete cap forms a continuous beam 4.5 m wide and 2 m deep, supported on multiple piles. For the purposes of this thesis, this configuration was simplified to a single pile beneath a discrete concrete cap. A parametric study, in which the cap radius was varied around 500 mm and the height around 400 mm, demonstrated that both increases and decreases in these dimensions produced negligible changes in the bearing stress at the pile–cap interface. From these analyses, it was determined that an axisymmetric cap with a radius of 500 mm and a height of 400 mm suffices to capture the full influence zone around the pile head. The concrete cap is divided into 3 segments to apply mesh refinement and stiffness reduction.

As explained in subsection 5.1.1 the radial reinforcement in the concrete cap is modelled as a reinforcement grid with zero equivalent thickness in the local y-direction and an equivalent thickness of 3.93 mm in the local x-direction to represent 25mm rebars at 125mm spacing. The longitudinal reinforcement is modelled as hoops by modelling embedded bar elements with a diameter of 32mm, arranged at 125mm centre-to-centre spacing.

The pile is discretised into four regions: two representing the concrete core, one with a fine mesh refinement and one with a coarser mesh, both assigned an identical Young's modulus equal to the initial concrete stiffness, reflecting the assumption of full confinement by the steel casing. Likewise, the steel casing is divided into a fine-meshed region and a coarse-meshed region to ensure accurate node alignment at the interface. The casing steel is modelled as a linear-elastic material, since the applied load magnitudes remain well below its yield strength.

5.3.2. Case study FEA boundary and interface conditions

Since a linear-elastic analysis is conducted, there is no need for compliant supports; therefore, simple rigid boundary conditions are applied. Along the axis of symmetry, translation in the x-direction is restrained, while at the base of the model, translation in the y-direction is fixed.

To simulate a fully unbonded interface (as prescribed by NEN-EN 1992-4), an interface with zero shear stiffness and very high normal stiffness, are applied between the concrete core and the steel casing, as described in subsection 5.1.1. The full geometry including boundary and interface conditions is shown in Figure 5.29.

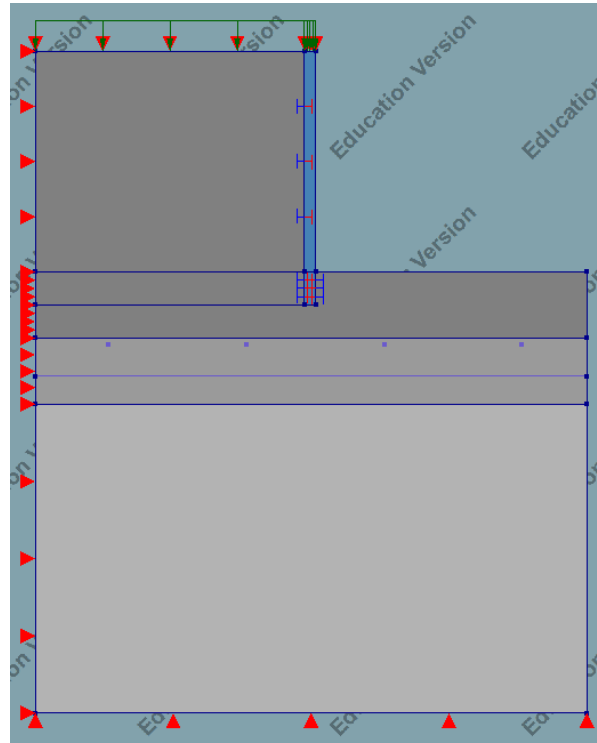


Figure 5.29: Geometry of the case study FEA including boundary and interface conditions

Pile reinforcement has been omitted from the FEA model. This simplification does not affect the local response under investigation, since the reinforcement, while contributing to the overall axial and bending capacity of the connection, does not influence the confinement mechanism or the local stress distribution at the pile–cap interface.

5.3.3. Equivalent load

From the application of the Markic dual wedge stress field (DWSF) model to the case study presented in section 4.5, a maximum bearing capacity of 149.05 MPa was determined. However, this analytical model does not provide the corresponding penetration of the casing into the concrete cap. To estimate this displacement, a method based on energy conservation and Hooke's law was employed.

It is important to note that the finite element model used in this study represents the physical system in an inverted orientation, primarily to improve load control. That is, the load is applied at the physical bottom of the pile but represented at the top of the model in the FEA. The interface between the steel pile casing and the concrete core is modelled as fully unbonded, which implies that the normal stress at the physical top of the casing is equal to the stress at the bottom, and no energy is lost along the casing length.

Given that the casing material is modelled as linear elastic, its deformation can be determined using Hooke's law:

$$\Delta L_{\text{casing}} = \frac{\sigma_{x0} \cdot L_{\text{casing}}}{E_{\text{steel}}} \quad \text{Eq. 5.9}$$

where σ_{x0} is the average axial stress in the casing, L_{casing} is the effective length, and E_{steel} is the Young's modulus of the steel casing.

The axial deformation at the casing-concrete interface results in the transmission of stress into the concrete cap through the DWSF. According to the principle of conservation of energy, the external work applied to the system must be equal to the total internal energy dissipated or stored. In this

case, the external work is the product of the bearing stress and the vertical displacement of the load application surface, which corresponds to the interface between the casing and the concrete cap:

$$W_{\text{ext}} = \sigma_{x0} \cdot t_{\text{casing}} \cdot u \quad \text{Eq. 5.10}$$

Once the stress is transferred into the concrete, energy dissipation occurs through different internal mechanisms. The most significant dissipation occurs along the inclined flanks of the DWSF (discontinuity line FK) due to shear deformation. Additionally, compressive stress is transmitted downward through the DWSF into the concrete below. This results in vertical displacement at the base of the DWSF and induces internal compressive work. However, because the region below the DWSF is modelled as linear elastic and the bottom support is assumed to be rigid, this compressive work is fully transferred to the support without internal energy loss.

Accordingly, the energy balance simplifies to include only the dissipated shear energy along the DWSF flanks. The internal energy components can be written as:

$$W_{\text{int}} = W_{\text{DWSF, shear}} + W_{\text{DWSF, } \sigma_{xd}} + W_{\text{cap, support}} \quad \text{Eq. 5.11}$$

where:

$W_{\text{DWSF, shear}}$	Energy dissipated by shear along the sides of the DWSF [N mm]
$W_{\text{DWSF, } \sigma_{xd}}$	Energy transmitted through the DWSF by distributed compressive stress [N mm]
$W_{\text{cap, support}}$	Compressive energy transferred into the support from the base of the cap [N mm]

In the linear elastic FEA framework applied here, $W_{\text{DWSF, } \sigma_{xd}}$ and $W_{\text{cap, support}}$ cancel each other out due to the assumption of full elastic transfer and perfect support. This results in a simplified energy balance where $W_{\text{ext}} = W_{\text{int}}$:

$$\sigma_{x0} \cdot t_{\text{casing}} \cdot \delta = W_{\text{DWSF, shear}} \quad \text{Eq. 5.12}$$

This expression reflects that, under the stated assumptions, all external work input is dissipated through shear along the DWSF. This is consistent with the theoretical interpretation of the DWSF in partially loaded concrete regions.

It is important to note that all energies are expressed in N mm, as the analysis is conducted in two dimensions and results are interpreted per millimetre of casing perimeter.

The casing penetration u is calculated by equating the external work to the internal shear dissipation:

$$\sigma_{x0} \cdot d_1 \cdot u = \tau \cdot l_{\text{shear}} \cdot \cos(\alpha) \quad \text{Eq. 5.13}$$

where:

- σ_{x0} is the average bearing stress at the casing-concrete interface [MPa],
- d_1 is the effective load width [mm],
- u is the vertical penetration [mm],
- τ is the shear stress acting along the DWSF plane [MPa],
- l_{shear} is the length of the shear plane in the DWSF [mm],
- α is the angle of the DWSF with respect to the horizontal [deg].

Solving for the penetration u gives:

$$u = \frac{\tau \cdot l_{\text{shear}} \cdot \cos(\alpha)}{\sigma_{x0} \cdot d_1} \quad \text{Eq. 5.14}$$

The shear stress τ is determined from the rotated stress state of the concrete along the discontinuity line FK from the DWSF. The initial stress element is subjected to a uniaxial stress $\sigma_s = \sigma_{\text{conf}}$ in the

horizontal direction, which is the confining stress at the base of the casing. To obtain the shear stress acting along the inclined flank of the DWSF (e.g., along line FK in the stress field), the stress tensor is rotated over an angle α . The Mohr's circle representation shows that the shear stress at an inclined plane at angle α corresponds to a rotation of 2α in the Mohr plane.

To support the explanation visually, two figures are proposed:

- **Figure 5.30:** Mohr's circle construction illustrating the stress transformation from a uniaxial stress state to the inclined DWSF plane (rotation over 2α).

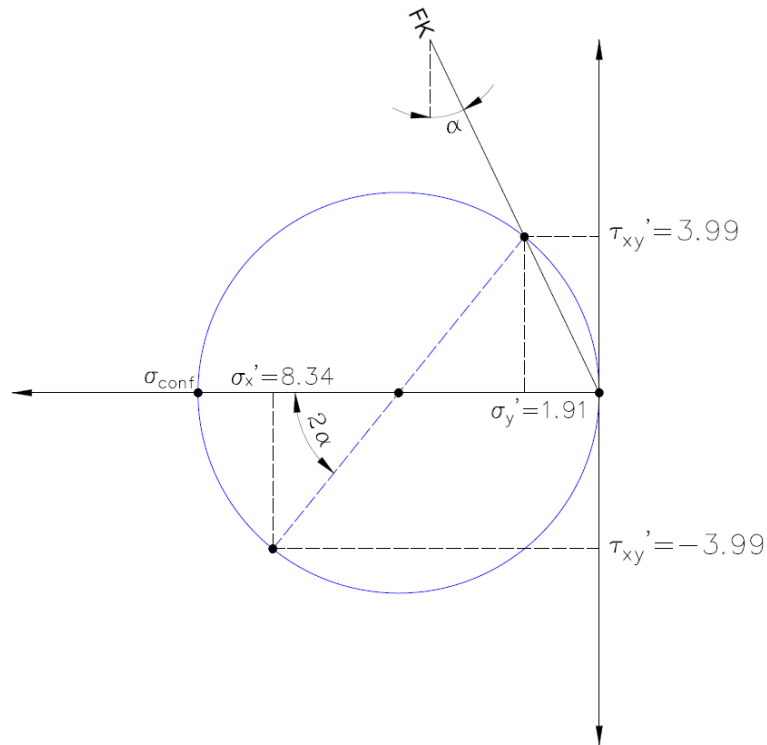


Figure 5.30: Mohr's circle showing stress transformation from uniaxial stress to shear on inclined plane at angle α .

- **Figure 5.31:** Initial stress element subjected to horizontal stress σ_{conf} , rotated to align with the DWSF flank to illustrate the development of shear stress along line FK.

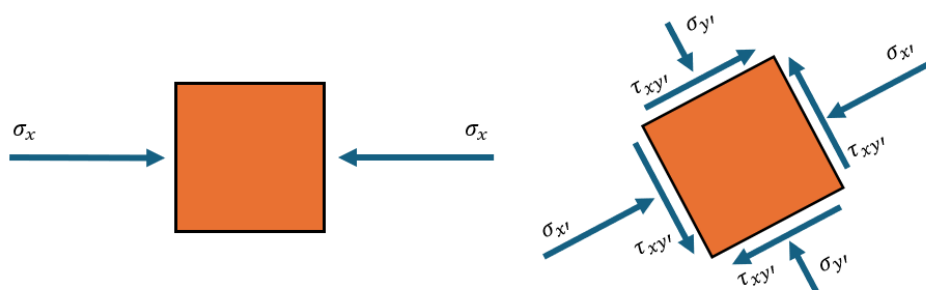


Figure 5.31: Stress element under horizontal confinement, rotated over angle α to represent shear stress along the DWSF plane.

The rotated shear stress is therefore calculated as:

$$\tau = -\frac{\sigma_x - \sigma_y}{2} \cdot \sin(2\alpha) + \tau_{xy} \cdot \cos(2\alpha) \quad \text{Eq. 5.15}$$

where:

- $\sigma_x = \sigma_s = \sigma_{conf}$ is the initial horizontal confining stress [MPa],
- $\sigma_y = 0$ is the initial vertical stress component (initially zero) [MPa],
- τ_{xy} is the initial shear component (initially zero) [MPa].

This results in a shear stress acting on the inclined shear planes of the DWSF that is proportional to the applied confinement stress and the angle of the wedge. The angle α and the length of the shear plane l_{shear} are known from the geometry of the DWSF:

$$l_{\text{shear}} = \frac{x_E}{\cos(\alpha)} \quad \text{Eq. 5.16}$$

where x_E is the height of the DWSF.

The Python function in appendix C.1 implements this procedure numerically. This python script also includes the linear elastic deformation of the steel casing to obtain a total corresponding prescribed deformation of 0.46 mm for the case study.

This comprehensive energy-based approach, validated through linear elastic FEA assumptions and consistent with the geometry of the DWSF, provides a means to estimate the load-penetration response of the steel casing in absence of direct displacement output from the Markic analytical model.

The concrete core is also subjected to a load, but for accuracy and simplicity the core is loaded by imposing a distributed force proportional to the relative stiffnesses of the steel casing and the concrete, as detailed in Section 2.2. When applied to the present FEA model, this procedure yields:

$$q_{\text{core}} = \sigma_{x0} \cdot \frac{E_{\text{core}}}{E_{\text{casing}}} \quad \text{Eq. 5.17}$$

Here, σ_{x0} denotes the normal stress in the steel casing, E_{core} the Young's modulus of the concrete core, and E_{casing} the Young's modulus of the steel casing. Equation 5.17 is derived in Appendix D.

Substituting $E_{\text{core}} = 30 \text{ GPa}$ and $E_{\text{casing}} = 200 \text{ GPa}$ into Equation 5.17 yields a distributed core stress of 22.36 N/mm^2 .

5.3.4. Quasi-Non-linear Modelling Approach for the Concrete Cap

To approximate the non-linear mechanical behaviour of the concrete cap situated above the CFSP pile while preserving the computational efficiency and convergence stability of a linear finite element analysis, a quasi-non-linear modelling approach is employed. This method captures the progressive stiffness degradation of concrete in compression (particularly near peak stress levels) without the need for a fully non-linear material model. The principle of a quasi-non-linear analysis is illustrated by the stress–strain curves in Figure 5.32. The dashed line represents the linear-elastic response of a material with a Young's modulus of 30 GPa. The curved yellow line depicts the enhanced, non-linear behaviour of confined concrete. The straight blue line, which connects the origin to the endpoint of the non-linear curve, defines the manipulated stress–strain path that the material follows in a quasi-non-linear analysis. This method permits verification of the plausibility of the calculated bearing stress; however, it requires a well-substantiated determination of the reduced Young's modulus in those regions where stiffness is intentionally decreased.

In this study, the technique is applied to the concrete cap directly above the CFSP pile, where vertical loading induces the highest compressive stresses. The reduction in stiffness is governed by the analytically defined secant modulus of confined concrete, derived from a constitutive relationship based on Mander's model (Mander et al. 1988b).

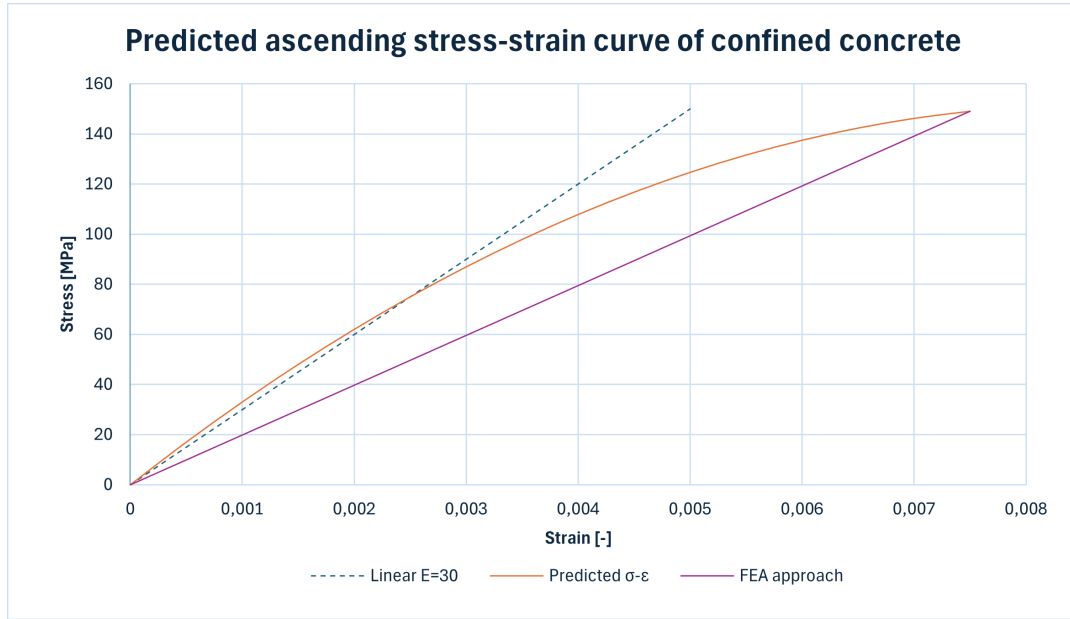


Figure 5.32: Quasi-non-linear FEA principle in a stress-strain curve

Mander's Model for reduced concrete stiffness

The stress-strain response of confined concrete is approximated using the model proposed by Mander et al., which was originally developed to represent the behaviour of transversely confined concrete columns under monotonic loading. The concrete cap in this case is only confined by transverse reinforcement near the pile head, particularly in the region directly above the CFSP pile. This condition resembles a partially confined state, for which Mander's model remains applicable with appropriate interpretation of confinement parameters.

The confined concrete stress σ_c at strain ε_c is defined as:

$$\sigma_c(\varepsilon_c) = \frac{f_{cc} \cdot x \cdot r}{r - 1 + x^r}, \quad \text{where } x = \frac{\varepsilon_c}{\varepsilon_{cc}}, \quad \text{Eq. 5.18}$$

with f_{cc} the peak compressive strength of confined concrete, and ε_{cc} the corresponding peak strain. The shape parameter r accounts for the curvature of the ascending branch and is defined as:

$$r = \frac{E_c}{E_c - E_{\text{sec}}}, \quad \text{where } E_{\text{sec}} = \frac{f_{cc}}{\varepsilon_{cc}}, \quad \text{Eq. 5.19}$$

and E_c is the initial young's modulus of unconfined concrete.

The stiffness of confined concrete at certain stress levels is defined by the secant modulus E_s , which represents the slope of the line that connects the origin of the the curve to the point in the stress-strain curve at a given stress and strain level. The value for E_s is obtained by dividing σ_c by ε_c :

$$E_s = \frac{\sigma_c}{\varepsilon_c} \quad \text{Eq. 5.20}$$

This expression is evaluated numerically using a discretised version of the curve, and only the ascending branch is considered to avoid post-peak softening effects which are not captured in the current modelling framework. The Python function in appendix C.2 implements this procedure numerically and plots the relation between the normal compressive stress, strain and secant modulus in one graph (see Figure 5.33 for an example of unconfined concrete C30/37).

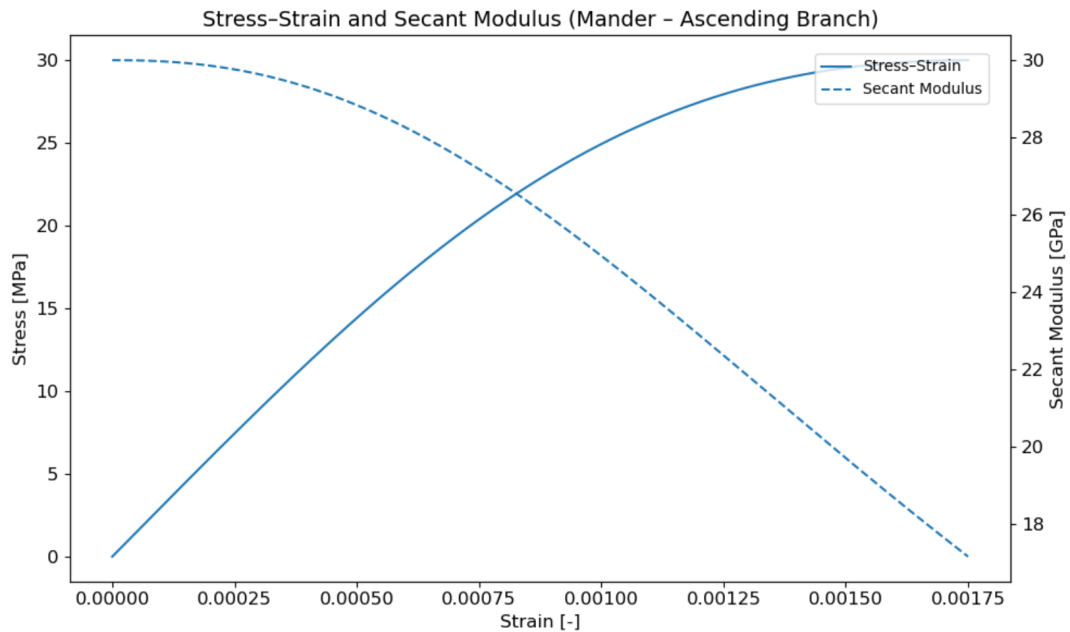


Figure 5.33: Stress, strain and secant modulus relationship according to Mander

Implementation in Quasi-Non-Linear FEA

The calculated values of E_s are used to define the elastic modulus of the concrete material in sequential FEA simulations, each corresponding to a higher load level. This process allows the global stiffness matrix to evolve in a manner that approximates the non-linear stress-strain path. The simulation aims to replicate the progression along the ascending branch of the confined concrete response, with the goal of confirming the analytically predicted peak strength in the confined region. This methodology enables the assessment of local stiffness degradation and load redistribution effects in the absence of a fully non-linear solver.

Assumptions and Limitations

The application of Mander's model in this context is subject to several assumptions:

- The concrete is assumed to behave in a quasi-uniaxial manner under monotonic compression. Multi-axial stress states, which may exist in reality due to the three-dimensional confinement, are not explicitly modelled.
- Confinement is considered passive and isotropic within the zone above the CFSP casing. This neglects potential local effects such as non-uniform restraint or microcracking.
- Only the ascending branch of the stress-strain response is used. Post-peak softening or confinement degradation are not included.
- Young's modulus is updated manually per simulation step; full strain-dependent material models are not implemented.

Despite these simplifications, the quasi-non-linear approach provides a rational and computationally feasible method to simulate the stiffness evolution of confined concrete and to validate the peak strength predictions derived from analytical models. It bridges the gap between linear elastic analysis and fully non-linear FEA in a context where numerical convergence poses a practical limitation.

Baseline Case Study FEA

To determine what the correct concrete stiffness for the quasi-non-linear analysis is, an iterative process needs to be performed, starting with a baseline linear FEA in which the entire concrete cap was assigned standard C30/37 properties: Young's modulus $E = 30 \text{ GPa}$, Poisson's ratio $\nu = 0.2$, and density $\rho = 0 \text{ kg/m}^3$ (which doesn't align with standard C30/37 properties but is judged more appropriate for the present, inverted (upside-down) model). The results are shown below. Note that the stresses are too high because no stiffness reduction has been applied yet.

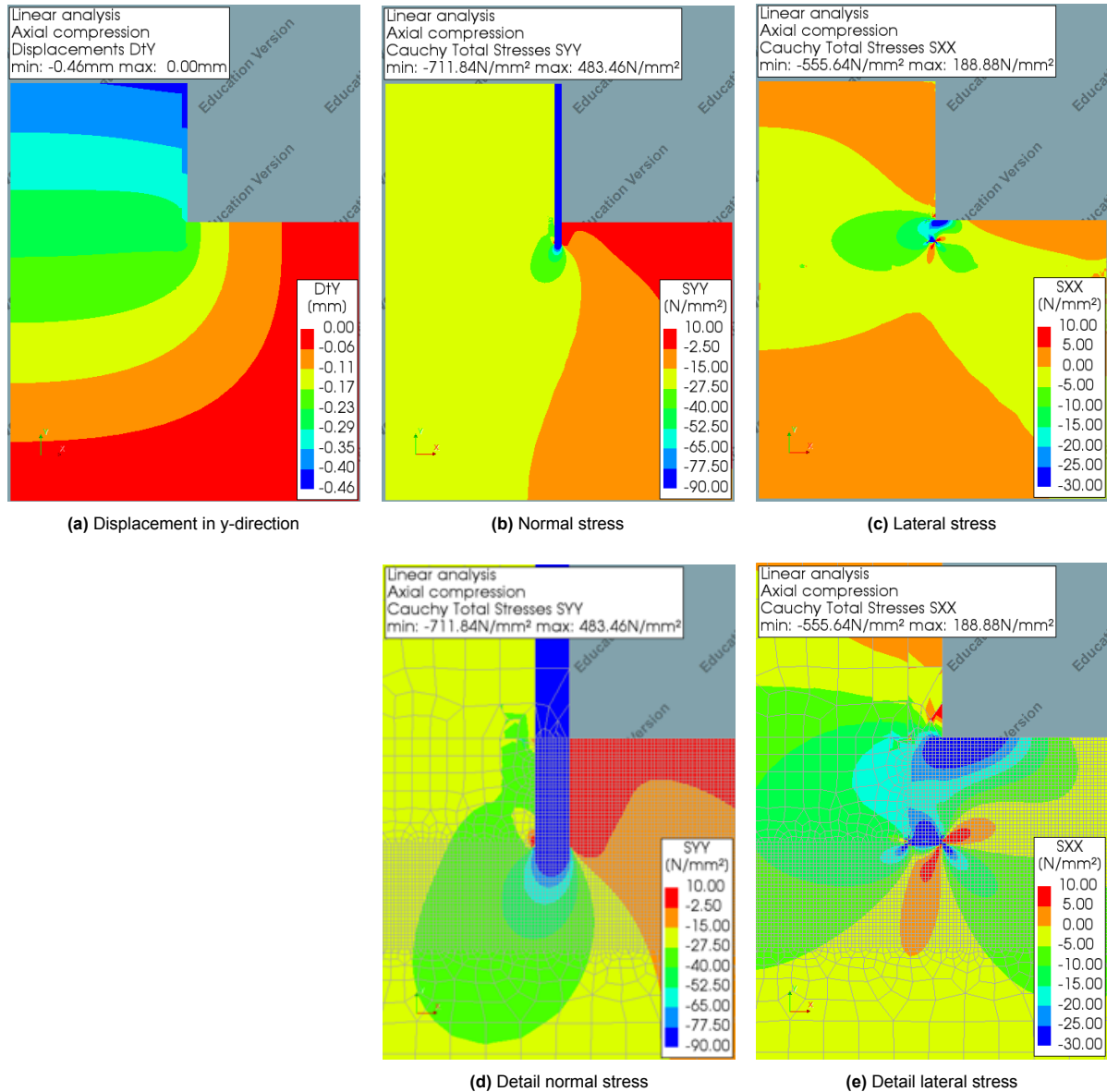


Figure 5.34: Results of the case study Linear FEA with initial linear elastic material properties

Figure 5.34a shows that the concrete core deforms independently of the steel casing (note that the displacement contours do not align across the interface) thus confirming a fully unbonded condition. Within the pile, the contours exhibit a convex, hyperbolic pattern: deformation of the concrete adjacent to the casing exceeds that at the pile centre, consistent with load transfer from the casing into the cap. The corresponding normal-stress field in Figure 5.34b illustrates a pronounced concentration just beneath and slightly to the left of the casing (green band, approximately -27.5 to -52.5 MPa), exceeding the uniaxial compressive strength of unconfined concrete. The detailed view in Figure 5.34d reveals a blue zone beneath the casing where compressive stresses surpass 77.5 MPa , indicating local crushing

in an unconfined scenario and a physical tendency for load to be redirected from the casing into the core.

In the lateral (x) direction, local stress concentrations are also evident. Outside the immediate vicinity of the casing, the cap experiences compressive stresses generally below the uniaxial capacity; however, the region adjacent to the casing shows compressive levels in excess of 25 MPa, which may precipitate spalling, loss of cover and, ultimately, durability issues (e.g. early reinforcement corrosion). Although important, such effects lie beyond the scope of this thesis. The lateral-stress detail in Figure 5.34e further shows a red band indicating tensile stresses exceeding 5 MPa, consistent with the onset of cracking.

The working hypothesis in this thesis is that the concrete directly beneath the casing attains an increased compressive capacity due to passive confinement by the lower reinforcement net. Under this assumption, the modified theory yields an optimal bearing stress of $\sigma_{x0} = 149.05$ MPa. Outside this narrowly confined zone, any confinement by the surrounding (unloaded) concrete is neglected here because the case-study model dimensions were deliberately limited; the stiffness reduction in the bulk of the cap can therefore be taken from the unconfined relationship in Figure 5.33. The initial (secant) modulus is taken as $E = 30$ GPa throughout the cap, including the confined region beneath the casing; as indicated by Figure 2.10 and Figure 3.4, the secant moduli of confined and unconfined concrete coincide, with divergence occurring only in the post-linear regime. Assigning the correct *secant* modulus to each segment requires knowledge of the average segmental stress, which is obtained from the baseline analysis shown in Figure 5.34. The geometric segmentation used for this purpose is depicted in Figure 5.29; an additional, thin segment is introduced immediately beneath the casing to represent the optimally confined region, which behaves distinctly from the surrounding concrete.

The height of the optimally confined zone is determined from the Dual-Wedge stress field (DWSF). The ultimate bearing strength is mobilised in region ABK , where both passive and geometric confinement are most effective. The width of this region equals the loaded width; its height depends on the angle γ , given by Markic et al. as

$$\tan \gamma = \frac{\sigma_{\alpha} \sin \alpha \cos \alpha}{\sigma_{x0} - \sigma_{\alpha} \cos^2 \alpha} \quad \text{Eq. 5.21}$$

With $\sigma_{\alpha} = 66.63$ MPa the compressive stress in strut BFK , $\alpha = 25.57^\circ$ the strut inclination, and $\sigma_{x0} = 149.05$ MPa the optimal bearing stress. Substitution gives $\gamma = 15.3^\circ$, corresponding to an optimal confined height of 18.3 mm.

For all concrete segments other than the confined region, the initial uniaxial compressive strength is taken as 30 MPa; in the optimally confined region ABK , the modified theory indicates a peak strength of 149.05 MPa. Because the peak strength increases from 30 to 149.05 MPa, the peak strain is expected to be markedly larger; a value of $\varepsilon_{c, \text{peak}} = 0.0075$ is therefore adopted, consistent with the extrapolated non-linear stress–strain curve based on a 30 GPa initial secant modulus (see Figure 5.32).

To assign appropriate secant moduli to the segments, an iterative procedure was employed. A baseline analysis with uniform $E = 30$ GPa provided average normal stresses for each segment (Figure 5.35). Using the Python routine in Appendix C.2, Mander's model was evaluated at these average stresses to compute the corresponding secant moduli. These moduli were then assigned to the segments and the analysis repeated. The cycle of (i) extracting updated segmental average stresses and (ii) re-evaluating the secant moduli was continued until the change in segmental normal stress between successive iterations fell below a prescribed tolerance, at which point convergence was declared. Results from the first and final iterations are reported in this appendix.

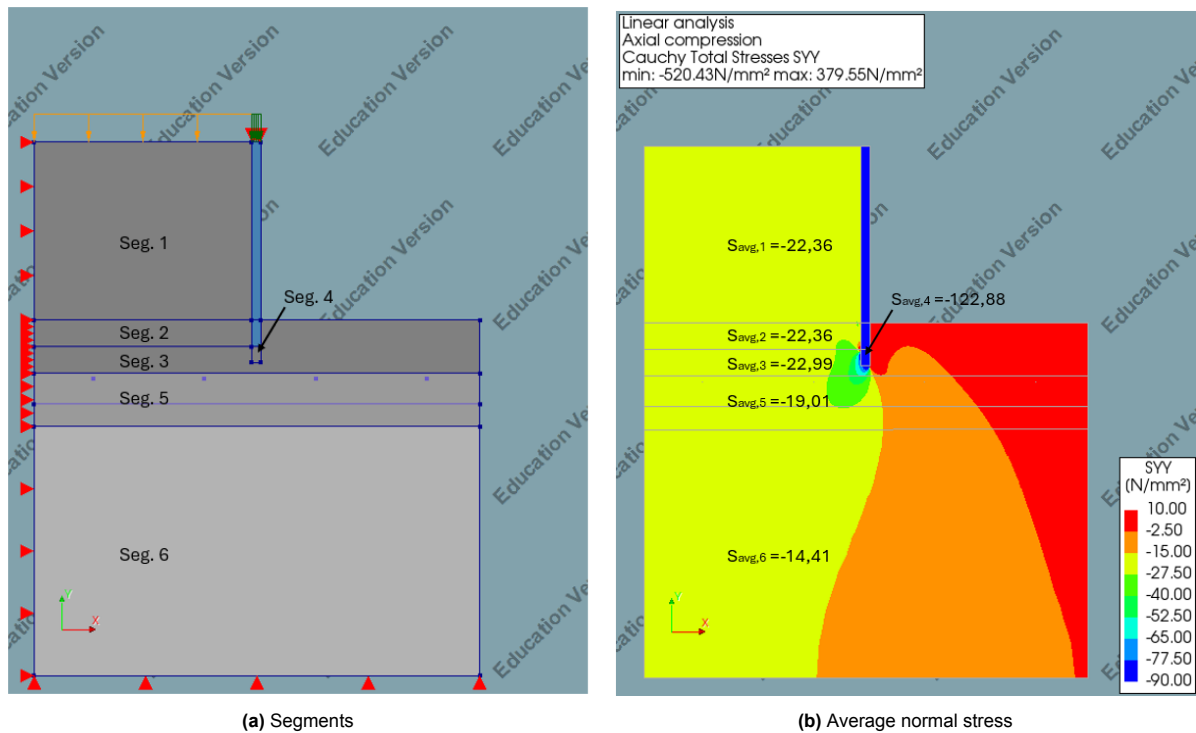


Figure 5.35: Normal stress in different segments according to the baseline analysis

For the pile core (segments 1 and 2), no stiffness reduction was applied: full confinement by the steel casing was assumed to elevate compressive capacity and extend the linear response. For segments 3, 5 and 6, the reduced stiffness followed Mander's unconfined stress–strain–secant modulus relationship (Figure 5.33). For the confined segment 4, confined concrete properties were used within Mander's framework to obtain the appropriate stress–strain–secant modulus relationship and, hence, the reduced stiffness for the converged analysis. The results of the first iteration are plotted in appendix E and summarized in Table 5.4.

Table 5.4: First iteration (baseline): segmental average normal stress and secant modulus.

Segment	Compressive strength f_c [MPa]	peak strain $\varepsilon_{c,peak}$ [-]	Initial modulus E_c [GPa]	Average normal stress $S_{seg,i}$ [MPa]	Secant Modulus $E_{sec,i}$ [GPa]
1	30	0.00175	30	-22.36	30
2	30	0.00175	30	-22.36	30
3	30	0.00175	30	-22.19	26.42
4	30	0.0075	149.05	-84.85	29.09
5	30	0.00175	30	-19.73	27.41
6	30	0.00175	30	-14.86	28.74

The iterative update was then initiated and continued until the change in segmental average normal stress between successive iterations fell below 0.05 MPa. The iteration history is reported in Appendix E.3. Convergence was achieved after seven iterations, at which point the final segment stiffnesses were obtained. Table 5.5 summarizes the results of the final iteration.

Table 5.5: Final iteration: segmental average normal stress and secant modulus.

Segment	Compressive strength f_c [MPa]	peak strain $\varepsilon_{c,peak}$ [-]	Initial modulus E_c [GPa]	Average normal stress $S_{seg,i}$ [MPa]	Secant Modulus $E_{sec,i}$ [GPa]
1	30	0.00175	30	-22.36	30
2	30	0.00175	30	-22.36	30
3	30	0.00175	30	-22.04	26.49
4	30	0.0075	149.05	-83.36	29.14
5	30	0.00175	30	-19.01	27.65
6	30	0.00175	30	-14.59	28.79

5.3.5. Mesh Refinement

The primary output of the FEA model is the bearing stress in the concrete directly above the steel casing. To minimise numerical bias arising from discretisation, a systematic mesh-refinement study was undertaken.

Because displacement control is applied to the casing, a support is introduced on the loaded side of the casing to recover reaction forces. Owing to the fully unbonded interface, the bearing stress at the steel-concrete interface can be obtained by dividing the casing support reaction by the casing's cross-sectional area. Hence, the sought FEA output is the reaction force at the casing support, and adequate mesh refinement is required within the casing at the support location and in the adjacent concrete elements that transfer load into the casing.

Baseline discretisation

Using the element distribution proposed in subsection 5.1.3 (see Figure 5.4), the casing support reaction was $-2.608.222$ N. Assuming a uniform interface pressure, the corresponding bearing stress is:

$$q_x = \frac{R_{\text{casing}}}{A_{\text{casing}}} = \frac{R_{\text{casing}}}{0.25 \cdot \pi \cdot (R_{\text{out}}^2 - R_{\text{in}}^2)} = -166.71 \text{ N/mm}^2, \quad \text{Eq. 5.22}$$

Where $R_{\text{out}} = 508$ mm and $R_{\text{in}} = 488$ mm.

Refining the casing mesh

Reducing the casing element size from 10 mm to 5 mm yielded a reaction of $-2.605.958$ N and a bearing stress of 166.57 N/mm^2 . The negligible change indicates that refining the casing alone has limited influence on the result.

Refining the load-transfer region

Attention then shifted to the elements directly transferring load into the casing: the confined region (segment 4) and the fine mesh layer of the cap (segment 3) (see Figure 5.35a). With the casing held at 5×5 mm, refining segments 3 and 4 from 5×5 mm to 2.5×2.5 mm increased the bearing stress to 171.60 N/mm^2 . Further refinement to 1×1 mm gave 174.64 N/mm^2 . These modest increases show that local refinement around the casing tip improves accuracy.

Element-count constraint and segmentation update

Due to the element limit in the educational DIANA licence, further global refinement was not feasible. Moreover, adopting 1×1 mm elements in segments 3 and 4 produced poor node alignment with neighbouring 5×5 mm regions, necessitating local re-meshing. To resolve this while respecting the element limit, segment 3 was split, creating a seventh segment to facilitate graded transitions and better node alignment, as shown in Figure 5.36.

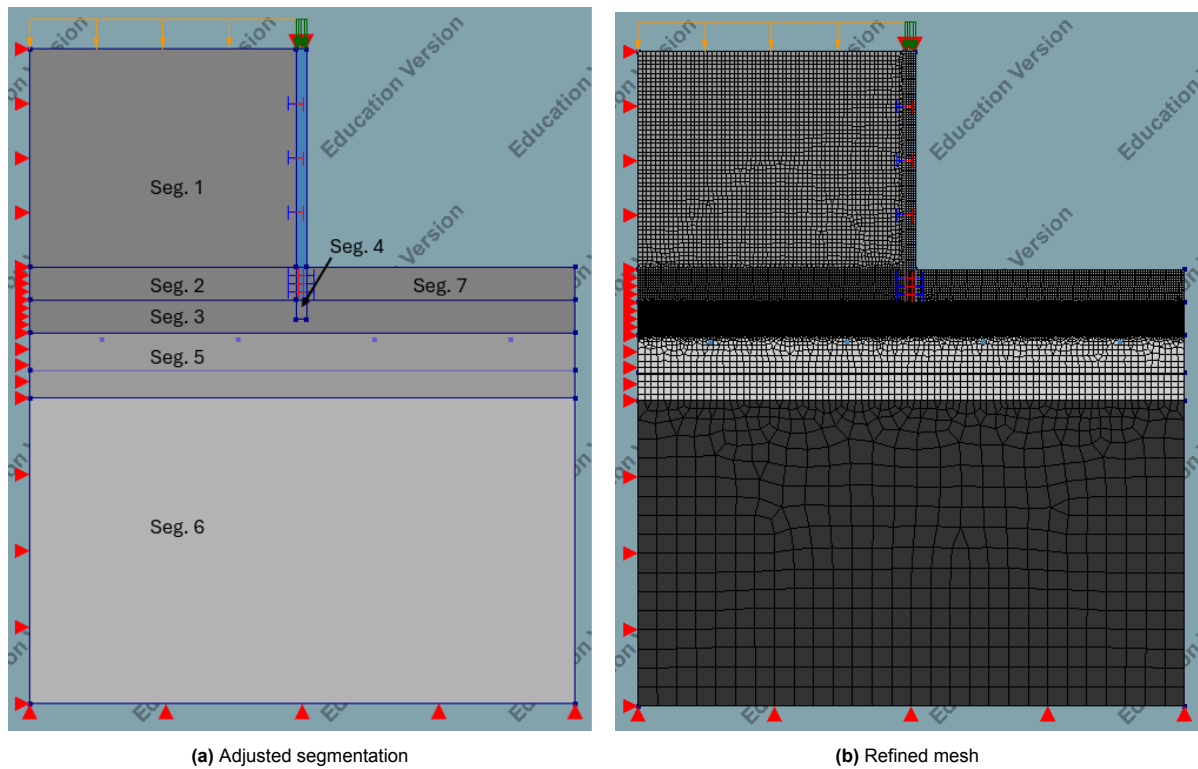


Figure 5.36: Adjusted segmentation and refined mesh of the case-study FEA model.

Refined mesh with node alignment

Re-analysis with the updated mesh, enforcing node alignment with neighbouring regions, yielded a bearing stress of 174.62 N/mm^2 . All boundary conditions were checked and confirmed correct. The difference from the pre-refinement value of 174.64 N/mm^2 is 0.02 N/mm^2 (approximately 0.01%), indicating mesh-independent results. Accordingly, 174.62 N/mm^2 is taken as the most accurate estimate achievable within the present discretisation and licensing element amount constraints.

5.3.6. Results and Verification

At this stage, the ingredients introduced throughout the chapter are synthesised into a single, comprehensive FEA model of the case study. The axisymmetric modelling approach, element formulation, and meshing strategy are described in section 5.1, and the selected material properties in section 5.2. This chapter has established why a fully non-linear analysis is infeasible and how a quasi-non-linear procedure is implemented to estimate the peak concrete strength in the region of interest. The theoretical framework for reducing the concrete stiffness has been derived and applied to the case study.

By invoking conservation of energy for the DWSF model of Markic et al. and applying Hooke's law to the case-study geometry and material properties, a load was computed that is equivalent to the predicted increased bearing capacity of 149.05 MPa . The quasi-non-linear FEA is then used to assess whether the concrete can indeed sustain this bearing stress under the corresponding equivalent load. This verification assumes that the concrete follows a stress-strain trajectory consistent with Mander et al. The mesh configuration is refined to ensure mesh-independent results (see subsection 5.3.5).

Verification is carried out against the following criteria:

- The interface bearing stress in the concrete above the casing attains is consistent with the DWSF model under the equivalent load.
- Principal stress trajectories and directions are consistent with the DWSF model.
- The lateral confining stress in the FEA corresponds to σ_{conf} obtained by Mander et al. theorem for confined concrete.
- The reinforcement is activated similar to Markic et al. DWSF theorem reinforcement activation.
- The magnitude of shear stress along the discontinuity line FK is within the expected range.
- The vertical normal stress at distance X_E is comparable to the target value σ_{xd} .

Bearing Stress

As outlined in subsection 5.3.5, the bearing stress is obtained by reading the reaction at the casing support used to impose the prescribed deformation. Because the casing is fully unbonded along its side face, resistance develops only at the casing tip within the optimally confined region of the cap (segment 4). Consequently, the support reaction equals the force transferred across the steel–concrete contact at the tip. The bearing stress is therefore computed by dividing the casing support reaction by the steel casing's cross-sectional area (i.e. the contact area at the tip). For the case-study model, the recovered reaction is $R_{casing} = -2.731.899$ N.

$$q_x = \frac{R_{casing}}{A_{casing}} = \frac{R_{casing}}{0.25 \pi (R_{out}^2 - R_{in}^2)} = -174.62 \text{ N/mm}^2, \quad \text{Eq. 5.23}$$

where $R_{out} = 508$ mm and $R_{in} = 488$ mm.

This value is slightly higher than the analytically predicted bearing strength of 149.05 MPa, with a difference of 25.57 MPa (i.e. 17.15 %). This level of deviation is comparable to the differences observed between experimental and FEA results for the specimens reported by Markic et al. (see Figure 5.28), bearing in mind that their experimental outcomes closely matched the corresponding analytical predictions. Given that the equivalent applied load is wholly determined by the dimensions and parameters prescribed by Markic et al.'s DWSF model in combination with the modified Mander et al. formulation, the close correspondence, including the expected bias, between prediction and computation supports the applicability of these analytical models to the CFSP-pile-to-concrete-cap connection.

Dual-Wedge Stress Field and Principal Stress Evaluation

The Dual-Wedge Stress Field (DWSF) model discretises the stress distribution into wedges bounded by discontinuity lines, within which the stress state is assumed to be uniform. Although this representation is idealised, it provides a useful means of comparing principal stress magnitudes and orientations with those obtained from the finite element analysis (FEA). To enable this comparison, the average stresses within the struts of the DWSF are evaluated directly from the FEA results.

Determining the average results requires knowledge of the dimensions of the DWSF wedges. The Python scripts provided in Appendix A.2 and Appendix A.3 generate the necessary output to establish the wedge geometry for the case study. Figure 3.6 defines the geometric parameters that govern the DWSF. For the case study, the following values are obtained from the Python output:

- $d_1/2 = 5$ mm,
- $d_2/2 = 30.40$ mm,
- $X_E = 53.10$ mm,
- $\alpha = 25.57^\circ$,
- $\gamma = 15.30^\circ$ (see Equation 5.21),
- $\beta = 41.40^\circ$.

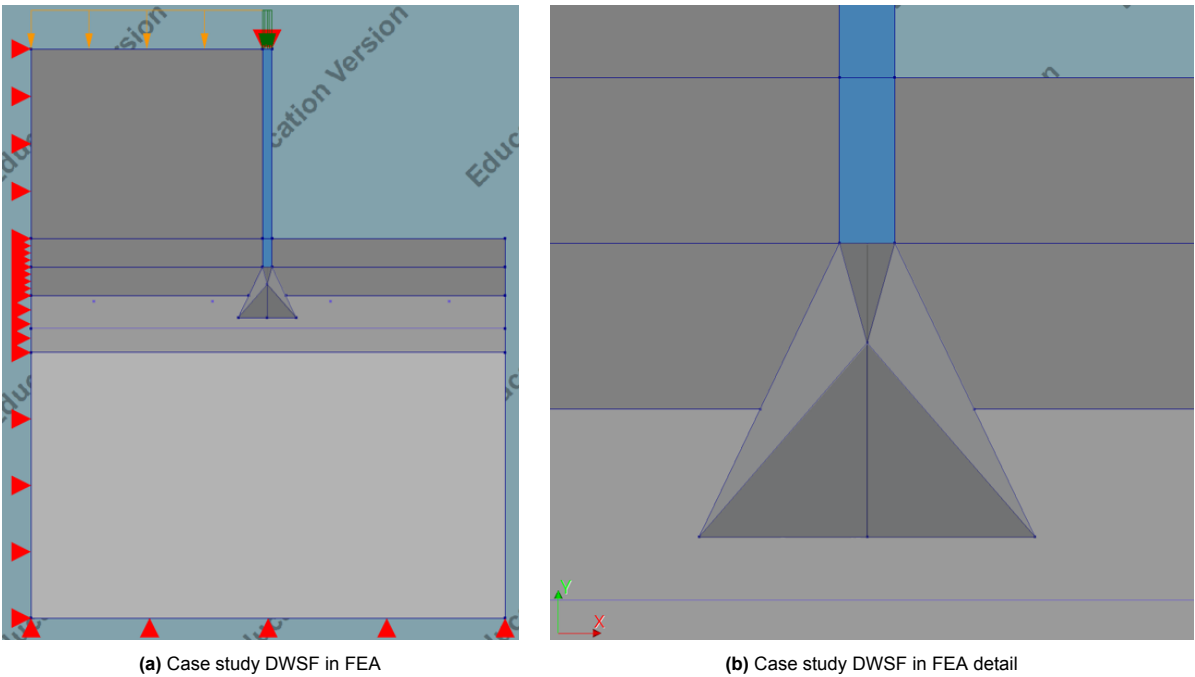


Figure 5.38: Case study DWSF modelled in FEA.

To improve the clarity of the in-plane principal stress distribution, the FEA mesh was coarsened to a size of 5 by 5 mm, thereby reducing the number of stress vectors. The resulting in-plane principal stress distribution is shown in Figure 5.39.

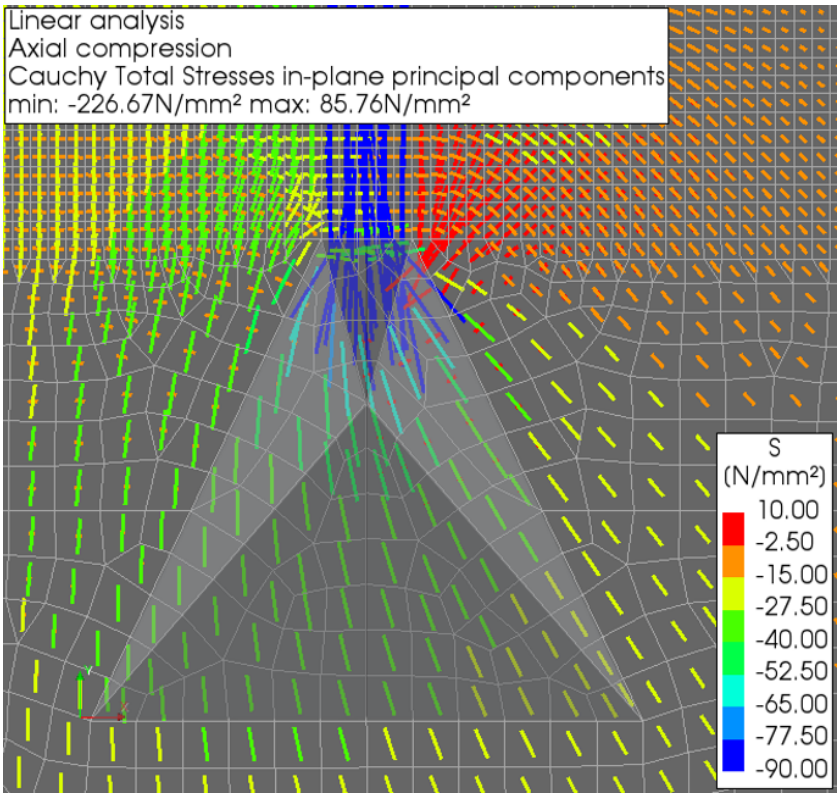


Figure 5.39: In-plane principal stress case study FEA.

From the analytical calculations, the principal stress in the struts is known to be $\sigma_\alpha = 66.63$ MPa at an inclination of $\alpha = 25.57^\circ$ from the vertical plane. Figure 5.39 shows that the principal stress orientation differs between the left and right struts. The right strut aligns closely with the analytically predicted inclination, whereas the left strut deviates. This deviation arises because the analytical model assumes confinement only by reinforcement. While this assumption holds for the right-hand side, on the left-hand side the pile core generates an additional normal compressive stress in the concrete cap, producing lateral confinement not accounted for in the analytical model.

The FEA results therefore indicate that the effect of active confinement due to the pile core is more significant than the passive confinement provided by the reinforcement. However, for this active confinement to govern the bearing stress, it must be present symmetrically on both sides of the DWSF. Since this condition is not met, the analytical bearing stress based on passive confinement remains the appropriate design approach.

For consistency with the analytical assumptions, the principal stresses were calculated from the FEA results using only the right-hand strut. At each node within the strut, the global stress components S_{xx} , S_{yy} and S_{xy} were extracted. These components were then transformed into the principal stress system. The state of stress at a point in two dimensions can be written as

$$\sigma = \begin{bmatrix} S_{xx} & S_{xy} \\ S_{xy} & S_{yy} \end{bmatrix}.$$

The principal stresses, corresponding to the eigenvalues of this stress tensor, are given by

$$\sigma_{1,2} = \frac{S_{xx} + S_{yy}}{2} \pm \sqrt{\left(\frac{S_{xx} - S_{yy}}{2}\right)^2 + S_{xy}^2}, \quad \text{Eq. 5.24}$$

where σ_1 is the maximum principal stress and σ_2 the minimum principal stress. The corresponding orientation of the principal axes is defined by:

$$\tan(2\theta_p) = \frac{2S_{xy}}{S_{xx} - S_{yy}}. \quad \text{Eq. 5.25}$$

Here, θ_p is measured counter-clockwise from the y -axis. This transformation ensures that, even in cases where one axis is in tension and the other in compression, the stress state is expressed in terms of purely tensile and compressive principal stresses acting on orthogonal planes.

The procedure described above was applied to all nodes within the right strut of the DWSF. According to the finite element results, the average value of the principal compressive stress was -43.89 MPa, and the average inclination of the principal stress plane was 30.53° . These values show a deviation from the analytically obtained results, which can be attributed to both the influence of the pile core and the modelling assumptions used in the numerical analysis.

Although the interfaces between the casing, the pile core, and the cap were modelled as fully unbonded, the pile core still acts as a stiff boundary that constrains the lateral expansion of the adjacent wedge. On the side of the DWSF facing the pile core, this passive restraint reduces the lateral dilation of the compression band and keeps the load path oriented closer to the vertical axis. Consequently, the inclination of the in-plane principal stresses on this side is smaller than the analytical wedge angle. On the opposite side, where no such restraint is present, the stresses are free to fan out more widely, and with the stimulation from the pile core reaction force resulting in a larger inclination of the principal directions than predicted analytically. This asymmetric confinement effect partially explains the discrepancy between the numerical and analytical outcomes: while the analytical DWSF formulation by Markič et al. assumes symmetric confinement primarily provided by reinforcement, the FEA captures the additional stiffening influence of the pile core on one side of the wedge.

Another notable discrepancy between the expectations of the Markic et al. DWSF model and the numerical results concerns the lateral principal stress components. In the FEA, the stress tensors within the

DWSF and in the passively confined zone immediately outside it show only normal principal stresses. By contrast, the schematic representation of the DWSF in Figure 3.6 clearly illustrates the presence of lateral compressive stresses both within the strut and nodal regions, as well as in the effectively confined area adjacent to the DWSF. This discrepancy provides further evidence of insufficient activation of the confining reinforcement in the FEA and, consequently, an absence or near absence of passive lateral confining stress.

This conclusion is supported by the strain results at the casing–cap interface. While the analytical approach predicts a strain of 0.0075, the FEA yields only 0.00178. Combined with the recognition that the quasi-non-linear FEA does not account for cracking, it follows that the lateral deformation required to mobilise the confining reinforcement is severely underestimated. As a result, the model produces negligible passive lateral confinement compared to what would be expected in reality, which is why no lateral stress tensors are present in the in-plane principal stress components plot.

A further source of deviation arises from the material modelling. In the finite element analysis no distinction was made between the stiffness of the strut and that of the surrounding concrete. In reality, the effective stiffness within the strut is increased (at increased stress levels) due to active confinement: the lateral expansion of the compression band is restrained by the adjacent concrete and reinforcement, thereby enhancing the local compressive strength. The analytical assessment therefore idealises the strut as a uniform block subjected to an elevated compressive stress, whereas the FEA does not capture this mechanism and consequently produces a lower average principal stress in the strut. The impact is expected to be limited, since the struts are already assigned a Young's modulus of 27.65 GPa; under optimal confinement their stiffness would not exceed 30 GPa.

Finally, the numerical simulations were carried out using a quasi-non-linear procedure rather than a fully non-linear constitutive model. This approach does not represent several key mechanisms, such as confinement-induced hardening, plastic stress redistribution, cracking-induced anisotropy, and non-linear Poisson effects. A fully non-linear analysis would be expected to predict higher average principal stresses within the strut and an inclination more closely aligned with the analytical DWSF prediction. The present FEA therefore provides a conservative approximation, in which the beneficial influence of confinement on the stress development within the strut is underestimated.

Passive confinement by reinforcement

Immediately outside the DWSF, Markic et al. assume that the concrete is subjected solely to lateral confining stress. In the case-study FEA, however, the concrete on the left side of the DWSF is additionally influenced by the pile–core reaction, which introduces both a normal compressive stress and lateral tensile stress resulting in active lateral confining stress on the DWSF. This constitutes a direct departure from the assumptions of Markic et al. By contrast, the right side of the DWSF remains unloaded by the core reaction and should therefore be affected only by passive confinement. For verification purposes, the right side is thus adopted as the reference region, with the understanding that any lateral stress arising from the pile–core reaction on the left would merely augment confinement and potentially effect the bearing capacity.

Figure 4.2 delineates the effectively passive-confined zone. Extracting the horizontal stress from the nodes within this region and taking the average yields a lateral confining stress of 5.25 MPa, which is substantially lower than the analytically predicted 10.25 MPa. This discrepancy is expected: in the present quasi-non-linear model the reinforcing bars do not mobilise the non-linear lateral dilatation that, in reality, enhances confinement, and the resulting passive confinement effect is therefore under-represented in the FEA.

Activation of the reinforcement

Since the lateral confining stress provided by the reinforcement is modest, only limited reinforcement activation is expected. In the experimental campaign of Markic et al. (Markic et al. 2022a), Section 3.11 (*Reinforcement activation*) reports that the upper reinforcement layers generally reach yield. As Markic et al. do not furnish a closed-form expression for the tensile stress in the reinforcement at peak load, it is assumed in the present case study that the confining reinforcement attains yield at the peak bearing stress.

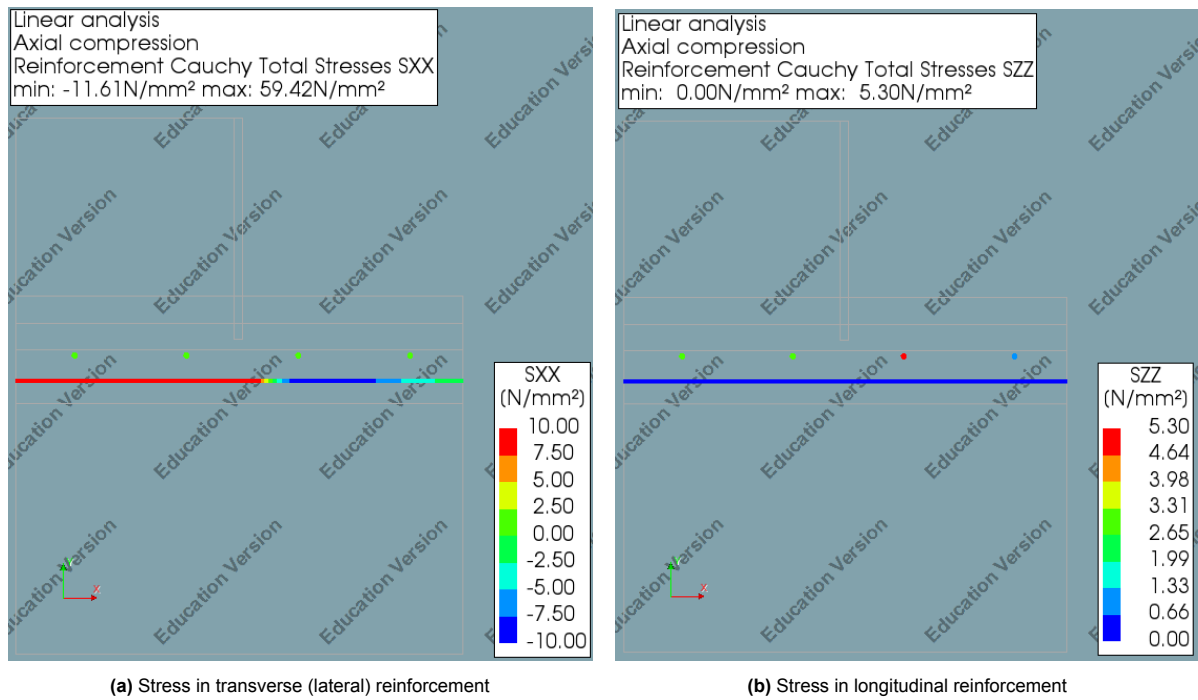


Figure 5.40: Reinforcement stresses in the case-study FEA.

According to the quasi-non-linear FEA, the maximum stress in the transverse reinforcement is 59.42 MPa; however, this peak occurs at the first node adjacent to the axis of symmetry and is therefore interpreted as an artificial concentration arising from the effectively rigid boundary. In the region of the cap where the pile bearing stress induces normal compression, the lateral reinforcement carries tension (maximum is 27.78 MPa); outside the bearing-load dispersion zone, the concrete is laterally compressed and the reinforcement correspondingly goes into compression.

Figure 5.41 illustrates this behaviour: an initial singular peak at the symmetry boundary is followed by a tensile plateau that increases towards the casing (dashed lines in the graph represent the steel casing); beyond the casing, the tensile stress diminishes and eventually becomes compressive. While the curve clearly evidences activation of the lateral reinforcement by the casing's bearing action, the stress magnitudes remain well below yield. This confirms that reinforcement activation is under-represented in the quasi-non-linear FEA compared with the levels implied by the DWSF model of Markic et al., chiefly because non-linear dilation and associated confinement effects are not fully mobilised in the present analysis.

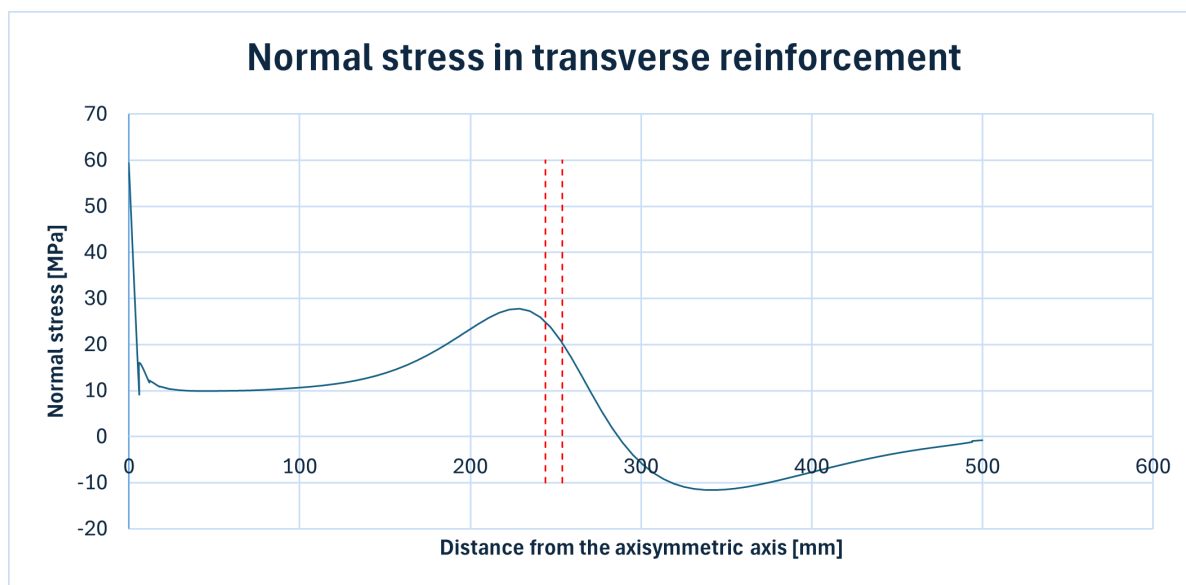


Figure 5.41: Normal stress in transverse reinforcement obtained by quasi-non-linear case study FEA

The longitudinal reinforcement bars (indicated by the coloured points in Figure 5.40) are all in tension; however, the maximum tensile stress is only 5.30 MPa, far below the yield strength of the B500B reinforcement. This again indicates that the present quasi-non-linear model under-represents the lateral confinement mechanisms anticipated by the DWSF theorem of Markic et al.

Shear stress along the discontinuity line

According to the finite element analysis, the average shear stress along discontinuity line FK amounts to 20.53 MPa. This value is significantly larger than the shear stress of 3.99 MPa that was considered in the calculation of the prescribed deformation corresponding to the maximum bearing stress. The discrepancy can be explained by the limitations inherent to a quasi-non-linear finite element approach. First, the analysis assumes a purely linear-elastic material response, which implies that the material continues to resist shear stresses proportionally to the applied load. In reality, both the concrete and the steel reinforcement exhibit non-linear behaviour once cracking or yielding occurs, leading to a reduction and redistribution of stresses that the linear model cannot capture. Second, the linear analysis does not allow for any form of stress redistribution. Localised peaks in shear stress therefore remain concentrated within the same region, while in practice these stresses would be partially redistributed to adjacent zones once local yielding or cracking takes place. Finally, the linear model assumes that the material can indefinitely carry tensile stresses. In concrete, however, the development of cracks leads to a significant reduction of shear transfer across planes such as FK. Because the model does not incorporate this mechanism, it yields shear stresses that are much higher than what the dual wedge stress field model of Markič et al. predicts and what is likely to occur in reality.

It should also be noted that the magnitude of 20.53 MPa obtained from the finite element analysis is implausible when compared with the material properties of concrete C30/37. The mean tensile strength of this concrete is approximately 3 MPa, and its effective shear capacity is consequently only a few megapascals. As such, the linear elastic analysis produces shear stresses far in excess of the realistic material capacity, further underlining that the dual wedge stress field model provides a more credible representation of the physical behaviour.

Vertical normal stress at distance X_E

According to Markić et al.'s DWSF theorem, the bearing stress σ_{x0} spreads through the stress field and becomes uniform at the characteristic distance X_E , taking the value σ_{xd} . The ratio σ_{xd}/σ_{x0} is governed by the geometric ratio d_1/d_2 . For the peak bearing stress $\sigma_{x0} = 149.05$ MPa,

$$\sigma_{xd} = \sigma_{x0} \frac{d_1}{d_2} = 149.05 \text{ MPa} \times \frac{10}{60.8} = 24.51 \text{ MPa.} \quad \text{Eq. 5.26}$$

In the FEA, the average vertical normal stress evaluated over the nodes at the base of the DWSF region is -23.67 MPa (negative sign denoting compression) indicated by the dashed line in Figure 5.42. In magnitude, this is within approximately 3.5% of the analytical prediction, indicating that the level of vertical stress transmission is consistent with the DWSF assumption.

However, Figure 5.42 demonstrates that the distribution of this stress is not uniform at a distance X_E from the loaded area, contrary to the DWSF idealisation. The plot shows the normal stress along the base of the DWSF from left to right, and the curve clearly reveals higher compressive stresses on the left than on the right. This asymmetry confirms the influence of the pile–core reaction on the stress field beneath the casing and explains the departure from the uniformly distributed stress assumed by the DWSF model.

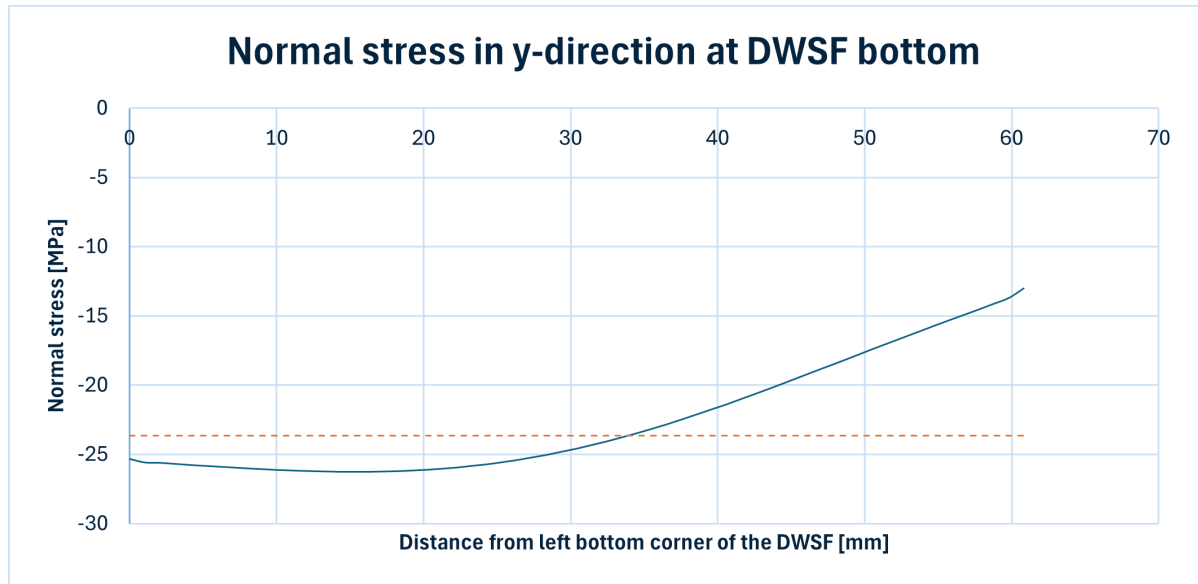


Figure 5.42: Case study FEA obtained stress at DWSF bottom (σ_{xd})

Verification of the DWSF in the FEA model

The verification demonstrates that the quasi-non-linear finite element model captures several key characteristics of the Dual–Wedge Stress Field (DWSF) proposed by Markić et al., albeit with some deviations that can be attributed to modelling assumptions and the influence of the pile core. The predicted peak bearing stress of 149.05 MPa was reproduced with close accuracy by the FEA, confirming that the global load–bearing capacity of the connection is consistent with the analytical framework. The orientation of the principal stress trajectories within the right-hand strut also showed reasonable agreement with the analytical inclination, whereas the left-hand strut deviated due to additional confinement effects induced by the pile core. Similarly, the evaluation of vertical stress at the characteristic distance X_E matched the theoretical magnitude, but its distribution was found to be asymmetric rather than uniform.

The confining stresses generated by the reinforcement and their associated activation were significantly under-represented in the quasi-non-linear FEA, reflecting the absence of non-linear dilation and hardening mechanisms in the adopted modelling approach. Likewise, the shear stresses obtained along discontinuity line FK were far in excess of realistic material capacities, highlighting the limitations of a

linear elastic representation when compared with the physically consistent redistribution mechanisms captured by the analytical DWSF model.

An overview of the comparison reveals close agreement in the vertical stress response, but pronounced discrepancies in the horizontal (lateral) stresses (see Figure 5.43).

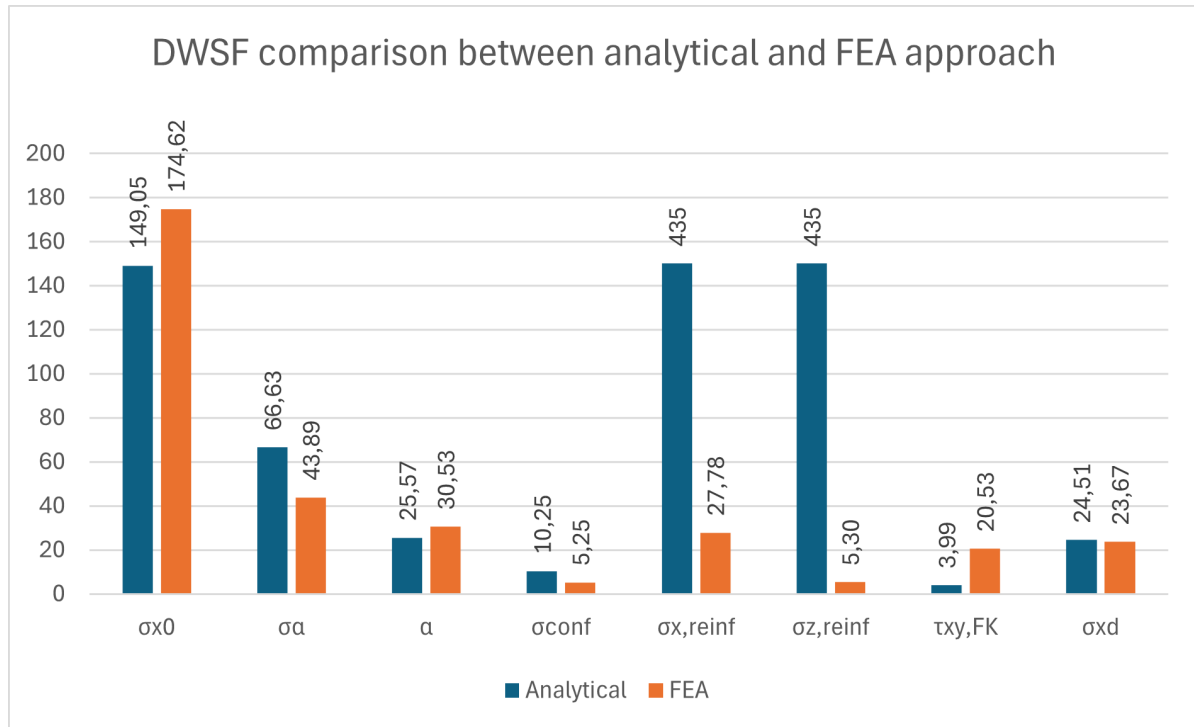


Figure 5.43: DWSF comparison between analytical and FEA approach

Overall, the numerical analysis substantiates the presence of the DWSF in the case-study configuration, particularly with respect to bearing capacity and stress propagation. However, discrepancies in reinforcement activation, shear response, and stress symmetry underline that the analytical model remains a more reliable predictor of confinement effects under peak load. The FEA thus provides an incomplete representation of the mechanisms underlying the DWSF in CFSP pile-to-cap connections leaving the question if passive confinement is actually activated.

An increase in bearing capacity is clearly evident in the results. However, the material response has been *implicitly* influenced by prescribing stiffness from confined-concrete stress-strain relations, while the analysis itself does not conclusively demonstrate that passive confinement is fully mobilised. This raises a legitimate question as to whether assuming a confined state is entirely justified. Which this quasi-non-linear FEA is unable to answer; experimental confirmation (or a fully non-linear analysis with explicit cracking) would be required to substantiate the degree of confinement actually achieved.

5.3.7. Sensitivity analysis

A central assumption in this study is that the peak strain in the optimally confined concrete beneath the casing is $\varepsilon_{c,peak} = 0.0075$. This parameter is an explicit input to Mander's model for confined concrete and therefore directly affects the secant modulus assigned to the concrete segments in the FEA, with a consequent influence on the predicted bearing response.

To quantify the robustness of the results to this assumption, two additional analyses were performed to bracket $\varepsilon_{c,peak}$ within a plausible range. Specifically, lower and upper bounds of 0.0065 and 0.0085, respectively, were adopted. Figure 5.44 presents three stress-strain curves: the baseline curve used in the case-study FEA (blue), the lower-bound curve (red), and the upper-bound curve (green).

The choice of bounds is justified as follows. For concrete with a secant modulus of 30 GPa, only a mod-

est deviation from linear elasticity is required to reach $\varepsilon \approx 0.0065$ at the target stress level, placing the lower limit close to the onset of noticeable nonlinearity. By contrast, exceeding $\varepsilon = 0.0085$ would necessitate a substantially more pronounced curvature of the ascending branch, implying levels of dilation and softening that are unlikely for the confinement level considered here. The interval $[0.0065, 0.0085]$ is therefore regarded as a prudent, engineeringly defensible range for $\varepsilon_{c,peak}$ in the present application.

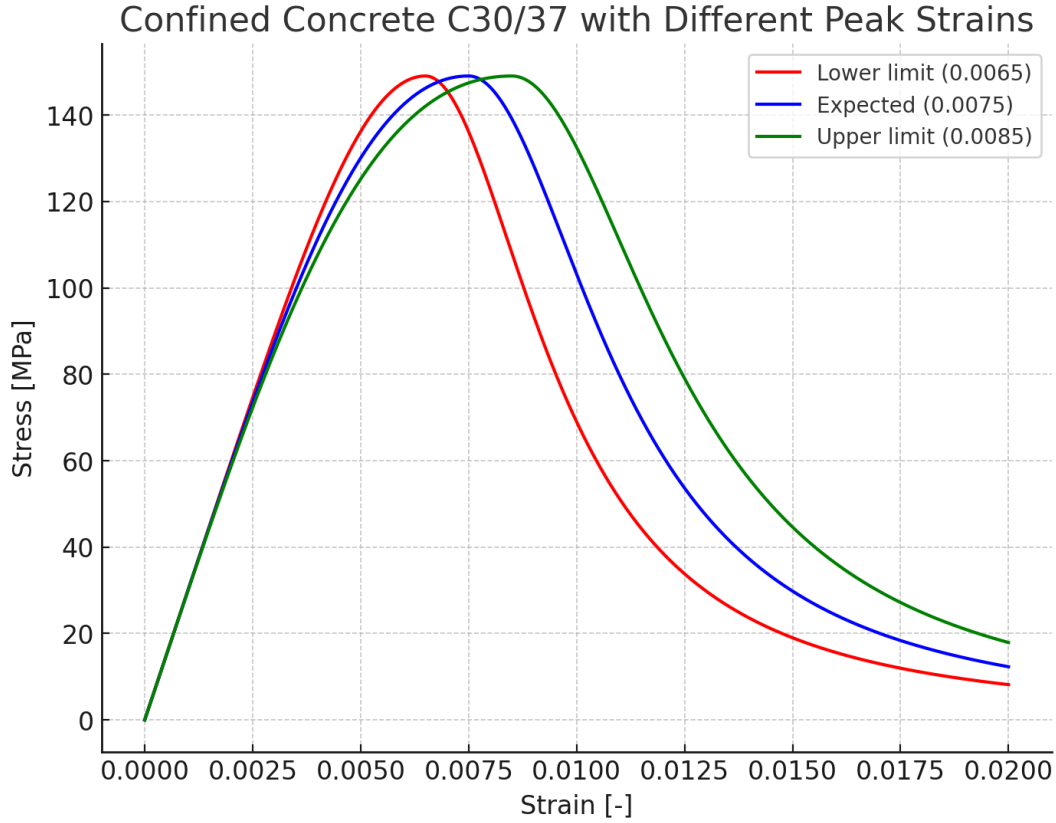


Figure 5.44: Stress-strain for confined concrete C30/37 with different strain levels at peak stress

The same segment partitioning used previously in this thesis is adopted for both sensitivity analyses (see Figure 5.35a). As before, no stiffness reduction is applied to the pile core (segments 1 and 2): full confinement by the steel casing is assumed to enhance compressive capacity and extend the linear response. For segments 3, 5 and 6, the reduced stiffness follows Mander's unconfined stress-strain-secant modulus relationship (Figure 5.33). For the confined segment 4, confined-concrete properties are again employed within Mander's framework, but with the peak strain set to the respective lower and upper limits.

Because the baseline FEA assigns a uniform Young's modulus of $E = 30$ GPa to all concrete segments, the first-iteration results for both the lower- and upper-bound strain cases coincide with those obtained for the baseline (expected) peak-strain analysis presented earlier. These baseline secant-modulus results are plotted in Appendix E.1 and summarised in Table 5.4.

Again the iterative update was then initiated and continued until the change in segmental average normal stress between successive iterations fell below 0.05 MPa. The iteration history for both the lower and upper limit analysis are reported in Appendix E.4 and Appendix E.5. For both analysis, convergence was achieved after five iterations, at which point the final segment stiffnesses were obtained. Table 5.6 summarizes the results of the final iteration for the lower bound and Table 5.7 for the upper bound.

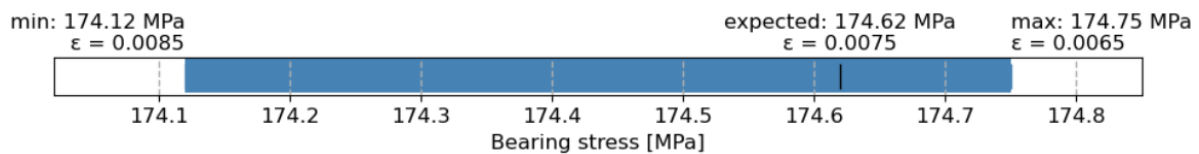
Table 5.6: Final iteration (lower bound): segmental average normal stress and secant modulus.

Segment	Compressive strength f_c [MPa]	peak strain $\varepsilon_{c,peak}$ [-]	Initial modulus E_{sec} [GPa]	Average normal stress $S_{seg,i}$ [MPa]	Secant Modulus $E_{tan,i}$ [GPa]
1	30	0.00175	30	-22.36	30
2	30	0.00175	30	-22.36	30
3	30	0.00175	30	-22.04	26.49
4	30	0.0065	149.05	-83.88	29.73
5	30	0.00175	30	-19.52	27.48
6	30	0.00175	30	-14.69	28.78

Table 5.7: Final iteration (upper bound): segmental average normal stress and secant modulus.

Segment	Compressive strength f_c [MPa]	peak strain $\varepsilon_{c,peak}$ [-]	Initial modulus E_{sec} [GPa]	Average normal stress $S_{seg,i}$ [MPa]	Secant Modulus $E_{tan,i}$ [GPa]
1	30	0.00175	30	-22.36	30
2	30	0.00175	30	-22.36	30
3	30	0.00175	30	-22.04	26.49
4	30	0.0085	149.05	-82.61	28.48
5	30	0.00175	30	-19.50	27.49
6	30	0.00175	30	-14.66	28.79

Substituting the final segment stiffnesses into the case-study FEA yields interface bearing stresses of 174.12 MPa for the upper-bound peak strain and 174.75 MPa for the lower-bound peak strain.

**Figure 5.45:** Sensitivity of bearing stress to the assumed strain at peak stress

The sensitivity analysis on the peak strain in the optimally confined concrete shows that the bearing stress varies only marginally across the tested bounds, indicating low sensitivity to this parameter. This limited influence is attributable to the relatively small extent of the optimally confined region compared with the overall stress-transfer zone and also to the marginal difference (1.25 MPa) in secant modulus between the upper and lower limit.

6

Comparative analysis

This chapter compares the analytical and FEA results with data from the experimental campaigns identified in the literature review and with the provisions of the current Eurocode. The comparison clarifies both the agreements and the discrepancies between methods and, crucially, demonstrates the improvement in force transfer achieved by the proposed theoretical method relative to the capacity implied by the present design standard.

6.1. Comparison criteria

To enable a meaningful comparison between methods, it is first necessary to catalogue the outputs from each approach and assess their mutual comparability. The analytical model, the FEA, and the Eurocode provisions yield results that are directly applicable to the case study. By contrast, the experimental campaigns concern specimens that exhibit similar confinement mechanisms and partial loading conditions, but are not geometrically or procedurally identical to the case study. Accordingly, the experimental results will be used in terms of their lower and upper bounds to provide a benchmarking envelope. The extent to which the analytical, numerical, and code-based results fall within this envelope will indicate whether their magnitudes are appropriate and if capacity is increased.

The comparison is performed for the following results:

1. Normalised bearing stress, σ_{x0} ;
2. Effective height of the stress distribution, X_E ;
3. Distributed bearing stress at X_E , σ_{xd} ;
4. Lateral confining stress, σ_{conf} ;
5. Reinforcement activation (tensile stress), σ_{reinf} ;
6. Strut inclination, α ;
7. Compressive stress in the strut, σ_{α} .

6.1.1. Analytical results

All of the above mentioned results are analytically calculated in Appendix A.2 and Appendix A.3 specifically for the case study. A summary of the results is illustrated in the bar chart plotted in Figure 5.43.

6.1.2. FEA results

The FEA results are all specific to the case study and are all described in subsection 5.3.6. A summary of the results is illustrated in the bar chart plotted in Figure 5.43.

6.1.3. Experimental results

The enhanced bearing capacity proposed in this thesis arises from the combined effects of passive and geometric confinement. Since Mander et al. (see (Mander et al. 1988a)) investigated only passive confinement on concrete specimens, their results are less directly comparable to the present case study. By contrast, the experimental programme of Markic et al. (see (Markic et al. 2022a)) explicitly considers the joint action of passive and geometric confinement on bearing capacity. This aligns with the analytical approach adopted here and therefore provides a more appropriate basis for comparison with both the case-study analytics and the FEA results.

As noted in section 3.5, the experimental campaign by Markic et al. reports increases in bearing capacity ranging from approximately 2.0 to 6.5 times the uniaxial compressive strength of concrete, depending on the reinforcement arrangement and the dimensions of the loaded area. Normalising the bearing capacity in this way enables comparison across different concrete strength classes: the normalised bearing strength is defined as the measured bearing capacity divided by the material's initial uniaxial compressive strength.

Although defined analytically within the DWSF framework, Table C1 of (Markic et al. 2022a) reports, for each specimen, the base width of the DWSF d_2 , the lateral confining stress σ_{conf} , and the maximum DWSF height $X_{E,\text{max}}$, all associated with analytically derived bearing stresses that closely match the experimental values. From these data, the corresponding distributed bearing stress σ_{xd} at distance X_E follows directly as:

$$\sigma_{xd} = \frac{d_1}{d_2} \sigma_{x0}. \quad \text{Eq. 6.1}$$

By contrast, the compressive stress in the strut σ_α , the strut inclination α , and the operative DWSF height X_E are not tabulated. These quantities can be obtained using the Python routine in Appendix B, which, when supplied with the experimental inputs, returns σ_α , α , and X_E corresponding to the state at which the optimal bearing stress is achieved.

Given the reinforcement configuration of the case study, the preferred comparators would have been specimens NC-4.5, NC-18 and NC-27 from Markic et al., as these exhibit the most similar reinforcement layouts and concrete class. However, the experimental report does not provide the specific results required for the present comparison (as outlined above), which precludes their direct use.

Instead, two specimens with broadly comparable properties were selected to define a benchmarking envelope: one with a relatively low normalised bearing capacity and one with a relatively high value. Specimen C8 was adopted as the lower bound (tested normalised bearing capacity = 3.01), and specimen C15 as the upper bound (= 6.39).

Table 6.1 summarises the parameters reported in Table 1 of the experimental paper, Table 6.2 summarises the additional quantities computed using the Python routine in Appendix B, for both specimens.

Table 6.1: Overview of experimental specimen properties reported in the experimental paper (Markic et al. 2022a)

Spec.	f_{c0} [MPa]	d_1 [mm]	d_2 [mm]	$\sigma_{\text{conf}}/f_{c0}$ [-]	σ_s/f_{c0} [-]	$X_{E,\text{max}}$ [mm]	$q_{x,u,\text{test}}/f_{c0}$ [-]	$q_{x,u,\text{model}}/f_{c1}$ [-]
C8	38.90	70	303	0.05	0.35	525	3.01	2.54
C15	51.50	40	303	0.54	0.54	525	6.09	6.39

Table 6.2: Overview of experimental specimen calculated parameters

Specimen	X_E [mm]	σ_α [MPa]	α [deg]
C8	246.06	45.87	25.33
C15	231.38	145.36	29.61

6.1.4. Eurocode 2 results

According to Eurocode 2, the design of partially loaded areas is governed by the provisions of Article 6.7 of NEN-EN 1992-1-1:2004 (Standardization (CEN) 2011). The design bearing strength on the loaded area A_{c0} may be enhanced by load spreading into a larger effective area A_{c1} , provided that the limiting conditions set out in the code are satisfied. In the context of the present case study, this implies that the normalised bearing stress σ_{x0} is governed by the code's limit of $\sqrt{3} f_{cd}$ for the loaded area. For reasons of consistency with the analytical, numerical and experimental results, which are all expressed in characteristic values rather than design values, the comparison will be made on the basis of the characteristic uniaxial compressive strength f_{ck} .

The maximum effective height of the stress distribution zone can equally be determined according to Article 6.7. Assuming an optimal stress dispersion, the code specifies that the width at the bottom of the distribution region may be taken as three times the width of the loaded area, subject to the geometric conditions illustrated in Figure 2.7. For the case study, the loaded area is defined by the thickness of the steel casing, $t_{\text{casing}} = 10$ mm. As the loading is transferred as a uniformly distributed line load on the concrete cap, the stresses are assumed to disperse in a two-dimensional plane. This implies that $b_1 = b_2$, and hence the effective height depends solely on the ratio between d_1 and d_2 . With the factor prescribed as three, the effective height becomes:

$$X_E = 3 \cdot d_1 - d_1 = 2 \cdot d_1 = 2 \cdot t_{\text{casing}} = 20 \text{ mm.} \quad \text{Eq. 6.2}$$

The Eurocode further specifies that the maximum stress within the distributed region may not exceed the uniaxial compressive strength of the concrete. Consequently, the normalised distributed bearing stress σ_{xd} is equal to unity.

The potential enhancement of concrete strength due to confinement is formally recognised in Eurocode 2, Article 3.1.9, which allows an increase in f_{cd} when lateral pressure σ_2 is present. The expression for σ_2 is provided in Volume 2 of the CEB-FIP Model Code 2010 (Structural Concrete (fib) 2012):

$$\sigma_2 = \omega_c f_{cd} \left(1 - \frac{s_c}{a_c}\right) \left(1 - \frac{s_c}{b_c}\right) \left(1 - \frac{\sum b_i^2/6}{a_c b_c}\right). \quad \text{Eq. 6.3}$$

The parameters in this formulation are defined in subsection 2.3.1, with guidance on their determination. However, application of this expression requires multiple confining reinforcement layers in order to define the spacing parameter s_c . Since the case study involves only a single reinforcement mesh, no valid value of σ_{conf} can be obtained using the Eurocode approach.

Although the lateral confining stress generated by reinforcement cannot be defined within the Eurocode framework for the present configuration, both Eurocode 2 and the CEB-FIP Model Code 2010 (Structural Concrete (fib) 2012) relate the confining action of reinforcement to the yield strength of the bars in cases where the theory is applicable. For the purpose of comparison, it is therefore assumed that the tensile stress in the reinforcement at peak bearing stress is equal to the yield strength of the reinforcement.

The inclination of the compressive strut α can be derived from the geometry of the stress dispersion. With a minimum stress-distribution height of $2t_{\text{casing}} = 20$ mm and a distribution width of $3d_1$, the lower bound of the inclination angle follows from

$$\tan \alpha \leq \frac{d_2 - d_1}{2(d_2 - d_1)} = \frac{1}{2} \Rightarrow \alpha \leq \arctan\left(\frac{1}{2}\right) = 26.57^\circ. \quad \text{Eq. 6.4}$$

Finally, the maximum compressive stress in the strut is defined by the strut-and-tie provisions of Article 6.5. According to Eurocode 2, the limiting stress in a strut without transverse tension is f_{cd} , while with transverse tension it is reduced to $0.6 \nu' f_{cd}$. For comparison with the analytical, FEA and experimental data, which are again expressed in terms of characteristic rather than design strengths, the maximum strut stress is normalised to the uniaxial compressive strength of concrete, i.e. $\sigma_\alpha = 1$.

6.2. Comparison

This section consolidates the results from all approaches in a single comparative table (see Table 6.3). To enable like-for-like comparison across methods, the following normalisations are applied:

- Quantities dependent on concrete strength are normalised by the unconfined uniaxial compressive strength f_{c0} .
- Geometric measures of the DWSF are normalised by the loaded width d_1 .
- Reinforcement-related quantities are normalised by the reinforcement yield strength f_{yk} .

The reference values used for these normalisations are listed in the first three rows of the table.

Table 6.3: Comparison of key parameters across methods

Criteria	Unit	Analytical	FEA	Experiment	Eurocode
Concrete uniaxial compressive strength, f_{c0}	[MPa]	30	30	38.9 / 51.5	30
Reinforcement yield strength, f_{yk}	[MPa]	500	500	528 / 474	500
Width of the loaded area, d_1	[mm]	10	10	70 / 40	10
Normalised bearing stress, σ_{x0}/f_{c0}	[-]	4.97	5.82	3.01 / 6.09	1.73
Effective height of the stress distribution, X_E/d_1	[-]	5.31	5.31*	3.51 / 5.78	2.00
Distributed bearing stress, σ_{xd}/f_{c0}	[-]	0.82	0.79	0.70 / 0.80	1.00
Lateral confining stress, σ_{conf}/f_{c0}	[-]	0.34	0.18	0.20 / 0.54	x
Reinforcement activation (tensile stress), σ_{reinf}/f_{yk}	[-]	1.00	0.01	1.00 / 1.00	1.00
Strut inclination, α	[°]	25.57	30.53	25.33 / 29.61	26.57
Compressive stress in strut, σ_α/f_{c0}	[-]	2.22	1.46	1.18 / 2.82	1.00

Notes: * The tabulated value 5.31 is not a direct FEA output; rather, the FEA-derived σ_{xd} values are reported at this prescribed level. x No value is given, as the Eurocode does not provide a procedure to determine this quantity.

To complement the table and highlight agreements and discrepancies at a glance, a bar chart is provided for visual comparison (see Figure 6.1) together with a figure illustrating the location of the compared parameters in the DWSF (see Figure 6.2). To accommodate all quantities within a single plot, the strut inclination α is normalised by the maximum observed value, 30.53° (from the FEA). The experimental bounds are shown as a single, two-tone bar: the lighter red segment denotes the lower bound and the darker red segment the upper bound.

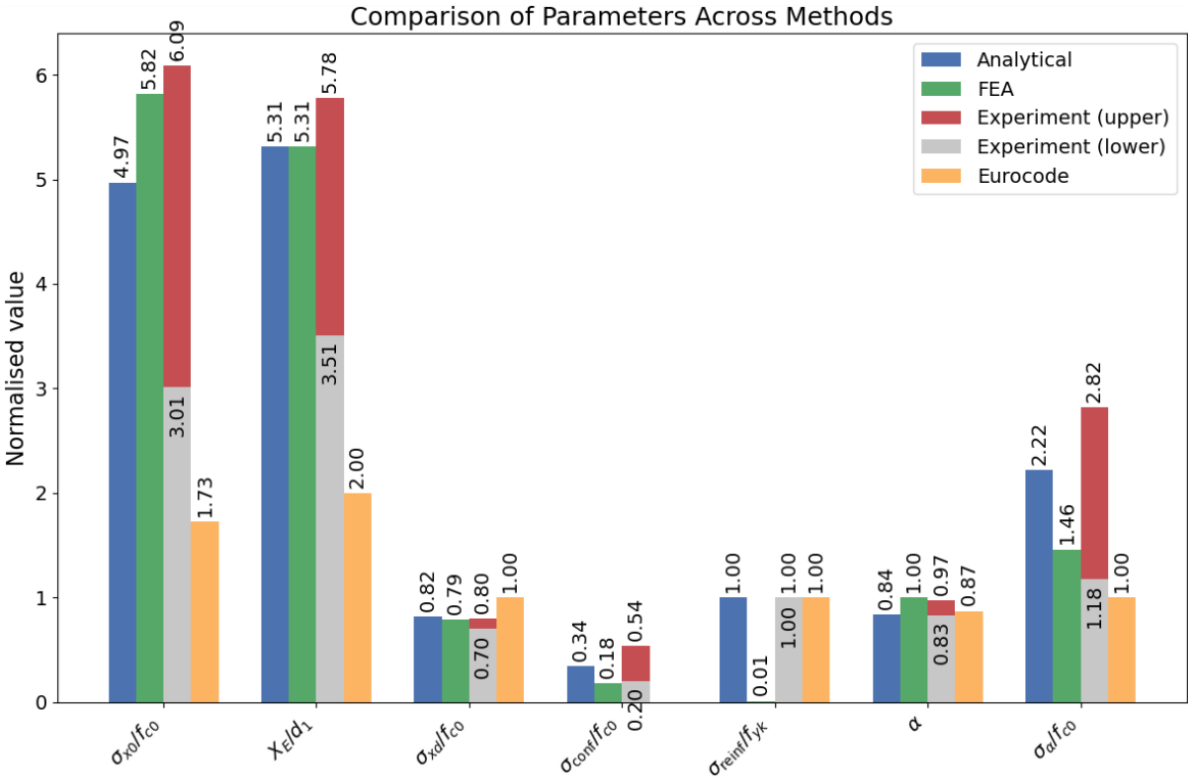


Figure 6.1: Comparison of the key parameters across methods in a bar chart

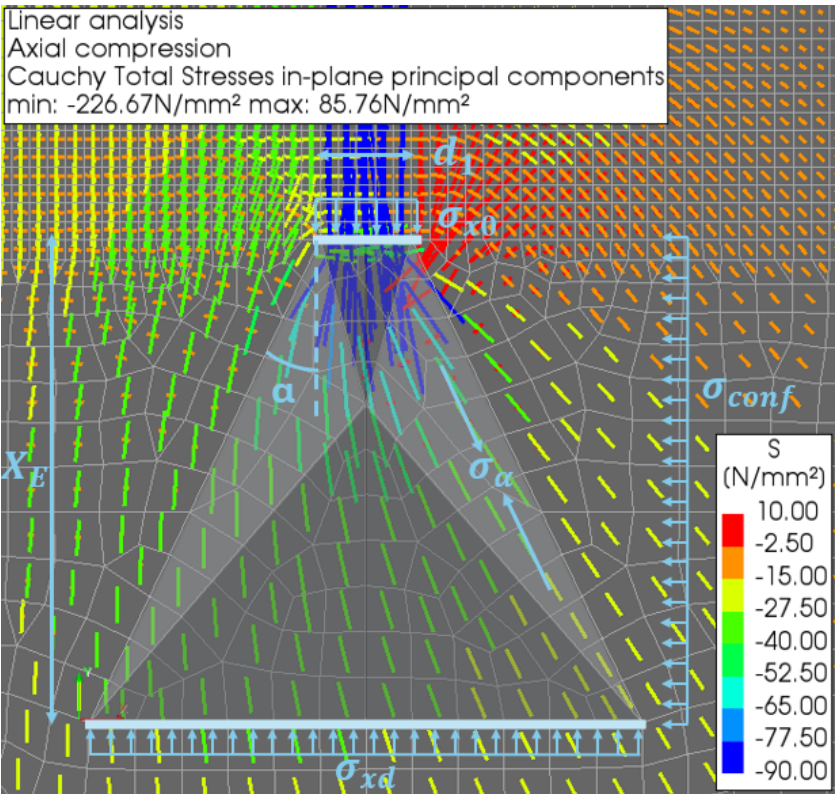


Figure 6.2: Location of the compared key parameters across methods in Figure 6.1

6.3. Implications of the results

Direct comparison with the Eurocode is inherently limited. The Eurocode results used here are an aggregation of provisions drawn from different clauses that operate largely independently. In particular, the bearing resistance (Clause 6.7 of NEN-EN 1992-1-1) is not formulated to interact with the effects of lateral confining reinforcement. In short, the current Eurocode offers no effective, unified procedure to quantify the beneficial increase in bearing strength arising from lateral confinement by a single reinforcement layer. Consequently, the Eurocode values in the bar chart reflect only those quantities obtainable under the present code framework—effectively assuming plain concrete for bearing (with splitting forces to be taken by reinforcement)—whereas the analytical model, the experiments, and the FEA explicitly include confinement effects.

The bar chart further shows that the experimental upper bound exceeds both the analytical prediction and the lower experimental bound. This is attributable to the relatively high lateral confining stress mobilised by the dense reinforcement in that specimen. Even after normalisation, and noting that the corresponding uniaxial compressive strength is $f_c = 51.5$ MPa, the normalised confinement level remains markedly larger than for the other cases ($\sigma_{\text{conf}}/f_c = 0.54$), implying an absolute lateral confining stress of about 27.8 MPa. This magnitude is substantial and helps to explain the superior bearing performance.

It is noteworthy that the analytical and FEA predictions lie closer to the experimental upper bound than to the lower bound. A plausible explanation is the relatively large-diameter confining reinforcement ($\varnothing 32$ at 125 mm centre-to-centre), which provides a comparatively high volumetric confinement ratio and stiffness. Although each bar must confine a substantial region of concrete, the large diameter increases the steel area per unit length, thereby elevating the attainable lateral confining stress.

Overall, the results confirm a clear trend: increasing lateral confinement enhances the compressive capacity of the inclined strut and expands the effective Dual-Wedge stress field (DWSF). A larger DWSF widens the region over which vertical stress is distributed, which in turn is associated with higher achievable bearing capacity. While the Eurocode provides a conservative baseline, methods that account explicitly for confinement (whether experimental, analytical, or numerical) consistently predict greater bearing resistance in partially loaded regions.

7

Discussion

This chapter critically evaluates the findings presented in the preceding chapters, with a particular focus on the practical applicability and robustness of the proposed theoretical confinement model for CFSP-pile to concrete cap connections. The purpose of this discussion is to bridge the theoretical developments and the requirements of engineering practice by examining how well the model performs under realistic conditions, and by reflecting on its assumptions, limitations, and areas where future research is warranted. In doing so, the discussion also highlights the degree to which the analytical formulations and finite element analyses are able to capture the complexities of local failure phenomena in reinforced concrete systems.

7.1. Modelling Assumptions and Idealisations

The proposed confinement model synthesises the theoretical frameworks of Mander et al. and Markic et al. To render the Mander et al. formulation applicable to the present case, where only a single reinforcement net is available to mobilise passive confinement, we adopt the following idealisation of the effectively confined region. Whereas Mander et al. bound the effectively confined area by hyperbolae (which depart from and return to the reinforcement at 45°) between orthogonal reinforcement layers, we assume that, in the absence of a second (orthogonal) net, the initial 45° inclination continues as a straight line. This linearisation permits a tractable determination of the effectively confined area, after which the Mander et al. stress–strain model can be applied and combined with the Dual–Wedge Stress Field (DWSF) of Markic et al. to predict bearing strength.

This geometric assumption has not been verified numerically for the present geometry, as the fully non-linear finite-element analyses did not satisfy convergence criteria. Whether this assumption ultimately under- or over-predicts the bearing capacity is still unknown, and the direction of the error is likely influenced by the reinforcement spacing and the amount of cover. Experimental verification is recommended to validate (or refine) the assumed confinement boundary and the resulting bearing capacity, ideally complemented by a sensitivity study on the confinement geometry and a calibrated non-linear analysis once a robust convergence strategy is available.

Another important modelling assumption concerns the use of an axisymmetric FEA model. To manage computational cost and because the educational licence of DIANA limits the allowable number of elements an axisymmetric formulation was adopted. The simplifications needed to render the physical system axisymmetric are described in subsection 5.1.1. Although subsequent checks showed no material differences in the stress–strain response between the axisymmetric and full 3D models, the geometric idealisations inevitably modify the global structural response and may, in turn, influence local quantities such as the bearing stress at the steel casing. This does not invalidate the FEA for comparative purposes; however, a small, systematic discrepancy relative to the physical system should be expected and borne in mind when interpreting the results.

It is common engineering practice to neglect composite action between the pile core and the steel casing. Accordingly, structural verification calculations typically assume no shear transfer across this

interface. In the present study a fully unbonded condition is adopted, i.e. zero friction. In the FEA model this is implemented via interface elements between the core and casing with zero shear stiffness and a very high normal stiffness ($10,000 \text{ N/mm}^3$) to preclude non-physical interpenetration; this is a standard and defensible numerical choice.

In reality, some shear transfer may occur, depending on factors such as pile diameter, concrete curing/hardening behaviour, and the loading history. Because these conditions are project-specific and cannot be quantified reliably here, a zero-bond assumption is taken as conservative: it maximises relative slip, minimises composite action, and therefore does not overstate the bearing contribution of the interface. This approach is appropriate for the present research focus, while recognising that a targeted sensitivity study on interface shear stiffness could be undertaken in future work.

The adoption of a very high normal stiffness at the core–casing interface is consistent with the working assumption that the concrete core is effectively confined by the steel casing. Under this assumption, the core remains on the linear branch of its stress–strain response throughout loading and no stiffness degradation need be invoked. In the present analysis the maximum compressive normal stress in the core is only -22.36 MPa , i.e. a small fraction of the expected capacity of optimally confined concrete; accordingly, modelling the core as linear elastic with an unchanged modulus over the full loading path is justified.

7.2. Applicability and Versatility of the Proposed Model

The practical utility of the proposed confinement model rests on its versatility, i.e. how readily it can be applied to differing geometries and reinforcement layouts. The governing cross-section in the case study places the steel casing approximately midway between two transverse bars. Because the clear distance from the casing to the confining bar is an explicit input to the modified Mander et al. formulation (and directly influences the lateral confining stress), the bar–to–casing spacing exerts a strong influence on the predicted bearing capacity. This sensitivity is beneficial from an application standpoint: the spacing is a simple, measurable parameter, and the model can therefore be applied straightforwardly to the governing cross-section.

In practice, however, the uniaxial compressive limit is commonly reached at multiple elevations along the casing rather than solely at the outer fibre at the governing section. As indicated in Figure 4.5, the interface stress exceeds the unconfined limit over a significant depth below the cap surface; hence, regions of the casing that are oblique to the transverse reinforcement also become critical. In those regions the lateral confining stress in the global x -direction ($f_{\text{eff},lx}$) is smaller than in the y -direction ($f_{\text{eff},ly}$). For a conservative assessment of bearing capacity away from the bar line, it is therefore appropriate to adopt the governing confinement as

$$f_{\text{eff}} = \min(f_{\text{eff},lx}, f_{\text{eff},ly}) \quad \text{Eq. 7.1}$$

This choice may reduce the predicted bearing capacity locally, but it is trivial to implement within the proposed framework and better reflects the directional character of confinement.

A further modelling idealisation concerns the geometry of the effectively confined region. The analytical model assumes that the circular pile generates a *rectangular* zone of effective confinement by the reinforcement (see Figure 4.5). In reality, the reaction from the pile core produces a load-spread resembling a *cone* (see Figure 2.8), raising the question of whether bars outside this cone are sufficiently activated to contribute to passive confinement. Due to time constraints this could not be verified, and it remains an open point for future work (e.g. targeted non-linear 3D simulations or testing) to quantify the degree of participation of reinforcement located outside the principal load-spread.

Finally, as discussed in Figure 5.3.6, the lateral stress induced by the pile-core reaction modifies the formation of the DWSF above the casing. Although this interaction was recognised in subsection 2.2.2, it is not currently included in the closed-form confinement model. The FEA results demonstrate that a high bearing stress on the core can bias the DWSF and, consequently, the attainable bearing capacity at the casing. To improve applicability, the analytical model should be extended to account for this superposed lateral stress field, e.g. by limiting the effective confinement region to the intersection of

the reinforcement-confined zone and the load-spread cone, and by evaluating the confinement using the local (directional) lateral stress resultant.

In summary, the method accommodates a wide range of reinforcement configurations through simple geometric inputs and a conservative directional confinement rule. Its principal limitations arise from (i) the assumed shape of the effectively confined region and (ii) the omission of lateral stresses generated by the pile core's reaction. Addressing these two aspects will further enhance the robustness and breadth of applicability of the proposed confinement model.

7.3. Sources of Uncertainty and Limitations

Since the proposed model is not fully verified by experimental results and non-linear FEA similarities there are still some uncertainties. As discussed above, one of the big questions still is if the reinforcement required for confinement is properly activated by the lateral deformation of the concrete. The insecurity factors are the distance between the steel casing and the confining reinforcement, if the distance becomes too big, will the reinforcement still be activated and how much would it then be activated. And the other uncertainty about the reinforcement is if the reinforcement in the corners of the square effective confined region are actually activated since the stress distribution above the pile is a cone and not a rectangle. To get clear if the reinforcement in the uncertain region is activated it is recommended to perform an experimental campaign in which concrete specimens with Fibre Optic Sensor on the reinforcement are applied.

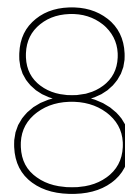
And then maybe the biggest uncertainty and also worry of the researcher of this thesis is that concrete is inherently a heterogeneous material, composed of cement paste, aggregates of varying sizes, and interfacial transition zones (ITZ) between these phases. While the analytical and finite element models in this study treat concrete as a homogeneous continuum, such an assumption may be less valid when the investigated region is highly localised, as is the case here with a failure zone of only 60.8×53.1 mm. The concrete mix design plays an important role in this respect: a lower water-cement ratio and a higher binder content generally result in a denser matrix and stronger ITZs, which enhance the uniformity of stress transfer on a local scale. Conversely, higher porosity or weaker ITZs can promote microcracking, making the actual material response deviate from the idealised homogeneous model. The maximum aggregate size further amplifies this effect. In such a small region, only a few coarse aggregates may dominate the stress distribution, depending on whether the load path traverses an aggregate, the surrounding paste, or an ITZ. Since aggregates typically exhibit higher stiffness and strength, stress concentrations tend to develop in the ITZ, which often forms the weakest link. When smaller aggregates are used, the stress field is distributed more uniformly, and the homogeneous material assumption becomes more representative. Consequently, the discrepancy between the real behaviour of the concrete and the predictions of the analytical and numerical models is strongly influenced by mix design and aggregate size, particularly when failure occurs at such a local scale.

In conclusion, the discussion has shown that the applicability of the proposed confinement model is strengthened by its reliance on simple geometric input parameters and by the conservative treatment of directional confinement. These features make the model versatile and relatively straightforward to apply to a range of reinforcement configurations. At the same time, several limitations and uncertainties remain. Key among these are the geometric assumption of a rectangular confinement zone, the neglect of lateral stresses generated by the pile core reaction, and the uncertainty surrounding the degree of activation of reinforcement positioned away from the primary load-spread.

A further concern arises from the intrinsic heterogeneity of concrete, which is not reflected in the homogeneous continuum assumptions of both the analytical and numerical models. In a highly localised failure region, the concrete mix design and aggregate size may exert a pronounced influence on the stress transfer mechanisms and ultimate capacity, leading to discrepancies between predicted and actual behaviour.

Taken together, these findings underline that while the proposed model provides a useful and conservative framework for assessing confinement in CFSP-pile to cap connections, its predictive accuracy remains contingent on assumptions that require experimental validation. Future research should therefore focus on refining the confinement geometry, incorporating the influence of pile-core induced stresses, and validating the model against targeted experimental campaigns. Such efforts will enhance

confidence in the model's reliability and extend its applicability to a broader range of structural configurations.



Conclusion and Recommendations

This chapter synthesises the principal findings of the research, providing clear, evidence-based answers grounded in the analytical, numerical and (where applicable) experimental results. On this basis, the main research question is then resolved.

All conclusions are drawn under the assumption of full activation of the confining reinforcement. For complete validation of the proposed model, this assumption should be verified experimentally. The chapter closes with recommendations for further work, identifying opportunities to extend and refine the present findings.

8.1. Conclusion

The conclusion is structured around the sub-questions introduced in section 1.5. By addressing these in sequence, the final answer to the main research question — *“What is the impact of confinement on the structural performance of CFSP-pile to concrete element connections in the absence of force transfer provisions, such as dowels or rings?”* — is established.

8.1.1. Answers to the Sub-Research Questions

Sub-question 1: What are the underlying mechanisms of confinement in structural elements?

The literature review demonstrated that confinement enhances the compressive behaviour of concrete by mobilising lateral stresses that delay cracking and increase ductility. Confinement can be passive, provided by reinforcement or surrounding material, or active, arising from external forces inducing lateral stress. The key mechanisms identified include the restriction of lateral strains, the activation of passive confining reinforcement, and the beneficial effects of adjacent unloaded concrete. Together these mechanisms explain why confined concrete exhibits increased strength and improved post-peak behaviour compared to unconfined material.

Sub-question 2: Which structural components contribute to the development of lateral confining stress in CFSP-pile to concrete element connections?

Application of the theoretical insights to the case study confirmed that the lower reinforcement net in the concrete cap contribute to confinement. The steel casing of the pile, due to its high stiffness, also governs the stress distribution at the pile–cap interface. Analytical schematisation and supporting Python calculations indicated that these components mobilise lateral confinement that enhances bearing capacity. The outcome is a connection in which the concrete directly above the casing benefits from both passive and geometric confinement.

Sub-question 3: What is the most comprehensive approach for modelling confinement in CFSP-pile to concrete connections?

A fully non-linear finite-element analysis (FEA) remains the most comprehensive means of modelling concrete confinement. Where convergence cannot be achieved, a quasi-non-linear strategy (i.e. a

nominally linear analysis augmented by stress-dependent reductions of the concrete Young's modulus in high-stress regions) offers a practical alternative. In this study that approach was benchmarked against experimental data; mesh-refinement and sensitivity studies confirmed that the chosen discretisation and material parameters capture the vertical stress–strain response with good fidelity.

The principal limitation of the quasi-non-linear approach is its treatment of lateral deformation. Because cracking, dilation and compression-softening are not represented explicitly and a single, constant Poisson's ratio was used throughout the model and loading history, the analysis under-activates the reinforcement and thereby underestimates passive confinement effects. This explains the otherwise favourable agreement in the vertical response: the calibrated reduction $E(\sigma)$ is grounded in the verified confined-concrete stress–strain model of Mander et al., so vertical stiffness and bearing stress are reproduced well, whereas lateral quantities (e.g. confining stress and bar stresses) are underestimated. To improve lateral realism within a quasi-non-linear framework, one could introduce a stress- or damage-dependent Poisson's ratio $\nu(\sigma)$ that increases with confinement/damage.

In conclusion, when a fully non-linear FEA is infeasible due to singularities or severe stress concentrations, the quasi-non-linear approach with $E(\sigma)$ reduction provides a robust second-best option for predicting vertical bearing response. Augmenting this with a mechanism for lateral dilation via $\nu(\sigma)$ would better capture reinforcement activation and the resulting passive confinement, yielding a more faithful representation of the stress fields in confined regions.

Sub-question 4: What are the effects of confinement on structural performance according to the finite element results of the test setup?

The FEA results demonstrate that confinement significantly improves the structural performance of the connection. The confined concrete sustains higher bearing stresses ($\sigma_{x0} = 5 \cdot f_{c0}$), exhibits reduced localisation of crushing, and develops a wider stress-distribution zone. The dual-wedge stress field (DWSF) is clearly discernible in the numerical output, and the analytical and numerical predictions lie within the range of the experimental results reported by Markić et al. This corroborates the analytical finding that confinement increases the effective width and height of the stress-transfer region, translating into greater load-transfer capacity at the pile–cap interface and improved ductility of the connection.

Sub-question 5: How do the theoretical model and FEA results compare with existing literature and Eurocode guidelines?

Comparisons with the experimental campaign of Markić et al. and with Eurocode 2 reveal both agreements and divergences. The analytically and numerically predicted DWSF dimensions and vertical stress fields align closely with the experimental upper bound. By contrast, the FEA under-represents lateral confinement: reinforcement activation and the resulting confining stresses are modest, as discussed in the conclusion to Sub-question 3, yielding lower lateral effects than observed experimentally. Aside from this lateral shortfall, the agreement in trends across the analytical, numerical and experimental results supports the validity of the analytical treatment of confinement. Eurocode 2, which does not explicitly account for lateral confinement in partially loaded areas, systematically underestimates the attainable bearing stress, underscoring the conservatism of current provisions and the added value of approaches that incorporate confinement mechanisms.

8.1.2. Answer to the Main Research Question

Bringing together the findings from the theoretical framework, analytical models, numerical simulations, and comparative analyses, it can be concluded that confinement exerts a decisive and beneficial influence on the structural performance of CFSP-pile to concrete element connections in the absence of dedicated force transfer provisions such as dowels or rings.

The results of the literature review established that confinement fundamentally enhances the compressive behaviour of concrete by restricting lateral strains and mobilising passive confinement through reinforcement and surrounding concrete. Applied to the CFSP-to-cap connection, the study demonstrated that both passive and geometric confinement increase the load-carrying capacity of the concrete directly above the casing and improve the ductility of the connection. However, the study was unable to demonstrate that the lower reinforcement net contributes to confinement, leaving it uncertain whether this reinforcement layer has any influence on the bearing capacity of the concrete at the tip of the steel casing.

The analytical formulations, particularly the modified Mander's model and the Dual-Wedge Stress Field concept of Markić et al., confirmed that confinement leads to higher effective compressive strength and a larger distribution region for stresses. The quasi-non-linear finite element simulations, despite certain limitations in reproducing lateral dilation, validated these findings by showing that confinement raises bearing stress capacity, mitigates crushing localisation, and activates a stress field consistent with experimental observations. Comparison across methods further revealed that both the analytical and numerical approaches reproduce the upper bound of the experimental evidence, while Eurocode 2 systematically underestimates capacity due to its omission of confinement effects.

Overall, the thesis demonstrates that, in the absence of additional provisions for direct force transfer, confinement mechanisms inherent to the connection substantially enhance structural performance in case confinement is activated. The mobilised confinement results in increased bearing strength, improved ductility, and a more favourable distribution of stresses within the connection. Consequently, properly detailed confinement at the pile–cap interface can in practice reduce or even obviate the need for costly supplementary force transfer measures, provided that the confinement effects are reliably accounted for in design. This conclusion underscores both the structural significance of confinement and the limitations of current design codes, highlighting the potential benefits of adopting confinement-based design approaches in engineering practice.

8.2. Relevance for the 'Oostertoegang' case study

For the governing load combination on the pile head, the calculations described in section 4.3 indicate a maximum bearing stress of 134 MPa at the interface between the steel casing and the concrete cap. In contrast, according to current Eurocode provisions outlined in subsection 2.2.2, the design value of the maximum allowable bearing stress is limited to 34.64 MPa. This comparison highlights a substantial exceedance of the codified bearing resistance, which, under conventional design assumptions, would imply crushing of the concrete above the steel casing.

Although this thesis cannot provide full experimental verification, the results strongly suggest that the reinforcement embedded in the concrete cap contributes to an enhanced bearing capacity through passive confinement activated by the pile's reaction force. The analytical framework developed in this thesis predicts an increased characteristic bearing capacity of up to 149.05 MPa. Applying the Eurocode partial safety factor for concrete of 1.5, this corresponds to a design resistance of 99.36 MPa.

From these findings, it may be concluded that although confinement effects provide a substantial increase in bearing capacity, this enhancement is still insufficient to demonstrate theoretical safety of the connection in the case study. The limitation arises primarily from the exceptionally high maximum stress demand, rather than from a deficiency in the enhanced capacity itself. Consequently, it is of particular importance to minimise bending moments at pile heads, as these tend to concentrate peak stresses at the outer fibres of the steel casing. Reducing these moments would promote a more uniform stress distribution along the casing, as would occur under predominantly axial reaction forces, thereby reducing the risk of localised crushing and improving the overall reliability of the connection.

8.3. Recommendations for Further Research

While this thesis provides a comprehensive analysis of confinement effects in CFSP-pile to concrete element connections, several avenues remain open for further investigation. These recommendations are intended to extend the current knowledge base and to refine the applicability of confinement-based design approaches in practice.

First, experimental research is required to validate the analytical and numerical findings presented in this thesis. The conclusions rely on theoretical modelling and finite element simulations that have been benchmarked against existing experimental data, but no direct physical testing of CFSP-to-cap connections under representative loading was performed within this research. Full-scale laboratory tests, in which the degree of confinement activation can be directly measured, would be invaluable to confirm the accuracy of the dual-wedge stress field and modified Mander's formulations, and to assess the reliability of the finite element modelling strategies under realistic boundary conditions.

Second, further development of finite element modelling strategies should be pursued to improve the

representation of lateral dilation and passive confinement activation. The quasi-non-linear approach adopted here successfully captured global stress distributions but showed limitations in reproducing local confinement phenomena. Incorporating advanced constitutive models for confined concrete, or adopting fully non-linear analyses with damage-plasticity formulations, could enhance the predictive capability of FEA for such connections. Parallel improvements in meshing techniques and contact formulations may also lead to more accurate stress-transfer characterisation.

Third, parametric studies on geometric and material variations would help to systematically identify the boundaries of confinement effectiveness. Variables such as pile casing thickness, reinforcement configuration, concrete strength class, and cap depth could be altered to establish thresholds at which confinement ceases to provide sufficient enhancement. These studies would not only broaden the understanding of confinement mechanics but also support the development of simplified design guidelines tailored to CFSP-to-cap connections.

A specific research need concerns the role of passive confinement in mobilising tensile stresses within the reinforcement. The activation of passive confinement may lead to locally increased tensile demands in the reinforcement, potentially influencing overall structural capacity or requiring reconsideration of reinforcement diameters. Furthermore, it remains unclear whether bending moments in the concrete cap contribute to a pre-stressing effect on the reinforcement, thereby enhancing the mobilisation of confinement. Investigating these mechanisms experimentally and numerically could provide valuable guidance for reinforcement detailing in pile-to-cap interfaces.

Another important aspect is the contribution of unloaded concrete surrounding the loaded region. While this thesis identified geometric confinement as a beneficial factor, the quantitative effect of adjacent unloaded concrete on confinement remains insufficiently defined. Dedicated studies are needed to determine how surrounding concrete restrains lateral expansion and how its stiffness and geometry influence the stress distribution in the loaded zone.

In addition to strength enhancement, the potential increase in ductility due to confinement warrants further study. Confinement is known to delay the onset of crushing and extend the deformation capacity of concrete, yet this effect has not been systematically quantified for CFSP-to-cap connections. The quasi-non-linear FEA approach employed in this thesis replicated only the ascending branch of the stress-strain curve, leaving the post-peak behaviour unrevealed. Understanding how confinement alters the ductility of the interface could significantly affect serviceability design considerations and improve resilience against extreme loading scenarios.

Fourth, integration of confinement effects into existing design codes should be explored. Eurocode 2, in its current form, does not explicitly incorporate confinement by a single net in partially loaded areas and therefore likely underestimates bearing capacity. Further research should focus on developing code-conformant design expressions that account for confinement, ensuring that engineers can reliably and safely exploit the beneficial effects identified in this thesis without resorting to costly additional provisions.

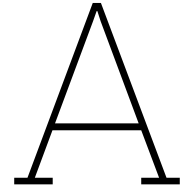
Finally, long-term performance under cyclic or fatigue loading, as well as environmental influences such as corrosion of the steel casing or degradation of concrete, remain largely unaddressed. Since pile-to-cap connections are critical structural interfaces in marine and infrastructural applications, research into durability and time-dependent behaviour of confined regions would provide essential insights for service-life predictions and maintenance strategies.

In summary, future research should combine experimental validation, advanced numerical modelling, parametric exploration, and code development to fully establish the role of confinement in CFSP-pile to cap connections. Particular attention should be devoted to reinforcement tensile stresses during confinement activation, the influence of bending moments on passive confinement, the confinement effect of unloaded surrounding concrete, and the quantification of ductility improvements. Addressing these areas will not only enhance the scientific understanding of confinement but also enable its safe and efficient application in engineering practice.

References

- Adebar, P. and Z. Zhou (1993). "Bearing Strength of Compressive Struts Confined by Plain Concrete". In: *ACI Structural Journal* 90.5, pp. 534–541.
- Ami, M. and V.I. Patel (2023). "Numerical investigation and design of P-M interaction capacity of CFRP-jacketed hexagonal CFST short beam-columns". In: *Elsevier*, p. 2.
- Betoniek (2024). *Betoniek Standaard 17/19: Beton, een rekbaar begrip*. URL: <https://www.betoniek.nl//artikelen/betoniek-standaard-17/19-beton-een-rekbaar-begrip> (visited on 06/17/2025).
- DIANA, TNO (2015a). *20.2.7 Compressive Behaviour*. URL: <https://manuals.dianafea.com/d100/MatLib/node328.html> (visited on 05/21/2025).
- (2015b). *6.2.3 Compressive Behaviour*. URL: <https://manuals.dianafea.com/d100/MatLib/node87.html> (visited on 04/09/2025).
- (2017a). *16.4 Axisymmetric Models*. URL: <https://manuals.dianafea.com/d102/ElmLib/node529.html> (visited on 04/03/2025).
- (2017b). *7.5.4 CQ16A - quadrilateral, 8 nodes*. URL: <https://manuals.dianafea.com/d100/ElmLib/node183.html> (visited on 04/03/2025).
- Filaj, E., A. Seranaj, and E. Leka (2016). "Confined concrete behavior influencing factors". In: *International Research Journal of Engineering and Technology (IRJET)* 03.07, p. 43.
- Leskela, M. V. and S. Eronen (2005). "CONCRETE FILLED CIRCULAR STEEL TUBES AS FOUNDATION PILES". In: *University of OULU, FINLAND*, p. 1.
- Liu, X. et al. (2023). "Theoretical analysis of dynamic performance of concrete-filled steel tube pile under vertical load". In: *Elsevier*, p. 1.
- Mander, J.B., M.J.N. Priestley, and R. Park (1988a). "Observed stress strain-model for confined concrete". In: *Journal of Structural Engineering* 114.08, pp. 1827–1849.
- (1988b). "Theoretical stress strain-model for confined concrete". In: *Journal of Structural Engineering* 114.08, pp. 1804–1826.
- Markic, T., W. Kaufmann, and A. Amin (2018). "Stress field solution for strip loaded reinforced concrete blocks". In: *Elsevier*, p. 3.
- Markic, T., F. Morger, and W. Kaufmann (2022a). "Partially loaded areas in reinforced concrete: Experimental campaign and model validation". In: *Elsevier*, pp. 1–28.
- (2022b). "Partially loaded areas in reinforced concrete: Mechanical modelling". In: *Elsevier*, p. 1.
- Rodenhuis, A. (2023). *DO berekeningsrapport onderbouw pijlers brug 1 t/m 4*.
- Standardization (CEN), European Committee for (2011). *NEN-EN 1992-1-1: Eurocode 2: Design of Concrete Structures – Part 1-1: General Rules and Rules for Buildings*. Standard.

- Standardization (CEN), European Committee for (2018). *NEN-EN 1992-4: Eurocode 2: Design of Concrete Structures – Part 4: Design of fastenings for use in concrete*. Standard.
- Structural Concrete (fib), International Federation for (2012). *Model Code 2010 Final draft Volume 2*. Standard.
- Tabsh, S.W. (2007). “Stress-Strain Model for High-Strength Concrete Confined by Welded Wire Fabric”. In: *JOURNAL OF MATERIALS IN CIVIL ENGINEERING (ASCE)* 19.04, p. 287.
- Tan, C., J. Xu, and R. Aboutaha (2019). “Extension of bridge cap beams with CFRP composites: experimental investigation”. In: *IOP Conference Series: Earth and Environmental Science*, p. 1.
- Wang, X., F. Fan, and J. Lai (2021). “Strength behavior of circular concrete-filled steel tube stub columns under axial compression: A review”. In: *Elsevier*, p. 1.



Python Scripts for Analytical Bearing Stress Calculations

This appendix presents the complete set of Python scripts developed to perform the analytical determination of the maximum bearing stress in the concrete directly above the steel casing, in accordance with the modified theoretical models introduced earlier in this thesis. Each script implements the relevant equations and iterative procedures required to evaluate the enhanced bearing capacity of partially loaded concrete regions under the specified load combinations.

A.1. Python Script Stress Distribution at Pile to Cap Interface

```
1 import numpy as np
2 from scipy.optimize import fsolve
3 import matplotlib.pyplot as plt
4
5 # Input Parameters
6 # Geometry
7 d_concrete = 488 # diameter of concrete core (mm)
8 r_concrete = d_concrete / 2 # radius of concrete core (mm)
9 A_concrete = np.pi * (r_concrete ** 2) # Area of the concrete core
10 t_steel = 10 # thickness of steel casing (mm)
11 d_outer = d_concrete + 2 * t_steel # outer diameter (mm)
12 r_outer = d_outer / 2 # outer radius (mm)
13
14 # Reinforcement
15 n_bars = 8 # number of reinforcement bars
16 d_bar = 32 # diameter of each reinforcement bar (mm)
17 A_bar = np.pi * (d_bar / 2) ** 2 # area of one reinforcement bar (mm^2)
18 A_reinforcement = n_bars * A_bar # total area of reinforcement (mm^2)
19 r_bar = 162 # distance of reinforcement from center (mm)
20
21 # Steel casing area divided into compression and tension zones
22 A_steel_casing = np.pi * ((d_outer / 2) ** 2 - (d_concrete / 2) ** 2) # total steel casing
    area (mm^2)
23
24 # Material properties
25 E_concrete = 20e3 # modulus of elasticity of concrete (MPa)
26 E_steel = 200e3 # modulus of elasticity of steel (MPa)
27 E_reinforcement = 210e3 # modulus of elasticity of reinforcement steel (MPa)
28 concrete_compressive_strength = 30 # MPa, design concrete compressive strength
29 steel_yield_strength = 500 # MPa, yielding limit for steel
30
31 # Applied loads
32 M = 258 * 1e6 # moment (N·mm) (always positive)
33 N = -2061 * 1e3 # normal force (N) (negative in compression)
34
35 # Function to calculate the equivalent modulus of elasticity
```

```

36 def calculate_equivalent_modulus(E_concrete, E_steel, E_reinforcement, A_concrete,
37     A_steel_casing, A_reinforcement):
38     E_equivalent = (E_concrete * A_concrete + E_steel * A_steel_casing + E_reinforcement *
39         A_reinforcement) / (A_concrete + A_steel_casing + A_reinforcement)
40     return E_equivalent
41
42 E_equivalent = calculate_equivalent_modulus(E_concrete, E_steel, E_reinforcement, A_concrete,
43     A_steel_casing, A_reinforcement)
44 strain_N = N / (E_equivalent * 0.25 * np.pi * d_outer**2)
45 print(f"Strain by normal force = {strain_N:.6f}")
46 print(E_equivalent)
47
48 # Stress in elements by Normal force
49 if strain_N < 0:
50     stress_conc_N = max(strain_N * E_concrete, -concrete_compressive_strength)
51     stress_segment_N = max(strain_N * E_steel, -steel_yield_strength)
52     stress_rebar_N = max(strain_N * E_reinforcement, -steel_yield_strength)
53 else:
54     stress_conc_N = 0
55     stress_segment_N = min(strain_N * E_steel, steel_yield_strength)
56     stress_rebar_N = min(strain_N * E_reinforcement, steel_yield_strength)
57
58 def calculate_forces(strain_bottom, strain_top):
59
60     # Split strain due to normal force and bending moment
61     strain_bottom_M = strain_bottom - strain_N
62     strain_top_M = strain_top - strain_N
63
64     # Initialize force and moment summations
65     total_force = 0
66     total_moment = 0
67
68     # Storage arrays for stress- and strain-diagrams
69     strain_distribution = [[d_outer, strain_top], [0, strain_bottom]]
70     rebar_strain_distribution = []
71     concrete_stress_distribution = []
72     casing_stress_distribution = []
73     rebar_stress_distribution = []
74
75     if ((strain_bottom_M + strain_top_M == 0) or (M == 0)):
76         na = r_outer # Neutrale as ligt halverwege
77     else:
78         na = (strain_bottom_M / (strain_bottom_M + abs(strain_top_M))) * d_outer
79
80     # Make sure to stay within the physical boundaries
81     na = np.clip(na, 0, d_outer)
82
83     print(f"neutral axis: {na:.2f}")
84
85     # Concrete contribution (only compression zone above neutral axis)
86     concrete_layers = 100 # Number of concrete layers (discrete strips)
87     strip_height = (d_concrete + t_steel - max(na, t_steel)) / concrete_layers # Height of
88         each concrete strip
89
90     for i in range(concrete_layers):
91         y_conc = max(na, t_steel) + i * strip_height + 0.5 * strip_height # Centre position
92             of the strip
93
94         # Calculate the width of the concrete core at height y
95         b_y = 2 * np.sqrt(r_concrete**2 - (y_conc - r_outer)**2) # Width at height y
96
97         # Calculate strain in the strip
98         strain_conc = strain_bottom_M + ((strain_top_M - strain_bottom_M) / d_outer) * y_conc
99         # Strain in the strip (positive in compression)
100         if strain_conc < 0: # Only consider compression zone (strain < 0)
101             stress_conc_M = max((strain_conc + strain_N) * E_concrete, -
102                 concrete_compressive_strength) - max(strain_N * E_concrete, -
103                 concrete_compressive_strength)
104         else:
105             stress_conc_M = 0

```

```

99     force = stress_conc_M * strip_height * b_y # Correct force in this strip
100     total_force += force
101     if strain_top == strain_bottom:
102         total_moment += 0
103     else:
104         total_moment += abs(force) * abs(y_conc - na) # Moment contribution from this
105         strip
106
107     # Save concrete stresses for stress diagram
108     concrete_stress_distribution.append((y_conc, stress_conc_M + stress_conc_N ))
109
110 # Steel casing contribution (split into small segments)
111 steel_segments = 100 # Number of segments around the steel casing circumference
112 segment_angle = 2 * np.pi / steel_segments # Angle covered by each segment
113
114 for i in range(steel_segments):
115     angle = i * segment_angle # Current angle for the segment
116     y_segment = ((d_outer + d_concrete) / (2 * 2)) * np.sin(angle) + (d_outer / 2) #
117     # Vertical position of the segment from bottom
118     # Calculate the strain in the segment
119     strain_segment = strain_bottom_M + ((strain_top_M - strain_bottom_M) / d_outer) *
120     y_segment # Strain in the segment (negative in compression)
121
122     # Determine the stress in the segment based on the strain
123     if strain_segment < 0: # Compression zone
124         stress_segment_M = max((strain_segment + strain_N) * E_steel, -
125         steel_yield_strength) - max(strain_N * E_steel, -steel_yield_strength)
126     else: # Tension zone
127         stress_segment_M = min(strain_segment * E_steel, steel_yield_strength)
128
129     # Calculate the force in the segment
130     segment_area = 0.25 * np.pi * (d_outer**2 - d_concrete**2) / steel_segments # Area
131     of the steel segment
132     force_segment = stress_segment_M * segment_area
133
134     # Add the force and moment contributions of this segment
135     total_force += force_segment
136     if strain_top == strain_bottom:
137         total_moment += 0
138     else:
139         total_moment += abs(force_segment) * abs(y_segment - na) # Moment arm is the
140         vertical position
141
142     # Save casing stresses for stress diagram
143     casing_stress_distribution.append((y_segment, stress_segment_M + stress_segment_N))
144
145 # Reinforcement contribution (assume elastic-perfectly plastic)
146 for i in range(n_bars):
147     # Calculate the angle for each rebar
148     angle_rebar = i * (2 * np.pi / n_bars)
149
150     # Determine the position of the rebar (y-coordinate)
151     y_rebar = r_bar * np.sin(angle_rebar) + (d_outer / 2) # Vertical position of the
152     rebar from bottom
153
154     # Calculate the strain in the rebar based on the y-position of the rebar and neutral
155     axis
156     strain_rebar = strain_bottom_M + ((strain_top_M - strain_bottom_M) / d_outer) *
157     y_rebar
158
159     # Calculate the stress in the rebar based on the strain
160     if strain_rebar < 0: # Compression zone
161         stress_rebar_M = max((strain_rebar + strain_N) * E_reinforcement, -
162         steel_yield_strength) - max(strain_N * E_reinforcement, -steel_yield_strength)
163     else: # Tension zone
164         stress_rebar_M = min(strain_rebar * E_reinforcement, steel_yield_strength)
165
166     # Calculate the force in the rebar

```

```

159     force_rebar = stress_rebar_M * A_bar
160
161     # Add the force and moment contributions of this rebar
162     total_force += force_rebar
163     if strain_top == strain_bottom:
164         total_moment += 0
165     else:
166         total_moment += abs(force_rebar) * abs(y_rebar - na) # Moment arm is the y-
            position of the rebar
167
168     # Save rebar stresses and strains for stress- and strain-diagram
169     rebar_stress_distribution.append((y_rebar, stress_rebar_M + stress_rebar_N))
170     rebar_strain_distribution.append((y_rebar, strain_rebar + strain_N))
171
172     if M == 0:
173         total_force = total_moment = 0
174
175     return total_force, total_moment, np.array(strain_distribution), np.array(
        rebar_strain_distribution), np.array(concrete_stress_distribution), np.array(
        casing_stress_distribution), np.array(rebar_stress_distribution)
176
177 def iterate_strains_for_moment(target_moment, target_force):
178     """
179     Iteratively solve for the strain_bottom and strain_top values until both the internal
        moment and the internal force are in equilibrium with the specified values.
180
181     Parameters:
182     target_moment: External moment to be matched (N·mm)
183     target_force: External force to be matched (N)
184
185     Returns:
186     strain_bottom: Resolved stretch at the bottom of the cross-section
187     strain_top: Resolved stretch at the top of the cross-section
188     """
189     # If M > 0 we want to guarantee that strain_bottom > strain_top.
190     # We then reparameterize with:
191     # s = (strain_bottom + strain_top) / 2
192     # delta = (strain_bottom - strain_top) / 2, met delta > 0.
193     if M > 0:
194         def equilibrium_transformed(vars):
195             s, delta = vars
196             # Force delta to be positive by taking the absolute value
197             strain_bottom = s + abs(delta)
198             strain_top = s - abs(delta)
199             total_force, total_moment, *_ = calculate_forces(strain_bottom, strain_top)
200             return [total_force - target_force, total_moment - target_moment]
201
202         # Choose an initial guess for s and delta (make sure delta is positive)
203         initial_guess = [0, 1e-5]
204         s, delta = fsolve(equilibrium_transformed, initial_guess)
205         strain_bottom = s + abs(delta)
206         strain_top = s - abs(delta)
207     else:
208         # If M == 0 you can use the original parameterization.
209         def equilibrium(strains):
210             strain_bottom, strain_top = strains
211             total_force, total_moment, *_ = calculate_forces(strain_bottom, strain_top)
212             return [total_force - target_force, total_moment - target_moment]
213         initial_guess = [strain_N, strain_N]
214         strain_bottom, strain_top = fsolve(equilibrium, initial_guess)
215
216     return strain_bottom, strain_top
217
218 # External moment and force
219 target_moment = M # N·mm
220 target_force = 0 # N
221
222 # Iteratively solving for strains
223 strain_bottom, strain_top, *_ = iterate_strains_for_moment(target_moment, target_force)
224
225 # findings

```

```

226 total_force, total_moment, strain_distribution, rebar_strain_distribution,
    concrete_stress_distribution, casing_stress_distribution, rebar_stress_distribution =
    calculate_forces(strain_bottom, strain_top)
227
228 # Height of the neutral axis
229 if strain_bottom < 0 and strain_top < 0:
230     neutral_axis = 0
231     concrete_stress_distribution = np.insert(concrete_stress_distribution, 0, [t_steel,
    strain_N * E_concrete], axis=0)
232 else:
233     neutral_axis = (strain_bottom / (strain_bottom + abs(strain_top))) * d_outer
234     neutral_axis = np.clip(neutral_axis, 0, d_outer)
235     concrete_stress_distribution = np.insert(concrete_stress_distribution, 0, [neutral_axis,
    0], axis=0)
236
237 # Show results
238 print(f"Strain at bottom: {strain_bottom:.12f}")
239 print(f"Strain at top: {strain_top:.12f}")
240 print(f"Height of the neutral axis is: {neutral_axis:.2f}mm")
241
242 total_force, total_moment, *_ = calculate_forces(strain_bottom, strain_top)
243 print(f"total_force: {total_force/1e3:.2f} kN and total_moment: {total_moment/1e6:.2f} kNm")
244
245 # Plotting the cross-section
246 fig, ax = plt.subplots(figsize=(6, 6))
247
248 # Outer section
249 outer_circle = plt.Circle((r_outer, r_outer), r_outer, color='blue', fill=False, linewidth=2,
    label='Outer Section')
250 ax.add_artist(outer_circle)
251
252 # Concrete core
253 concrete_circle = plt.Circle((r_outer, r_outer), r_concrete, color='red', fill=False,
    linewidth=2, label='Concrete Core')
254 ax.add_artist(concrete_circle)
255
256 # Reinforcement bars
257 angles = np.linspace(0, 2 * np.pi, n_bars, endpoint=False) # Angles for bar positions
258 for angle in angles:
259     x_bar = r_bar * np.cos(angle) + r_outer
260     y_bar = r_bar * np.sin(angle) + r_outer
261     ax.plot(x_bar, y_bar, 'ko', markersize=8) # Black circles for reinforcement bars
262
263 # Neutral axis
264 ax.axhline(y=neutral_axis, color='green', linestyle='--', linewidth=2, label='Neutral Axis')
265
266 # Formatting the plot
267 ax.set_xlim([r_outer - 50, r_outer + 50])
268 ax.set_ylim([-50, d_outer + 50])
269 ax.set_aspect('equal', adjustable='datalim')
270 ax.set_xlabel('Width (mm)')
271 ax.set_ylabel('Height (mm)')
272 ax.set_title('Cross Section of the Pile with Reinforcement Bars and Neutral Axis')
273 ax.legend()
274
275 # Show the plot
276 plt.grid(True)
277 plt.show()
278
279 print(f"Height of the neutral axis: {neutral_axis:.2f}mm")
280
281 # Function to plot both strain and stress distributions with labels for max and min values
282 def plot_strain_and_stress_with_labels(strain_distribution, rebar_strain_distribution,
    concrete_stress_distribution, casing_stress_distribution, rebar_stress_distribution, na):
283     """
284     Plots both the strain and stress distributions in separate figures, with labels for the
    max and min values of strain and stress.
285     """
286
287     # Extract height and strain values from the arrays

```

```

288 heights_section = strain_distribution[:, 0]
289 strains_section = strain_distribution[:, 1]
290
291 heights_rebar_strain = rebar_strain_distribution[:, 0]
292 strains_rebar = rebar_strain_distribution[:, 1]
293
294 heights_concrete_stress = concrete_stress_distribution[:, 0]
295 stresses_concrete = concrete_stress_distribution[:, 1]
296
297 heights_casing_stress = casing_stress_distribution[:, 0]
298 stresses_casing = casing_stress_distribution[:, 1]
299
300 heights_rebar_stress = rebar_stress_distribution[:, 0]
301 stresses_rebar = rebar_stress_distribution[:, 1]
302
303 # Find max and min values for strain and stress in concrete and casing
304 max_strain_concrete = np.max(strains_section)
305 min_strain_concrete = np.min(strains_section)
306 max_strain_concrete_height = heights_section[np.argmax(strains_section)]
307 min_strain_concrete_height = heights_section[np.argmin(strains_section)]
308
309 min_stress_concrete = np.min(stresses_concrete)
310 min_stress_concrete_height = heights_concrete_stress[np.argmin(stresses_concrete)]
311
312 max_stress_casing = np.max(stresses_casing)
313 min_stress_casing = np.min(stresses_casing)
314 max_stress_casing_height = heights_casing_stress[np.argmax(stresses_casing)]
315 min_stress_casing_height = heights_casing_stress[np.argmin(stresses_casing)]
316
317 # Create two subplots: one for strain and one for stress
318 fig, ax = plt.subplots(1, 2, figsize=(14, 8))
319
320 # Plot the strain distribution on the left subplot
321 ax[0].plot(strains_section, heights_section, label='Strain_Distribution_(Cross-section)',
322           color='purple')
323
324 # Plot rebar strain distribution as horizontal lines
325 for i, height in enumerate(heights_rebar_strain):
326     ax[0].hlines(height, xmin=0, xmax=strains_rebar[i], colors='g', label='Rebar_Strain'
327                 if i == 0 else "")
328     ax[0].text(strains_rebar[i], height, f'{strains_rebar[i]:.5f}', va='top')
329
330 # Add labels for maximum and minimum strain in the concrete
331 ax[0].text(max_strain_concrete, max_strain_concrete_height, f'Max: {max_strain_concrete
332               :.5f}', va='top', color='red')
333 ax[0].text(min_strain_concrete, min_strain_concrete_height, f'Min: {min_strain_concrete
334               :.5f}', va='bottom', color='blue')
335
336 # Add solid vertical line at x=0 for the strain plot
337 ax[0].axvline(x=0, color='black', linestyle='-')
338
339 # Add labels and grid for the strain plot
340 ax[0].set_title('Strain_Distribution')
341 ax[0].set_xlabel('Strain')
342 ax[0].set_ylabel('Height_(mm)')
343 ax[0].axhline(y=na, color='r', linestyle='--', label='Neutral_Axis')
344 ax[0].grid(True)
345 ax[0].legend()
346
347 # Mirror the x-axis: negative values now appear on the right
348 ax[0].invert_xaxis()
349
350 # Plot the stress distribution on the right subplot
351 ax[1].plot(stresses_concrete, heights_concrete_stress, label='Concrete_Stress_(
352           Compression)')
353 ax[1].plot(stresses_casing, heights_casing_stress, label='Casing_Stress')
354
355 # Plot rebar stress distribution as horizontal lines
356 for i, height in enumerate(heights_rebar_stress):
357     ax[1].hlines(height, xmin=0, xmax=stresses_rebar[i], colors='b', label='Rebar_Stress'
358                 if i == 0 else "")
359     ax[1].text(stresses_rebar[i], height, f'{stresses_rebar[i]:.2f}_MPa', va='top')

```



```

353
354 # Add labels for maximum and minimum stress in the concrete and casing
355 ax[1].text(min_stress_concrete, min_stress_concrete_height, f'Min:_{min_stress_concrete:.2f}_MPa', va='bottom', color='red')
356
357 if M == 0:
358     ax[1].text(max_stress_casing, max_stress_casing_height, f'Min:_{min_stress_casing:.2f}_MPa', va='bottom', color='red')
359 else:
360     ax[1].text(max_stress_casing, max_stress_casing_height, f'Max:_{max_stress_casing:.2f}_MPa', va='top', color='red')
361     ax[1].text(min_stress_casing, min_stress_casing_height, f'Min:_{min_stress_casing:.2f}_MPa', va='bottom', color='blue')
362
363 # Add solid vertical line at x=0 for the stress plot
364 ax[1].axvline(x=0, color='black', linestyle='-')
365
366 # Add labels and grid for the stress plot
367 ax[1].set_title('Stress_Distribution')
368 ax[1].set_xlabel('Stress(MPa)')
369 ax[1].set_ylabel('Height(mm)')
370 ax[1].axhline(y=na, color='r', linestyle='--', label='Neutral_Axis')
371 ax[1].grid(True)
372 ax[1].legend()
373 # Mirror the x-axis: negative values now appear on the right
374 ax[1].invert_xaxis()
375
376 plt.tight_layout()
377 plt.show()
378
379 # Plot both the strain and stress distributions with labels for max and min values
380 plot_strain_and_stress_with_labels(strain_distribution, rebar_strain_distribution,
    concrete_stress_distribution, casing_stress_distribution, rebar_stress_distribution,
    neutral_axis)

```

A.2. Python Script Modified Mander's Model for Confined Concrete

```

1 import numpy as np
2 import math
3
4 # Input parameters
5 d_outer = 0.508 # Outer diameter of the pile (m)
6 d_bar_x = 0.025 # Diameter of the reinforcement in x-direction (m)
7 d_bar_y = 0.032 # Diameter of the reinforcement in y-direction (m)
8 w_x = 0.125 # C.t.c. of the reinforcement in the bottom net in x-direction (m)
9 w_y = 0.125 # C.t.c. of the reinforcement in the bottom net in y-direction (m)
10 neutral_axis = 0.14833 # Height of the neutral axis from the bottom fibre (m)
11 f_yh = 500 # Yield strength of reinforcement (MPa)
12
13 alpha = 25.57 # DW stress field strut inclination
14
15 b = 0.071 # Distance between outer fibre reinforcement and outer fibre pile casing (m)
16 c = 0.050 # Reinforcement cover (m)
17 e = 0.030 # Embedment pile casing in concrete cap (m)
18
19 # Number of reinforcement bars contributing to lateral confinement in x- and y-direction
20 n_bar_x = round((d_outer - neutral_axis) / w_x) + 2 # Number of bars in x-direction of the compressed area
21 n_bar_y = round(d_outer / w_y) + 2 # Number of bars in y-direction of the compressed area
22
23 # Confined area dimensions (to centerlines of reinforcement)
24 b_c = (n_bar_y - 1) * w_y # Width of the compressed area
25 d_c = (n_bar_x - 1) * w_x # Depth of the compressed area
26
27 # Effective distance between the bars
28 w_eff_x = w_x - d_bar_x # Effective distance between the bars in x-direction (m)
29 w_eff_y = w_y - d_bar_y # Effective distance between the bars in y-direction (m)
30

```

```

31 # Virtual c.t.c. distance between reinforcement net
32 s = 0.5 * (d_c - 0.5 * w_eff_y) + c + 0.5 * d_bar_x # Virtual c.t.c. distance between
    reinforcement assuming linear stress influence by 45 degrees
33
34 # Virtual ratio of area of longitudinal reinforcement to area in compression
35 rho_cc = 0 # No "longitudinal" reinforcement in the case of a concrete cap
36
37 def solve_for_x(w_eff_x, alpha, b, c, d_bar_x, e):
38     """
39     Solves the equation y1=y2 for x, where:
40     y1=x-w_eff_x/4
41     y2=-tan(90-alpha)*x+tan(90-alpha)*(b-tan(alpha)*(c+d_bar_x/2-e))
42
43     Parameters:
44     w_eff_x(float): The effective weight parameter.
45     alpha(float): The angle alpha in degrees.
46     b,c,d_bar_x,e(float): Additional parameters.
47
48     Returns:
49     float: The solution for x.
50     """
51     # Compute the tangent values needed, converting degrees to radians.
52     T = math.tan(math.radians(90 - alpha))
53     t = math.tan(math.radians(alpha))
54
55     # From the derivation:
56     # x * (1 + T) = T*(b - t*(c + d_bar_x/2 - e)) + w_eff_x/4
57     numerator = T * (b - t * (c + d_bar_x / 2 - e)) + w_eff_x / 4
58     denominator = 1 + T
59
60     if denominator == 0:
61         raise ValueError("The denominator is zero; cannot solve for x.")
62
63     return numerator / denominator
64
65 x = solve_for_x(w_eff_x, alpha, b, c, d_bar_x, e)
66
67 # Function describing the edge of the effectively confined area
68 y1 = x - w_eff_x / 4
69
70 # Function describing the edge of the dual wedge stress field
71 y2 = -math.tan(math.radians(90 - alpha)) * x + math.tan(math.radians(90 - alpha)) * (b - math
    .tan(math.radians(alpha)) * (c + d_bar_x / 2 - e))
72
73 def effective_lateral_conf_stress():
74     # Ineffectively confined concrete area at the level of the reinforcement
75     A_ix = (2 * (n_bar_y - 1)) * w_eff_y**2 / 6
76     A_iy = (2 * (n_bar_x - 1)) * w_eff_x**2 / 6
77     A_i = A_ix + A_iy
78
79     # Effectively confined concrete area at d2
80     A_e = b_c * d_c - A_i - y1 * (2 * (b_c + d_c - 2 * y1))
81
82     # Area of concrete within the center lines of the outer reinforcement
83     A_cc = b_c * d_c * (1 - rho_cc)
84
85     # Confinement effectiveness coefficient
86     k_e = A_e / A_cc
87
88     # Ratio of transverse reinforcement in x-direction
89     A_sx = n_bar_x * 0.25 * np.pi * d_bar_x**2
90     rho_x = A_sx / (s * d_c)
91
92     # Ratio of transverse reinforcement in y-direction
93     A_sy = n_bar_y * 0.25 * np.pi * d_bar_y**2
94     rho_y = A_sy / (s * b_c)
95
96     f_eff_lx = k_e * rho_x * f_yh
97     f_eff_ly = k_e * rho_y * f_yh
98
99     return f_eff_lx, f_eff_ly

```

```

100
101 f_eff_lx, f_eff_ly = effective_lateral_conf_stress()
102 print(f"d2: {(b_u - x_u) * 1000:.2f} mm, 0.5 * x_u_t_casing and x_Emax: {(y2_u + c_u + 0.5 * d_bar_x_u - e_u) * 1000:.2f} mm")
103 print(f"f_eff_lx: {(f_eff_lx:.2f)} MPa and f_eff_ly: {(f_eff_ly:.2f)} MPa")

```

A.3. Python Script Markic Dual-Wedge Stress Field Model

```

1 import numpy as np
2 from scipy.optimize import minimize_scalar
3
4 # Given parameters
5 f_c = 30 # MPa, compressive strength of concrete
6 sigma_conf = 10.25 # MPa, confinement pressure
7 sigma_s = 10.25 # MPa, stress in reinforcement (equal to sigma_conf)
8
9 d1 = 5 # mm, half the width of the steel strip
10 d2 = 30.40 # mm, width of load transfer
11 x_Emax = 53.10 # mm, available height for load transfer
12
13 # Function for sigma_b
14 def calculate_sigma_b(k_s, sigma_s, d2, d1):
15     return 0.5 * k_s * sigma_s * (d2 / d1 + 3)
16
17 # Function for sigma_a according to equation 12 (including missing term)
18 def calculate_sigma_a(f_c, sigma_alpha, sigma_conf, sigma_b, k_s, sigma_s, d1, d2):
19     return np.sqrt(0.25 * (f_c - sigma_alpha + 4 * sigma_conf) ** 2 + sigma_b ** 2 + 0.5 *
20                    k_s * sigma_s * ((f_c + 4 * sigma_conf) * ((d2 / d1) - 5) + sigma_alpha * (7 * (d2 /
21                    d1) - 3)))
22
23 # Function for k_s according to equation 10
24 def calculate_k_s(f_c, sigma_x0, sigma_conf, sigma_s, d1, d2):
25     return max(min(1 - ((d1 / d2) * sigma_x0 - f_c) / (4 * sigma_s), 1), 0)
26
27 # Function for sigma_x0
28 def calculate_sigma_x0(sigma_alpha, alpha_rad, k_s, sigma_s, d1, d2):
29     denominator = 1 + (sigma_alpha * np.sin(alpha_rad) ** 2) / (k_s * sigma_s)
30     return (d2 / d1) * (sigma_alpha * np.cos(alpha_rad) ** 2) / denominator
31
32 # Function for minimum value of sin^2(alpha) according to equation 14
33 def calculate_sin2_alpha_min(d1, d2):
34     return (d2 - d1) ** 2 / (4 * x_Emax ** 2 + (d2 - d1) ** 2)
35
36 # Function for sin^2(alpha) according to equations 11 + 14
37 def calculate_sin2_alpha(sigma_alpha, sigma_a, k_s, sigma_s, f_c, sigma_conf, d1, d2):
38     sigma_b = calculate_sigma_b(k_s, sigma_s, d2, d1)
39     numerator = (0.5 * (f_c + sigma_alpha) - (f_c + 4 * sigma_conf) * (d1 / d2) + 2 *
40                 sigma_conf + sigma_b - sigma_a)
41     denominator = (f_c + 4 * sigma_conf) * (d1 / d2) - 3 * k_s * sigma_s
42     sin2_alpha_calc = (
43         (k_s * sigma_s / sigma_alpha) * (numerator / denominator)
44         if denominator != 0 else np.inf)
45     sin2_alpha_min = calculate_sin2_alpha_min(d1, d2)
46     return max(sin2_alpha_calc, sin2_alpha_min)
47
48 # Function for sigma_alpha according to equations 15 and 16
49 def calculate_sigma_alpha(alpha_rad):
50     sigma_alpha_BHK = (1 / 16) * (6 * f_c + sigma_conf * (9 + 25 * np.cos(2 * alpha_rad)) +
51                                np.sqrt(64 * (f_c - sigma_conf) * (f_c + 4 * sigma_conf) + (6 * f_c + sigma_conf * (9
52                                + 25 * np.cos(2 * alpha_rad))) ** 2))
53     sigma_alpha_BHF = (1 / 16) * (6 * f_c + sigma_s * (9 + 25 * np.cos(2 * alpha_rad)) + np.
54                                sqrt(64 * (f_c - sigma_s) * (f_c + 4 * sigma_s) + (6 * f_c + sigma_s * (9 + 25 * np.
55                                cos(2 * alpha_rad))) ** 2))
56     return min(sigma_alpha_BHK, sigma_alpha_BHF)
57
58 # Improved iterative calculation for sigma_x0 and k_s
59 def fast_iterative_sigma_x0():
60     start_k_s_values = [1.0, 0.8, 0.6, 0.4, 0.2] # Initial guesses
61     tolerance = 1e-5 # Convergence criterion
62     alpha_rad = np.pi / 4 # Initial value for alpha_rad

```

```

56
57     for initial_k_s in start_k_s_values:
58         k_s = initial_k_s
59
60         for _ in range(20): # Maximum 20 iterations
61             sigma_alpha = calculate_sigma_alpha(alpha_rad)
62             sigma_b = calculate_sigma_b(k_s, sigma_s, d2, d1)
63             sigma_a = calculate_sigma_a(f_c, sigma_alpha, sigma_conf, sigma_b, k_s, sigma_s,
64                                     d1, d2)
65             sin2_alpha = calculate_sin2_alpha(sigma_alpha, sigma_a, k_s, sigma_s, f_c,
66                                     sigma_conf, d1, d2)
67             alpha_rad = np.arcsin(np.sqrt(sin2_alpha))
68
69             sigma_x0 = calculate_sigma_x0(sigma_alpha, alpha_rad, k_s, sigma_s, d1, d2)
70             k_s_new = calculate_k_s(f_c, sigma_x0, sigma_conf, sigma_s, d1, d2)
71
72             if abs(k_s - k_s_new) < tolerance:
73                 break # Convergence reached
74
75             k_s = k_s_new
76
77         return sigma_x0, k_s, sigma_alpha, np.degrees(alpha_rad)
78
79 # Compute sigma_x0 and k_s with improved iteration
80 sigma_x0, k_s_opt, sigma_alpha, alpha_deg = fast_iterative_sigma_x0()
81
82 print(f"Optimised k_s: {k_s_opt:.4f}")
83 print(f"Optimal sigma_alpha: {sigma_alpha:.2f} MPa")
84 print(f"Corresponding angle alpha: {alpha_deg:.2f} degrees")
85 print(f"Calculated sigma_x0 (bearing capacity): {sigma_x0:.2f} MPa")

```

B

Imitation of Markic et al. Experimental Campaign

B.1. Experimentally obtained curves

This appendix presents the normalised bearing stress–penetration curves obtained from the experimental campaign by Markić et al. (Markic et al. 2022a). The linear portions of each trajectory have been highlighted and extrapolated back to the penetration axis (zero stress) to facilitate a direct comparison with the fully linear results produced by the finite element analyses.

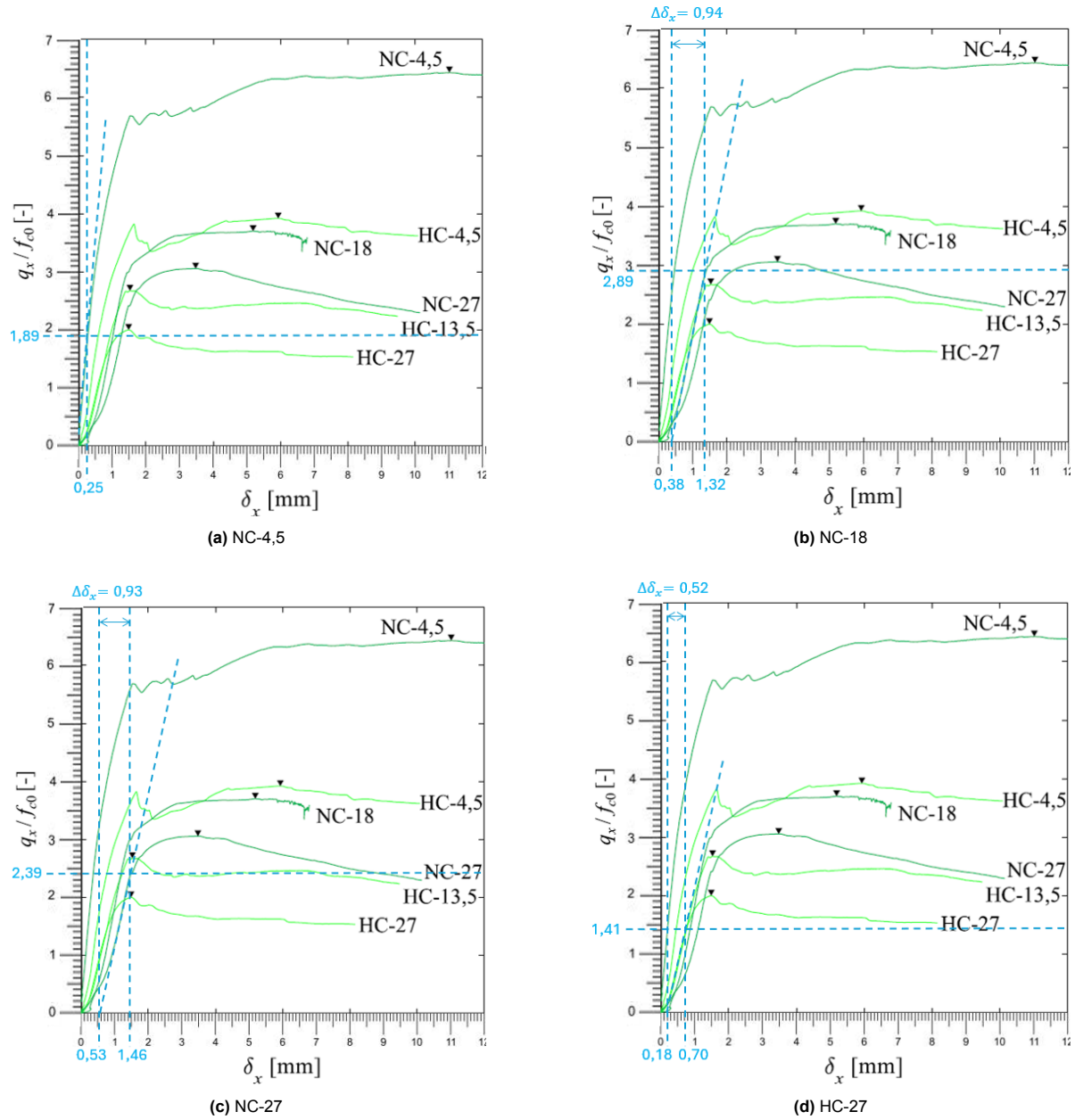
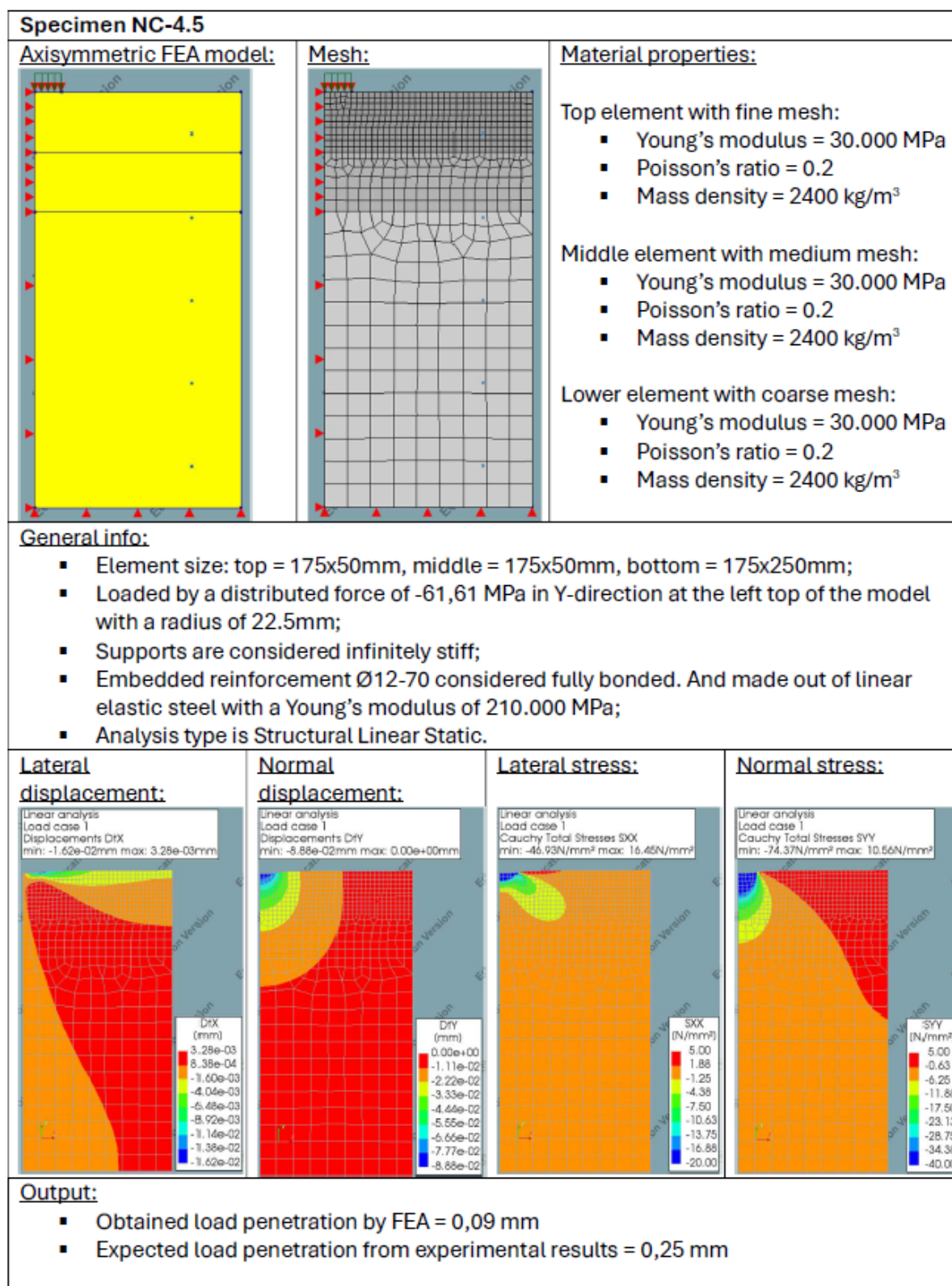
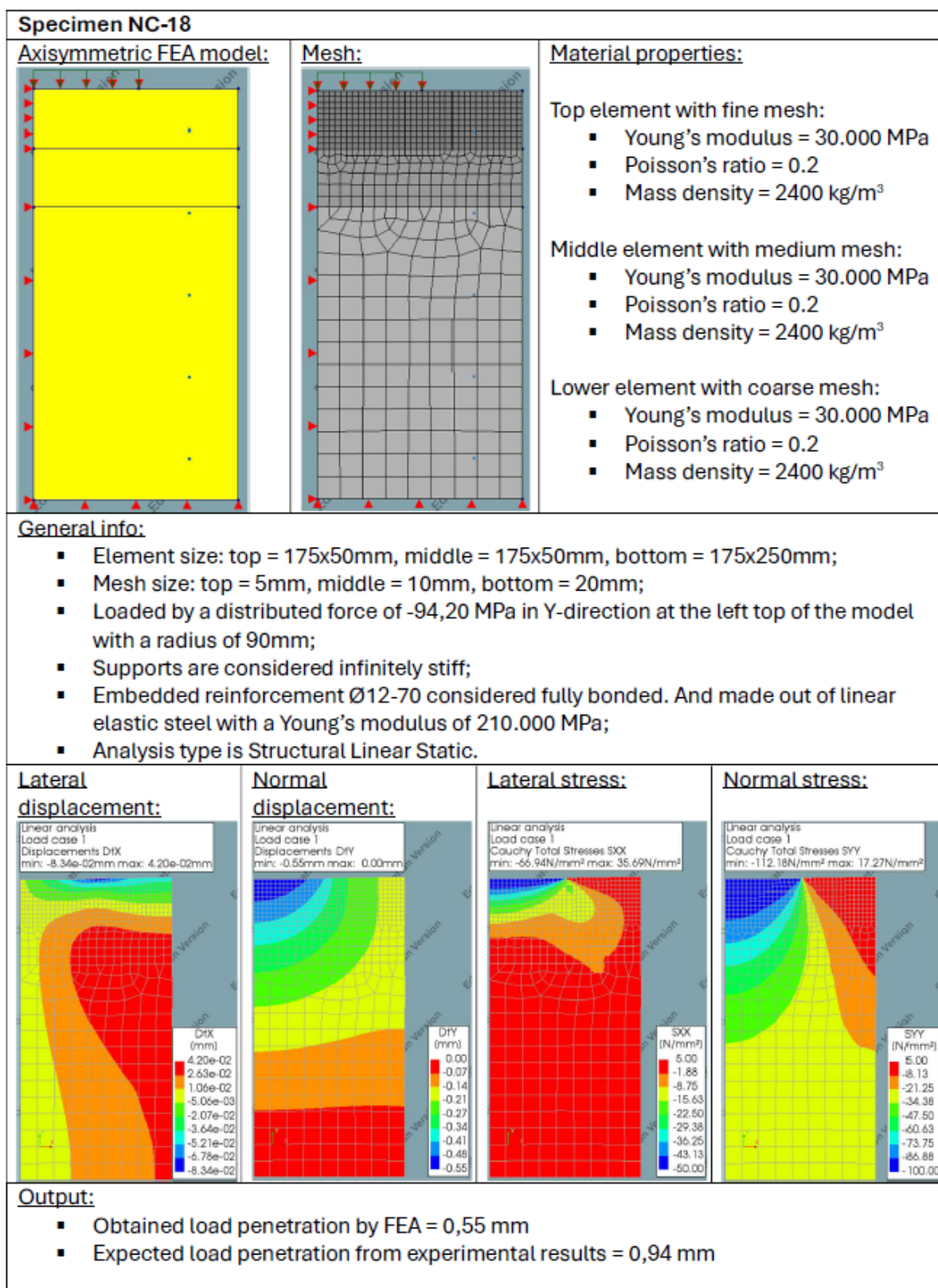


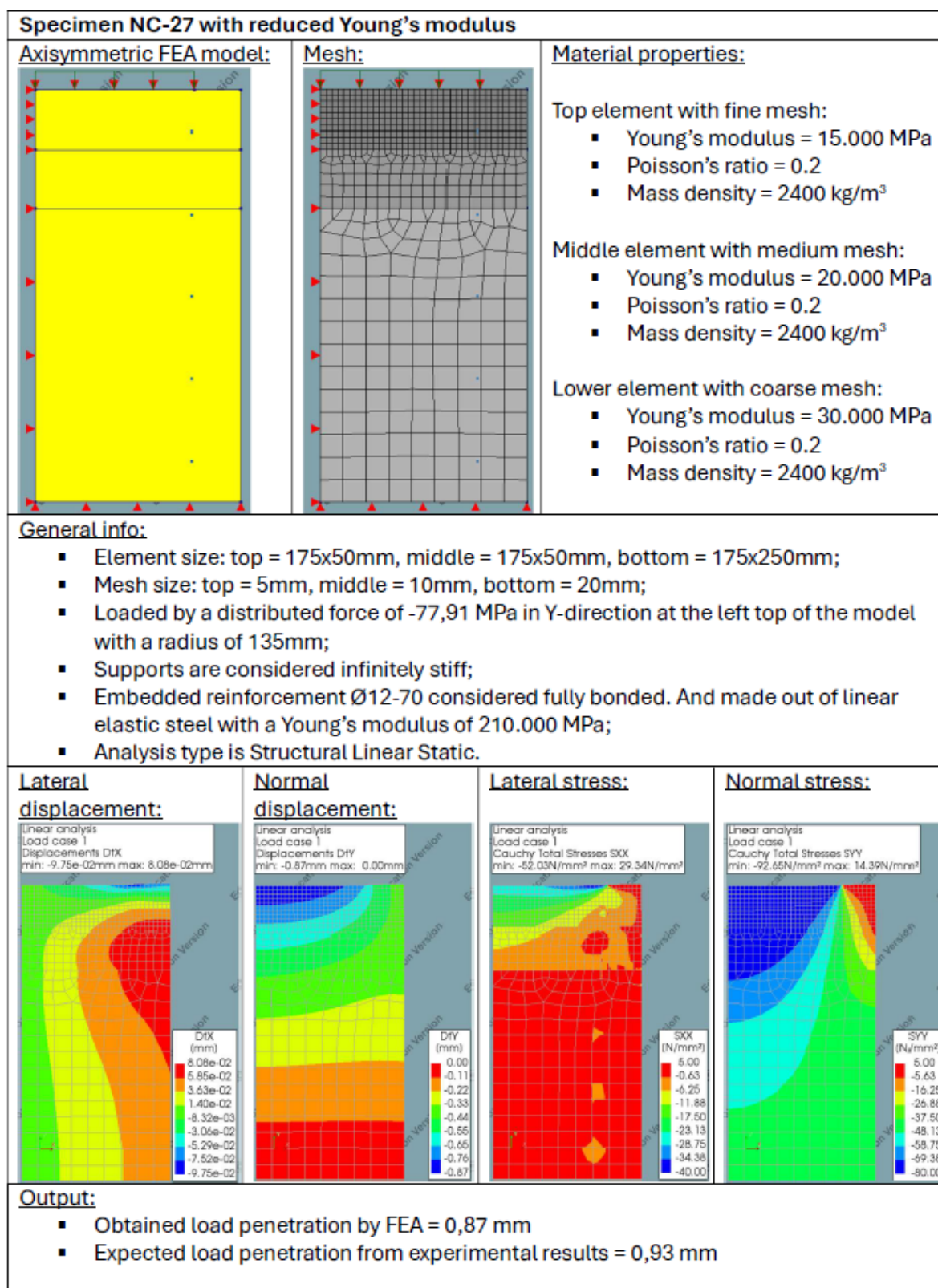
Figure B.1: Extrapolated linear experimentally obtained results

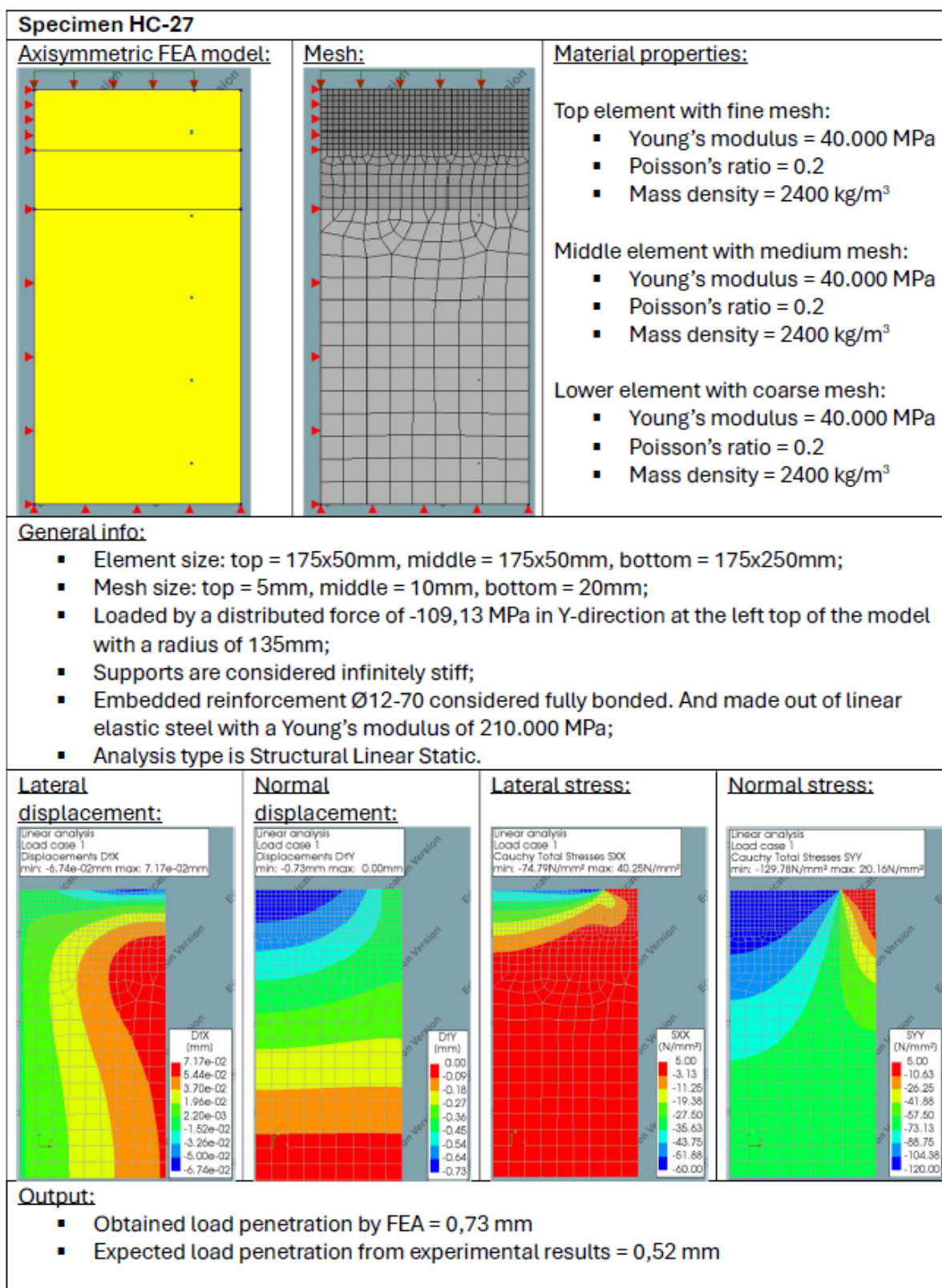
B.2. Linear Axisymmetric FEA of Markić et al. specimens

This appendix details the input parameters and output results of the linear-elastic, axisymmetric finite-element analyses conducted on the Markić et al. specimens NC-4,5, NC-18, NC-27 and HC-27. Simplified replications of the original reinforcement configurations and loading conditions were employed to facilitate comparison with the experimental linear-elastic trajectories. The input section includes a schematic of the geometry, a complete listing of the linear material properties, and a concise description of the applied loading and boundary conditions. The output section presents contour plots of deformations and stress distributions within the specimen, and concludes with a comparison of the FEA obtained versus experimentally observed load-penetration responses.



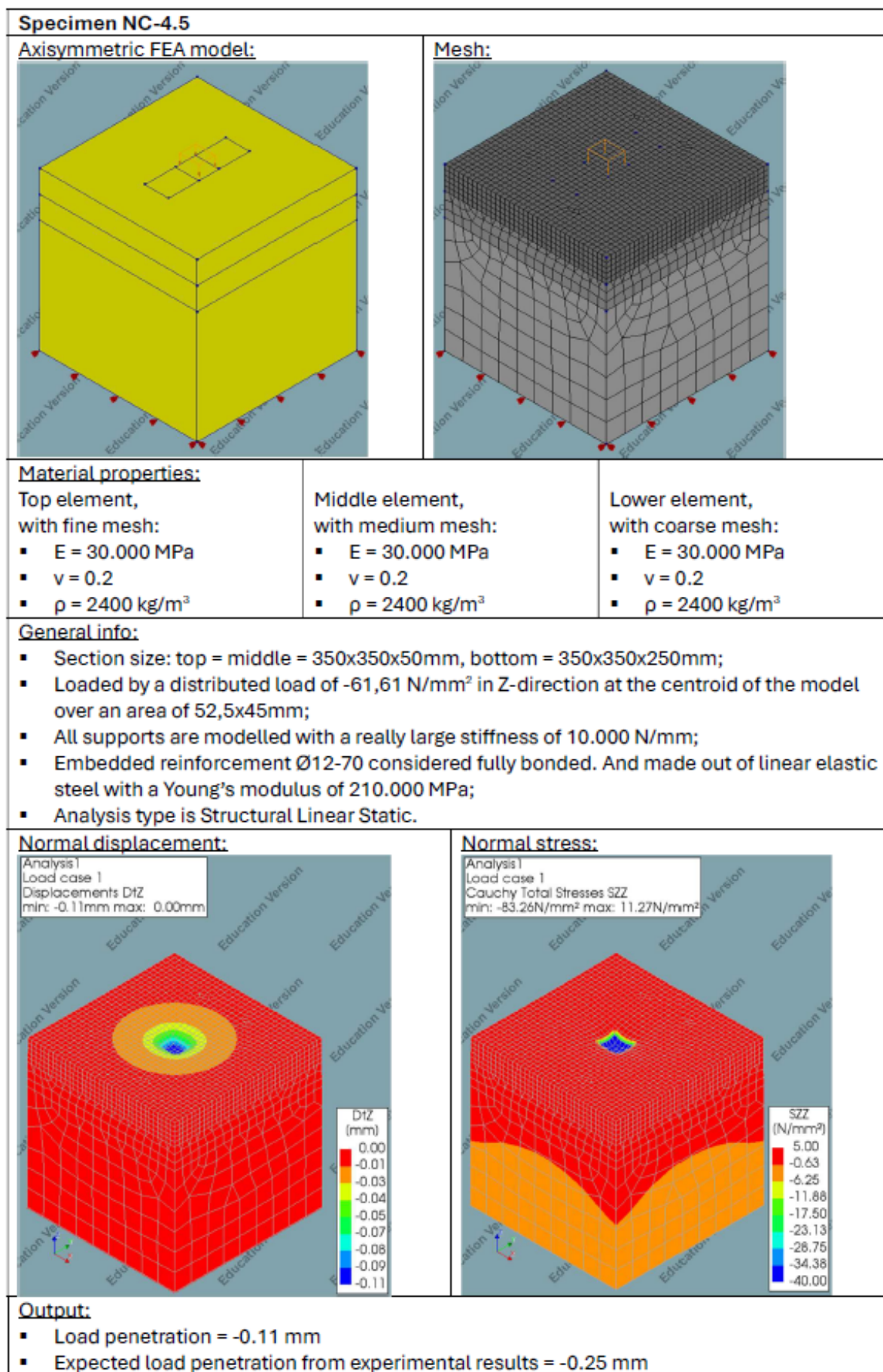


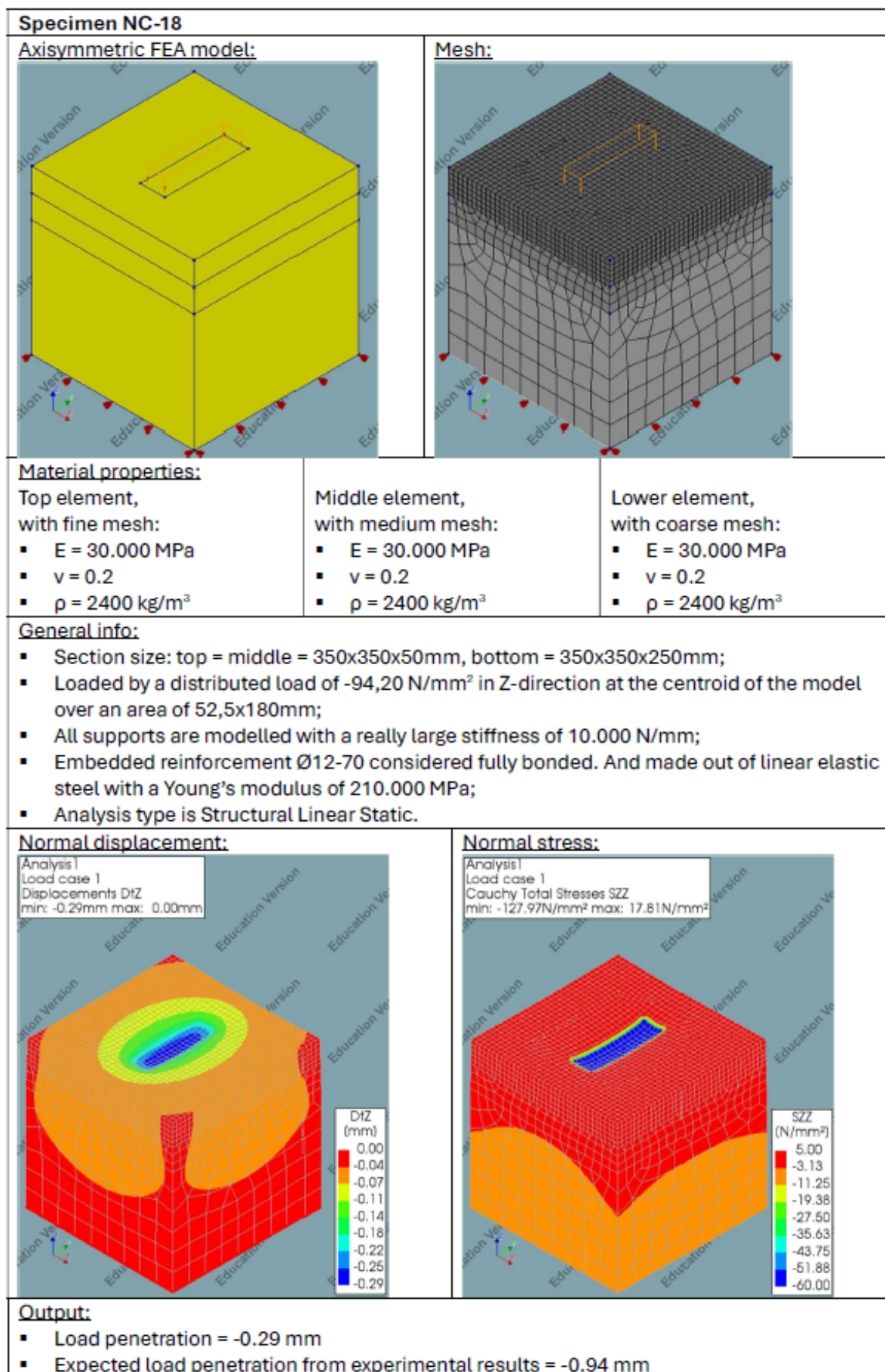


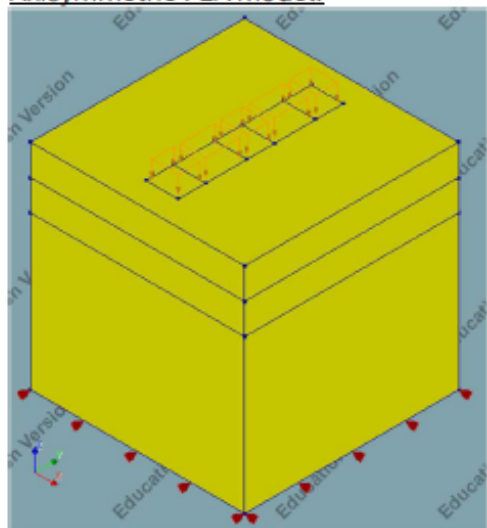
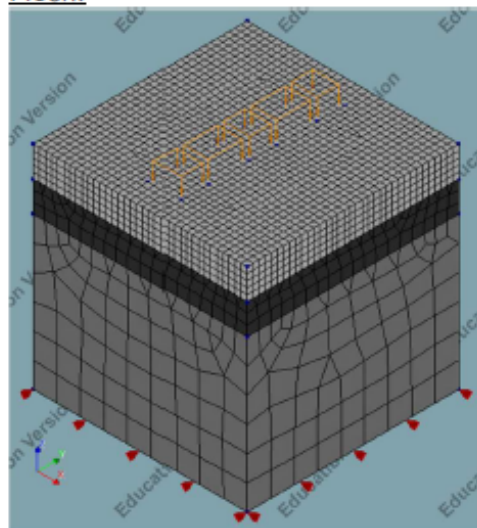


B.3. Linear 3D FEA of Markić et al. specimens

This appendix details the input parameters and output results of the linear-elastic, 3D finite-element analyses conducted on the Markić et al. specimens NC-4.5, NC-18, NC-27 and HC-27. Almost identical replications of the original reinforcement configurations and loading conditions were employed to facilitate the best possible comparison with the experimental linear-elastic trajectories. The input section includes a schematic of the geometry, a complete listing of the linear material properties, and a concise description of the applied loading and boundary conditions. The output section presents contour plots of deformations and stress distributions within the specimen, and concludes with a comparison of the FEA obtained versus experimentally observed load-penetration responses.





Specimen NC-27Axisymmetric FEA model:Mesh:Material properties:

Top element,
with fine mesh:

- $E = 30.000 \text{ MPa}$
- $\nu = 0.2$
- $\rho = 2400 \text{ kg/m}^3$

Middle element,
with medium mesh:

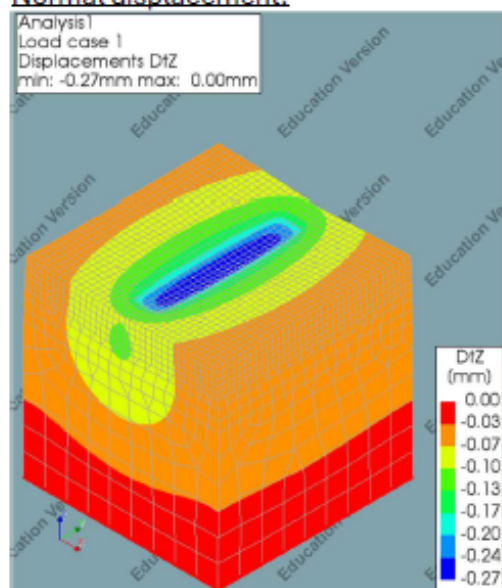
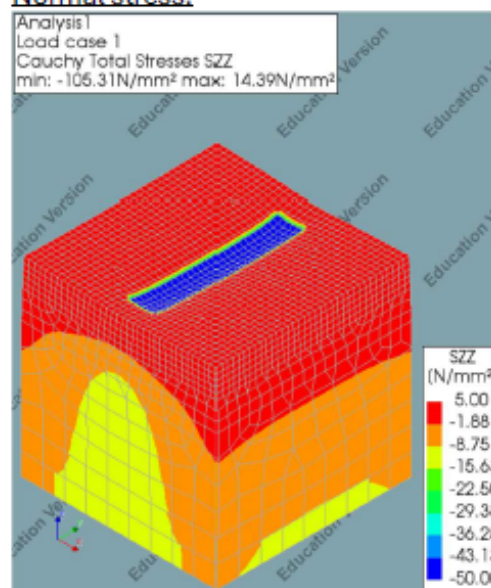
- $E = 30.000 \text{ MPa}$
- $\nu = 0.2$
- $\rho = 2400 \text{ kg/m}^3$

Lower element,
with coarse mesh:

- $E = 30.000 \text{ MPa}$
- $\nu = 0.2$
- $\rho = 2400 \text{ kg/m}^3$

General info:

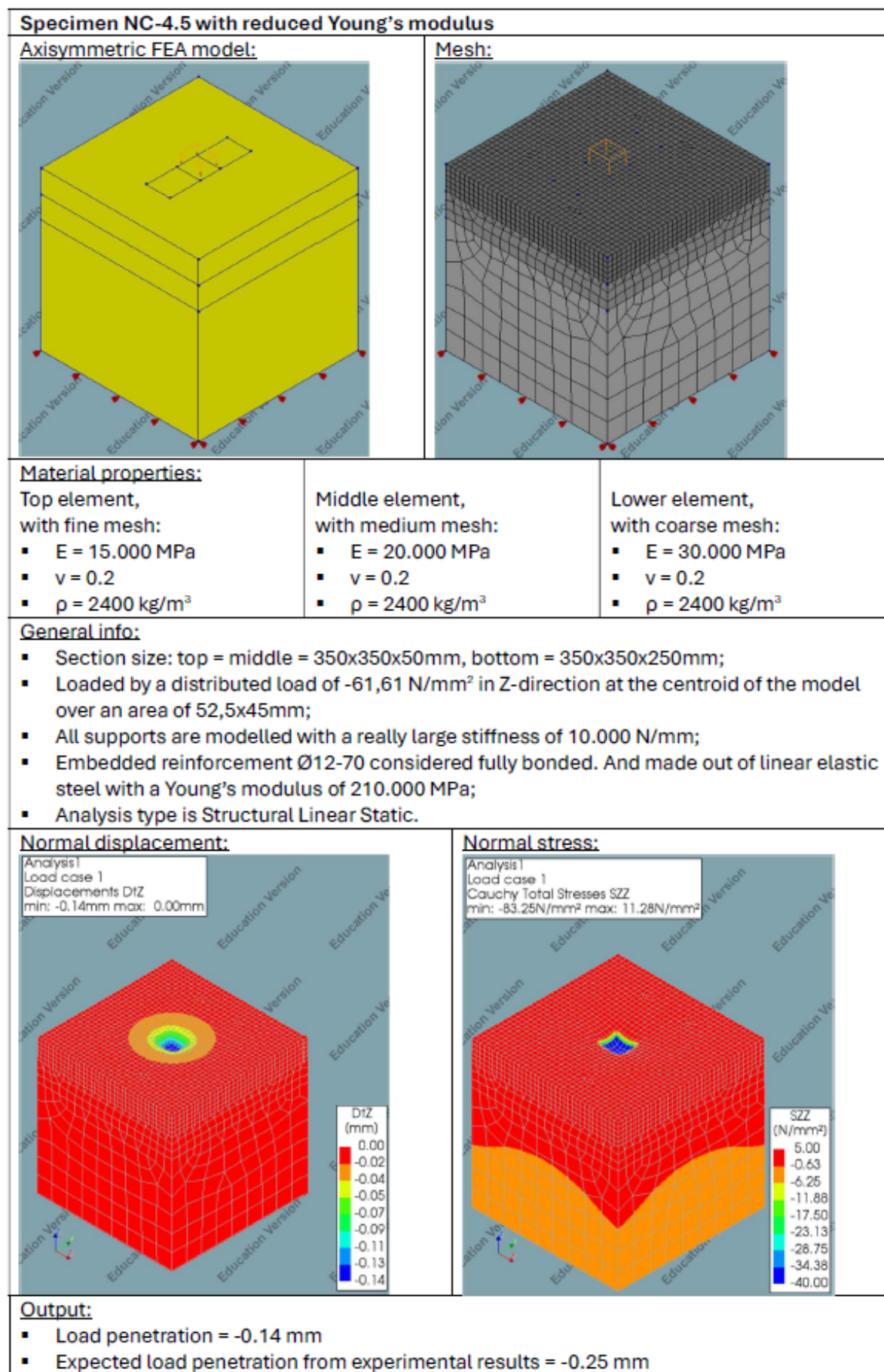
- Section size: top = middle = $350 \times 350 \times 50 \text{ mm}$, bottom = $350 \times 350 \times 250 \text{ mm}$;
- Loaded by a distributed load of $-77,91 \text{ N/mm}^2$ in Z-direction at the centroid of the model over an area of $52,5 \times 270 \text{ mm}$;
- All supports are modelled with a really large stiffness of 10.000 N/mm ;
- Embedded reinforcement $\varnothing 12-70$ considered fully bonded. And made out of linear elastic steel with a Young's modulus of 210.000 MPa ;
- Analysis type is Structural Linear Static.

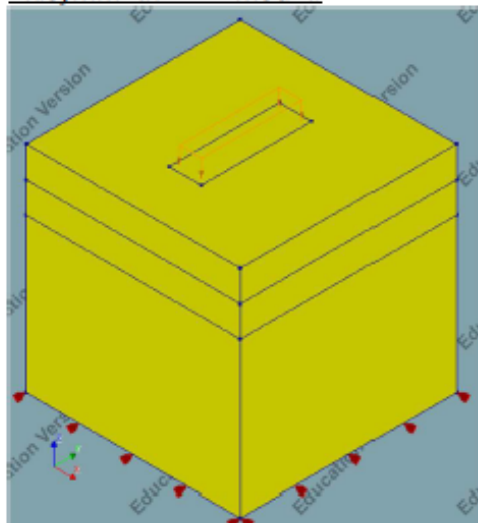
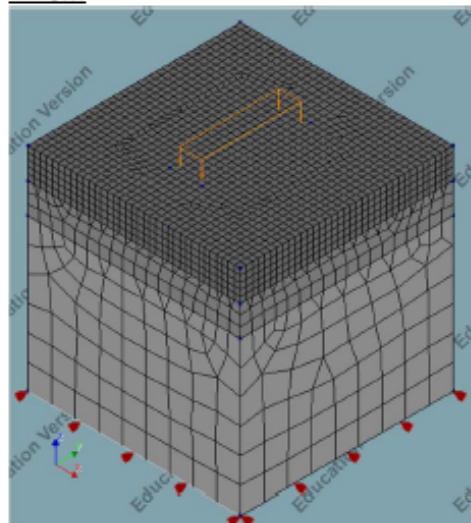
Normal displacement:Normal stress:Output:

- Load penetration = -0.27 mm
- Expected load penetration from experimental results = -0.93 mm

B.4. Linear 3D FEA of Markić et al. specimens with reduced E

This appendix details the input parameters and output results of the linear-elastic, 3D finite-element analyses with reduced young's modulus conducted on the Markić et al. specimens NC-4.5, NC-18, NC-27 and HC-27. Almost identical replications of the original reinforcement configurations and loading conditions were employed to facilitate the best possible comparison with the experimental linear-elastic trajectories. The input section includes a schematic of the geometry, a complete listing of the linear material properties (note the reduced young's modulus), and a concise description of the applied loading and boundary conditions. The output section presents contour plots of deformations and stress distributions within the specimen, and concludes with a comparison of the FEA obtained versus experimentally observed load-penetration responses.



Specimen NC-18 with reduced Young's modulus**Axisymmetric FEA model:****Mesh:****Material properties:**

Top element,
with fine mesh:

- $E = 10.000 \text{ MPa}$
- $\nu = 0.2$
- $\rho = 2400 \text{ kg/m}^3$

Middle element,
with medium mesh:

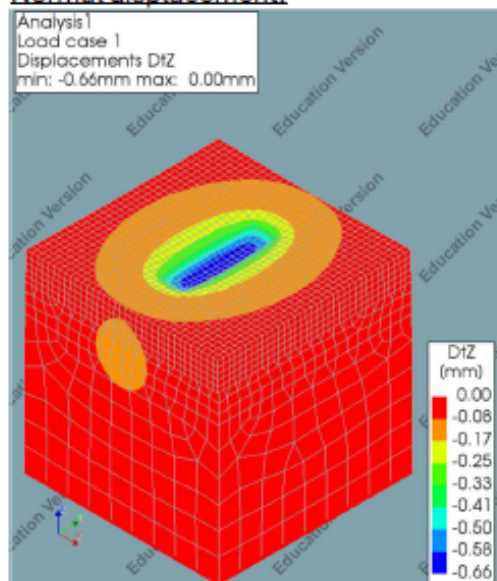
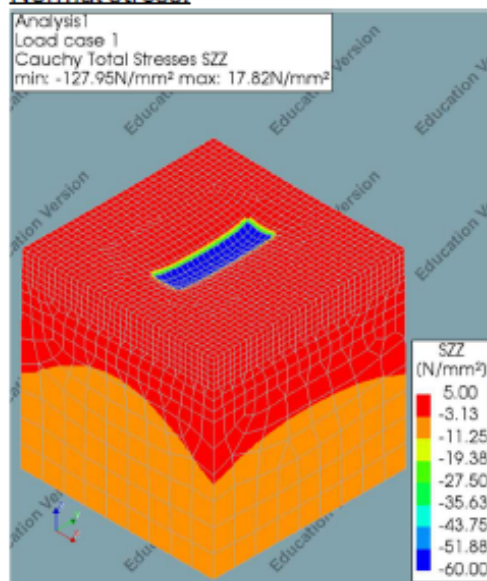
- $E = 15.000 \text{ MPa}$
- $\nu = 0.2$
- $\rho = 2400 \text{ kg/m}^3$

Lower element,
with coarse mesh:

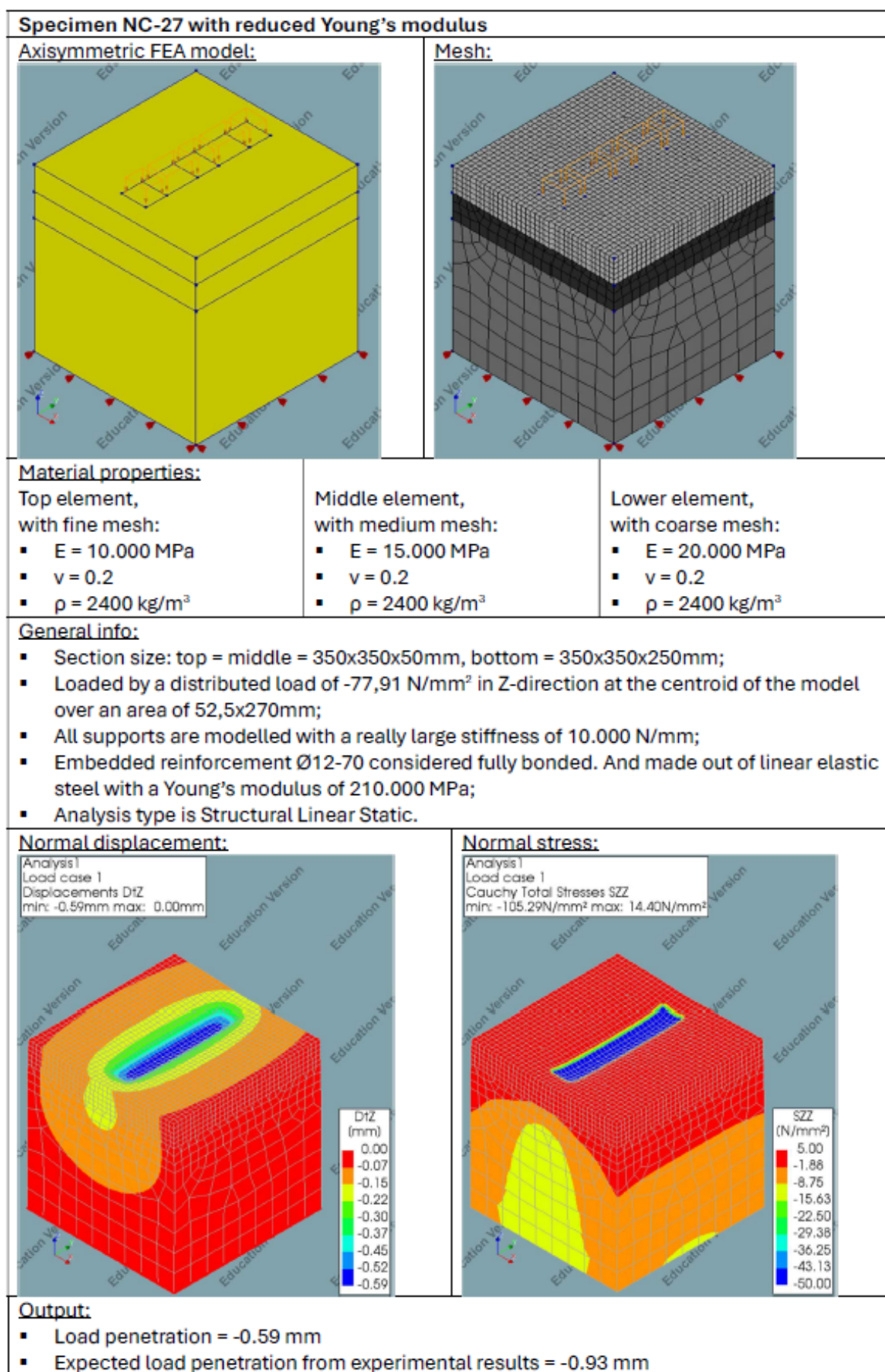
- $E = 20.000 \text{ MPa}$
- $\nu = 0.2$
- $\rho = 2400 \text{ kg/m}^3$

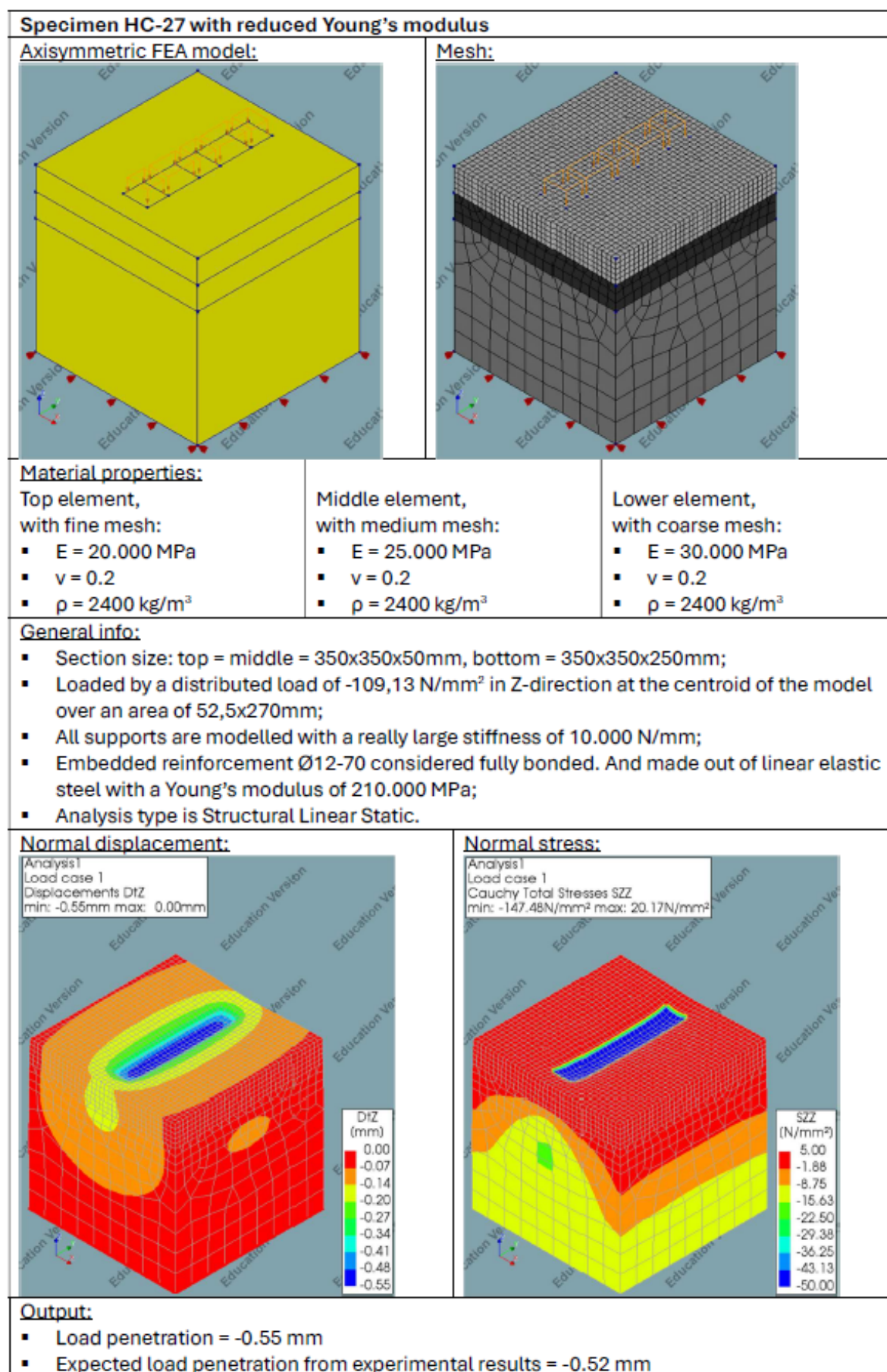
General info:

- Section size: top = middle = $350 \times 350 \times 50 \text{ mm}$, bottom = $350 \times 350 \times 250 \text{ mm}$;
- Loaded by a distributed load of $-94,20 \text{ N/mm}^2$ in Z-direction at the centroid of the model over an area of $52,5 \times 180 \text{ mm}$;
- All supports are modelled with a really large stiffness of 10.000 N/mm ;
- Embedded reinforcement $\varnothing 12-70$ considered fully bonded. And made out of linear elastic steel with a Young's modulus of 210.000 MPa ;
- Analysis type is Structural Linear Static.

Normal displacement:**Normal stress:****Output:**

- Load penetration = -0.66 mm
- Expected load penetration from experimental results = -0.94 mm





B.5. Analytical calculations for verification

This appendix presents an analytical calculation for the 4 selected specimens from the Markić et al. experimental campaign, aimed at verifying the reduction in Young's modulus at elevated stress levels. As described by (Betoniek 2024), once the applied compressive stress exceeds 40% of the concrete's uniaxial compressive strength, the initial Young's modulus diminishes, and the tangent modulus rather than the secant modulus should be employed.

The figure below schematises how the axisymmetric DIANA model is abstracted to a three-spring system that follows the trajectory of the experimental stress distribution. By applying Hooke's law, the stiffness of each spring is determined. Using these stiffness values, the load penetration corresponding to the linear portion of the experimental bearing stress trajectory is calculated.

The analytical calculations performed with the original Young's modulus produce penetration values that closely match those from the corresponding FEA models. However, both methods predict much smaller penetrations than observed experimentally. When a reduced Young's modulus is applied in both the analytical and numerical models, the resulting load–penetration behaviour aligns far more closely with the experimental data. This discrepancy confirms that the test specimens exhibited an effective stiffness significantly lower than the standard secant modulus of the concrete.

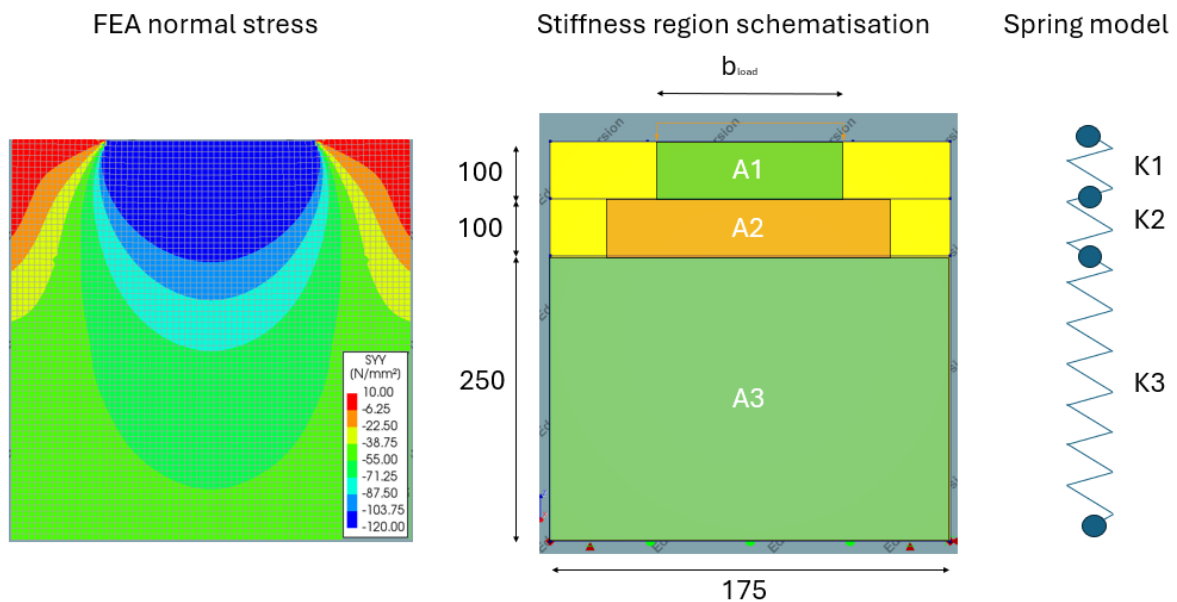


Figure B.2: Schematic simplification of the 3D DIANA model and experimental specimen into an equivalent three-spring system

Specimen NC-4.5, Simplified analytical calculation

Prescribed deformation:

 $q_x = -61,61$ [MPa]

Applied equation:

$$u = \frac{\sum \frac{L_{seg}}{E_{seg} \times A_{seg}}}{A_{load} \times q_x}$$

Simplified model:

Spring stiffness 1:

E1 = 30000 [MPa]

L1 = 50 [mm]

d1 = 45 [mm]

A1 = 2362,50 [mm²]

K1 = 1,42E+06 [N/mm]

Spring stiffness 2:

E2 = 30000 [MPa]

L2 = 50 [mm]

d2 = 145 [mm]

A2 = 22112,50 [mm²]

K2 = 13267500 [N/mm]

Spring stiffness 3:

E3 = 30000 [MPa]

L3 = 250 [mm]

d3 = 245 [mm]

A3 = 61862,50 [mm²]

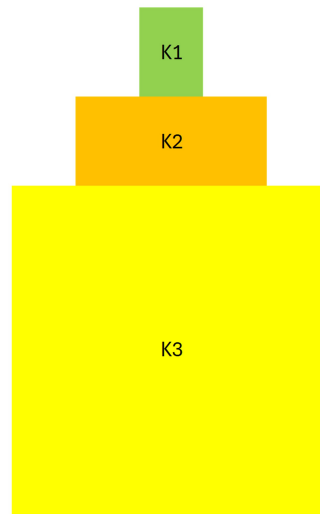
K3 = 7,42E+06 [N/mm]

Combined spring stiffness:

Ktot = 1,09E+06 [N/mm]

Spring force and bearing force:

F = -1,46E+05 [N]

u = -0,13 [mm] / $u_{exp} = 0,53$ **Specimen NC-4.5, Simplified analytical calculation with reduced young's modulus**

Prescribed deformation:

 $q_x = -61,61$ [MPa]

Applied equation:

$$u = \frac{\sum \frac{L_{seg}}{E_{seg} \times A_{seg}}}{A_{load} \times q_x}$$

Simplified model:

Spring stiffness 1:

E1 = 20000 [MPa]

L1 = 50 [mm]

d1 = 45 [mm]

A1 = 2362,50 [mm²]

K1 = 9,45E+05 [N/mm]

Spring stiffness 2:

E2 = 25000 [MPa]

L2 = 50 [mm]

d2 = 145 [mm]

A2 = 22112,50 [mm²]

K2 = 11056250 [N/mm]

Spring stiffness 3:

E3 = 30000 [MPa]

L3 = 250 [mm]

d3 = 245 [mm]

A3 = 61862,50 [mm²]

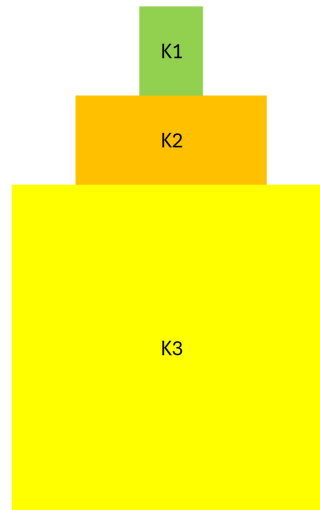
K3 = 7,42E+06 [N/mm]

Combined spring stiffness:

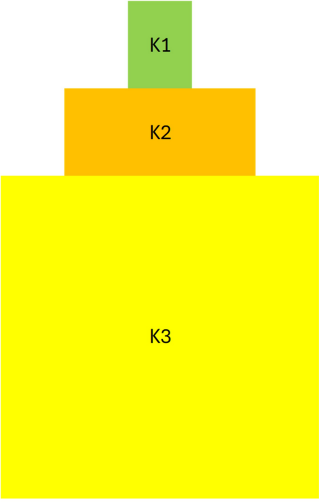
Ktot = 7,79E+05 [N/mm]

Spring force and bearing force:

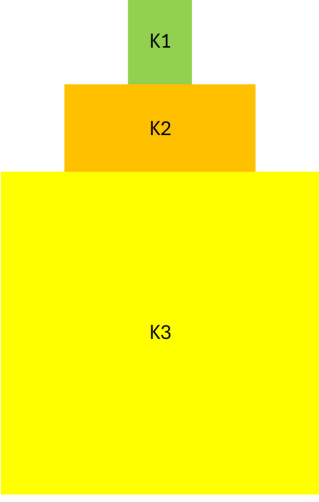
F = -1,46E+05 [N]

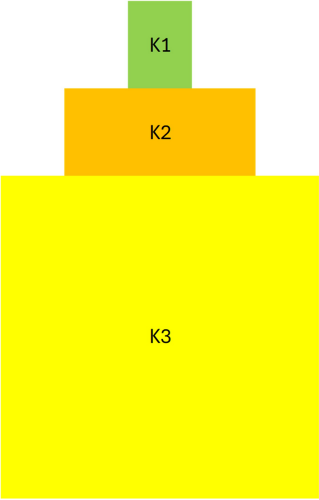
u = -0,19 [mm] / $u_{exp} = 0,75$ 

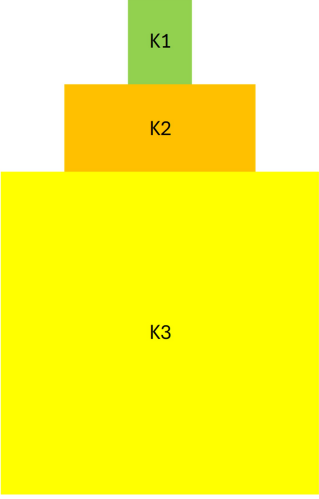
Specimen NC-18, Simplified analytical calculation			
Prescribed deformation: $q_x =$	-94,2 [MPa]	Applied equation: $u = \frac{\sum \frac{L_{seg}}{E_{seg} \times A_{seg}}}{A_{load} \times q_x}$	Simplified model:
Spring stiffness 1: E1 = L1 = d1 = A1 = K1 =	30000 [MPa] 50 [mm] 180 [mm] 9450,00 [mm ²] 5,67E+06 [N/mm]	Spring stiffness 2: E2 = L2 = d2 = A2 = K2 =	30000 [MPa] 50 [mm] 280 [mm] 42700,00 [mm ²] 25620000 [N/mm]
Spring stiffness 3: E3 = L3 = d3 = A3 = K3 =	30000 [MPa] 250 [mm] 350 [mm] 88375,00 [mm ²] 1,06E+07 [N/mm]	Combined spring stiffness: Ktot =	3,23E+06 [N/mm]
Spring force and bearing force: F = u =	-8,90E+05 [N] -0,28 [mm]	/ U _{exp} =	0,29

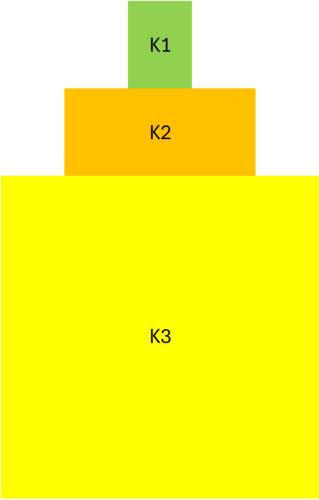


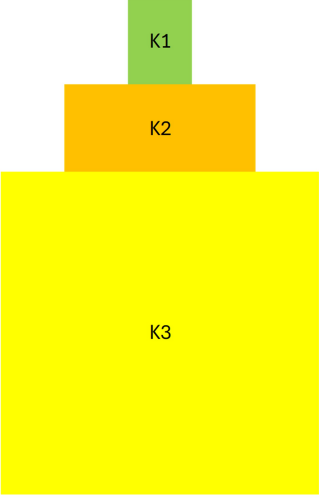
Specimen NC-18, Simplified analytical calculation with reduced young's modulus			
Prescribed deformation: $q_x =$	-94,2 [MPa]	Applied equation: $u = \frac{\sum \frac{L_{seg}}{E_{seg} \times A_{seg}}}{A_{load} \times q_x}$	Simplified model:
Spring stiffness 1: E1 = L1 = d1 = A1 = K1 =	10000 [MPa] 50 [mm] 180 [mm] 9450,00 [mm ²] 1,89E+06 [N/mm]	Spring stiffness 2: E2 = L2 = d2 = A2 = K2 =	15000 [MPa] 50 [mm] 280 [mm] 42700,00 [mm ²] 12810000 [N/mm]
Spring stiffness 3: E3 = L3 = d3 = A3 = K3 =	20000 [MPa] 250 [mm] 350 [mm] 88375,00 [mm ²] 7,07E+06 [N/mm]	Combined spring stiffness: Ktot =	1,34E+06 [N/mm]
Spring force and bearing force: F = u =	-8,90E+05 [N] -0,67 [mm]	/ U _{exp} =	0,71

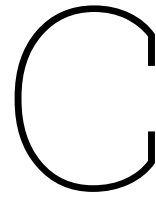


Specimen NC-27, Simplified analytical calculation			
Prescribed deformation: q _x = -77,91 [MPa]		Applied equation: $u = \frac{\sum \frac{L_{seg}}{E_{seg} \times A_{seg}}}{A_{load} \times q_x}$	Simplified model:
Spring stiffness 1: E1 = 30000 [MPa] L1 = 50 [mm] d1 = 270 [mm] A1 = 14175,00 [mm ²] K1 = 8,51E+06 [N/mm]		Spring stiffness 2: E2 = 30000 [MPa] L2 = 50 [mm] d2 = 350 [mm] A2 = 53375,00 [mm ²] K2 = 32025000 [N/mm]	
Spring stiffness 3: E3 = 30000 [MPa] L3 = 250 [mm] d3 = 350 [mm] A3 = 88375,00 [mm ²] K3 = 1,06E+07 [N/mm]		Combined spring stiffness: Ktot = 4,11E+06 [N/mm]	
Spring force and bearing force: F = -1,10E+06 [N] u = -0,27 [mm]		/ u _{exp} = 0,29	

Specimen NC-27, Simplified analytical calculation with reduced young's modulus			
Prescribed deformation: q _x = -77,91 [MPa]		Applied equation: $u = \frac{\sum \frac{L_{seg}}{E_{seg} \times A_{seg}}}{A_{load} \times q_x}$	Simplified model:
Spring stiffness 1: E1 = 10000 [MPa] L1 = 50 [mm] d1 = 180 [mm] A1 = 9450,00 [mm ²] K1 = 1,89E+06 [N/mm]		Spring stiffness 2: E2 = 15000 [MPa] L2 = 50 [mm] d2 = 280 [mm] A2 = 42700,00 [mm ²] K2 = 12810000 [N/mm]	
Spring stiffness 3: E3 = 20000 [MPa] L3 = 250 [mm] d3 = 350 [mm] A3 = 88375,00 [mm ²] K3 = 7,07E+06 [N/mm]		Combined spring stiffness: Ktot = 1,34E+06 [N/mm]	
Spring force and bearing force: F = -7,36E+05 [N] u = -0,55 [mm]		/ u _{exp} = 0,59	

Specimen HC-27, Simplified analytical calculation			
Prescribed deformation: q _x = -109,13 [MPa]		Applied equation: $u = \frac{\sum \frac{L_{seg}}{E_{seg} \times A_{seg}}}{A_{load} \times q_x}$	Simplified model:
Spring stiffness 1: E1 = 40000 [MPa] L1 = 50 [mm] d1 = 270 [mm] A1 = 14175,00 [mm ²] K1 = 1,13E+07 [N/mm]		Spring stiffness 2: E2 = 40000 [MPa] L2 = 50 [mm] d2 = 350 [mm] A2 = 53375,00 [mm ²] K2 = 42700000 [N/mm]	
Spring stiffness 3: E3 = 40000 [MPa] L3 = 250 [mm] d3 = 350 [mm] A3 = 88375,00 [mm ²] K3 = 1,41E+07 [N/mm]		Combined spring stiffness: Ktot = 5,48E+06 [N/mm]	
Spring force and bearing force: F = -1,55E+06 [N] u = -0,28 [mm]		/ u _{exp} = 0,54	

Specimen HC-27, Simplified analytical calculation with reduced young's modulus			
Prescribed deformation: q _x = -109,13 [MPa]		Applied equation: $u = \frac{\sum \frac{L_{seg}}{E_{seg} \times A_{seg}}}{A_{load} \times q_x}$	Simplified model:
Spring stiffness 1: E1 = 20000 [MPa] L1 = 50 [mm] d1 = 180 [mm] A1 = 9450,00 [mm ²] K1 = 3,78E+06 [N/mm]		Spring stiffness 2: E2 = 25000 [MPa] L2 = 50 [mm] d2 = 280 [mm] A2 = 42700,00 [mm ²] K2 = 21350000 [N/mm]	
Spring stiffness 3: E3 = 30000 [MPa] L3 = 250 [mm] d3 = 350 [mm] A3 = 88375,00 [mm ²] K3 = 1,06E+07 [N/mm]		Combined spring stiffness: Ktot = 2,46E+06 [N/mm]	
Spring force and bearing force: F = -1,03E+06 [N] u = -0,42 [mm]		/ u _{exp} = 0,80	



Python Scripts for Quasi-Non-Linear FEA Verification

This appendix provides the complete Python scripts developed to perform the quasi-non-linear finite-element analyses used to verify the analytically derived results from the modified confinement models presented in this thesis.

The first script computes the load penetration corresponding to the analytically obtained bearing stress, incorporating energy dissipation through the Markić Dual-Wedge stress-field model. The second script automates the reduction of local concrete stiffness and the implementation of a compliant cushion layer beneath the loading area.

C.1. Python script corresponding load penetration

```
1 import numpy as np
2 import math
3
4 def calculate_penetration(sigma_x0, k_s_opt, sigma_s, d1, x_Emax, alpha_deg):
5     """
6     Calculates the penetration (vertical displacement) at maximum support
7     stress based on energy dissipation in the Dual-Wedge Stress-Field model.
8
9     Returns:
10     Penetration in mm
11     """
12     alpha_rad = math.radians(alpha_deg)
13     l_shear = x_Emax / math.cos(alpha_rad) # length shearplane (mm)
14
15     sigma_x = sigma_s
16     sigma_y = 0
17     tau_xy = 0
18
19     sigma_avg = 0.5 * (sigma_x + sigma_y)
20     sigma_diff = 0.5 * (sigma_x - sigma_y)
21     tau = -sigma_diff * np.sin(2 * alpha_rad) + tau_xy * np.cos(2 * alpha_rad)
22
23     Wdiss = tau * l_shear * math.cos(alpha_rad) # total dissipation (N·mm per mm width)
24     F = sigma_x0 * d1 # Force per mm width (N/mm)
25     u = Wdiss / F # penetration in mm
26     return u
27
28 sigma_x0 = 149.05
29 k_s_opt = 1
30 sigma_s = -10.25
31 d1 = 5
32 x_Emax = 53.10
33 alpha_deg = 25.57
```

```

34
35 u_shear = calculate_penetration(sigma_x0, k_s_opt, sigma_s, d1, x_Emax, alpha_deg)
36 print(f"Estimated penetration caused by shear along wedge: {u_shear:.2f} mm")
37
38 E_steel = 200000
39 L_casing = 230
40 u_casing = sigma_x0 * L_casing / E_steel
41
42 u_tot = u_shear + u_casing
43 print(f"Corresponding prescribed deformation on the steel casing: {u_tot:.2f} mm")

```

C.2. Python script secant moduli

```

1 import numpy as np
2 import matplotlib.pyplot as plt
3 import pandas as pd
4
5 # === Parameters (confined concrete - Mander model) ===
6 f_cc = 30e6 # Peak stress of confined concrete [Pa]
7 eps_cc = 0.00175 # Strain at peak stress [-]
8 E_c = 30e9 # Initial modulus of elasticity [Pa]
9
10 # === Derived parameters for Mander ===
11 E_sec_peak = f_cc / eps_cc
12 r = E_c / (E_c - E_sec_peak)
13
14 # === Mander stress-strain function (ascending branch) ===
15 def mander_stress(eps):
16     x = eps / eps_cc
17     # Avoid 0/0 at eps=0 by returning 0 stress there
18     sig = np.zeros_like(eps, dtype=float)
19     mask = eps > 0
20     x_m = x[mask]
21     sig[mask] = (f_cc * x_m * r) / (r - 1 + x_m ** r)
22     return sig
23
24 # === Discretize strain range up to peak (ascending branch only) ===
25 # Start slightly above zero to avoid division by zero in E_sec = sigma/eps
26 eps_vals = np.linspace(1e-10, eps_cc, 1000)
27 stress_vals = mander_stress(eps_vals)
28
29 # === Secant modulus E_sec = sigma / eps ===
30 secant_modulus = stress_vals / eps_vals # [Pa]
31
32 # === Compute average SECANT modulus per 5 MPa stress range ===
33 stress_ranges = [(i, i + 5e6) for i in range(0, int(f_cc), int(5e6))]
34 avg_moduli = []
35 for s_min, s_max in stress_ranges:
36     mask = (stress_vals >= s_min) & (stress_vals < s_max)
37     if np.any(mask):
38         Esec_avg = np.mean(secant_modulus[mask]) / 1e9 # GPa
39         avg_moduli.append((f"[{s_min/1e6:.1f}, {s_max/1e6:.1f})", f"{Esec_avg:.2f}"))
40     else:
41         avg_moduli.append((f"[{s_min/1e6:.1f}, {s_max/1e6:.1f})", "-"))
42
43 # === Print table as DataFrame (optional) ===
44 df_avg = pd.DataFrame(avg_moduli, columns=["Stress Range (MPa)", "Avg Secant Modulus (GPa)"])
45
46 # === Plot 1: -Stressstrain and SECANT modulus curve ===
47 fig, ax1 = plt.subplots(figsize=(10, 6))
48 ax1.set_xlabel("Strain [-]", fontsize=12)
49 ax1.set_ylabel("Stress [MPa]", fontsize=12)
50 ax1.plot(eps_vals, stress_vals / 1e6, label="-StressStrain")
51 ax1.tick_params(axis='y', labelsize=12)
52 ax1.tick_params(axis='x', labelsize=12)
53
54 ax2 = ax1.twinx()
55 ax2.set_ylabel("Secant Modulus [GPa]", fontsize=12)
56 ax2.plot(eps_vals, secant_modulus / 1e9, linestyle='--', label="Secant Modulus")
57 ax2.tick_params(axis='y', labelsize=12)

```

```

58
59 plt.title("-StressStrain and Secant Modulus (Mander Ascending Branch)", fontsize=14)
60 fig.tight_layout()
61 # Build a combined legend
62 lines1, labels1 = ax1.get_legend_handles_labels()
63 lines2, labels2 = ax2.get_legend_handles_labels()
64 fig.legend(lines1 + lines2, labels1 + labels2, loc="upper_right", bbox_to_anchor=(0.92, 0.92)
65 )
66 plt.show()
67
68 # == Plot 2: Formatted table with matplotlib ==
69 fig, ax = plt.subplots(figsize=(6, max(3, len(avg_moduli)*0.3)))
70 ax.axis('off')
71 table = ax.table(cellText=avg_moduli,
72                  colLabels=["Stress Range (MPa)", "Avg Secant Modulus (GPa)"],
73                  loc='center',
74                  cellLoc='center',
75                  colLoc='center')
76 table.auto_set_font_size(False)
77 table.set_fontsize(12)
78 table.scale(2, 1.5)
79 plt.title("Average Secant Modulus per Stress Range", pad=20)
80 plt.show()
81
82 # == Plot 3: Secant modulus and secant line at a specific stress level ==
83 target_stress = 20e6 # e.g., 20 MPa in Pascal
84
85 # Find closest point on curve to target stress
86 idx_target_candidates = np.where(stress_vals >= target_stress)[0]
87 if len(idx_target_candidates) == 0:
88     idx_target = len(stress_vals) - 1 # default to last point if target exceeds f_cc on
89     ascending branch
90 else:
91     idx_target = idx_target_candidates[0]
92
93 eps_target = eps_vals[idx_target]
94 sigma_target = stress_vals[idx_target]
95 Esec_target = (sigma_target / eps_target) / 1e9 # GPa
96 stress_target_MPa = sigma_target / 1e6
97
98 fig, ax = plt.subplots(figsize=(10, 6))
99 ax.set_xlabel("Strain [-]", fontsize=12)
100 ax.set_ylabel("Stress [MPa]", fontsize=12)
101 ax.plot(eps_vals, stress_vals / 1e6, label="-StressStrain")
102 ax.scatter([eps_target], [stress_target_MPa])
103 ax.axhline(y=stress_target_MPa, linestyle=':', label=f"{stress_target_MPa:.1f} MPa")
104
105 # Draw the secant line from origin to the target point
106 ax.plot([0.0, eps_target], [0.0, stress_target_MPa], linestyle='-.', label=f"Secant: {
107     Esec_target:.2f} GPa")
108
109 plt.title(f"Secant Modulus at {stress_target_MPa:.1f} MPa = {Esec_target:.2f} GPa", fontsize
110 =14)
111 ax.legend(loc="lower_right")
112 fig.tight_layout()
113 plt.show()

```

D

Derivation of the Distributed Force Function on the Pile Core

This appendix derives the expression for the distributed axial force in the pile core, based on the stiffness ratio between the steel casing and the concrete core, and relates it to the known normal stress in the casing, σ_{x0} .

Under the assumption that all connection components behave linear elastic, the total force is partitioned according to relative stiffness. The axial force carried by the casing is

$$F_{\text{casing}} = \sigma_{x0} A_{\text{casing}} , \quad \text{Eq. D.1}$$

where A_{casing} is the cross-sectional area of the steel casing.

Similarly, the axial force in the core is

$$F_{\text{core}} = q_x A_{\text{core}} , \quad \text{Eq. D.2}$$

where q_x is the unknown bearing stress in the concrete core and A_{core} its cross-sectional area.

Denote the total pile reaction by R_{pile} . The force in both components is related to R_{pile} via

$$F_{\text{casing}} = r_{\text{casing}} R_{\text{pile}} \implies R_{\text{pile}} = \frac{F_{\text{casing}}}{r_{\text{casing}}} , \quad \text{Eq. D.3}$$

$$F_{\text{core}} = r_{\text{core}} R_{\text{pile}} . \quad \text{Eq. D.4}$$

The stiffness ratios are defined as

$$r_{\text{casing}} = \frac{E_{\text{casing}} A_{\text{casing}}}{E_{\text{casing}} A_{\text{casing}} + E_{\text{core}} A_{\text{core}}} , \quad r_{\text{core}} = \frac{E_{\text{core}} A_{\text{core}}}{E_{\text{casing}} A_{\text{casing}} + E_{\text{core}} A_{\text{core}}} , \quad \text{Eq. D.5}$$

where E_{casing} and E_{core} are the respective Young's moduli.

Substituting $R_{\text{pile}} = F_{\text{casing}}/r_{\text{casing}}$, both stiffness ratio equations and both equations for total normal force in the segments $F_{\text{casing}} = \sigma_{x0} A_{\text{casing}}$ and $F_{\text{core}} = q_x A_{\text{core}}$ into the expression for F_{core} gives

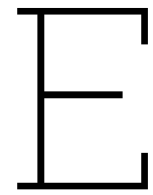
$$q_x A_{\text{core}} = \frac{E_{\text{core}} A_{\text{core}}}{E_{\text{casing}} A_{\text{casing}} + E_{\text{core}} A_{\text{core}}} \frac{\sigma_{x0} A_{\text{casing}}}{\frac{E_{\text{casing}} A_{\text{casing}}}{E_{\text{casing}} A_{\text{casing}} + E_{\text{core}} A_{\text{core}}} + \frac{E_{\text{core}} A_{\text{core}}}{E_{\text{casing}} A_{\text{casing}} + E_{\text{core}} A_{\text{core}}} , \quad \text{Eq. D.6}$$

Rewriting the equation by cancelling out the term $E_{\text{casing}} A_{\text{casing}} + E_{\text{core}} A_{\text{core}}$ in the numerator and the denominator after moving this term in the second part to the numerator. And finally, dividing by A_{core} and A_{casing} yields the distributed core stress,

$$q_x = \sigma_{x0} \frac{E_{\text{core}}}{E_{\text{casing}}}$$

Eq. D.7

as required.



Secant Modulus according to Mander's Model for Confined Concrete

To determine appropriate stiffnesses for the concrete segments in the case-study FEA, an iterative procedure was adopted. First, a baseline analysis was performed in which a uniform Young's modulus of 30 GPa was assigned to the entire concrete domain, irrespective of the prevailing compressive stress. The average stress in each segment was then extracted from this baseline. Using the Python script in section C.2, Mander's model for confined concrete was applied to compute the corresponding secant moduli for those average stress levels. These secant moduli were subsequently assigned to the respective segments, and the analysis was repeated with the reduced stiffnesses. The process was iterated until the change in segmental normal stress between iterations fell below a prescribed tolerance, at which point the solution was deemed converged. The results from the first and final iterations are presented in this appendix:

E.1. Secant Modulus according to the First Iteration

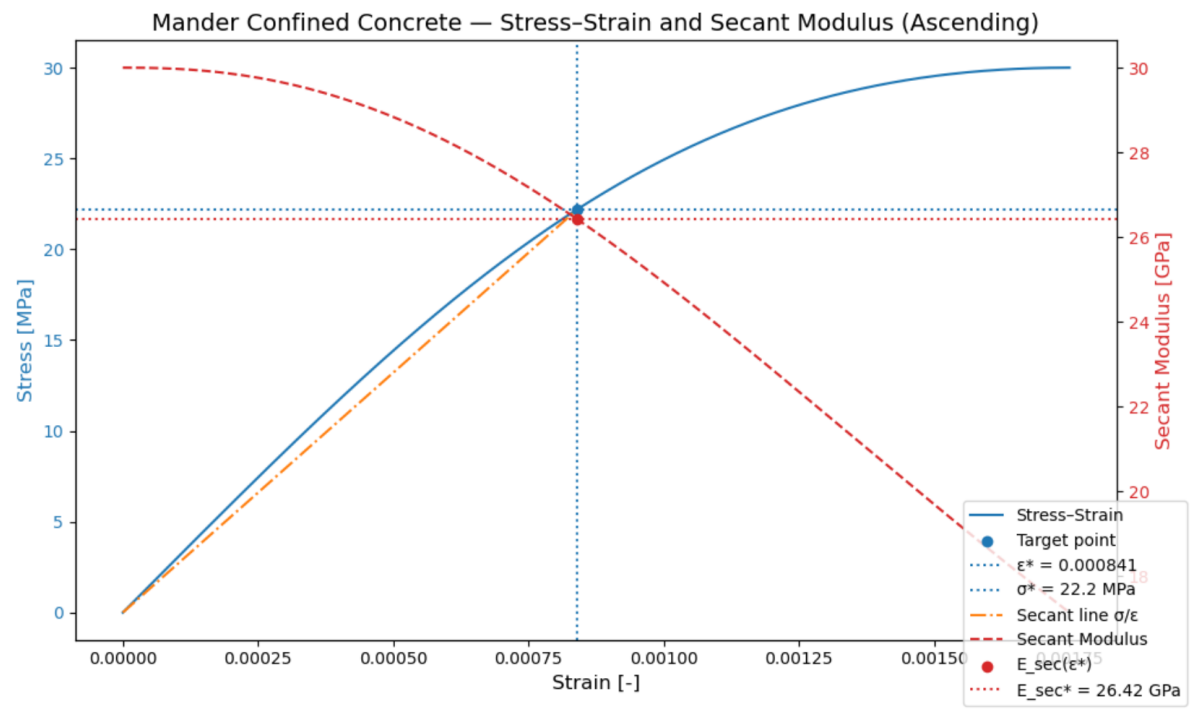


Figure E.1: First iteration secant modulus segment 3

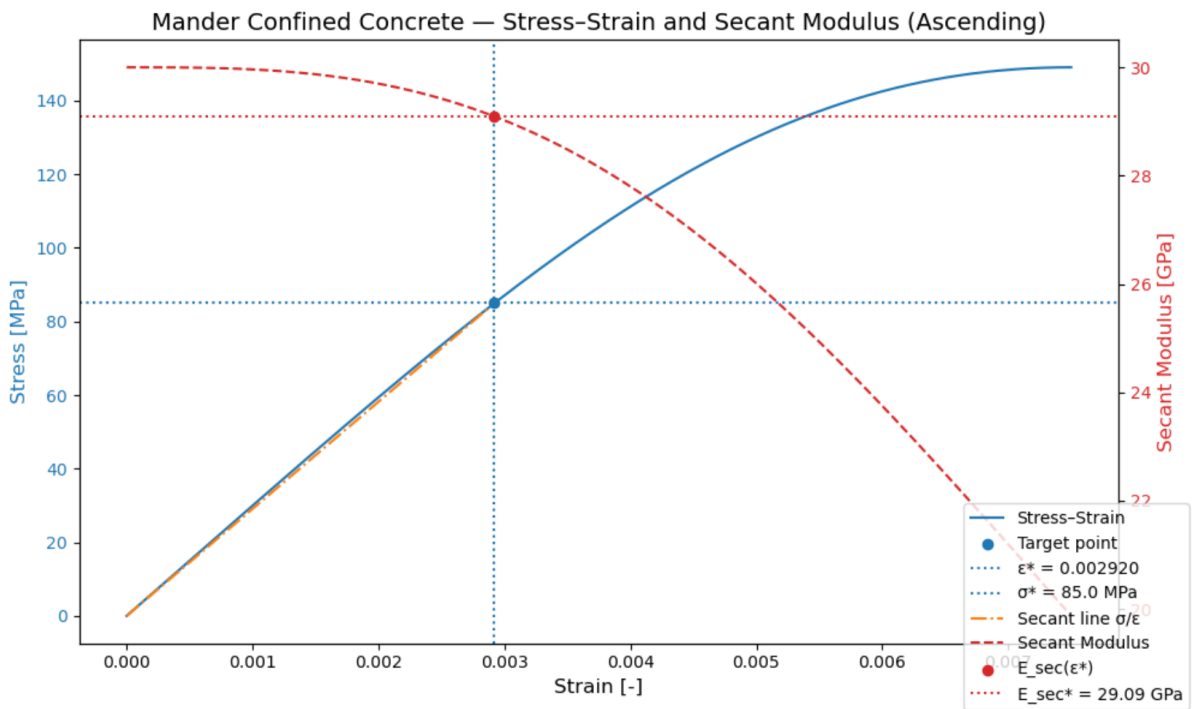


Figure E.2: First iteration secant modulus segment 4

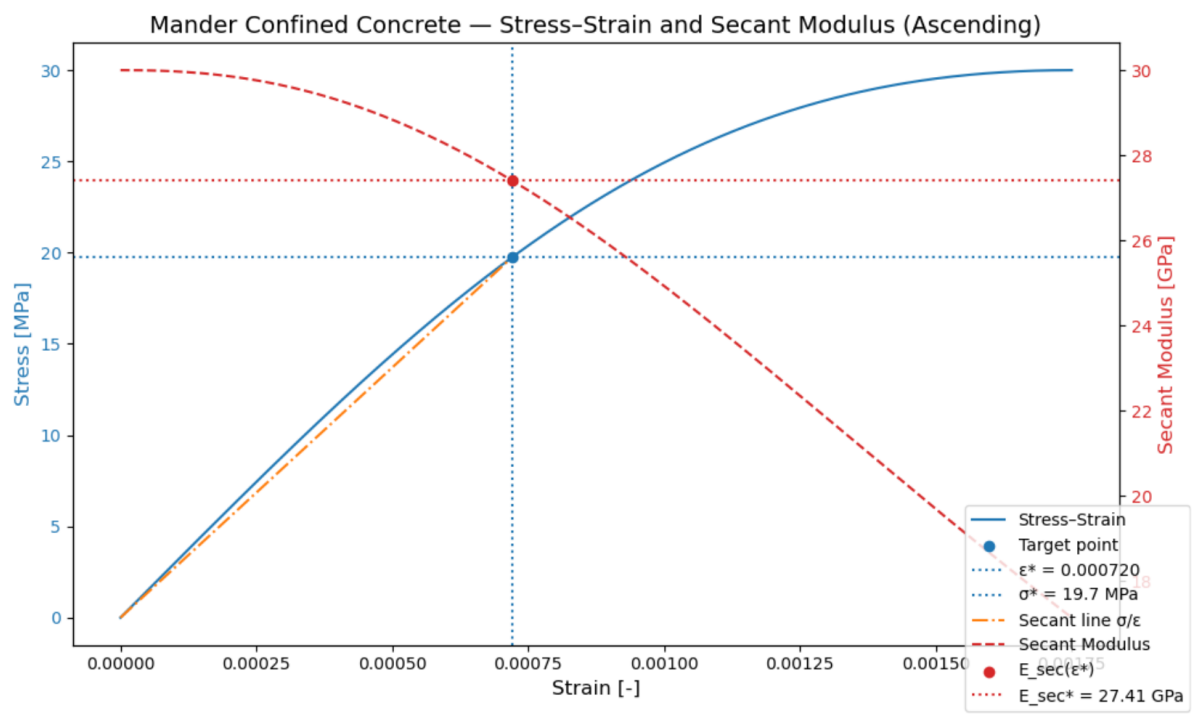


Figure E.3: First iteration secant modulus segment 5

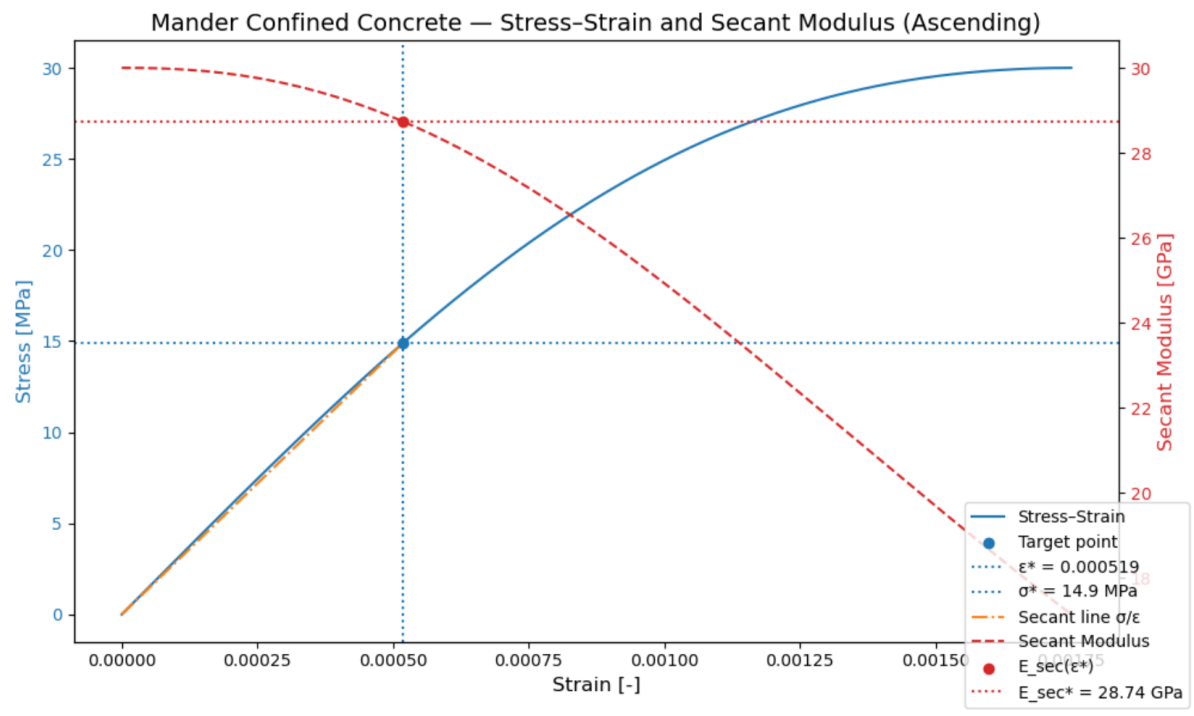


Figure E.4: First iteration secant modulus segment 6

E.2. Secant modulus according to the final iteration

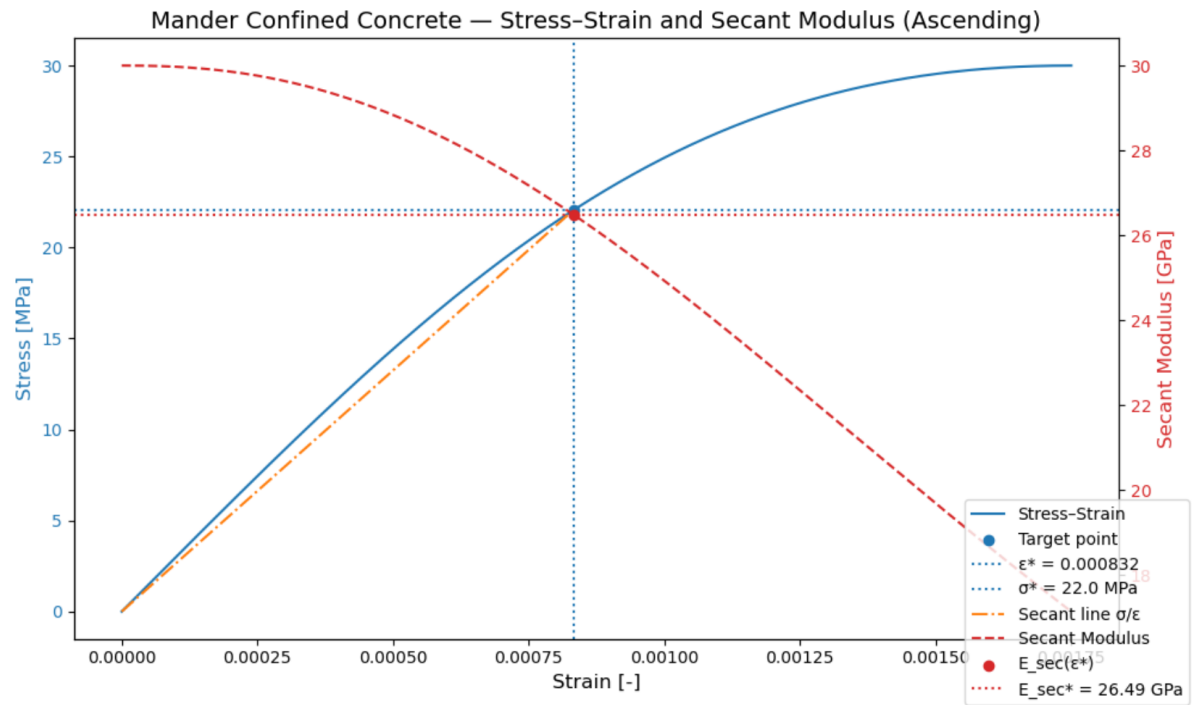


Figure E.5: Final iteration Secant modulus segment 3

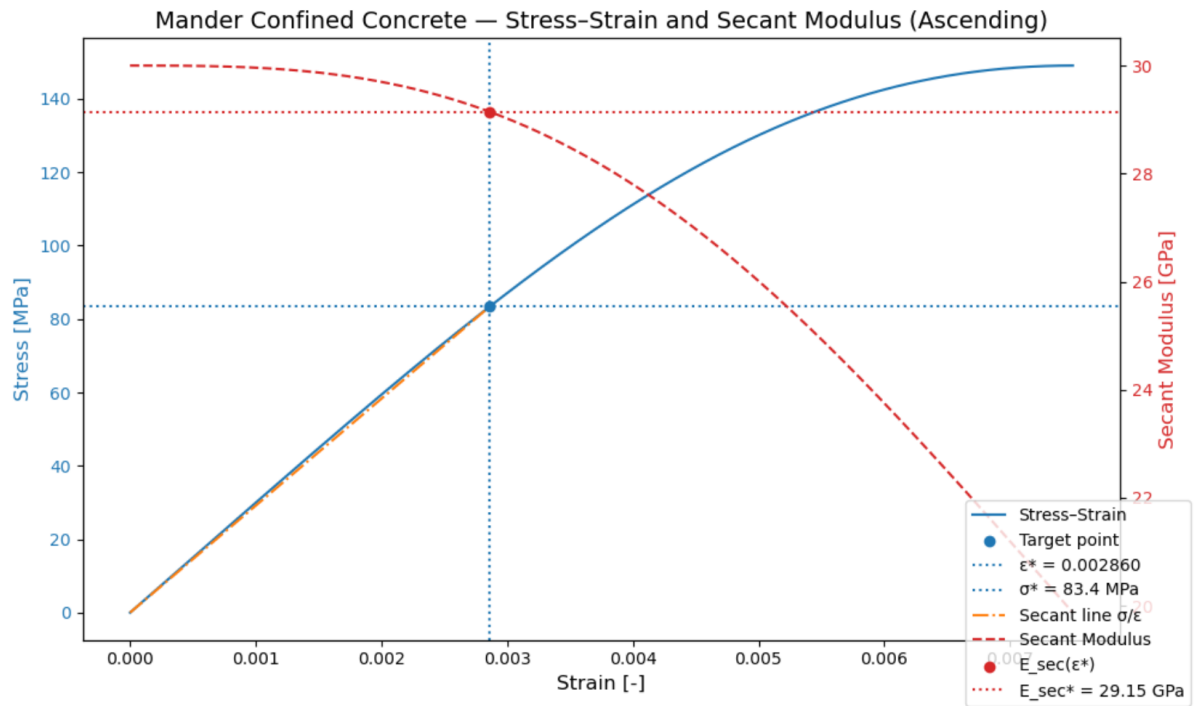


Figure E.6: Final iteration Secant modulus segment 4

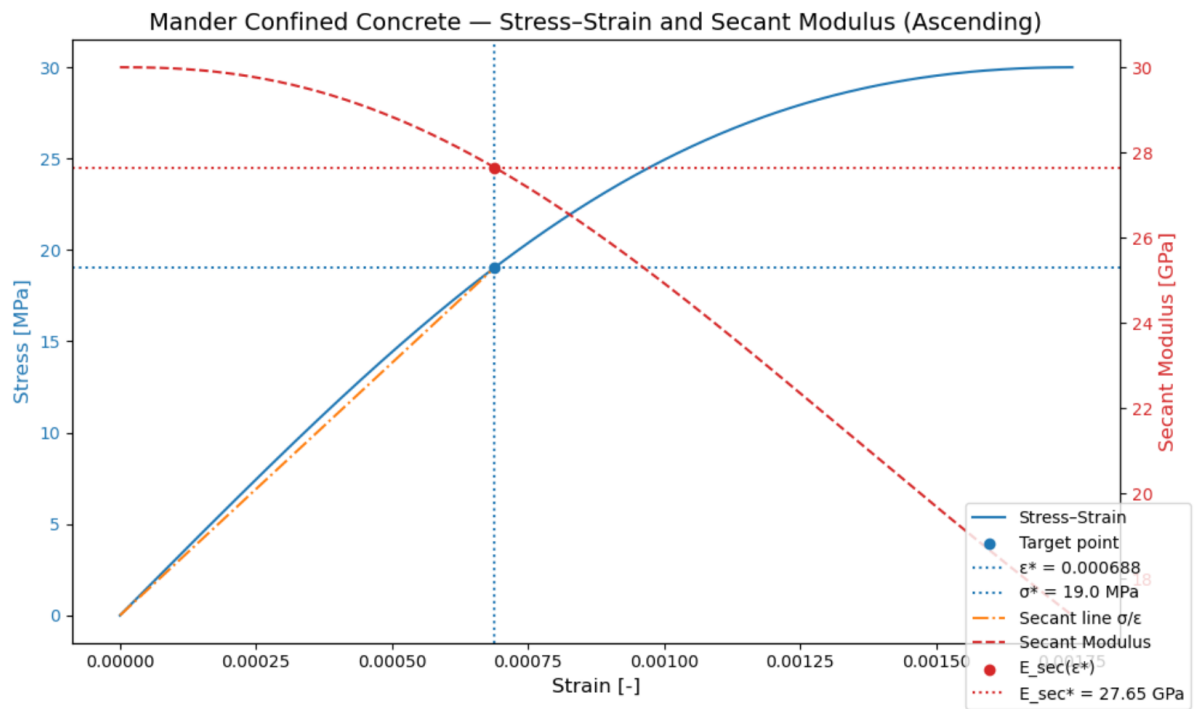


Figure E.7: Final iteration Secant modulus segment 5

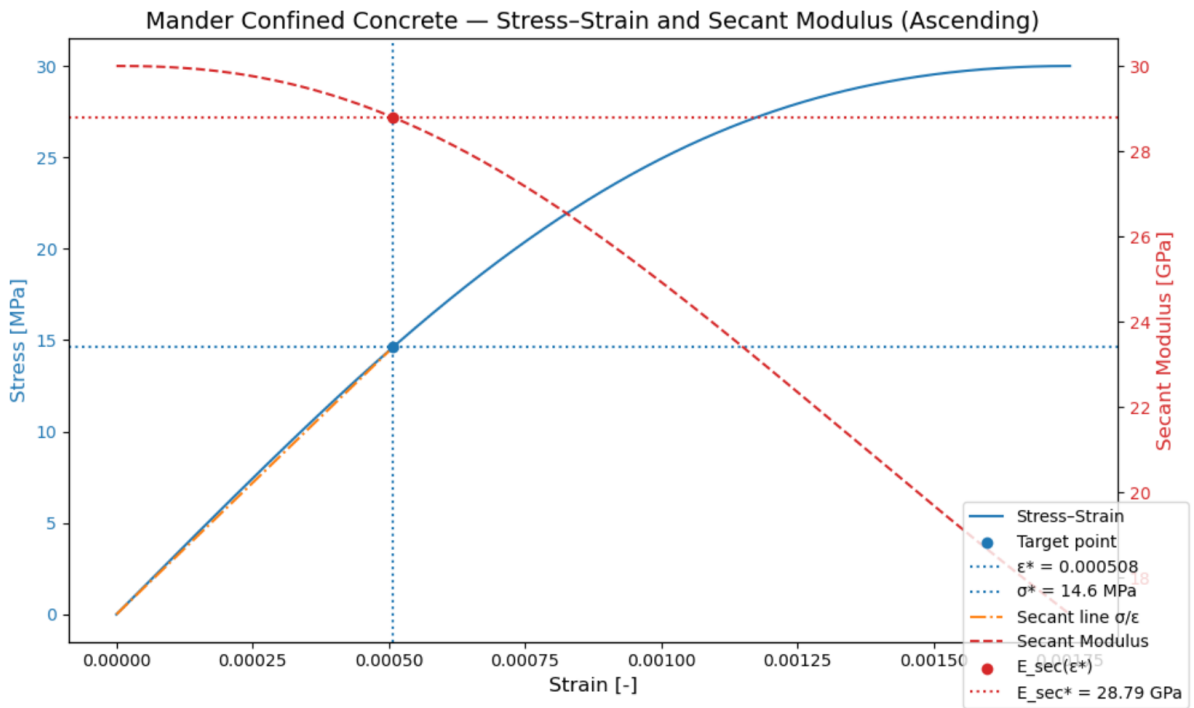


Figure E.8: Final iteration Secant modulus segment 6

E.3. Iteration history for the Expected Stress–Strain Behaviour

The table below shows the progress of the iterations and the steps that were performed to obtain the final concrete segment stiffness.

Table E.1: Iteration history of the case study FEA model

Iteration	Metric	Segments					
		1	2	3	4	5	6
1	S_{seg} [MPa]	-22.36	-22.36	-22.19	-84.85	-19.73	-14.86
	E_{sec} [GPa]	30.00	30.00	26.42	29.09	27.41	28.74
	ΔS_{seg} [MPa]	n.v.t.	n.v.t.	n.v.t.	n.v.t.	n.v.t.	n.v.t.
2	S_{seg} [MPa]	-22.36	-22.36	-22.04	-81.39	-19.18	-14.54
	E_{sec} [GPa]	30.00	30.00	26.49	29.20	27.60	28.80
	ΔS_{seg} [MPa]	0.00	0.00	0.15	3.46	0.54	0.32
3	S_{seg} [MPa]	-22.36	-22.36	-22.04	-83.41	-19.52	-14.59
	E_{sec} [GPa]	30.00	30.00	26.49	29.14	27.48	28.79
	ΔS_{seg} [MPa]	0.00	0.00	0.00	2.02	0.33	0.05
4	S_{seg} [MPa]	-22.36	-22.36	-22.04	-83.28	-19.51	-14.58
	E_{sec} [GPa]	30.00	30.00	26.49	29.15	27.48	28.80
	ΔS_{seg} [MPa]	0.00	0.00	0.00	0.13	0.00	0.00
5	S_{seg} [MPa]	-22.36	-22.36	-22.04	-83.30	-19.01	-14.59
	E_{sec} [GPa]	30.00	30.00	26.49	29.15	27.65	28.79
	ΔS_{seg} [MPa]	0.00	0.00	0.00	0.02	0.51	0.00
6	S_{seg} [MPa]	-22.36	-22.36	-22.04	-83.37	-19.01	-14.59
	E_{sec} [GPa]	30.00	30.00	26.49	29.14	27.65	28.79
	ΔS_{seg} [MPa]	0.00	0.00	0.00	0.07	0.00	0.00
7	S_{seg} [MPa]	-22.36	-22.36	-22.04	-83.36	-19.01	-14.59
	E_{sec} [GPa]	30.00	30.00	26.49	29.14	27.65	28.79
	ΔS_{seg} [MPa]	0.00	0.00	0.00	0.09	0.00	0.00

E.4. Iteration history for the lower limit Stress–Strain Behaviour

The table below summarises the iteration history and the steps taken to obtain the final segmental concrete stiffnesses consistent with the lower-bound stress–strain behaviour.

Table E.2: Iteration history of the lower strain bound case study FEA model

Iteration	Metric	Segments					
		1	2	3	4	5	6
1	S _{seg} [MPa]	-22,36	-22,36	-22,19	-84,85	-19,73	-14,86
	E _{sec} [GPa]	30	30	26,42	29,72	27,41	28,74
	ΔS _{seg} [MPa]	n.v.t.	n.v.t.	n.v.t.	n.v.t.	n.v.t.	n.v.t.
2	S _{seg} [MPa]	-22,36	-22,36	-22,03	-83,82	-19,57	-14,68
	E _{sec} [GPa]	30	30	26,49	29,73	27,47	28,78
	ΔS _{seg} [MPa]	0	0	0,16	1,03	0,15	0,18
3	S _{seg} [MPa]	-22,36	-22,36	-22,04	-83,86	-19,52	-14,59
	E _{sec} [GPa]	30	30	26,49	29,73	27,48	28,79
	ΔS _{seg} [MPa]	0	0	0,00	0,05	0,05	0,09
4	S _{seg} [MPa]	-22,36	-22,36	-22,04	-83,88	-19,52	-14,69
	E _{sec} [GPa]	30	30	26,49	29,73	27,48	28,78
	ΔS _{seg} [MPa]	0	0	0,00	0,02	0,00	0,10
5	S _{seg} [MPa]	-22,36	-22,36	-22,04	-83,88	-19,52	-14,69
	E _{sec} [GPa]	30	30	26,49	29,73	27,48	28,78
	ΔS _{seg} [MPa]	0	0	0,00	0,00	0,00	0,00

E.5. Iteration history for the upper limit Stress–Strain Behaviour

The table below summarises the iteration history and the steps taken to obtain the final segmental concrete stiffnesses consistent with the upper-bound stress–strain behaviour.

Table E.3: Iteration history of the upper strain bound case study FEA model

Iteration	Metric	Segments					
		1	2	3	4	5	6
1	S _{seg} [MPa]	-22,36	-22,36	-22,19	-84,85	-19,73	-14,86
	E _{sec} [GPa]	30	30	26,42	29,09	27,41	28,74
	ΔS _{seg} [MPa]	n.v.t.	n.v.t.	n.v.t.	n.v.t.	n.v.t.	n.v.t.
2	S _{seg} [MPa]	-22,36	-22,36	-22,04	-82,41	-19,54	-14,65
	E _{sec} [GPa]	30	30	26,49	28,48	27,48	28,79
	ΔS _{seg} [MPa]	0	0	0,15	2,44	0,19	0,21
3	S _{seg} [MPa]	-22,36	-22,36	-22,04	-82,59	-19,50	-14,57
	E _{sec} [GPa]	30	30	26,49	28,48	27,49	28,80
	ΔS _{seg} [MPa]	0	0	0,01	0,18	0,05	0,09
4	S _{seg} [MPa]	-22,36	-22,36	-22,04	-82,61	-19,50	-14,66
	E _{sec} [GPa]	30	30	26,49	28,48	27,49	28,79
	ΔS _{seg} [MPa]	0	0	0,00	0,02	0,00	0,10
5	S _{seg} [MPa]	-22,36	-22,36	-22,04	-82,61	-19,50	-14,66
	E _{sec} [GPa]	30	30	26,49	28,48	27,49	28,79
	ΔS _{seg} [MPa]	0	0	0,00	0,00	0,00	0,00